EuO and Eu on metal crystals and graphene: interface effects and epitaxial films

I n a u g u r a l - D i s s e r t a t i o n

zur

Erlangung des Doktorgrades

der Mathematisch-Naturwissenschaftlichen Fakultät

der Universität zu Köln

vorgelegt von

Dipl.-Phys. Daniel F. Förster

aus Stolberg (Rheinland)

Köln 2011

Berichterstatter:	Prof. Dr. Thomas Michely
(Gutachter)	Prof. Dr. L. Hao Tjeng
Vorsitzender der Prüfungskommission:	Prof. Dr. Achim Rosch

Tag der mündlichen Prüfung: 14.10.2011

Abstract

Growth of the ferromagnetic semiconductor EuO was studied on the metal crystals Ni(100) and Ir(111) and on graphene. Primarily, characterisation was done by means of in-situ scanning tunnelling microscopy (STM) and low energy electron diffraction. The epitaxy on the metal crystals is strongly influenced by interface effects which lead to a complicated growth behaviour in the sub-monolayer regime, especially on Ni(100). Therefore, also films of sub-monolayer thickness were analysed in detail for these substrates.

Eu oxide on Ni(100) shows a variety of different surface phases in the sub-monolayer regime, depending on the growth temperature and the ratio of the Eu and O fluxes. Hence, a careful selection of the initial growth parameters is decisive to obtain a surface oxide suitable for subsequent epitaxy of single phase EuO(100). After creation of a 3 layer thick coalesced oxide film, for subsequent growth a distillation technique can be applied. Ex-situ X-ray adsorption spectroscopy and magneto-optical Kerr effect microscopy measurements of thicker films on Ni(100) are consistent with stoichiometric single phase EuO with bulk properties.

On Ir(111) initially only islands of polar EuO(111) grow, but formation of EuO(100) sets in before the first oxide layer is completed. The ratio of EuO(100) to EuO(111) is thereby influenced by the ratio of the Eu and O fluxes. Thus, the EuO films on Ir(111) consist of a phase mixture of EuO(111) and three rotational domains of EuO(100). The thinnest structure of the EuO(111) is a bilayer. Field emission resonances revealed a work function increase of 6 eV for this structure compared to EuO(100). Despite the polarity, the bilayer shows no obvious reconstruction which could reduce the high electric field. Triangular reconstruction motifs were found for the third EuO(111) layer.

On graphene EuO can be grown as thin film of distinct, {100}-faceted grains which are oriented to the substrate at a sufficiently high growth temperature. As the EuO on graphene is not affected by interface effects, the initial growth stage is not crucial. Thus, the growth of these grains is far less sensitive to the ratio of Eu and O fluxes than the EuO growth on Ni(100).

Appropriate annealing of EuO(100) films generates sufficient conductivity for STM and electron spectroscopies, even for films of 100 nm thickness. Oxygen vacancies were

directly imaged by STM. They are of decisive importance for the metal-to-insulator transition of EuO around the temperature of the ferromagnetic-to-paramagnetic transition. Tunnelling spectra of EuO were recorded for the first time. For EuO(100) with 1% O vacancies in the topmost layer they exhibit states about 500 meV above the Fermi level which are most probably related to O vacancies.

On all substrates, monolayer high EuO(100) films have a contracted lattice which expands with increasing film thickness. Even if the substrate applies compressive biaxial stress, the EuO bulk lattice constant is almost reached for 5 nm film thickness. This leaves little hope for an increase of the Curie temperature through epitaxial compression.

During the investigation of the EuO on graphene, intercalation of Eu between the graphene and its Ir(111) substrate was observed and analysed further. For Eu deposition at 720 K a variety of equilibrium intercalate structures occur, dependent on the deposited Eu amount, all of which have a height of one monolayer. The dimensions and orientations of these structures are determined by binding energy differences within the unit cell of the graphene moiré on Ir(111). The energetically preferred lattice of the intercalated Eu is a p(2×2) structure, but intercalation continues until a denser $(\sqrt{3} \times \sqrt{3})$R30° structure is saturated. Angular resolved photoemission spectroscopy finds a shift of the graphene's Dirac cone by -1.5 eV for both of these structures.

For closed graphene films, intercalation is hindered by a penetration barrier for temperatures below 400 K. The adsorption and equilibrium surface phases of Eu on graphene were investigated in the temperature range from 35 K to 400 K and for coverages ranging from a small fraction of a saturated monolayer to the second layer. Using density functional theory, including the 4f-shell Coulomb interactions and modelling of the electronic interactions, excellent agreement with the experimental results for the equilibrium adsorbate phase, adsorbate diffusion, and work function was obtained. Most remarkable, at 300 K in an intermediate coverage range a phase of uniformly distributed Eu clusters coexists in two dimensional equilibrium with large Eu-islands in a $(\sqrt{3}\times\sqrt{3})$R30° structure. The formation of the cluster phase is driven by the interplay of three effects: First, the metallic Eu-Eu binding leads to the local stability of $(\sqrt{3} \times \sqrt{3})$R30° structures. Second, electrons lower their kinetic energy by leaving the Eu clusters, thereby doping graphene. Third, the Coulomb energy penalty associated with the charge transfer from Eu to graphene is strongly reduced for smaller clusters.

Contents

Frequently used symbols and abbreviations

Θ	exposure: amount of material hitting the surface with or without sticking
f_{Eu}	Europium atom flux
f_{O}	Oxygen atom flux
I_{t}	Tunnelling current
T_{C}	Critical Temperature; here mostly the ferromagnetic transition temperature
U_{s}	Sample bias voltage
ARPES	Angle Resolved PhotoEmission Spectroscopy
DOS	Density Of States
FWHM	Full Width at Half Maximum
LDOS	Local Density Of States
LEED	Low Energy Electron Diffraction
MIT	Metal to Insulator Transition
STM	Scanning Tunnelling Microscopy
STS	Scanning Tunnelling Spectroscopy
UHV	Ultra High Vacuum
E_{F}	Fermi level
bcc	base centred cubic
BL	BiLayer
DFT	density functional theory
fcc	face centred cubic
hcp	hexagonal close packed
ML	MonoLayer
MLE	MonoLayer Equivalents
MOKE	Magneto Optical Kerr Effect
NN	Nearest Neighbour
CVD	Chemical Vapour Deposition
FER	Field Emission Resonance

L	Langmuir = 10^{-6} Torr $\cdot$ s $\approx 1.33 \times 10^{-6}$ mbar $\cdot$ s
QMS	Quadrupole Mass Spectrometer
SBZ	Surface Brillouin Zone
TPG	Temperature Programmed Growth

1 Introduction

Europium Monoxide (EuO) is a compound with several unique properties and was first grown in the 1950s [1]. Since 1961 it has aroused considerable interest, especially due to the discovery of the simultaneous presence of ferromagnetism and semiconductivity [2], which is a rare combination. At room temperature stoichiometric EuO is a paramagnetic semiconductor with a band gap of 1.1 eV [3] and becomes ferromagnetic below 69 K. Its high exchange splitting of the conduction band below T_C results in a high spin polarisation of the charge carriers at the Fermi edge [4; 5]. This, together with the semiconductivity makes EuO an attractive material for spin-injection into semiconductor-based spintronic devices. Hence spintronics was the main motivation for EuO research during the last decade [4–35]. This was boosted by the improvements of thin film deposition techniques, which lead to the possibility of epitaxially integrating EuO with mainstream semiconductors such as silicon and GaN [16].

Spintronics [36] is an abbreviation for spin-based electronics, which means either the addition of the spin degree of freedom to conventional charge-based electronic devices or the usage of the spin alone as carrier for the information. Potential advantages of spintronics compared to conventional semiconductor devices are non-volatility, increased data processing speed, decreased electric power consumption, and increased integration densities [37]. Achieving efficient coherent spin injection into a semiconductor is a key requirement for spintronics and needs a material which has highly spin polarised charge carriers at the Fermi edge and whose conductivity can be matched to the same order of magnitude as that of the semiconductor [36; 38]. EuO fulfils these criterions [16] but has for applications the practical disadvantage of the low ferromagnetic transition temperature of 69 K. An increase of T_C can be achieved either by doping [8; 14; 39] or by compressive strain [17; 40; 41]. Increasing T_C by doping has the disadvantage of influencing the conductivity and thus creates conflicts with the requirement of conductivity matching. This leaves the possibility of compressive strain, whereby due to the low Poisson ratio of EuO already biaxial strain increases T_C [17]. Biaxial compressive strain can be achieved by compressive epitaxial stress (i.e., by epitaxial growth of thin films on a substrate with slightly smaller surface lattice constant). By fulfilling the principal aim of this thesis, the epitaxial growth of EuO thin films on conductive substrates, it was also possible to analyse the possibility of introducing compressive biaxial strain by using substrates with smaller surface lattice constants, which are Ni(100) and graphene on Ir(111).

The second most remarkable peculiarity of EuO is the metal to insulator transition (MIT) which occurs simultaneously with the ferromagnetic transition. The change in resistivity can exceed 10 orders of magnitude [42–44], which is the largest value ever observed during an MIT. Hence it motivated several investigations [45–56], especially as the mechanism of the MIT is still not fully understood. It only occurs for doped EuO and the reason is supposed to lie in the presence of oxygen vacancies [57], although there exist models for an MIT in purely Gd doped samples [55] and also reports of an MIT in Gd doped samples which are claimed to be non oxygen-deficient [8; 42; 46].

Proposed models to describe the MIT are the helium model [45] and the bound magnetic polaron (BMP) model [47; 53], which lack experimental proof up to now. More recently the MIT was calculated within a ferromagnetic Kondo lattice model [49; 51; 52].

An experimental ansatz to gain insight into the mechanism of the MIT is the observation of inhomogeneities in EuO, which are theoretically connected to the BMP model [53]. Evidence for magnetic inhomogeneities in EuO was found by Raman scattering studies [50], nuclear magnetic resonance measurements [10], and by infrared reflectivity measurements [58], the latter including spatial imaging. The inhomogeneities were found to be static in the time-scale of hours in the temperature range of 40 K to 80 K, i.e., around T_C, but due to the spatial resolution of 5 µm only and the lack of a connection to structural features (e.g., grain boundaries, dislocations, or oxygen vacancies) these measurements could not lead to a detailed understanding of the inhomogeneities. Scanning tunnelling spectroscopy is a powerful tool to reveal, atomically resolved, the local electronic differences [59–61], while being able to detect possible structural origins. For example, BMPs located at the oxygen vacancies should form percolative paths during an MIT which are easily observable in STS conductivity maps of flat EuO terraces.

A prerequisite for reasonable STS measurements and other electron spectroscopies of insulating oxides is the growth of high quality epitaxial thin films on metallic substrates, thereby creating samples with sufficient conductivity. Tailoring properties such as grain size and defect density enables a systematic analysis of the connection between structural and electrical inhomogeneities or even to the magnetic inhomogeneities when using spin polarised STS [62; 63]. The main motivation for the growth of EuO films on conductive substrates is thus the fundamental interest to analyse EuO films by STS and other electron spectroscopies.

For this thesis, the growth and characterisation of EuO was performed on Ni(100) (chapter 5), Ir(100) and Ir(111) (chapter 6) and graphene on Ir(111) (chapter 7). The latter substrate gives also a connection to a possible system for spintronics [64] and lead to the interesting analysis of Eu intercalation patterns on the graphene moiré on Ir(111) and of a novel phase coexistence of Eu clusters and islands on graphene (chapter 8). The experimental setup which was used to realise the experiments is described in chapter 3 together with necessary design modifications. The details of the growth process as well as some of the used measurement techniques are explained in chapter 4. The necessary physical background for this thesis is given in chapter 2, following this introduction.

2 Background

In the introduction already the most prominent peculiarities of EuO were described. This chapter now starts with a description of the basic properties of EuO and of additional important features of this astonishing material. Then in Sec. 2.2 an introduction to surface oxides is given, the knowledge of which is necessary to understand the formation of oxide structures on metal substrates and the importance of the initial film growth parameters for the film morphology. Even if a steady growth of the bulk like oxide has started, the formation of a high electrostatic potential can occur for certain film orientations. This happens for the so called polar surfaces, a brief overview of which is given in Sec. 2.3. Additionally to the metal substrates Ni(100), Ir(100), and Ir(111) also graphene on Ir(111) was used in this thesis. Therefore, in Sec. 2.4 a short introduction to graphene, especially to the system graphene/Ir(111), is given.

2.1 EuO - a manifold material

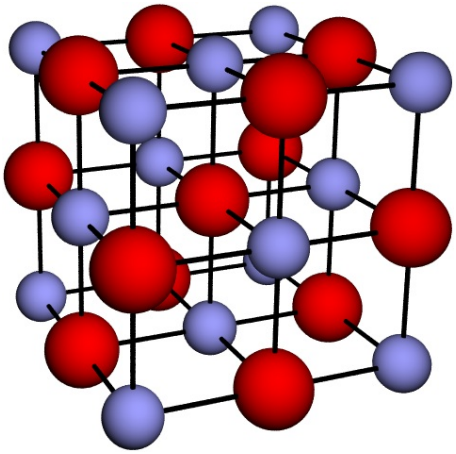

Figure 2.1: Ball and stick model of the rock-salt crystal structure of EuO. Red balls represent O atoms and blue balls Eu atoms.

Despite its outstanding and manifold properties, EuO crystallises in the simple rock-salt structure (Fig. 2.1), i.e. in an fcc lattice with a two atom basis, and has a lattice constant of $a = 5.144\,\text{Å}$ at room temperature [4]. EuO has an ionic $Eu^{2+}O^{2-}$ character with the electronic configuration $[Xe]4f^7 5d^0 6s^0$ of the Eu^{2+}-ion. The energy levels which are important for the magnetic and electronic properties of EuO, i.e. those which are near the the Fermi level, are the O $2p$ orbitals, the Eu $4f$ orbitals, and the Eu $5d$-$6s$ conduction band. EuO is formed by oxidation of the highly reactive Eu metal ($[Xe]4f^7 5d^0 6s^2$) with a heat of formation of $\Delta H_f(\text{EuO}) = -608\,\text{kJ/mol}$ (i.e. $6.3\,\text{eV/Eu atom}$) which is not a stable composition but further oxidises to Eu_2O_3 with $\Delta H_f(Eu_2O_3) = -1730\,\text{kJ/mol}$ (i.e. $9.0\,\text{eV/Eu atom}$) [9].

In connection to the ferromagnetism and the MIT several additional effects were observed in EuO, such as colossal magneto-resistance (CMR) [43], photoconductivity [65], and large magneto-optical effects [66; 67]. Because of the spherical symmetric $^8S_{7/2}$ ground state (i.e. the magnetic moment is a pure spin moment of $7\,\mu_B$/ion) the magnetic exchange interactions are isotropic and the Heisenberg model can be applied to EuO [39], i.e. the magnetic interactions can be described by the Hamiltonian

$$\mathcal{H} = -\sum_{i,j} J_{ij}\vec{S}_i\vec{S}_j. \tag{2.1}$$

Since there are models available to treat this Hamiltonian in lattices with cubic symmetry, EuO is often considered as benchmark system for an ideal Heisenberg ferromagnet and thus numerous theoretical studies were carried out [11; 39; 49; 52; 68–71].

The most important exchange mechanism in EuO is indirect exchange between Eu nearest neighbours (NN), consisting of virtual transitions of $4f$ electrons to a $5d$ or $6s$ state [39; 71]. These can be represented by an exchange constant J_1, whereby the sum in Eq. 2.1 has to be taken for all NN j of the i atoms. Additional contributions come from superexchange mechanisms which occur between Eu next nearest neighbours (NNN) and are mediated by p electrons of the anion [39]. The corresponding sum in Eq. 2.1 has to be taken for all NNN j of the i atoms using the exchange constant J_2. Inelastic neutron-scattering studies on EuO single crystals determined the exchange constants to be $J_1/k_B = 0.625\,\mathrm{K}$ and $J_2/k_B = 0.125$ [72] (i.e. both ferromagnetic), but these values give a too low Curie temperature of $T_C = 56\,\mathrm{K}$ in the Heisenberg model [70]. A refined theoretical model, using a combination of local-spin-density and Hubbard 1 approximations [71], suggests that only the indirect exchange ($J_1/k_B = 0.60\,\mathrm{K}$) effectively contributes and the superexchange ($J_2/k_B = 0.03\,\mathrm{K}$) is negligible [71]; but this model overestimates T_C to 81 K.

2.1.1 Electronic structure

The first experimental determination of the EuO band structure was done by optical measurements [39] and later refined using modern electron spectroscopies [4; 30; 73]. Also several band structure calculations were performed [17; 49; 68; 71; 74]. In the paramagnetic state, the bottom of the conduction band (mainly a Eu $5d_{t_{2g}}$[1] band) is situated 1.1 eV above the top of the Eu $4f$ valence band. Below T_C the conduction bands split by 0.6 eV [4], thereby reducing the band gap by half of this value. This effect was first observed as redshift of the optical absorption edge in bulk EuO [57].

Figure 2.2 shows the spin-split EuO band structure, calculated by Ingle and Elfimov with the full-potential linearised augmented plane-wave density functional theory (DFT) code WIEN2K

[1] In oxide crystals like EuO the degeneracy of the d orbitals is lifted. Bands of t_{2g} symmetry consist of orbitals which point into the direction of neighbouring Eu atoms ($3d_{xy}$, $3d_{xz}$, and $3d_{yz}$) and are (for the same spin orientation) lower in energy than bands of e_g symmetry, which consist of orbitals which point into the direction of the O atoms ($3d_{z^2}$ and $3d_{x^2-y^2}$).

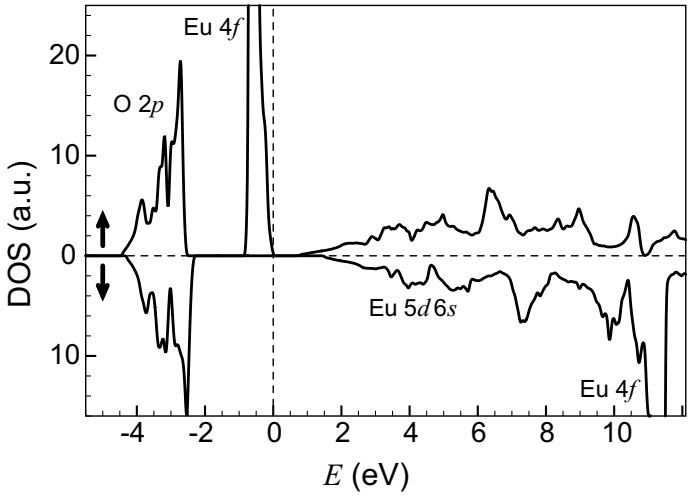

Figure 2.2: The spin resolved DOS of bulk EuO, reproduced from [17]. The contributions of the different bands are labelled and the zero of energy is at the Fermi level E_F .

[17][1]. Albeit other calculations of the density of states (DOS) differ in details, the general positions of the bands are certain.

2.1.2 N-Doping

There exist several ways to electron-dope EuO whereby the most extensively used methods are the introduction of O vacancies and the substitution of Eu by Gd [8; 14; 28; 39; 46; 57]. The electronic configuration of Gd is $[Xe]4f^7 5d^1 6s^2$, i.e. the same as Eu plus one additional $5d$ electron. Hence the Gd^{3+}-ion has the same electronic configuration as the Eu^{2+}-ion and leaves the $4f$ spin-system untouched, i.e. it only supplies carriers to the solid. O vacancies are introduced by supplying excess Eu which cannot be incorporated as interstitials due to the large size of the Eu atom.

The doping affects T_C of EuO as well as the transport properties, but there exist several discrepancies about the details. For example, it is not clear whether a threshold of the Gd concentration has to be exceeded before T_C starts to increase or if Gd doping alone is sufficient for the MIT to occur [28]. At least, the existence of the MIT in Eu-rich EuO is undoubted as well as the absence of the MIT in undoped EuO. The conductivity of EuO at room temperature was reported to change drastically from $3 \times 10^{-8}\ \Omega^{-1}\ cm^{-1}$ for stoichiometric EuO over $5 \times 10^{-5}\ \Omega^{-1}\ cm^{-1}$ for 0.3% O vacancies to metallic conductance with $27\ \Omega^{-1}\ cm^{-1}$ for 0.5% O vacancies [75].

Infrared absorption spectra of Eu-rich samples display two discrete humps at 0.55 eV and 0.65 eV in the absorption coefficient which have to be related to O vacancies [57]. As the adsorption edge itself corresponds to a $4f^7$-$4f^6 5d_{t_{2g}}$ transition [57], i.e. to the EuO band gap of 1.1 eV, these two humps possibly belong to transitions involving vacancy states which hence should lie close to the centre of the intrinsic band gap.

[1]They treated the exchange and correlation effects within the generalized gradient approximation (GGA) and the local spin density approximation + U (LSDA+U) method was used to account for strong correlations between the electrons in the Eu $4f$ shell, because standard GGA or LSDA predict EuO to be a metal whereas measurements clearly show the existence of a conductivity gap.

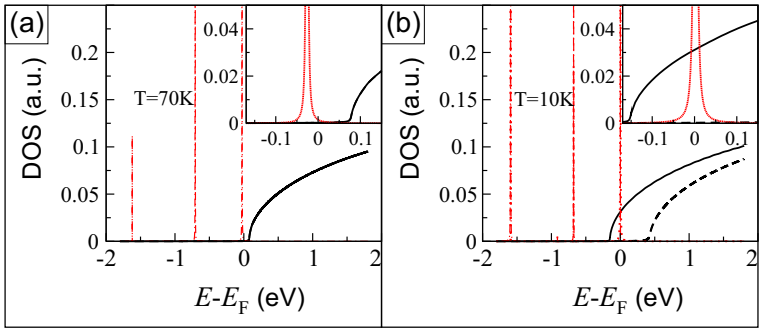

Figure 2.3: DOS of Eu-rich EuO calculated in the FKL model, reproduced from [51]. Impurity states of the O vacancies are represented by red lines and conduction band states by black lines. The insets shows details of the region around the Fermi level. **(a)** $T = 70\,\mathrm{K}$, i.e. just above T_C. Due to the impurity states the Fermi level is shifted considerably towards the conduction band compared to the case of stoichiometric EuO shown in Fig. 2.2. **(b)** $T = 10\,\mathrm{K}$, the conduction band is spin split (continuous and dashed lines indicate different spin orientations) and one branch moves below the impurity level at E_F.

Figure 2.3 displays the DOS of EuO calculated within the ferromagnetic Kondo lattice (FKL) model [51]. It enables a qualitative understanding of the MIT in EuO, which differs from the simple He model just in the number of the impurity states of the O vacancies, the positions of which are temperature independent. Compared to stoichiometric EuO the Fermi level is shifted considerably towards the conduction band due to the impurity states (represented by red lines). Above T_C [Fig. 2.3(a)] the conductivity behaves like usual for an n-doped semiconductor. Due to the spin splitting of the conduction band (black lines) below T_C the down-shifted part overlaps the impurity state, thereby transferring impurity electrons into the conduction band which is almost 100% spin polarised.

2.1.3 Surface State

As one goal of this thesis is to create high quality EuO films for STS, differences in the local density of states (LDOS) at the surface compared to the usually considered bulk states have to be taken into account. Calculations within the ferromagnetic Kondo lattice model [48; 49] predict a surface state for stoichiometric EuO(100) which is spin split below T_C and leads to a surface metal to insulator transition. This is shown in Fig. 2.4 by the corresponding spin resolved spectral DOS[1] (SDOS) of a 20 layer thick EuO film at the $\overline{\Gamma}$ point [48]. The surface state lies 0.8 eV below the edge of the bulk conduction band, a downshift which is nearly temperature independent. By the additional spin splitting below T_C of 0.6 eV [4] the spin-up branch (left hand side in Fig. 2.4) is shifted 0.3 eV further downwards, thereby crossing the Fermi level [48]. Thus, differently to the bulk MIT this surface transition should also occur for undoped EuO films.

In STM/STS measurements the tunnelling current is, for small voltages (i.e. at energies near the Fermi level), dominated by contributions from states near the $\overline{\Gamma}$ point [76], hence one would

[1]The spectral DOS is directly related to observable quantities within angle-resolved direct and inverse photoemission experiments.

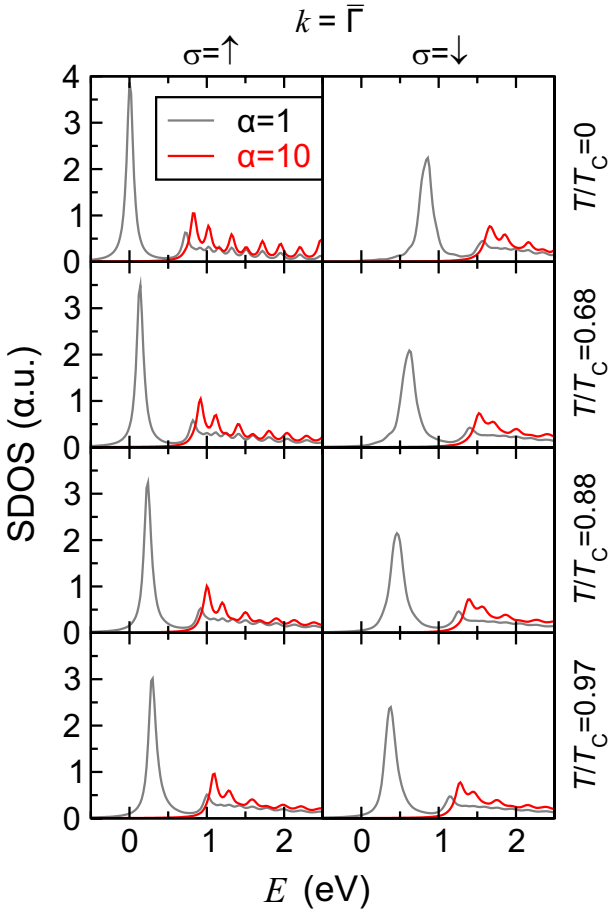

Figure 2.4: The spin resolved spectral DOS of a 20 layer thick stoichiometric EuO film at the $\overline{\Gamma}$ point, reproduced from [48]. The grey lines represent the SDOS of the topmost layer and the red lines that of the central layer.

expect the DOS features as displayed in Fig. 2.4 to be present in STS spectra.

2.1.4 Thin Films

The first EuO thin films were grown in 1967 [77] as alternative synthesis routes for preparing EuO, as stoichiometric single crystals are difficult to prepare due to the required accurate starting compositions and very high temperatures of about 2100 K [75]. Additionally, the thin film preparation facilitated doping dependence studies using rare earth and transition metals as impurities [67; 78–80].

The films grown in the 1960s and 1970s were prepared with high growth rates under technical vacuum conditions, i.e., at pressures in the range of 10^{-6} - 10^{-5} mbar [27; 67; 81]. After a pause of two decades, a strong renewed interest in EuO thin films emerged in recent years [27], motivated by the attempt to utilise the extraordinary properties of EuO for device applications [4; 6–9; 13; 14; 16; 21; 27; 73; 82]. These newer studies benefited from the tremendous progress in preparation technologies since the 1970s (e.g., MBE under UHV conditions) and from the availability of new

analysis methods (e.g., synchrotron based spectroscopies). These new efforts have culminated in the possibility to grow high quality, stoichiometric EuO thin films by a Eu-distillation technique [27] and to epitaxially integrate EuO with mainstream semiconductors such as silicon and GaN [16].

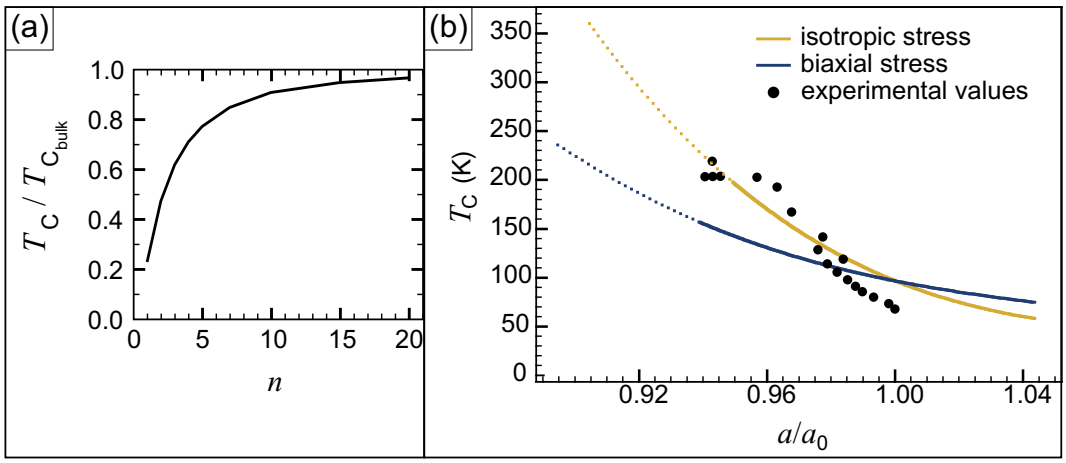

Figure 2.5: Theoretically predicted influences on T_C in thin films. **(a)** Evolution of the normalised T_C of a EuO(100) film with thickness measured in monolayers n, reproduced from [49]. **(b)** DFT results on the dependence of T_C of EuO on biaxial (dark blue curve) and isotropic strain (yellow curve), normalised to the relaxed lattice constant a_0, reproduced from [17]. The theoretical model fits the known experimental values for isotropic stress [40; 83; 84] quite well.

The Curie temperature of EuO ultra thin films is influenced by finite size effects, whereby a substantial reduction compared to the bulk value for films thinner than 10 ML was predicted [69; 85] as displayed in Fig. 2.5(a). Such effects were already observed for polycrystalline films grown on Si/SiO_2 substrates [56], but the polycrystalline nature impeded a substantial quantitative analysis of the thickness dependence on T_C. For films grown on conductive substrates - as used in this thesis - image charge screening counteracts the final size effects [86; 87], thereby complicating the predictability of T_C. A further factor influencing T_C in thin films is epitaxial strain which occurs due to lattice mismatch between the film and the substrate. Figure 2.5(b) shows the dependence of T_C on biaxial strain (dark blue curve) as predicted by DFT calculations [17]. Although the general trend of the calculations coincides with the known measurements [40; 83; 84], this DFT model exaggerates T_C by ≈ 30 K for the relaxed state, hence a similar exaggeration for the strained state should be expected.

2.2 Surface oxides

When a metal surface is oxidised, or an oxide is grown supported by a metal substrate, one often finds oxide structures or clusters which have no counterpart in oxide bulks. Even if a bulk-like structure is formed, the reduced dimensionality and the dominance of surface and interface effects may lead to novel physical and chemical properties which are intrinsically different from those of the corresponding bulk counterparts [88].

Surface oxide formation was extensively investigated for several transition metals because of the fundamental importance in both solid state physics and chemistry and because of the importance of oxygen interaction with metal surfaces in heterogeneous catalysis [89]. For catalysis, the surface oxides of the noble metals Pd [90–96] and Rh [89; 97] were of main interest. Thereby two common but not mandatory building rules became apparent:

1. Often surface oxides are characterized by an oxygen lattice equivalent to that in the respective bulk oxides, and metal atoms distributed in between in a fashion resembling more or less that of the bulk oxides [89].

2. In contrast to adsorbed oxygen, which prefers hollow sites (fcc hollow sites on (111) surfaces), the surface oxides get their strongest bonding to the substrate if oxygen is placed in on-top positions of the substrate lattice, sometimes resulting in an alignment of the O rows of the surface oxide with close-packed rows of the substrate. Although the oxides of the late transition metals are not very ionic, in this respect they behave like ionic crystals which bind to electropositive substrate atoms by their anions [89].

Closer to the case of Eu oxide on Ni or Ir are the studies of interfacial phases of foreign metal oxides on noble metal substrates, e.g., Fe oxide on Pt [98; 99] and Ru [100], V oxide on Pd [101] and Rh [102], Ni oxide on Pd [103] and Ag [104; 105], Co oxide on Ir [106], and Mn oxide on Pt [107] and Pd [88; 108]. Especially for the systems V oxide on Rh(111) [102] and Mn oxide on Pd(100) [108] exist complex surface phase diagrams, whereby the largest structural variety was found in the latter case with nine different two-dimensional phases within a range of two orders of magnitude difference in the O partial pressure, not counting the different metastable phases with low reproducibility. As some of these phases are stable only in a narrow parameter range, phase coexistence occurs due to small local variations of the O density on the substrate [108]. The existence of such surface phases considerably influences the growth behaviour of an oxide film in the beginning and, especially in the case of phase coexistence, may prevent the growth of a single phase oxide film as intended in this thesis.

2.3 Polar oxide surfaces

As the atoms in an oxide are ionically bound, high electric fields should build up if certain oxide surfaces terminate the bulk lattice. Such oxide surfaces are called ‘polar’. For example, the (111) surfaces of rock-salt crystals like EuO consist either of negatively charged O ions or positively charged metal ions. Without modifications, a rock-salt oxide crystal with {111} surfaces would have a huge electrostatic energy [109] which is proportional to its dimensions and the surface charge of the {111} layers (σ) and dominates the surface free energy. This phenomenon is known as the polar catastrophe. For the one dimensional case this is sketched in Fig. 2.6. On the contrary, the (100) face of rock-salt crystals like EuO has the lowest surface free energy [110; 111] as it is electrically neutral and has the highest atom density.

As the electrostatic potential (V) is of the order of several volts per layer such polar surfaces cannot exist as a simple termination of the crystal’s bulk structure. To circumvent this problem it

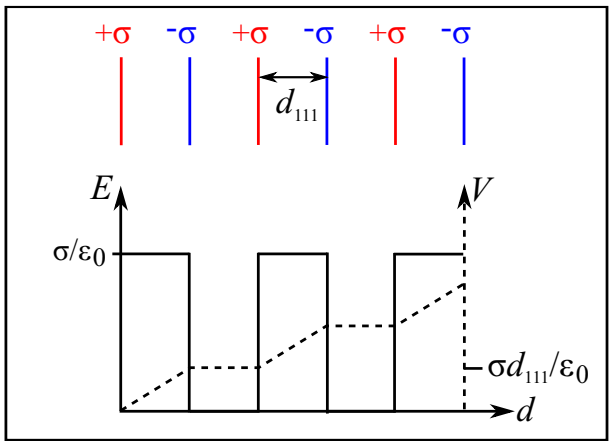

Figure 2.6: One dimensional model of the polar catastrophe. The electric field (E, solid line) and the electrostatic potential (V, dashed line) are shown in dependence of the width d, which is quantised in {111}-layer spacings d_{111}. Every layer is assumed to carry a surface charge of density σ, either negative for oxygen layers or positive for metal layers. ε_0 is the vacuum permittivity.

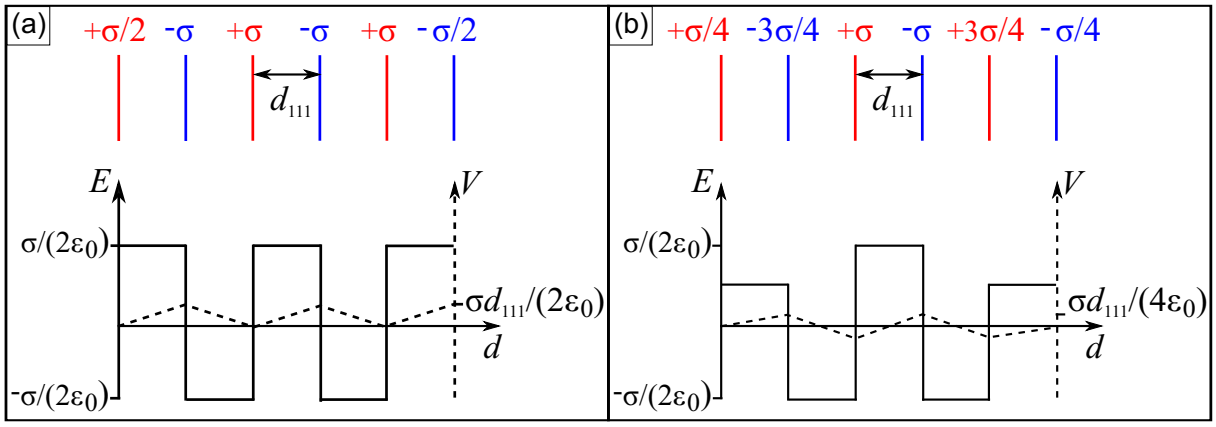

Figure 2.7: One dimensional models for the avoidance of the polar catastrophe. **(a)** The surface charge σ is decreased to half of the usual value for both outermost layers. **(b)** The surface charge σ is decreased for the outermost and their neighbouring layers.

is sufficient to change the charge density of the outermost layers, e.g., as shown in Fig. 2.7. In Fig. 2.7(a) σ is decreased to half of the usual value for both outermost layers. In this case V oscillates around an average value of $\sigma d_{111}/(4\varepsilon_0)$. For a configuration as in Fig. 2.7(b) V oscillates with the same amplitude, but is 0 on average.

For the different polar surfaces exist numerous mechanisms to realise such charge compensations [112]. They can be divided into three primary categories:

- *Direct electronic modifications*
  Direct electronic modification means that the geometrical structure of the oxide surface is similar to that in the bulk, but the electronic properties at the surface are different without the presence of adsorbates. Possible mechanisms are a modification of the electronic population of

the ions, 'metallisation' of the surface (i.e. loss of the insulating character), and off-site charge localization [112]. Examples are the systems MgO(111) on Ag(111) [113] and NaCl(111) on Al [114].

- *Adsorbate induced charge modifications*
  In this case the charge of the oxide surface is modified by the adsorbate. For example, hydroxyl groups carry a single negative charge and stabilise the systems CoO(111) on Au(111) [115] and NiO(111) on Ni(111) [116]. Also annealing in air can lead to adsorbed gases which stabilise the surface as was shown for the case of NiO single crystals [117].

- *Surface reconstructions*
  This is the most common mechanism found under UHV conditions. Surface reconstructions are a widespread phenomenon in surface science. The structure of a reconstructed surface deviates from a simple termination of the bulk lattice. These reconstructions minimise the surface free energy which is usually generated by the loss of bonds compared to the bulk. The most famous examples are the 7×7 reconstruction on Si(111) [118] and the herringbone reconstruction of Au(111) [119]. More often reconstructions are found for more open surfaces (i.e. surfaces with lower atom densities), e.g., Ir(100) [120] or Pt(100) [121].

  For oxide surfaces the energetic situation becomes more complicated due to the electrostatic field created by the ions. For (111) surfaces of rock-salt crystals in principle an octopolar reconstruction is sufficient to avoid the polar catastrophe [110]. Examples are MgO(111) [122] and NiO(111) [122] single crystals, BaO(111) thin films on Pt(111) [111], and NiO(111) thin films on Au(111) [123].

Reconstructions of polar surfaces with threefold symmetry [1] often show triangular motifs, which are an important feature to identify reconstructed areas in STM topographs and are found, e.g., for (0001)-Zn surfaces of ZnO single crystals [124], for the p(2×2) of NiO(111) on Au(111) [125], and for the p(2×2) of BaO(111) on Pt(111) [111]. In both latter cases the p(2×2) reconstructions correspond to {100} micro-faceted pyramids. Under suitable conditions also formation of much larger {100} faceted pyramids with edge lengths of the order of 100 nm can occur as stabilisation mechanism for oxide grains in polar orientation, e.g., for MnO(111) on Pd(100) [126].

Polar surfaces have been a subject of intensive work in the past [112; 127]. Also oxide growth on polar surfaces has attracted considerable interest due to the unconventional properties of the interfaces. The most prominent system is $LaAlO_3$ grown on the TiO_2-terminated (001) surface of $SrTiO_3$, where a conductive interface can form between the insulating oxides [128]. The conductivity was thereby attributed to electrons originating from charge compensation. Recently structural changes due to the internal electric field were found to contribute to the conductivity [129].

[1] For the reconstructions one has to consider not only the outermost layer, but at least additionally the adjacent, oppositely charged layer. Hence the sixfold symmetry of hexagonal surfaces is reduced to a threefold symmetry.

2.4 Graphene

Graphene is a two dimensional sheet of carbon with a hexagonal lattice ($a_C = 2.46\,\text{Å}$) and a two atom basis. Thereby the atoms build a honeycomb with a nearest neighbour distance of 1.42 Å [130]. The word 'graphene' was invented to simply describe a single graphite layer. At least this could be an interpretation of a surface scientist, but this is different from the chemist point of view. In the official nomenclature of the 'International Union of Pure and Applied Chemistry' (IUPAC) it is stated that it is not correct to speak of 'graphite layers' when meaning single, two-dimensional carbon sheets. Instead, the term 'graphene' has to be used, which is considered as final member of the series of fused polycyclic aromatic hydrocarbons which use the suffix '-ene' [131].

Nevertheless, if one removes a single layer of a graphite crystal the result is a graphene sheet. This removal can be achieved simply by using a scotch tape and is called exfoliation [132]. This method works because of the sp^2 hybridisation of the C atoms in graphene, which leads to strong σ-bonding and weak π-bonding within a graphene layer and van-der-Waals bonding between the layers. This leads also to a very low surface free energy of graphene of $0.3\,\text{eV}\,\text{nm}^{-2}$ [133]. While the exfoliation is a simple task it is difficult to find the graphene sheets. This became possible by a combination of optical, electron-beam and atomic-force microscopy for graphene put on a SiO_2 substrate [132].

A more controlled fabrication of graphene can be achieved by epitaxy, either on SiC [134; 135] or on metal substrates [136–140]. The latter method is used in this thesis, with Ir(111) as substrate. As every substrate induces modifications to the idealised properties of graphene, this system graphene/Ir(111) is described in more detail in Sec. 2.4.2. Before these specialities are discussed, graphene's universal electronic properties are described in the following section.

2.4.1 Electronic Properties

The most prominent peculiarity of graphene is related to its band structure with its linear energy dispersion of the π-band at the K and K' points of the Brillouin zone, which arises from the lattice symmetry and the monatomic thickness [141]. Such a linear dispersion resembles the energy of relativistic particles which can be quantum mechanically described by the massless Dirac equation [142]. Thus, these conically shaped parts of the π-band at the K and K' points of graphene are known as Dirac cones. Two such cones, one for the occupied and one for the unoccupied states, meet at the Fermi level (E_F) in the Dirac point; as there are no other bands at E_F, the DOS vanishes there, making graphene a zero band gap semiconductor. The high mobility of the electrons in graphene and its strong electric field effect encourage work to realise graphene based electronics [142].

Graphene has also potential for spintronic applications. For example, for spintronic devices it is very important to find leads which are non-magnetic and where a spin-polarised current can be injected and flow without becoming depolarised [143]. Graphene shows ballistic electron transport over distances up to the µm range [142; 144] and also negligible spin-orbit coupling [145], i.e., large spin relaxation times. This makes graphene an ideal material for leads in spintronic devices. Further possible applications include spin qubits [146] and spin filters [147].

Another possibility to achieve spin dependent transport is to put graphene in close proximity to a magnetic insulator. Via the magnetic proximity effect, exchange splittings will be induced in graphene. EuO would be a suitable magnetic insulator for such a system, inducing an exchange splitting of $\approx 5\,\mathrm{meV}$ in graphene [64].

In the recent years, several studies [148–156] about the influence of adsorbates on the properties of graphene were carried out for several reasons. Firstly, it has become apparent that the electronic properties of graphene - even if present in high structural quality - depend critically on its environment, e.g., on the type and distribution of chemical species bond to graphene [157]. As an example, the enormous mobilities for charge carriers in graphene predicted from theory are not realised for adhered graphene, be it on SiC [158] or for exfoliated graphene on SiO_2 [159]. Only for suspended graphene mobilities come close to the theoretical values [160]. Secondly, graphene lacks a band gap around the Fermi level, which is the defining concept for semiconductor materials and essential for controlling the conductivity by electronic means. Adsorbates are a way to tune the band gap of graphene [153; 154]. Thirdly, the fabrication of devices requires a contacting of the graphene, thus electronic modifications are unavoidable when integrating graphene into devices.

Depending on the degree of interaction, adsorbates can also destroy the π - electronic system of graphene, i.e. the Dirac cone and the related properties. For example, this is the case for chemisorbing metals like Co, Fe, Ni, and Pd [148; 149], while for weakly adsorbing metals like Al, Cu, Ag, Au, or Pt graphene's electronic structure is preserved [149]. In the latter cases, the sign and amount of graphene doping can be deduced from the differences in the work functions of the metal (W_m) and of graphene ($W_\mathrm{gr} = 4.5\,eV$), whereby the crossover from p-type to n-type doping occurs for $W_\mathrm{m} \approx 5.4$ eV. The offset of ≈ 0.9 eV comes from the distance dependent chemical interaction between the metals and the graphene [149].

For the system used in this thesis, graphene on Ir(111), the interaction is also weak but nevertheless very important for a detailed understanding of the experiments. Thus, the peculiarities of this system are described in the following section.

2.4.2 Graphene on Ir(111)

Graphene on Ir(111) can be grown in exceptional quality by decomposition of hydrocarbons at elevated temperatures. A growth recipe can be found in Sec. 4.1.4. Fully coalesced graphene films grown by this TPG+CVD method are continuous over substrate steps [161]. The nearest neighbour distance of Ir atoms in the (111) surface is $a_\mathrm{Ir} = 2.715\,\text{Å}$, while that of unbuckled graphene is $a_\mathrm{gr} = 2.461\,\text{Å}$ [162]. Highly accurate measurements revealed that on Ir(111) the graphene is compressed by 0.4% to $a_\mathrm{gr} = (2.452 \pm 0.004)\,\text{Å}$ [162] due to large differences in the thermal expansion coefficients and the high growth temperature used. From calculations, the compression should be larger than 0.4% but is partially relaxed by the formation of wrinkles [163].

The differences of the surface lattice constants result in an incommensurate 9.32×9.32 superstructure with a periodicity of $a_\mathrm{moiré} = 25.3\,\text{Å}$ which can be viewed as a moiré [162]. Such a moiré lattice is a superposition of the two smaller lattices and can be calculated using the corresponding reciprocal lattice vectors ($\vec{k}$):

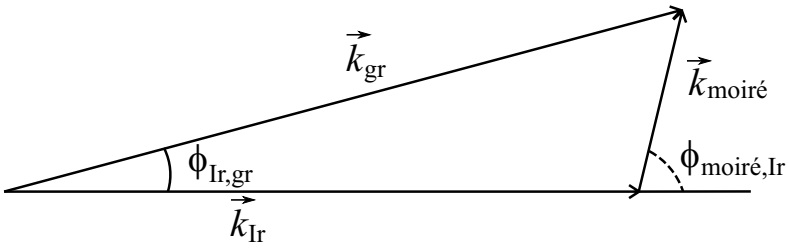

Figure 2.8: Sketch illustrating the dependency of the moiré reciprocal lattice vector ($\vec{k}_{\text{moiré}}$) on the reciprocal lattice vectors of Ir ($\vec{k}_{\text{Ir}}$) and graphene ($\vec{k}_{\text{gr}}$) and the angles in between.

$$\vec{k}_{\text{moiré}} = \vec{k}_{\text{gr}} - \vec{k}_{\text{Ir}}. \tag{2.2}$$

If all vectors are parallel, one can directly calculate $a_{\text{moiré}}$:

$$\frac{2\pi}{a_{\text{moiré}}} = \frac{2\pi}{a_{\text{gr}}} - \frac{2\pi}{a_{\text{Ir}}}. \tag{2.3}$$

For graphene grown by the recipe in Sec. 4.1.4 the $\vec{k}$ vectors, i.e. the dense packed lattice rows, are parallel for most of the graphene surface. But, there are also parts where a slight misalignment of the graphene and Ir lattices exists. As can be seen in Fig. 2.8, the angle $\phi_{\text{moiré,Ir}}$ between $\vec{k}_{\text{moiré}}$ and $\vec{k}_{\text{Ir}}$ is much larger than the angle $\phi_{\text{Ir,gr}}$ between the Ir and graphene lattices.

For small angles $\phi_{\text{Ir,gr}}$ and $\phi_{\text{moiré,Ir}}$ is:

$$\phi_{\text{Ir,gr}} \approx \frac{|\vec{k}_{\text{gr}}| - |\vec{k}_{\text{Ir}}|}{|\vec{k}_{\text{gr}}|} \cdot \phi_{\text{moiré,Ir}}, \tag{2.4}$$

with the constant factor $\frac{k_{\text{gr}} - k_{\text{Ir}}}{k_{\text{gr}}} = 0.093$ [162]. This means that $\phi_{\text{moiré,Ir}} \approx 10.7 \cdot \phi_{\text{Ir,gr}}$, i.e. the moiré misalignment is amplified by a factor of 10.7 compared to the misalignment of the graphene to the substrate.

So far, only the moiré lattice was discussed. To fully understand the system, the anatomy of the single moiré cell has to be analysed. For simplicity, only the case of perfect alignment is discussed, but all considerations also hold for slightly rotated meshes, as they are present in the experiments. Within a moiré unit cell the positions of the C atoms with respect to the substrate change. This leads to contrast differences in STM topographs as can be seen in Fig. 2.9(a). Although STM contrast is not unambiguously correlated to topographic height, in this case the brighter regions are higher than the darker ones. This was confirmed by density functional theory calculations [164; 165], which lead to a height distribution as shown in Fig. 2.9(b).

The colour code of the three Ir surface layers [grey: 1st (topmost) layer, red: 2nd layer, green: 3rd layer] allows one to identify three different regions within the moiré unit cell which are denoted *fcc*, *hcp*, and *ontop* regions [162] as shown in Fig. 2.9(c). This denotation is given with respect to the C ring centre position on the substrate. If the centre is above an Ir atom of the 1st layer it belongs to the *ontop* region, if it is above a 2nd layer Ir atom it belongs to the *hcp* region, and if

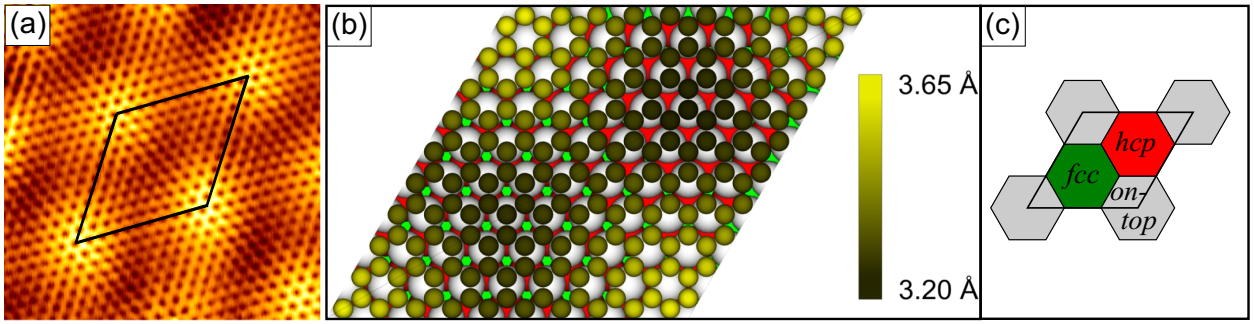

Figure 2.9: **(a)** STM topograph of graphene on Ir(111), size 6 nm × 6 nm. The moiré unit cell is indicated and the bright regions correspond to these denoted as *ontop* in (c). Reproduced from [166]. **(b)** Top view DFT model of the moiré unit cell of graphene on Ir(111). First layer Ir atoms are coloured grey, second layer Ir atoms are red, and third layer Ir atoms are green. The C atoms are yellow and their brightness depends on the distance to the substrate which is given by the adjacent scale. This figure is reproduced from [165]. **(c)** Simple extended area model with the three regions *fcc*, *hcp*, and *ontop*. This denotation is given with respect to the position of the C ring centre on the substrate [162].

it is above a 3rd layer Ir atom it belongs to the *fcc* region. Although the exact C ring positions change within these regions and no sharp borders exist, the model in Fig. 2.9(c) is a reasonable simplification in many cases.

The height differences in the moiré unit cell are caused by differences in the C-Ir bonding, which itself are caused by the differences of the lateral C atom positions on the substrate. On average, the C-Ir binding energy is −50 meV/C atom, but the binding is not pure physisorption, although it is dominated by van der Waals interactions. In the *fcc* and *hcp* regions, a C atom sits directly on top of an Ir atom [see Fig. 2.9(b)] and forms a weak covalent bond [165]. This is not the case for *ontop* regions where the chemical interaction is repulsive.

These chemical interactions between graphene and Ir(111) also influence graphene's band structure. The moiré thereby imposes a superperiodic potential giving rise to Dirac cone replicas and the opening of minigaps at the crossing points with the original cone [167]. Additionally, the graphene is slightly p-doped [167; 168] and a small band gap opens due to hybridisation of the graphene π bands with the Ir 5*d* bands [168]. Furthermore, Raman-active phonons were not observed, suggesting that the hybridisation of the bands near E_F is sufficient to quench the resonant conditions needed to observe the graphene phonons with Raman scattering [168]. The strong phonon damping was confirmed by high-resolution electron energy loss spectroscopy (HREELS). Thereby it was found that the sheet plasmon is strongly damped despite the exceptional quality of graphene on Ir(111) [169]. The only plausible reason is again the modulation of the graphene films caused by the hybridisation at the interface [169].

2.4.3 Adsorption

Atoms adsorbed on graphene can be roughly divided into two groups, the ionically bonded and the covalently bonded [151]. Very reactive open-shell adsorbates, e.g., alkali and halogen ad-atoms

(except for F), act as direct dopants [151]. They accept or donate one electron and bind ionically to graphene but hybridise only weakly with the graphene bands and experience very low migration barriers [151]. This is in contrast to the class of strongly hybridised, covalently bonded adsorbates, (including H and OH) which can induce universal midgap states, subsequently leading to high migration barriers [152].

DFT calculations of Eu adsorbed on graphene grown on Si-terminated SiC showed that the adsorbed Eu has a very low diffusion barrier and at the same time a relatively large adsorption energy with respect to its bulk cohesive energy [170]. This result was backed by large scale STM topographs which show flat Eu islands on the graphene [170]. Due to the lack of higher resolved STM data and the limitation of the DFT to a p(4×4) Eu superstructure [170], this description of the system Eu on graphene is far from complete.

The graphene moiré on Ir(111) is a new and unique support for cluster superlattices. This was shown first for Ir adsorption [164], but works also for some other metals, e.g., like Pt and W [171]. The reason is that these adsorbates induce re-hybridisation of the C bonds from sp^2 to sp^3 at *fcc* or *hcp* regions, thereby forming strong carbon metal bonds [172]. The strongest bonds of Ir clusters are located at the *hcp* regions as was found out experimentally and by DFT calculations [162; 164; 172]. This collaborative effect including graphene-mediated interaction with the substrate distinguishes the binding mechanism on the moiré from the binding of adatoms or small clusters on free-standing graphene.

The re-hybridisation of graphene on Ir(111) to diamond-like sp^3 carbon occurs if the adsorbed metal atoms have a large extension of a localized valence orbital [171; 172]. Depending on the interactions strength of the adsorbed species with the carbon p_z orbitals, the π-electronic system of graphene even may be (locally) destroyed. For adsorption of Eu no re-hybridisation is expected because the valence electrons are *s*-electrons with an isotropic charge distribution. Thus, for Eu adsorption no ordering of clusters along the moiré lattice is expected. But, the system Eu on graphene is nevertheless interesting, as the large magnetic moment of 7 μ_B of the Eu's $4f$-shell could bestow graphene with magnetic properties. This question is concerned in chapter 8. Depending on the deposition conditions, the Eu does not stay on top of the graphene, but intercalates between the graphene and the Ir(111). An overview about intercalation phenomena for graphite and graphene is given in the following section.

2.4.4 Intercalation

In chemistry, intercalation describes the reversible inclusion of atoms (or molecules) between two other molecules. Graphite intercalation compounds (GICs) are known since 1926 [173; 174], whereby the first intercalants were the alkali elements K, Rb, and Cs [173]. In such compounds, the intercalants are placed between the graphene layers, whereby the intercalate layers are periodically arranged in a matrix of graphene layers [174]. Thus, the GICs are classified by a stage index n denoting the number of graphene layers between adjacent intercalate layers. This staging phenomenon is a general phenomenon in graphite intercalation compounds, even in those samples with very dilute intercalate concentrations ($n = 10$) [174]. The layer stacking is exemplarily shown in Fig. 2.10 for graphite, for a stage 3 GIC, and for a stage 1 GIC.

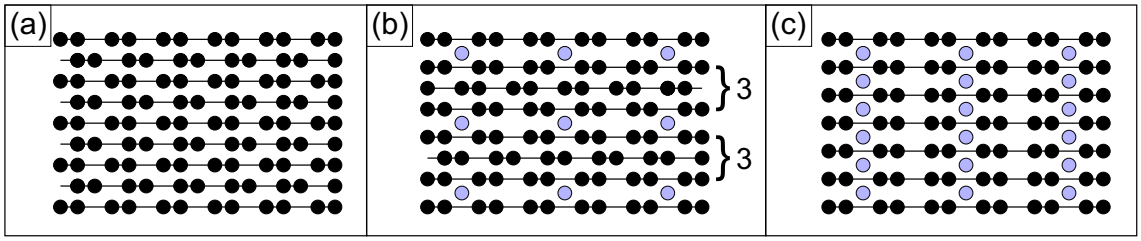

Figure 2.10: Side view sketches of the layer stacking of **(a)** graphite, **(b)** a stage 3 GIC, and **(c)** a stage 1 GIC. C atoms are represented by black balls and intercalate atoms by light blue balls.

The intercalation of the metals usually requires elevated temperatures, e.g., $> 500\,\mathrm{K}$ for K, Rb, and Cs. For higher temperatures the stage n increases, i.e. the intercalate becomes more dilute, already indicating the reversibility of the process for even higher temperatures which is called deintercalation [174]. At low temperatures, the intercalate is in-plane ordered, but not necessarily commensurate with the in-plane graphene site ordering; often also different ordered structures coexist [174]. In a few cases the ordering is simple, e.g., a p(2×2) structure for the stage 1 alkali GICs C_8K, C_8Rb and C_8Cs, a p($\sqrt{3}\times\sqrt{3}$)R30° structure for C_6Li, or a p($\sqrt{7}\times\sqrt{7}$)R19.1° structure for higher stage GICs with Rb and Cs [174]. These commensurate superstructures are shown as ball models in Fig. 2.11, where the graphene honeycomb is represented by black balls and lines.

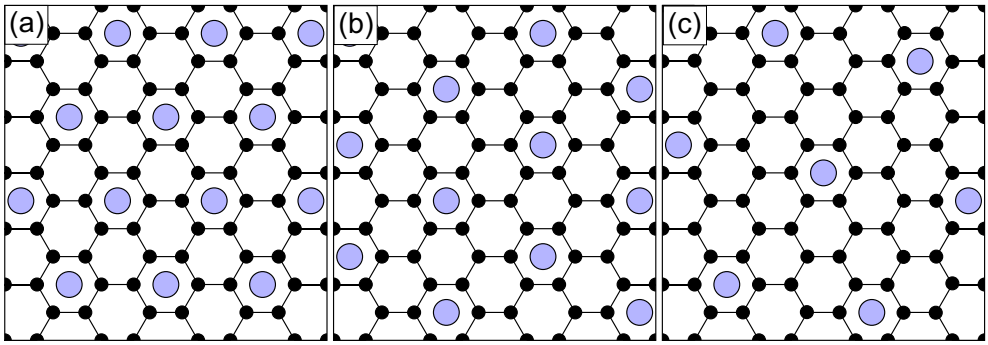

Figure 2.11: Top view sketches of commensurate superstructures in GICs. C atoms are represented by black balls and intercalate atoms by light blue balls. **(a)** p($\sqrt{3} \times \sqrt{3}$)R30° superstructure, **(b)** p(2×2) superstructure, **(c)** p($\sqrt{7} \times \sqrt{7}$)R19.1° superstructure.

Intercalation changes many of the physical properties of the host material. Because of the very low free carrier concentration in graphite ($\sim 10^{-4}$ free carriers/atom at 300 K), the doping caused by the intercalate permits a wide variation of the free carrier concentration and thus of the electrical, thermal and magnetic properties [174]. Most of the metal intercalants, especially the alkali, alkaline earth and lanthanide metals effect an n-doping of the graphene layers; such GICs are called donor GICs [131]. Thereby, the charge transfer per atom for the same intercalant is highest for dilute GICs and lowest for the stage 1 GIC, e.g., as measured for the case of Cs [175]. The effect of the intercalation on the electrical conductivity has probably attracted the greatest amount of attention because of the fabrication of an intercalation compound (C_xAsF_5) with a reported room

temperature conductivity exceeding that of copper [174]. Several GICs are even superconducting, with C_6Ca reaching a critical temperature of 11.5 K [176].

Intercalation phenomena are not restricted to graphite but also occur for graphene grown on substrates, e.g on SiC [177], on Ni(111) and Co(0001) [178], and also on Ir(111) [179; 180]. Thereby, for K and Rb intercalation on graphene on SiC the same structures (p(2 × 2)) were found as for intercalation in graphite [177]. Au intercalation between graphene on Ni(111) and graphene on Co(0001) enabled the lifting of the strong graphene-substrate interaction, thereby restoring the graphene's Dirac cone system [178].

Alkali metals, adsorbed on graphene on Ir(111) at 300-400 K, intercalate after heating of the sample to temperatures up to 700 K. Thereby, the intercalate thickness is limited to 1 monolayer [179], whereas the film thickness is unlimited for metals with a higher ionisation potential (e.g., Pt, Ni, and Mo) which are strongly bound to the metal substrate and require higher temperatures of $T \geq 900$ K to intercalate [179; 180]. Thermal desorption spectroscopy measurements of the system K on and beneath graphene on Ir(111) showed that the K deintercalates again at temperatures $T \geq 1500$ K [179].

2.4.4.1 Eu intercalation

Eu intercalation into graphite is saturated after formation of the stage 1 compound C_6Eu, which corresponds to a $p(\sqrt{3} \times \sqrt{3})R30°$ structure of the Eu with respect to the graphene lattice, whereby the Eu is placed in the centre of the hexagons [181]. The thickness of a C-Eu-C sandwich is 4.87 Å in this compound [181], i.e. the intercalated Eu layer increases the C-C layer distance compared to pristine graphite (3.36 Å [130]) by 1.51 Å.

No spontaneous magnetisation was found for C_6Eu down to 4.2 K, though the paramagnetic susceptibility shows anomalies below 40 K, indicating complex magnetic ordering states [182]. Photoemission measurements and band structure calculations revealed that the graphite-derived valence bands in C_6Eu are shifted toward higher binding energies compared to pristine graphite, which is caused by charge transfer of $\sim 0.5\,e$ from each Eu atom into the graphite π-bands (qualitatively, the behaviour is like in a rigid band model) [183]. Additionally, a hybridisation between graphite-derived bands and the Eu $5d$ states was found [183].

3 Experimental Setup

Most of the experimental results presented in this thesis were acquired in the ultra high vacuum system "*Athene*" in Cologne, which is shown in the sketch in Fig. 3.1 and briefly described in section 3.1. Several modifications of the system had to be carried out in order to perform the experiments. At first a new STM head had to be designed (see section 3.2), which had to be compatible with an STM electronic of the SPS-CreaTec GmbH [184]. Furthermore, the transferable sample holder and the supporting base plate had to be redesigned (section 3.1.1), as the sample had to be electrically isolated from the manipulator and equipped with thermocouples, an improved cooling power was necessary, and magnetic STM ramps had to be mounted. For MBE a station with two effusion cells for Eu and Gd, a local gas inlet for O_2, and a quartz crystal microbalance had to be fitted to the chamber, what is described in chapter 3.1.2. In appendix B the most relevant construction plans of the new parts and of the STM can be found.

3.1 UHV system *Athene*

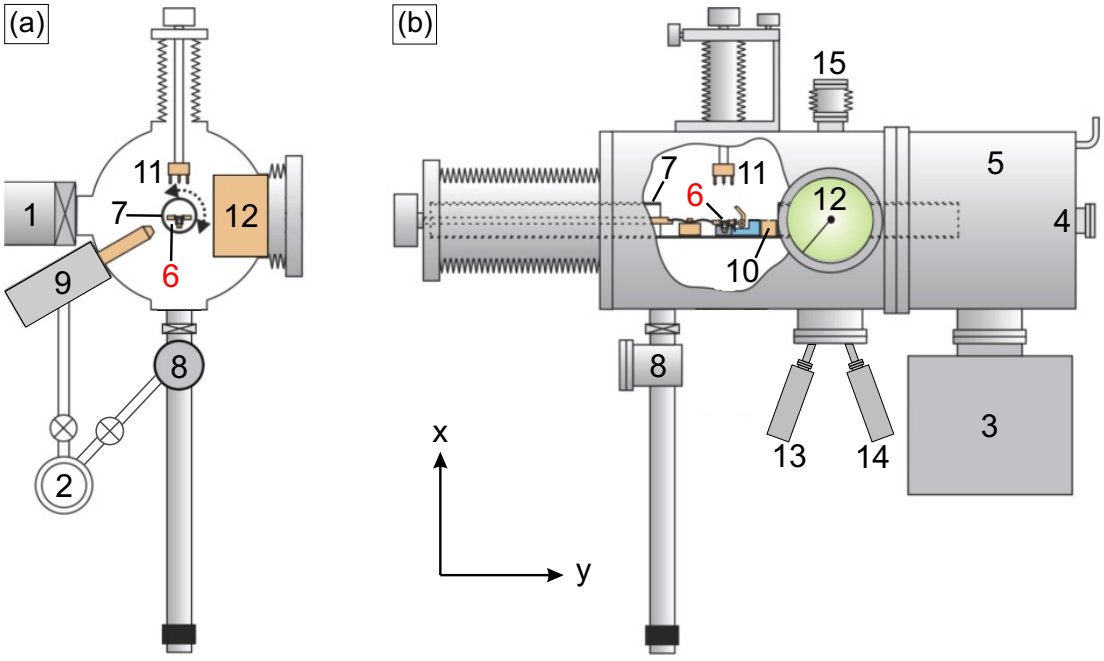

Figure 3.1: UHV system *Athene* as used for this thesis. **(a)** side view, **(b)** front view. The equipment is numbered as follows: (1,2) turbomolecular pumps, (3) sputter ion pump, (4) Ti sublimation pump, (5) LN_2 cooling trap, (6) sample holder, (7) manipulator, (8) load lock, (9) ion source, (10) Faraday cup, (11) STM, (12) 3-grid LEED system, (13) high temperature effusion cell for Gd, (14) low temperature effusion cell for Eu, (15) quartz crystal microbalance.

The main part of the system consists of a cylindrical vessel of 881 mm length and 306 mm diameter, to which the devices are mounted through flanges. There is a turbomolecular pump (1) for the main chamber, a small turbomolecular pump (2) for the differential pumping of the ion source (9) and for the pumping of the load lock (8) system, a sputter ion pump (3), and a Ti sublimation pump (4), which together achieve a chamber base pressure of 3×10^{-11} mbar. During the experiments additionally a LN_2 cooling trap (5) is filled, which has the highest pumping power in the 10^{-11} mbar range.

The largest part inside the chamber is the manipulator (7), which is a 960 mm long tube of 70 mm diameter mounted in the centre of the vessel. It can be moved by 300 mm in the y-direction and precisely rotated by ±180°. It contains the sample holder (6), which is transferable and hosted on a base plate. The sample heating, a W/Re alloy (97/3 %) filament can be supplied with a voltage of up to 2000 V for electron bombardment of the sample, which thus can be heated up to temperatures of over 1600 K. Cooling is provided by a LHe flow cryostat, which is connected by Cu breads to the base plate, whereby sample temperatures down to 35 K can be reached. The manipulator also hosts three sample holder garages and a Faraday cup (10) for accurately measuring the ion fluxes.

The samples can be grown by (reactive) molecular beam epitaxy using two effusion cells, one for Eu (14) and one for Gd (13). Oxygen in molecular form can be supplied via a leak valve and guided by a tube to the sample, which increases the local O_2 pressure by a factor of more than 50 with respect to the O_2 partial pressure in the chamber. The latter can be measured by a quadrupole mass spectrometer. A second gas inlet of the chamber is also fitted with such a tube and is used to provide ethylene for graphene growth. The fluxes of the effusion cells can be measured by a quartz crystal microbalance, which can be moved to the same position where the sample is located during MBE.

Characterisation of the sample can be done via a variable temperature (35 K - 700 K) scanning tunnelling microscope (11) and a three-grid rear view analyser low energy electron diffraction system (12) (35 K - 300 K).

3.1.1 Sample Holder and Base Plate

The sample holder design had to be changed (plans in Figs. B.1 through B.5) for the EuO experiments as it did not fulfil several requirements: The sample holder has to provide a high thermal conductivity while the ramps for the STM have to be ferromagnetic. During sample transfer a thermocouple contact has to be established. Also the length of the W flat springs had to be considerably enlarged as the sample was prone to vibrations with the shorter springs used before. The latter point was the easiest to achieve, as it was sufficient to move the sockets for the transfer fork (plans in Figs. B.7 and B.8) to the outer end of the sample holder and to choose a smaller diameter for the sockets. This increased the effective spring length from 4.25 mm to 7.33 mm.

Ferromagnetism of the STM ramps together with high thermal conductivity of the sample holder was obtained by a composite design as introduced by Alex Redinger during his PhD [185]. The ramps are separate parts (plan in Fig. B.6) made out of stainless ferritic steel and coated with TiNAlOx [186] to prevent vacuum welding. For the main body oxygen free high conductivity

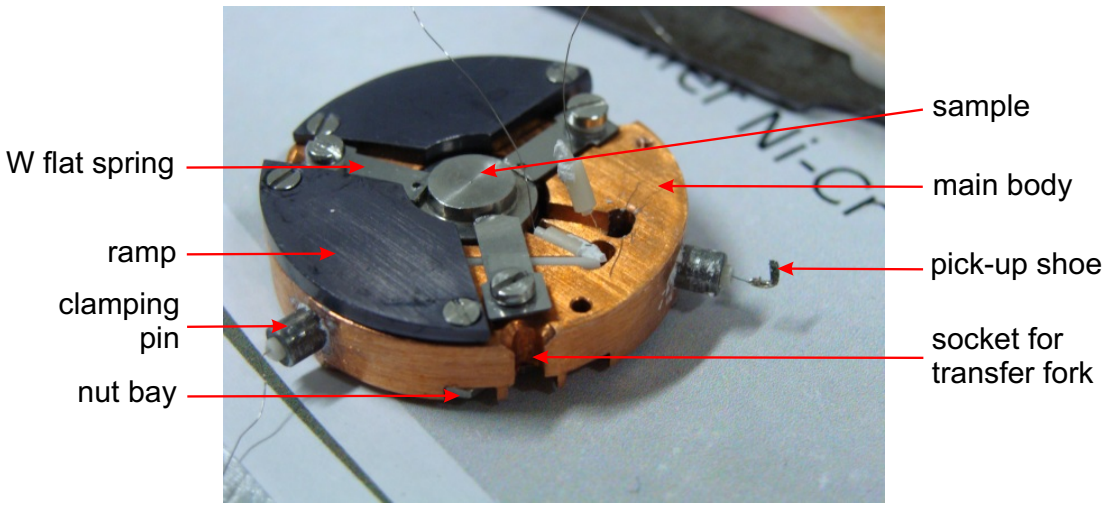

Figure 3.2: Sample holder in the stage of assembling. The sample sits on sapphire balls and is fixed by W clamp springs. The three clamping pins at the sides fit into the bayonet-like coupling of the base plate.

(OFHC) Cu was used for high thermal conductivity at low temperatures. In order to ease the assembling, nut bays were introduced at the bottom of the holder.

Figure 3.2 shows the sample holder during a test assembling with a dummy crystal inserted. Two of the three separate ramps, which are fixed with screws and nuts, are in position. At the position of the missing ramp one can see the channels for the ceramic tubes which isolate the thermocouple wires. These run from the sample to the end of the clamping pin where they are spot-welded to a pick-up shoe, which is finally fixed with ceramic glue [187]. At both outer ends the ceramic tubes are free-standing, i.e. they do not touch the metallic surrounding in order to prevent short circuits due to deposited material. The ramps and the main body were degassed for several hours at 600 °C at a pressure of about 10^{-9} mbar in a separate UHV system to avoid outgassing of these parts during the experimental procedures. This outgassing step was also done for the base plate (plan in Fig. B.9) and its Cu bread, making the latter softer and more flexible.

In Fig. 3.3 one contact for the thermocouple pick-up shoe is visible. It is a Ni sheet to which a Ni wire is spot welded and which itself is spot welded to a stainless steel flat spring. The bore in the base plate for the ceramic isolating the flat spring has a larger diameter than the ceramic in order again create a gap which prevents conductive paths. For the same reason the fixing screw is covered with ceramic glue. The larger flat spring on top of the base plate is for the clamping of the sample holder. It has to be quite thick in order to avoid a too large spring lift, which could lead to a bending of the thermocouple contact beneath. An additional type K thermocouple is fixed to the base plate by a screw.

Using LHe cooling, a temperature of −228 °C (45 K) was displayed at the Eurotherm controller[1] [188] for the sample as well as for the base plate thermocouple. Calibration measurements in ice

[1] As the Eurotherm usually used to measure the sample temperature was defective and did not work at low temperatures the Eurotherm of the NTEZ was used during LN_2 and LHe cooling.

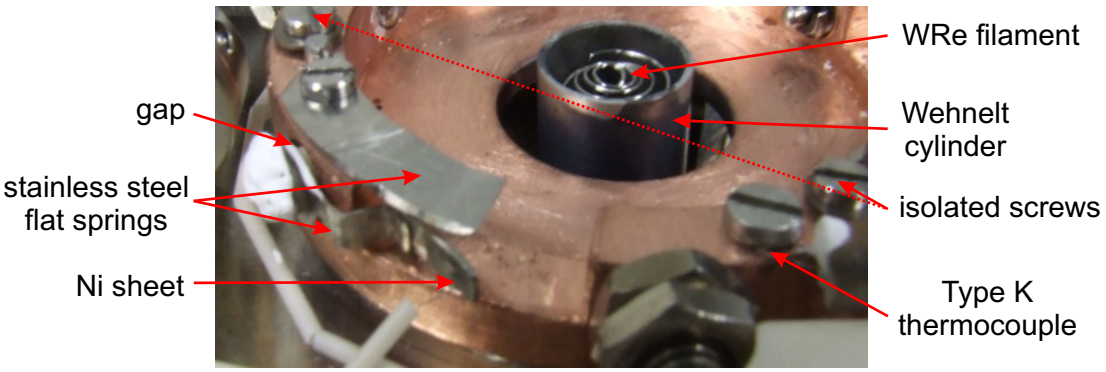

Figure 3.3: Part of the base plate which hosts the sample holder. In the centre the heating is visible, consisting of a filament made out of W(97%)Re(3%) wire with 0.25 mm diameter surrounded by a Wehnelt cylinder.

and in LN_2 yielded 0 °C and −192 °C, respectively, whereby the latter value is 4 °C higher than the boiling point of LN_2, corresponding to a thermovoltage error of 79 µV. By linear extrapolation this error increases to 94 µV at −228 °C, but this might be overestimated. Subtracting just the 79 µV from −6.243 mV (which is the thermovoltage difference between 0 °C and −228 °C [189]) gives then −6.322 mV, which correspond to −237 °C or 36 K. Thus, during LHe cooling the real temperature is probably ≈ 10 K lower than the one displayed by the Eurotherm. A more precise calibration of the sample temperature in the chamber requires thermal desorption spectroscopy, which cannot be performed with the current QMS setup in *Athene*. Thus, in the following it is assumed that the sample temperature during LHe cooling is ≈ 35 K.

For operation of the new STM electronic, a bias voltage has to be applied to the sample. The most reliable way to realise this was to isolate the whole base plate from the manipulator and from the cryostat, which both are grounded. While the base plate sits on glass balls, the three screws which fix the base plate on the massive damping block (see Fig. 3.4) had to be isolated. Therefore ceramic tubes were placed inside the base plate. To prevent short circuits by evaporated material a washer was used at every screw to shield the ceramic.

As the Cu bread connecting the base plate with the cryostat was in-vacuum welded [190] to the base plate and to the cryostat connector in order to maximise the thermal conductivity the electrical isolation had to be between the cryostat cold finger and the Cu bread connector. This was done via a sapphire plate placed between the two Cu planes and a ceramic split bush at the fixing screw as sapphire has a high thermal conductivity, especially at low temperatures.

The cryostat itself was prone to vibrations which were transmitted to the sample despite the Cu bread damping block. For high resolution STM at low temperatures it was therefore necessary to considerably damp the cryostat tube. This was achieved by a massive stainless steel tube (plan in Fig. B.10), which was fixed to the cryostat at eight positions, the distances between which were chosen to damp different normal modes of the cryostat. In order to prevent the loss of cooling power the fixations were done via screws pressing on Teflon pieces, thereby creating a thermal isolation between steel tube and cryostat. Figure 3.5 shows the cryostat with the mounted damping tube

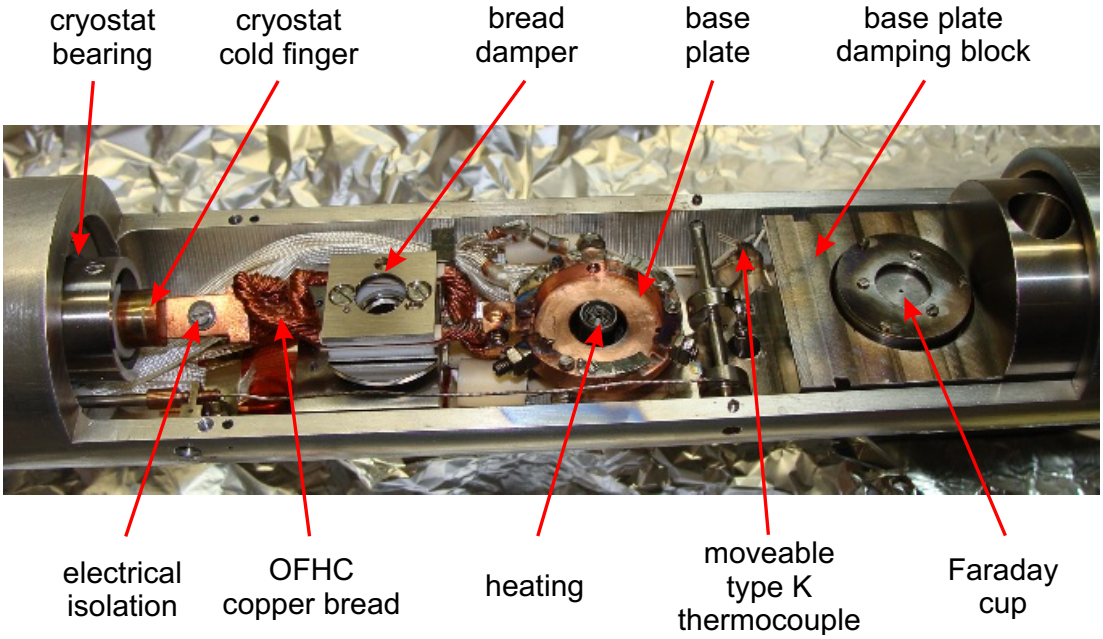

Figure 3.4: Equipment mounted inside the manipulator. The figure shows also parts not described in the text, like the moveable type K thermocouple used for Si experiments and the damper for the Cu bread which was intended to be used as sputter station for STM tips.

and its fixation points. Due to the heavy weight of the steel tube a bearing (plans in Figs. B.11 through B.13) was necessary to support the cryostat at the cold finger end. This was realised by a Teflon ring supported by an Al casing which is screwed to the manipulator tube.

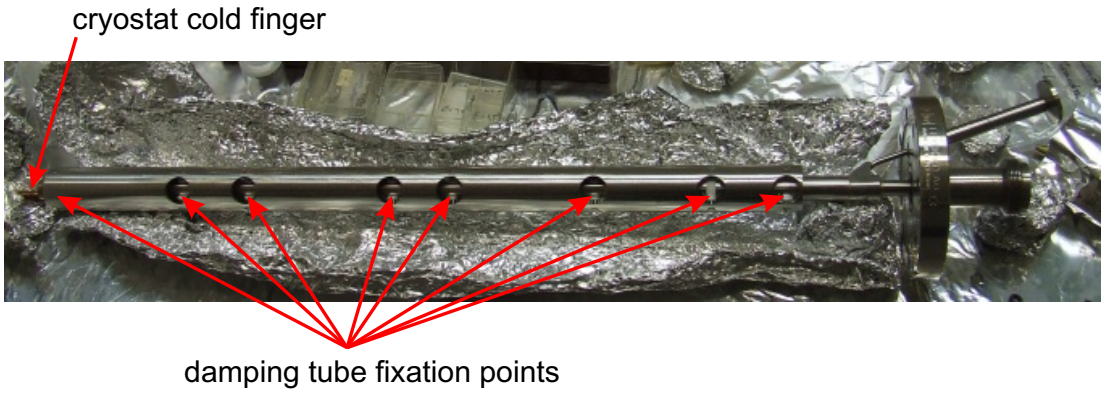

Figure 3.5: He flow cryostat on a DN63CF flange, surrounded by a heavy steel tube.

3.1.2 MBE station

For Eu evaporation a low temperature effusion cell of Dr. Eberl MBE-Komponenten GmbH [191] was used. Its design is optimised for highly stable temperature regulation at the typical Eu evaporation temperatures between 400 °C and 550 °C and its heater is surrounded by a stainless steel

shroud for water cooling. This, together with sufficient outgassing of the crucibles and evaporants, facilitated a low background pressure during film growth of around 1×10^{-10} mbar. For Gd evaporation a high temperature effusion cell of the same company was used as already the low evaporation rates for Gd doping of EuO require cell temperatures of more than 1000 °C.

Both cells were degassed in UHV for several hours with empty crucibles installed at their maximum allowable operating temperature of 1100 °C and 1900 °C, respectively. The used crucible materials were ceramic (Al_2O_3) for Eu and Ta for Gd. The Eu itself was also degassed for several hours at 600 °C, but wrapped in Ta foil as otherwise the whole ingot would have been evaporated.

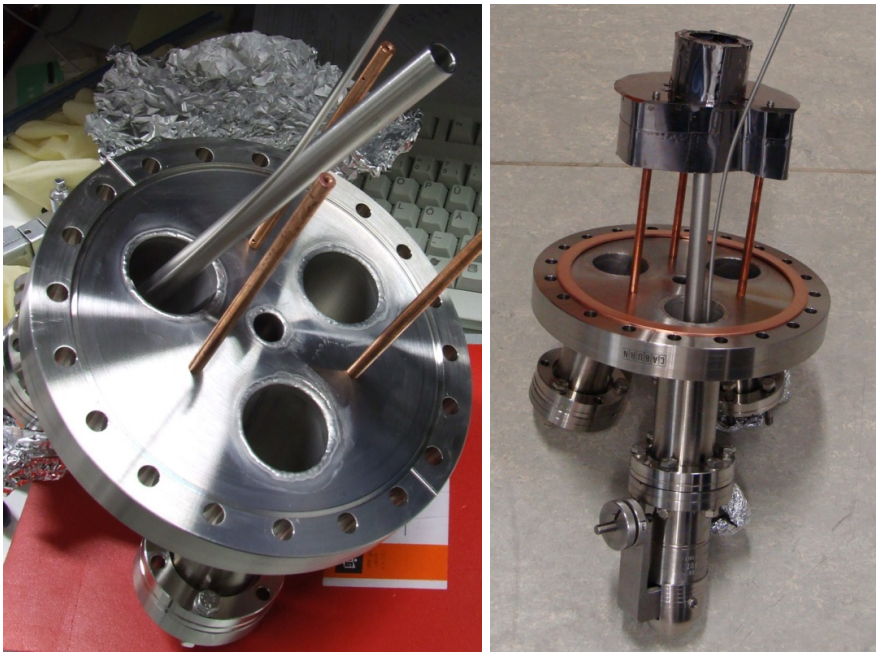

Figure 3.6: Left hand side image: MBE flange with leak valve and gas application pipe mounted. The small pipe pointing towards the mass spectrometer is partially visible. The Cu mounting cylinders of the Ta shield are already in position. Right hand side image: Flange with evaporator shield.

To realise reactive MBE of EuO and the possibility of Gd doping it was necessary to install the effusion cells at flanges where they are pointing to the same substrate position. Due to a lack of suitable smaller flanges a DN150CF flange was used, which was formerly occupied by the turbomolecular pump (1). To this larger flange three tubes with DN40CF flanges were welded. These tubes have a length of 110 mm and are oblique by 13° to the DN150CF normal, giving an evaporator-sample distance of 100 mm. The plans for this connection flange are shown in Figs. B.14 and B.15.

At the third DN40CF the leak valve for O_2 supply was installed. To this leak valve a tube of 293 mm length and with an inner diameter of 10 mm was connected, ending at a position 45 mm in front of the sample. The complete flange with leak valve and piping already in position can be seen in the left hand side image of Fig. 3.6. The pipe increases the O_2 pressure at the sample by a factor of about 400 compared to the O_2 partial pressure in the chamber. This factor was found out by

comparison of O_2 adsorption data [192] with calibration measurements carried out by LEED and subsequent refinement by STM coverage analysis using Eq. 4.1 as described in Sec. 4.2.1. Such a local pressure increase enables the avoidance of backfilling the whole chamber with the O_2-pressure needed for film growth, leading to a considerably faster pressure decrease at the sample when the leak valve is closed. This avoids a possible post-oxidation of the films after the growth is ceased. Additionally the chamber background pressure after growth is not influenced, contrary to the case of backfilling the chamber with O_2.

The O_2 partial pressure in the chamber was measured by a quadrupole mass spectrometer (QMS). As the typical O_2 pressure at the sample used for EuO film growth was about 4×10^{-9} mbar, the O_2 partial pressure in the chamber was only about 1×10^{-11} mbar, giving a quite small signal-to-noise ratio in the QMS, which was too low to achieve a good reproducibility. To increase the signal-to-noise ratio a smaller pipe of 2.5 mm diameter leading from the leak valve to the QMS was added. As turned out later this had a very small effect only. A calculation using formulas for gas conductance, assuming a laminar gas flow inside the smaller, longer pipe, revealed that only about 1/500 of the O_2 should flow through it. Therefore an aperture of 1 mm diameter and 1 mm thickness was added to the main pipe at the end mounted to the leak valve. This increased the signal-to-noise ratio of the QMS signal considerably while the pressure increase at the sample was reduced to a factor of 50, still enough for a fast O_2 pressure drop after growth.

Another problem which had to be solved was the low directivity of the effusion cells. Already after a few EuO experiments a coating became visible at the LEED screen. To prevent coating of devices and windows in the chamber it was therefore necessary to construct a complete shielding for the effusion cells, giving way for the vapour only to a small surrounding of the sample. This shielding was made out of Ta sheets, spot welded together and mounted by Cu cylinders to the DN150CF flange, as can be seen in the right hand side image of Fig. 3.6. Ta was selected as material because it has a high melting point together with low outgassing at higher temperatures, is soft and can be easily formed, and is highly suitable for spot welding. The mounting cylinders are made out of Cu for better heat conductance between the flange and the Ta, which is heated by radiation of the effusion cells.

For accurately measuring the Eu and Gd fluxes a quartz crystal microbalance was installed and two holes were drilled into the manipulator tube, allowing the positioning of the quartz exactly at the position where the substrate sits during film growth.

3.2 The hedgehog STM

Before the changes to the chamber were carried out, a new STM was constructed. This became necessary as a modern STM electronic of the SPS-CreaTec GmbH [184] was bought and the old STM with three-fold segmented piezos could not be operated by it. The magnetically stabilised beetle design [193] was used as basis. This consists of a main body (plans shown in Figs. B.16 and B.17) to which four piezo tubes are mounted. The outer three piezos have half balls mounted at the end and rest on ramps during the measurements. The half balls are made of steel and magnetised by a small SmCo magnet glued to the flat side of the half ball inside the piezo. At the

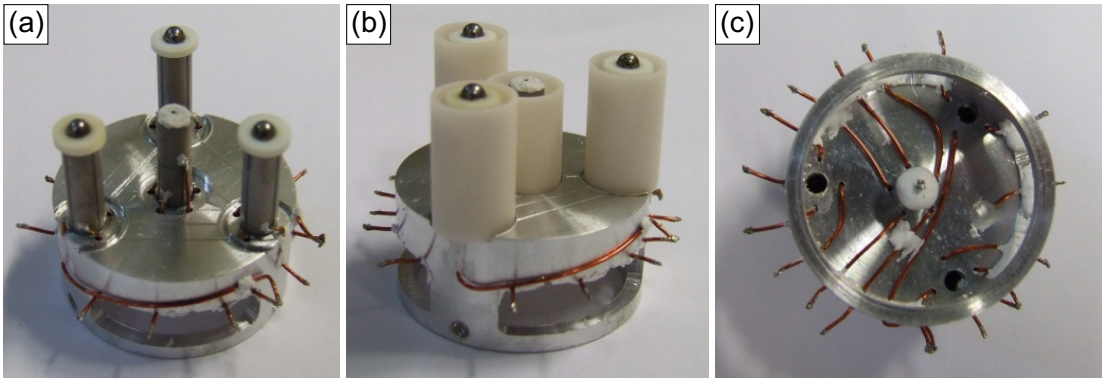

Figure 3.7: The hedgehog STM: **(a)** upside down without ceramic shields, **(b)** upside down with ceramic cylinders mounted, and **(c)** top view.

end of the central piezo the STM tip is mounted. The piezo tubes are coated with electrodes inside and outside, whereby the outer electrodes are four-fold segmented for displacement perpendicular to the long tube axis, i.e. for xy-scanning. Additionally to former designs the electrodes were protected against vapour, thereby enabling in-vivo STM during evaporation. Furthermore it was decided to use the central piezo also as xy-scanner as this is supported by the Createc electronic and avoids movement of the whole STM body during imaging, thereby reducing vibrational excitations. Therefore the upper half of the outer electrode was also four-fold segmented, while the lower half remained unsegmented for displacement in the direction of the long tube axis (z-direction), i.e. for height regulation of the tip. The segmentation plans for the piezos are shown in Fig. B.18.

Figure 3.7 shows the prototype of the hedgehog STM which was used for all STM measurements in this thesis. Due to the protective ceramic cylinders for the shielding of the electrodes from vapour [see Fig. 3.7 (b)], the wires for contacting the electrodes have to run through bores in the main body made out of Al. As there must not be a mechanical coupling of the STM to anything else than the sample holder, the electrodes are usually contacted through hair-thin Kapton®-isolated wires. As these very thin wires are prone for damage during the assembling stage they need to be exchanged sometimes. Therefore it was decided to use thicker, durable wires for electrode contacting, which end a few millimetres from the outer edge of the STM body [best visible in Fig. 3.7 (c)] and are fixed by ceramic glue. This allows one to build a completed STM unit which can be attached to its manipulator. To the end of these wires the hair-thin ones were fixed with conducting glue in the final stage of assembling. Due to the appearance of the STM with so many wires sticking out, it was called hedgehog STM. Interestingly, as was found out later, commercial STMs of the RHK company Inc. [194] exhibit the same hedgehog appearance.

As piezo material EBL#9 of EBL products Inc. [196] was used. This is a lead-zirconate-titanate (PZT) ceramic known as industry type PZT-4D. The advantage of this material compared to the for STMs commonly used PZT-5A is the smaller temperature dependence of the piezoelectric constant d_{31}. This is desirable for a variable temperature STM as this reduces the amount of calibration work at different temperatures, although the temperature of the STM should differ considerably from that of the sample holder: The heat has to be conducted through the half balls on which

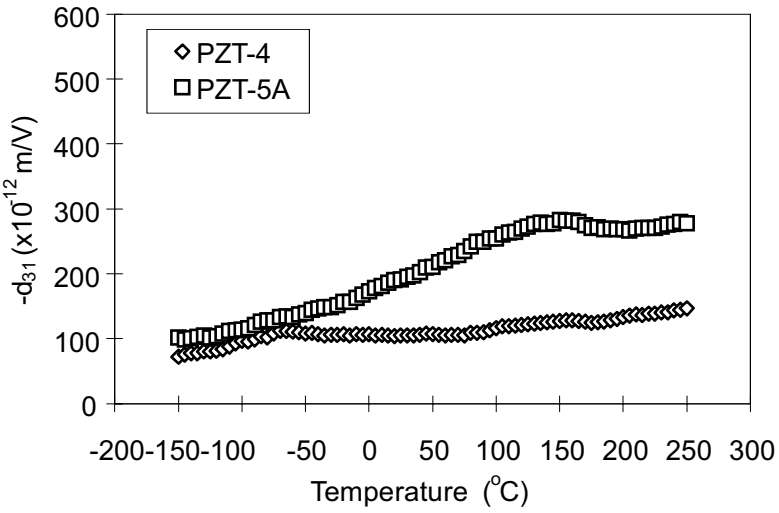

Figure 3.8: Temperature dependence of the relevant piezoelectric coefficient d_{31} for the PZT ceramic known as industry type PZT-4 and PZT-5A. Taken from reference [195].

the STM rests and through the electrical isolation pieces made out of MACOR® to which the half balls are glued. Figure 3.8 shows the temperature dependence of the piezoelectric constant d_{31} of PZT-5A and of PZT-4, the properties of which are very similar to those of PZT-4D.

The dimensions of the piezos were chosen such that the amplifier range between $-200\,\mathrm{V}$ and $+200\,\mathrm{V}$ is sufficient to achieve an image width of $2.5\,\mu\mathrm{m} \times 2.5\,\mu\mathrm{m}$. The displacement Δz for the central piezo was calculated to 300nm, using

$$\Delta z = \frac{|d_{31}| \cdot \Delta U \cdot l}{d_\mathrm{o} - d_\mathrm{i}},$$

with ΔU being the voltage difference, l the electrode length, d_o the outer and d_i the inner diameter of the piezo tube [197]. For a four-fold segmented outer electrode the displacement Δx is

$$\Delta x = \sqrt{2} \cdot \frac{|d_{31}| \cdot \Delta U \cdot l^2}{d_\mathrm{o}^2 - d_\mathrm{i}^2}$$

if the voltage U is supplied to one electrode segment [197]. If, as usual, the voltage $-U$ is supplied to the opposite electrode segment, the pre-factor is doubled to $2\sqrt{2}$.

3.2.1 Etching of Ir Tips

For STM usually W or Pt/Ir (90%/10%) tips are used. As a tip change in *Athene* requires a bake-out, a durable tip is necessary. For this thesis oxide films had to be tunnelled, thus an inert tip was preferred. But, due to a simultaneous project of pattern formation on Si and the relative hardness of Si, a harder material than the Pt/Ir alloy was needed. This lead to the decision to use pure Ir as tip material. For our home-made STMs, wires of 0.25 mm diameter and about 6 mm length are used as tips. In order to get a sharp end, tips may be cut or etched through electro-chemically.

For brittle materials like W or Ir etching is compulsory for getting suitable tips. A recipe for a

solution for electro-chemical etching of Ir is to solve 88 g of $CaCl_2$-$6H_2O$ in 156 ml distilled water and add 8 ml concentrated (35%) hydrochloric acid (density = 1.19 g cm^{-3}). Another possibility is to use dry calcium chloride. Then 45 g of $CaCl_2$ (dry) have to be solved in 200 ml distilled water and again 8 ml concentrated HCl have to be added. The dry calcium chloride is preferable, because it is easier to handle and as it dissolves exothermic (it becomes notably warmer) the dissolving process becomes faster.

For etching, the wire is dipped into the solution inside of a beaker. As counter-electrode graphite has to be used as nearly all other metals are etched faster than Ir. To get very sharp tips, the etching process has to be stopped at the right time because otherwise the tip will become blunt. The easiest way to achieve this is to isolate the lower part of the wire with Teflon® ribbon and then use this part which drops down after the wire is etched through, as the supplying voltage to the this part is cut off immediately. Thereby, the unisolated wire part should extend about 1 mm below the meniscus of the etching solution. Using this method, one has to ensure that the wire with the Teflon ribbon wrapped around is not buoyant as it otherwise will be bend when it becomes thinner during the etching process. Therefore the average density of the Ir wire and its isolation has to be larger than that of the etching solution. This can be ensured by wrapping around some Kapton®-isolated wire. Care must be taken that the part becomes not to heavy as this can lead to a premature tip drop off due to rupturing with a high risk of creating a multi-tip end.

Using an AC voltage of 7 V etching of an Ir wire of 0.25 mm diameter takes several hours. Higher voltages are not recommendable as then creation of too much bubbles sets in, giving rise to an inhomogeneous etching process with a high risk of formation of unsuitable tip shapes. Furthermore, scanning electron microscopy images of a tip etched with 25 V showed a droplet shaped end with a radius of 2 µm (Fig. 3.9), indicating a local tip melting at the end due to too much applied power. During the etching process the solution becomes opaque with a greyish and/or greenish appearance, corresponding to the colours of Ir^{4+}- and Ir^{3+}-ions, respectively. When the solution becomes too opaque it is recommended to renew it as otherwise the tip becomes coated by debris, which disturbs a proper etching. After the tip etching had finished the Teflon® was carefully removed. Remaining dirt on the tip as visible in an optical microscope can be easily removed by dipping the tip a few seconds into concentrated hydrochloric acid.

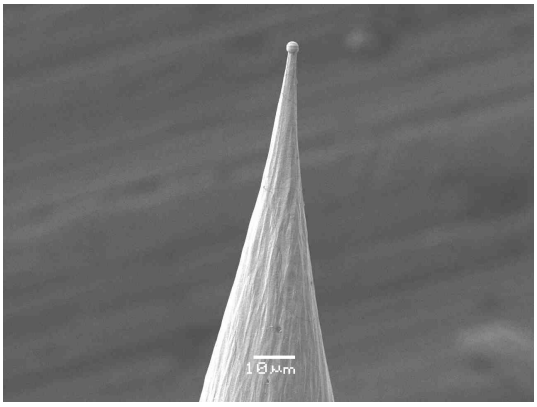

Figure 3.9: Ir tip exhibiting a droplet shaped end due to a too high etching voltage.

4 Experimental procedures

This chapter contains detailed descriptions of the experimental procedures used in this thesis. The main topics are sample preparation (Sec. 4.1) and film growth (Sec. 4.2) as well as measurement procedures like STS (Sec. 4.3) and lattice constant measurements by LEED (Sec. 4.4).

4.1 Sample preparation

During this thesis four different substrates were used for EuO growth, each of which needed different preparation procedures before the film growth could take place. In the following four subsections the preparation for each of these substrates is described.

4.1.1 Ni(100)

For the growth of EuO on Ni(100) a hat shaped single crystal was used as substrate. It was initially cleaned by annealing in oxygen atmosphere at 773 K and $p(O_2) \leq 10^{-6}$ mbar in order to reduce carbon impurities, which segregate to the surface during cooling to room temperature [198]. Preparation for each growth experiment was done by repeated cycles of sputtering with 1.5 keV Kr^+-ions between room temperature and 773 K, and annealing up to 1173 K. The resulting surface displayed flat, clean terraces separated by monatomic unpinned steps with a typical separation of 100 nm. Prior to EuO growth the substrate was flash annealed to 1100 K, and then cooled to the growth temperature (T_{growth}) between 623 and 723 K.

4.1.2 Ir(100)

For the EuO growth on Ir(100) again a hat shaped single crystal was used. It was usually cleaned by repeated cycles of sputtering with 1.5 keV Kr^+-ions between room temperature and 900 K, and annealing up to 1550 K. For initial cleaning also oxygen glowing at temperatures up to 1150 K and O_2 partial pressures up to 10^{-6} mbar was performed. After annealing to temperatures above 800 K Ir(100) forms the Ir(100)-1×5 reconstructed surface [120], which extends up to four layers deep into the bulk. This reconstruction can be lifted by adsorption of oxygen, which itself can be removed by hydrogen adsorption at elevated temperatures [199]. Therefore the crystal was exposed for 120 s to an O_2 pressure of 5×10^{-7} mbar at 475 K and subsequently annealed to 745 K for 30 s. This step lead to the desired Ir(100)-1×1 surface but with oxygen adsorbed in a p(1×2) superstructure. Finally the oxygen was removed by exposing the crystal for 60 s to an H_2 pressure of 5×10^{-7} mbar at 535 K. This lead to a pure Ir(100)-1×1 pattern in LEED. As a consequence of this reconstruction lifting the surface contains adislands, vacancy islands, and kinked step edges as imaged by STM. A more detailed description of the preparation steps and of the final substrate topography can be found in the diploma thesis of Stefan Schumacher [200].

4.1.3 Ir(111)

For the growth on the Ir(111) surface also a hat shaped single crystal was used. The basic cleaning procedure was similar to that for the Ir(100) crystal. As the Ir(111) surface does not reconstruct, the last preparation step before EuO or graphene growth was flash annealing to 1530 K. After that, the substrate was cooled to the EuO growth temperature or to room temperature for ethylene adsorption and subsequent graphene growth. The resulting surface displayed flat, clean terraces separated by monatomic unpinned steps with a typical separation of 100 nm.

4.1.4 Graphene on Ir(111)

The system graphene on Ir(111) was already described in Sec. 2.4. In the following the growth parameters for the graphene used in this thesis are given as well as an overview of the quality. Depending on the experimental requirements either graphene flakes or fully coalesced graphene sheets were grown. Prior to each graphene growth the Ir(111) crystal was prepared as described in Sec. 4.1.3.

The flakes were prepared by room temperature ethylene adsorption till saturation, followed by subsequent thermal decomposition at 1500 K, resulting in a fraction of 0.22 of the Ir(111) surface covered by graphene flakes with a characteristic lateral extension of 500 Å [162].

Fully coalesced graphene sheets were created by an additional CVD step, at which the sample was exposed to 1×10^{-7} mbar of ethylene for 1200 s at 1100 K or to up to 5×10^{-7} mbar of ethylene for 300 s at 1200 K. This two step process yields a nearly defect-free extended monolayer graphene sheet with the $\langle 11\bar{2}0 \rangle_{\mathrm{C}}$-directions aligned to the $\langle 1\bar{1}0 \rangle_{\mathrm{Ir}}$-directions [201].

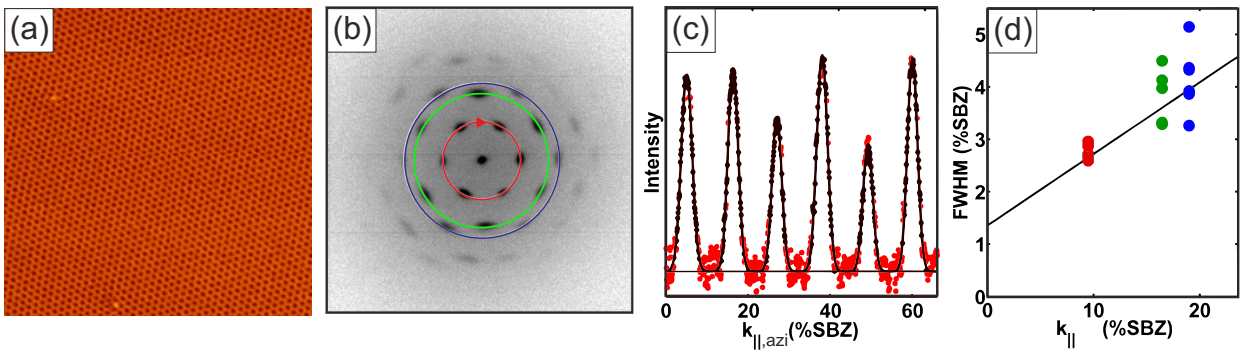

Figure 4.1: **(a)** STM topograph of graphene on Ir(111) (U_{s} = -0.57 V, I_{t} = 0.25 nA, 100 nm × 100 nm). **(b)** Inverted contrast LEED pattern of the surrounding of the central spot of a fully coalesced graphene sheet, recorded by a SPA-LEED system at a primary electron energy of 153 eV. Around the central spot the moiré spots of graphene on Ir are visible. Along the circles line scans were taken, as shown exemplarily for the inner spots in **(c)**, where the azimuthal angle has been re-calibrated in %SBZ. Thereby, 1 SBZ is defined as the diameter of the graphene surface Brillouin zone in Γ-M-direction (i.e., 100 %SBZ = 4.08 nm^{-1}) **(d)** With higher diffraction order the FWHM increases which indicates rotational disorder of the graphene films.

Figure 4.1 (a) shows the moiré pattern of a fully coalesced graphene sheet. On an area of 10^4 nm^2 only two defects are visible. As the atom density in graphene is 38.1 atoms nm^{-2} this

corresponds to a defect density of $\approx 5 \times 10^{-6}$. The high quality of the graphene was also observed by SPA-LEED measurements as shown in Fig. 4.1 (b). The moiré spots are visible up to the fifth order, representing an extremely long range ordered film with ultra-low defect densities [169]. While the FWHM of the moiré spots along the radial directions does not depend on the spot order, the FWHM along the azimuthal direction [see Fig. 4.1 (c)] increases with the spot order as shown by Fig. 4.1 (d). Although the FWHM of six equivalent spots varies between each other, the broadening is clearly visible. From the slope of 17.3% of the least square fit [solid line in Fig. 4.1 (d)] a rotational disorder of $\pm \arctan[0.173/(2\sqrt{2\ln 2})] = \pm 4.2°$ of the moiré superstructure is deduced. The moiré pattern amplifies the rotational misalignment of the graphene lattice with respect to the underlying Ir lattice by a factor of 10.7 (see Sec. 2.4), therefore the rotational disorder of the graphene is $\pm 0.4°$, which agrees reasonably with STM measurements [162]. Other rotational domains, as reported in Ref. [202], are not present.

4.2 Film growth

4.2.1 Gas Inlet Calibration

Oxygen was supplied in molecular form via a leak valve. It was guided through the tube pointing directly to the substrate described in Sec. 3.1.2. This increased the O_2 pressure at the substrate position by a factor of 50 compared to the chamber pressure, resulting in a very fast pressure decrease at the end of the growth. The O_2 pressure in the chamber was measured by a quadrupole mass spectrometer (QMS) and the local O_2 pressure at the substrate was calibrated using adsorption experiments on Ni(100) at 400 K where the progression from a p(2×2) adlayer to a c(2×2) adlayer was observed in-situ using LEED and then compared with known values. These values were improved afterwards by coverage analysis using STM.

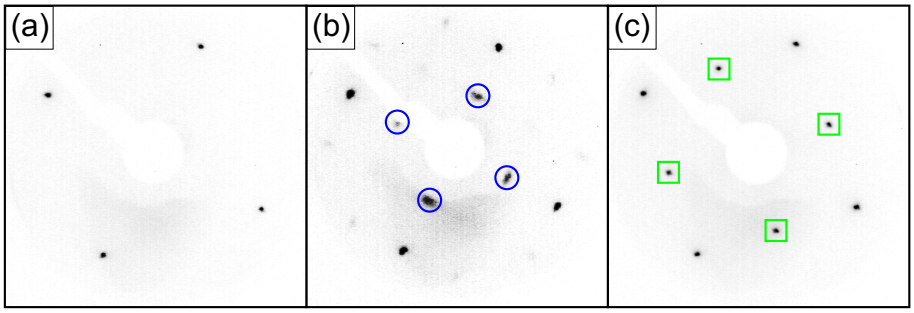

Figure 4.2: Inverted contrast LEED pattern of the Ni(100) surface at a primary electron energy of 72 eV. **(a)** Clean surface. **(b)** After exposition to about 1.8 L O_2 at 400 K. The spots indicated by blue circles are at positions where only O-p(2 × 2) superstructure spots may appear. **(c)** After exposition to about 200 L O_2 at 400 K. The spots indicated by green squares are at positions where both O-p(2 × 2) and O-c(2 × 2) superstructure spots may appear.

Figure 4.2 shows LEED patterns of the Ni(100) surface without adsorbates [Fig. 4.2(a)], with O_2 adsorbed as p(2 × 2) superstructure [Fig. 4.2(b)], and with a saturated oxygen adlayer in a

c(2 × 2) superstructure. The maximum intensity of the spots indicated by blue circles in Fig. 4.2(b) should be reached after exposing the Ni(100) surface to 1.8 L O_2 at 400 K [192]. This was used to determine the local O_2 pressure at the sample in dependence of the O_2 partial pressure measured in the QMS.

A more precise calibration was done later by coverage analysis of a monolayer high oxide structure of Eu on Ni(100), the p(5×5) superstructure described in Sec. 5.1.4. Assuming, due to the presence of Eu, a sticking coefficient of 1 for O_2, the deposited amount of oxygen was thereby calculated out of the substrate area covered by the p(5×5) Eu surface oxide and the density of O atoms of 4.52×10^{18} m^{-2} in this structure. The deposited amount (i.e. the fluence F_O) of oxygen atoms is connected via the kinetic gas theory to the pressure p_{O_2} and the exposition time t:

$$F_O = 2\frac{p_{O_2}}{\sqrt{2\pi m k_B T}} \cdot t = 5.37 \times 10^{24}\,\text{atoms}\,\text{m}^{-2}\text{s}^{-1}\,\text{mbar}^{-1} \cdot p_{O_2}[\text{mbar}] \cdot t = f_O \cdot t, \tag{4.1}$$

with m being the mass of the gas molecule, T the gas temperature, k_B the Boltzmann constant and f_O the oxygen atom flux density.

4.2.2 Evaporation

High purity Eu from the Ames laboratory [203] was evaporated out of the NTEZ (see Sec.3.1.2). Prolonged degassing of the Eu, which usually has a high hydrogen content, ensured a background pressure of about 1×10^{-10} mbar during growth. The degassing at 600 °C for several hours took place in a separate chamber, with Ta foil wrapped around the Eu ingot, as otherwise most of the material would have vanished due to the high evaporation rate. Prior to each film growth the quartz crystal microbalance was moved to the sample growth position for accurately measuring the Eu flux. Typical rates Q_{mb} at the microbalance were in the range between $Q_{mb} = 0.1$ Åmin^{-1} at 380 °C effusion cell temperature and $Q_{mb} = 3.5$ Åmin^{-1} at 470 °C effusion cell temperature. The corresponding Eu atom flux density f_{Eu} can be calculated by multiplying with the atom density $\rho_{at} = 2.08 \times 10^{18}$ atoms m^{-2}Å^{-1}:

$$f_{Eu}\left[\text{atoms m}^{-2}\text{s}^{-1}\right] = \rho_{at}\left[\text{atoms m}^{-2}\text{Å}^{-1}\right] \cdot Q_{mb}\left[\text{Às}^{-1}\right] \tag{4.2}$$

The Gd was evaporated out of the HTEZ. Similar to Eu, prolonged degassing was necessary to decrease the H_2 background pressure during growth. As Gd was used for doping only, the required rates were as low as ≈ 0.025 Åmin^{-1}, but still needed cell temperatures of ≈ 1250 K. The Gd flux (f_{Eu}) can be calculated similarly to f_{Eu} by Eq. 4.2.

4.2.3 EuO growth

As already mentioned in Sec. 2.1.4 finite size effects reduce T_C, compared to the bulk value, for films thinner than 10 ML. This is counteracted by image charge screening through the metal substrate and the compressive biaxial strain. It is therefore desirable to be able to grow high quality films with a tunable layer thickness in order to analyse the layer dependence of the combined effects. The growth of stoichiometric, single crystalline EuO films is difficult, as too high Eu deficiency

results in the formation of Eu_3O_4 or Eu_2O_3 grains and too high O deficiency leads to the inclusion of metallic Eu clusters. Additionally, EuO single crystals may contain up to 1.5% Eu vacancies or up to 0.5% O vacancies, the latter leading already to metallic conductivity at room temperature [75]. Hence, a steady state growth condition is necessary, preventing the use of post-oxidation of deposited Eu films, which would not only create problems with the homogeneity between different layers, but also with stoichiometry control.

The basic concept of stoichiometric EuO film growth by reactive molecular beam epitaxy is a distillation method [27]. Due to the high Eu vapour pressure, excess Eu, which does not react with O, re-evaporates into the vacuum at a sufficiently high T_{growth}. This is true for the growth on oxide substrates and not too high Eu excess. However, on a metallic substrate the initial growth is more complicated due to the formation of surface oxides (see Sec. 2.2). EuO on Ni(100) shows also a variety of surface phases. For a given growth temperature their formation sensitively depends on the flux ratio $f_{\mathrm{Eu}}/f_{\mathrm{O}}$. At least, a doubling of both fluxes did not change the outcome of the experiments. Hence the absolute values of the fluxes are less important and $f_{\mathrm{Eu}}/f_{\mathrm{O}}$ is the most crucial parameter for controlling the film properties. Together with either F_{Eu} or F_{O} and the growth temperature T_{growth} it fully characterises the films on a given substrate.

One experimental challenge was the establishment of the flux ratio $f_{\mathrm{Eu}}/f_{\mathrm{O}}$ at the beginning of the growth. Due to the short growth times, e.g., 30 s for some sub-monolayer experiments, both high accuracy and fast adjustment were necessary. While the Eu flux is established instantly after opening the evaporator shutter, the O_2 flux has to be tuned. Hence at the beginning of the growth $f_{\mathrm{Eu}}/f_{\mathrm{O}}$ differs from the desired value, depending on the sequence of shutter opening and leak valve adjustment: $f_{\mathrm{Eu}}/f_{\mathrm{O}}$ is initially higher if the Eu shutter is opened before the leak valve and lower for the other order. In most cases first the O_2 valve was opened quickly with low accuracy, i.e. with a deviation of up to 20% from the target pressure. This took about 2 seconds. Then the Eu shutter was opened and the O_2 pressure was fine adjusted. The precise value of $f_{\mathrm{Eu}}/f_{\mathrm{O}}$ was finally reached after a total time of about 5 seconds.

4.3 Scanning tunnelling microscopy and spectroscopy

If not stated otherwise, the STM and STS measurements were carried out at room temperature. In the chapters 5, 6, 7, and 8 the sample bias voltage U_{s} and the tunnelling current I_{t} are given for each topograph. The images were digitally post-processed with the WSxM software [204].

The following section gives a summary of the basics needed to understand tunnelling microscopy and spectroscopy. Then, in Sec. 4.3.2 a brief description of $\mathrm{d}I/\mathrm{d}U$ measurements is given. After that, two work function measurement techniques are explained, which are field emissions resonances (Sec. 4.3.3) and $I(s)$ measurements (Sec. 4.3.4).

4.3.1 The one dimensional tunnelling barrier

Figure 4.3 shows a simple one dimensional model for the tunnelling process between two conducting electrodes called tip and sample which are separated by a barrier (e.g., an insulating material or vacuum) with a trapezoidal potential. Thereby $E_{\mathrm{F,t}}$ and $E_{\mathrm{F,s}}$ denote the Fermi levels of tip and

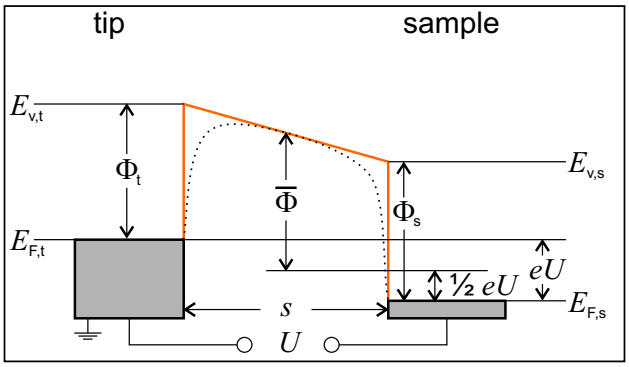

Figure 4.3: One dimensional model of a barrier (e.g., an insulating material or vacuum) separating two conducting electrodes. Image charge effects modify the trapezoidal shape as qualitatively indicated by the dotted line.

sample, respectively, and $E_{v,t}$ and $E_{v,s}$ the vacuum energies of tip and sample, respectively. Φ_t and Φ_s denote the work functions of tip and sample, respectively, U the voltage applied between tip and sample, s the distance between tip and sample, and e the elementary charge. Despite its simplicity and the restriction to the one-dimensional case, this model is suitable for approximating the tunnelling current of an STM [205].

Using a time-dependent perturbation approach and the Fermi golden rule the tunnelling current I between these two electrodes is [206]

$$I = \frac{4\pi e}{\hbar} \int_{-\infty}^{\infty} \left[f\left(E_{F,t} - eU + \epsilon\right) - f\left(E_{F,s} + \epsilon\right) \right] \rho_t\left(E_{F,t} - eU + \epsilon\right) \rho_s\left(E_{F,s} + \epsilon\right) |M|^2 \, d\epsilon, \tag{4.3}$$

with the tunnelling matrix element M being the surface integral on a separation surface between tip and sample, the distance between which is given in z-direction.

$$M = \frac{\hbar^2}{2m_e} \int dx dy \left(\psi_t^* \frac{\partial \psi_s}{\partial z} - \psi_s \frac{\partial \psi_t^*}{\partial z} \right), \tag{4.4}$$

whereby m_e is the electron mass, ρ_t and ρ_s are the densities of states (DOS) of tip and sample, $f(E)$ is the Fermi distribution function, and ψ_t and ψ_s are the wave functions of tip and sample. In the gap region ψ_t and ψ_s decay exponentially:

$$\psi_t(z) = \psi_t(0) e^{-\kappa_t (s-z)} \text{ and } \psi_s(z) = \psi_s(0) e^{-\kappa_s z}.$$

Considering elastic tunnelling conditions only, the two decay constants are equal:

$$\kappa_s = \kappa_t = \kappa = \frac{\sqrt{2m_e E}}{\hbar}. \tag{4.5}$$

Thereby one obtains the tunnelling matrix element M in dependence of s and of κ:

$$M = \frac{\hbar^2}{2m_e} e^{-\kappa s} \int dx dy \left[2\kappa \psi_s(0) \psi_t(s) \right], \tag{4.6}$$

whereby $e^{-\kappa s}$ represents the commonly known exponential decay of the tunnelling current.

By symmetrising Equation 4.4 using an average work function $\overline{\Phi}$ as indicated in Fig. 4.3, approximating $f(E)$ by a step function, and using $M(\epsilon) = M(0)\exp\left(\sqrt{\frac{m_e}{2\overline{\Phi}}}\epsilon s\right)$ one can simplify the expression for I [206] to:

$$I = \frac{4\pi e}{\hbar}\int_{-\frac{1}{2}eU}^{\frac{1}{2}eU} \rho_t\left(E_{F,t} - \frac{1}{2}eU + \epsilon\right)\rho_s\left(E_{F,s} + \frac{1}{2}eU + \epsilon\right)|M(0)|^2 \exp\left(\sqrt{\frac{2m_e}{\overline{\Phi}}}\epsilon s\right)\mathrm{d}\epsilon. \qquad (4.7)$$

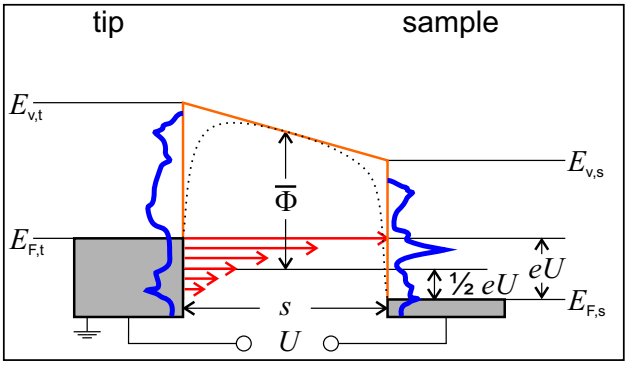

Figure 4.4: Sketch of a one dimensional barrier model describing the tunnelling process. The red arrows represent the tunnelling matrix elements ($M(\epsilon)$) and the blue lines the DOS of tip (ρ_t) and sample (ρ_s).

The meaning of Eq. 4.7 is sketched in Fig. 4.4. I is the integral over all contributions $\rho_s \cdot \rho_t \cdot M(\epsilon) \cdot \mathrm{d}\epsilon$ for energies between $E_{F,s}$ and $E_{F,s} + eU$. Apparently, due to the exponential factor in $M(\epsilon)$, higher values of ϵ contribute considerably stronger to I. For example, at typical tunnelling conditions and $U = 1\,\mathrm{V}$, the ratio of the maximal contribution (at $\epsilon = \frac{1}{2}eU$) and of the minimal contribution (at $\epsilon = -\frac{1}{2}eU$) is about one order of magnitude [206]. Hence I is mainly determined by $\rho_s(E_{F,s} + eU)\rho_t(E_{F,t})$.

Up to now the situation was described for tunnelling from the tip to the sample, i.e. for positive sample bias. As all descriptions were formulated independent of the denomination of the electrodes, the situation for negative sample bias can be described by just exchanging the indices t and s, i.e. the positions of tip and sample in the sketches of the barrier. Thus, for negative sample bias the current is mainly determined by $\rho_t(E_{F,t} + e\,|U|)\rho_s(E_{F,s})$. This means that for negative sample bias the main contributions of the sample come from E_F, independent of the sample bias U. This has an important impact on the possibilities of scanning tunnelling spectroscopy and the interpretation of the measured spectra.

4.3.2 $\mathrm{d}I/\mathrm{d}U$ measurements

One principal aim of STS measurements is the determination of the sample DOS. This is done by $\mathrm{d}I/\mathrm{d}U$ measurements, i.e. by measuring the derivative of I while modulating $U = U_b + \delta U\cos(\omega t)$. As a result of Eq. 4.7, if s and U are not too small, the dynamic tunnelling conductance at bias U_b

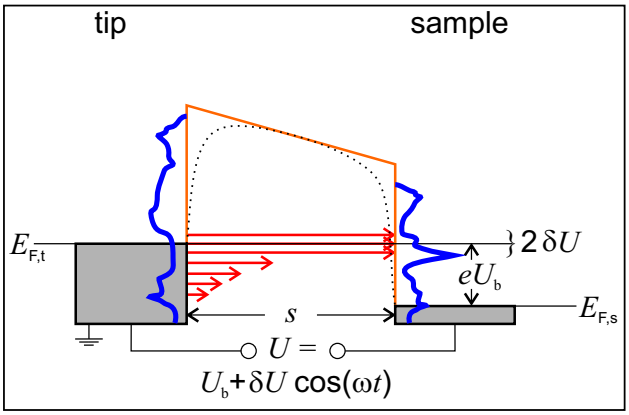

Figure 4.5: For $\mathrm{d}I/\mathrm{d}U$ measurements U is modulated by $\delta U\cos(\omega t)$.

$\left[(\mathrm{d}I/\mathrm{d}U)_{U=U_\mathrm{b}}\right]$ is governed by electrons tunnelling from tip states near the Fermi level into empty sample states at $E \approx E_\mathrm{F} + eU_\mathrm{b}$ [205; 206] and can be approximated by:

$$\left(\frac{\mathrm{d}I}{\mathrm{d}U}\right)_{U=U_\mathrm{b}} \propto T(s,U_\mathrm{b})\rho_\mathrm{s}(E_\mathrm{F}+eU_\mathrm{b})\rho_\mathrm{t}(E_\mathrm{F}), \tag{4.8}$$

with the tunnelling transmission probability [205]

$$T(s,U_\mathrm{b}) = \exp\left\{-2s\left[\frac{2m_\mathrm{e}}{\hbar^2}\left(\overline{\Phi}-\frac{e\,|U_\mathrm{b}|}{2}\right)\right]^{1/2}\right\}. \tag{4.9}$$

Correspondingly, for negative U_b it is governed by electrons tunnelling from sample states near the Fermi level into empty tip states:

$$\left(\frac{\mathrm{d}I}{\mathrm{d}U}\right)_{U=U_\mathrm{b}} \propto T(s,U_\mathrm{b})\rho_\mathrm{s}(E_\mathrm{F})\rho_\mathrm{t}(E_\mathrm{F}+e\,|U_\mathrm{b}|). \tag{4.10}$$

This has the consequence, that occupied sample states cannot be measured in most cases. But, as already mentioned, the contributions for the lowest values of ϵ in Eq. 4.7 (i.e. for $\epsilon = -1/2eU$ corresponding to $E = E_\mathrm{F,s} - e\,|U|$) are not zero but typically about one order of magnitude smaller than the strongest contributions (i.e. for $\epsilon = +1/2eU$ corresponding to $E = E_\mathrm{F,s}$,). Hence contributions at $E = E_\mathrm{F,s} - e\,|U|$ cannot be fully neglected and it is therefore possible to observe features of the occupied sample DOS if these are pronounced and the tip DOS is featureless between $E_\mathrm{F,t}$ and $E_\mathrm{F,t} + e\,|U|$. The latter criterion requires comprehensive tip treatment and verification measurements on reference samples.

The tunnelling transmission probability T depends exponentially on U_b, thus it crucially determines the course of $\mathrm{d}I/\mathrm{d}U$ spectra with increasing $|U_\mathrm{b}|$. This is shown for an exemplary T curve in Fig. 4.6. To evaluate the sample DOS, one can try to create a fit of T out of the $\mathrm{d}I/\mathrm{d}U$ spectrum and then normalise the spectrum with $1/T$. But, it might not be possible to create an unambiguous fit of T for every spectrum. Also, as already mentioned, Eq. 4.8 is only an approximation. It just takes into account the contributions at E_F.

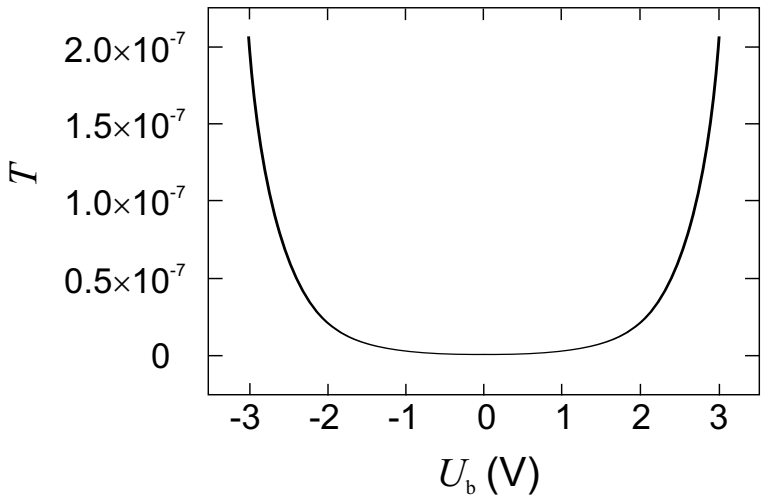

Figure 4.6: Exemplary plot of T for $\overline{\Phi} = 3\,\mathrm{eV}$ and a tip surface distance of 11.7 Å, reproduced from [205]. This corresponds to the course of a $\mathrm{d}I/\mathrm{d}U$ spectrum for constant ρ_s and ρ_t, i.e. totally flat sample and tip DOS.

Another simple possibility is to use I/U for the normalisation [207], but such a normalisation is mathematically not directly related to the LDOS [205; 208]. Additionally, this method is problematic at low currents. In such cases it is even possible that the measured current is zero at some points, caused by noise or offsets. Then singularities occur which lack any physical meaning, though it is possible to circumvent this problem by appropriate filtering [209]. Recently, more comprehensive analyses of the possibilities to extract the sample LDOS out of $\mathrm{d}I/\mathrm{d}U$ spectra were performed [208].

Technically, the modulation $\delta U \cos(\omega t)$ is done by a lock-in amplifier which also extracts the modulation out of the current signal and delivers a voltage directly proportional to $\mathrm{d}I/\mathrm{d}U$. Due to the modulation amplitude δU, $\mathrm{d}I/\mathrm{d}U$ is not precisely measured at U_b, but averaged between $U_\mathrm{b} - \delta U$ and $U_\mathrm{b} + \delta U$. Therefore, the $\mathrm{d}I/\mathrm{d}U$ signal is averaged by an integrator circuit inside the lock-in amplifier. The integration constant has to be set to multiples of the modulation time $T = 2\pi/\omega$. Longer integration times improve the signal-to-noise ratio but increase the time needed for the recording of the spectra. Another parameter which influences the signal-to-noise ratio is the modulation amplitude δU. While higher modulation voltages improve the signal-to-noise ratio they decrease the resolution of the spectra.

The modulation frequency ω has to be set such that it does not coincide with any of the noise frequencies present in the tunnelling junction. Additionally the effect of the current flowing through the bias line because of the parasitic capacitance has to be minimised. This is done by retracting the tip so far that no tunnelling current is detectable. Then the phase at the lock-in amplifier is set to that value where the $\mathrm{d}I/\mathrm{d}U$ signal is minimal. As the current flowing through the parasitic capacitance has a phase difference of ideally 90° to U, contrary to the tunnelling current, its influence on $\mathrm{d}I/\mathrm{d}U$ is minimised by this procedure without decreasing the wanted signal significantly.

$\mathrm{d}I/\mathrm{d}U$ spectra are recorded redundantly in that way that they are measured from U_1 to U_2 and then back to U_1, i.e. they end at the starting point. Only if the values for I and $\mathrm{d}I/\mathrm{d}U$ coincide for both directions, a change in the tunnelling conditions can be ruled out and the assumption of a reasonable spectrum is justified.

4.3.3 Field Emission Resonances (FERs)

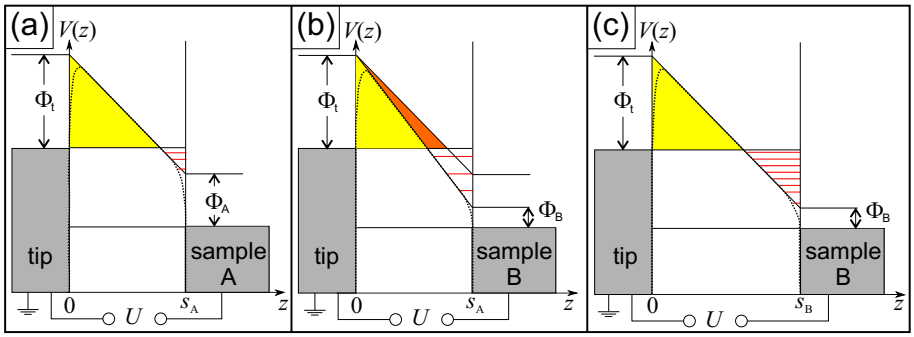

Figure 4.7: **(a)** Scheme of FERs (indicated by red lines) between the sample and the potential for the case of $U > \Phi_\mathrm{A}$. **(b)** Scheme similar to (a) with different sample work function Φ_B, but at the same distance Φ_A to the tip. **(c)** Scheme similar to (b) but now with the sample distance adjusted such that the barrier slope is the same as in (a). The area under the barrier is indicated in yellow for all sketches. The missing barrier area in (b) is indicated in orange.

If the bias voltage U exceeds the sample work function Φ_s, oscillations in the field emission current are manifested in $\mathrm{d}I/\mathrm{d}U(U_\mathrm{b})$ curves [210]. These field emission resonances, predicted theoretically by K. H. Gundlach [211] in 1966, are due to standing electron waves confined between the classical turning point of the potential and the sample surface. At the sample the reflection occurs due to the absence of bound states for energies higher than the vacuum level.

Figure 4.7(a) shows such a situation where $U > \Phi$. Electrons which tunnel through the barrier have a high probability to be reflected at the sample, then again at the barrier and so forth. At certain energies this leads to the formation of standing waves, which are indicated by red lines in Fig. 4.7. These energy values are determined by the barrier, which is substantially influenced by U and I, the properties of tip and sample, and the image potentials created by tip and sample. The image potential influences the shape of the barrier only in the vicinity of tip and sample as indicated by the dotted lines in Fig. 4.7. Typically, only the FER with the lowest energy value (i.e. the ground state) is influenced by the image potential. The relative peak positions of higher order FERs which are not influenced by the image potential are proportional to $(n+1)^{2/3}$ with n being the oscillation order [212]. Tip and sample influence the barrier not with their work functions alone, also their shapes are significant as they determine the electric field in dependence of U.

Consider a situation where the work function of the sample has changed. This is drawn exemplarily for the case of a lowered work function in Fig. 4.7(b). If the tip-sample distance is kept constant at s_A, the slope of the potential becomes steeper, i.e. the potential well becomes narrower. This leads to a decreased density of the FERs. Simultaneously the barrier has changed. Its area

(in Fig. 4.7 indicated in yellow) determines the tunnelling current and is decreased by the lowered work function, thereby leading to an increase of the tunnelling current.

If the feedback loop of the STM is turned on and the tip-sample distance is regulated for constant current at the sample areas A and B, the barrier is changed back to the same area. This situation is illustrated in Fig. 4.7(c). As long as Φ_t and U stay constant the barrier has to have the same shape for the same tunnelling current. Hence also the slope of the potential and thus the width of the potential well have to be the same for different Φ_s. This leads to the same densities of the FERs at sample positions with different work functions, just the positions of the oscillations are shifted due to the change in the work function.

Thereby the opportunity to measure work function differences between different sample areas is given. As already mentioned, between both measurements U must not be changed as well as Φ_t, i.e. it must be ensured that no tip change occurred. Additionally the feedback loop must be used to regulate for the same tunnelling current. As the FERs are seen in $\mathrm{d}I/\mathrm{d}U(U_\mathrm{b})$ curves, the feedback loop must be tuned to slow response as it would otherwise compensate the bias voltage modulation.

The easiest way to check the constance of the tip properties is to measure three $\mathrm{d}I/\mathrm{d}U(U_\mathrm{b})$ curves. First at position A, then at B, and then again at A. If both curves at A are the same the tip has kept its properties. This is a crucial point when measuring FERs as the applied voltages are considerably higher than during normal STM/STS and tip or even sample changes are more likely than usual. A comparison of oscillations of the same order for the curves from the different areas has to show a constant shift in energy. This energy shift directly is the work function difference $\Delta\Phi$.

4.3.4 $I(s)$ measurements

$I(s)$ measurements are another method to determine work function changes between different sample positions. Therefore I has to be expressed in dependence of s and $\bar{\Phi}$ [213]:

$$I(s) \propto \exp\left(-k\sqrt{\bar{\Phi}}s\right) \tag{4.11}$$

with the constant $k = \approx 1.025\,\mathrm{eV}^{-\frac{1}{2}}\,\mathrm{\AA}^{-1}$ and the apparent barrier height $\bar{\Phi}$.

By $I(s)$ measurements $\bar{\Phi}$ can be directly measured:

$$\bar{\Phi} = \left(\frac{1}{k}\frac{\mathrm{d}\ln(I)}{\mathrm{d}s}\right)^2. \tag{4.12}$$

For a simple trapezoidal barrier is

$$\bar{\Phi} = \frac{1}{s}\int_0^s \left(\Phi_\mathrm{t} - \frac{\Phi_\mathrm{t} - \Phi_\mathrm{s} + eU_\mathrm{b}}{s}\cdot z\right)\mathrm{d}z = \frac{\Phi_\mathrm{t} + \Phi_\mathrm{s} - eU_\mathrm{b}}{2}. \tag{4.13}$$

with Φ_t and Φ_s being the work functions of tip and sample, U_b the bias voltage and e the elementary charge.

This enables comparative measurements of work functions by $I(s)$ measurements if the same

bias voltage is used and Φ_t stays constant, i.e. no tip change occurs between the recording of the apparent barrier heights $\bar{\Phi}_{s1}$ and $\bar{\Phi}_{s2}$ at the different sample positions. Then the work function difference $\Delta\Phi$ is

$$\Delta\Phi = \Phi_{s1} - \Phi_{s2} = 2\left(\frac{\Phi_t + \Phi_{s1} - eU_b}{2} - \frac{\Phi_t + \Phi_{s2} - eU_b}{2}\right) = 2\left(\bar{\Phi}_{s1} - \bar{\Phi}_{s2}\right). \tag{4.14}$$

4.4 Low energy electron diffraction

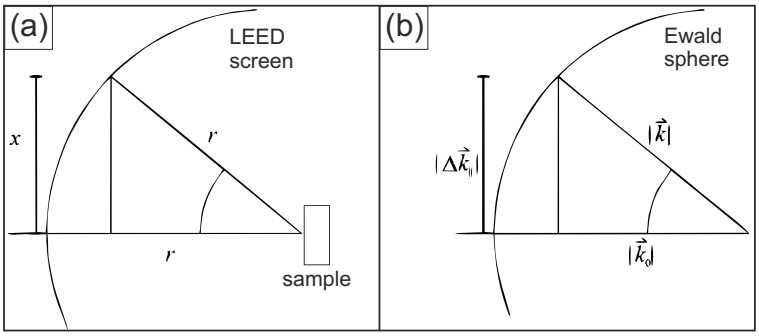

Figure 4.8: Connection between the geometric LEED values x and r and the reciprocal vectors $\Delta\vec{k}_{\parallel}$, $\vec{k}_0$, and $\vec{k}$.

LEED measurements were used extensively for determining the lattice constants of the films. Therefore, behind the LEED a video camera was mounted with its holder directly connected to the LEED flange in order to enable reproducible measurements of the spot distances x on the LEED screen. The connection between the geometrical values and the reciprocal vectors is sketched in Fig. 4.8. If the LEED is moved to the working distance (lateral distance between sample and µ-metal casing) of 25 mm, then the sample is in the centre of a sphere with radius r which coincides with the LEED screen and the surface lattice constant $a_1 = |\vec{a_1}|$ can be calculated [214]:

$$a_1 = \frac{h_p}{\sqrt{2m_e E}} \frac{r}{x} \frac{1}{\sin(\alpha)} \sqrt{h^2 + \left(\frac{k}{n}\right)^2 - \frac{2hk\cos(\alpha)}{n}} \tag{4.15}$$

E is the primary electron energy, h_p the Planck constant, m_e the electron mass, α the angle between the primitive surface lattice vectors $\vec{a_1}$ and $\vec{a_2}$ and n the length ratio between them: $n = |\vec{a_2}| / |\vec{a_1}|$. h and k are the corresponding Miller indices. In most cases square or hexagonal lattices were measured. Then is $n = 1$ and $\alpha = 90°$ and $\alpha = 120°$, respectively.

The distances x were measured by using the pixel coordinates of the spots' centres in the video data and subsequent averaging over values of equivalent spots. Calibration was done with the single crystals as reference at the same primary electron energies that were used to determine the unknown lattice constants. Intermittent test measurements on single crystals between the experiments verified a high reproducibility of this method with an error of less than 0.5%.

5 EuO on Ni(100)

This chapter describes the growth of Eu oxide on Ni(100), which was selected as a substrate for EuO growth as it is, beside Cu(100), the only conductive substrate which provides a lattice with a spacing that enables a quasi-pseudomorphic growth of EuO(100). Contrary to the Cu-Eu binary alloy phase diagram, the Eu-Ni phase diagram is simple without eutectic compositions [215]. Ni is an fcc metal with a lattice constant of 3.52 Å, while EuO has a rock-salt structure (fcc with a two atom basis) and a lattice constant of 5.14 Å. Thus, EuO(100) coincides the Ni(100) substrate in two different azimuthal epitaxial relations: EuO[001] ∥ Ni[011] with 3.1 % compressive biaxial strain as (quasi-)pseudomorphic case, and EuO[011] ∥ Ni[011] with 8.7 % compressive biaxial strain in a 3:4 relation or with 2.7 % tensile strain in a 2:3 relation. This gives the opportunity to test the possibility of applying biaxial strain on the EuO to increase T_C.

Oxidation of Ni during EuO growth is not an issue, as up to the highest EuO growth temperatures of 720 K no Ni oxide forms: Neither did we find any NiO structures, nor is this expected, as no Ni oxide formation could be observed by STM for oxygen exposures of several langmuir at elevated temperatures [216]. This is in accordance to the much lower reactivity of Ni compared to Eu and the differences in the heat of formation: $\Delta H_f(\mathrm{NiO}) = -240\,\mathrm{kJ/mol}$ (i.e. 2.5 eV/Ni atom) [217], and $\Delta H_f(\mathrm{EuO}) = -608\,\mathrm{kJ/mol}$ (i.e. 6.3 eV/Eu atom) (see Sec. 2.1). Thus, no Ni oxidation should take place in the presence of Eu metal.

The most important parameters for controlling the Eu oxide film properties on Ni(100) are the flux ratio $f_{\mathrm{Eu}}/f_{\mathrm{O}}$ and the growth temperature (T_{growth}). A doubling of both fluxes did not change the film properties, hence the film growth seems to be rather insensitive to the absolute values of the fluxes.

As already mentioned in Sec. 4.2.3, there exists a variety of Eu surface oxides on Ni(100) which were analysed in a flux ratio range $f_{\mathrm{Eu}}/f_{\mathrm{O}}$ between 0.8 and 1.7 at 623 K because of their influence on the subsequent film growth. Therefore, first these surface oxides are characterised in the following section before the desired bulk-like EuO films are described in Sec. 5.2.

5.1 The surface oxides

The surface oxides were analysed to support the search for the optimum growth parameters for bulk-like EuO(100) films, which is described in Sec. 5.2.1. Thus, the used parameters are restricted to the vicinity of these optimum parameters. Therefore, such values of $f_{\mathrm{Eu}}/f_{\mathrm{O}}$ where higher oxides (i.e., Eu_3O_4 and Eu_2O_3) or metallic Eu clusters may form were not analysed further. Nevertheless, the formation of other oxide structures was observed for drastically decreased values of $f_{\mathrm{Eu}}/f_{\mathrm{O}}$. Thus, the structures described in this thesis are just a part of the full spectrum of Eu surface oxides on Ni(100).

Due to the different stoichiometries and lattice constants, the EuO_x structures have different

densities on the surface and the coverage in layers measured by STM does not specify the amount of Eu and O. Therefore, it is advantageous to describe the deposited amount of Eu in MLE_{Ni}, whereby one $MLE_{Ni} = 1.61 \times 10^{19}$ Eu atoms m^{-2} is here defined with respect to the substrate atomic density of Ni(100). This means that 1 layer of EuO(100), (quasi-)pseudomorphically grown onto Ni(100) (EuO[001] ∥ Ni[011], EuO lattice constant 4.98Å), needs 0.5 MLE_{Ni} Eu in absence of re-evaporation.

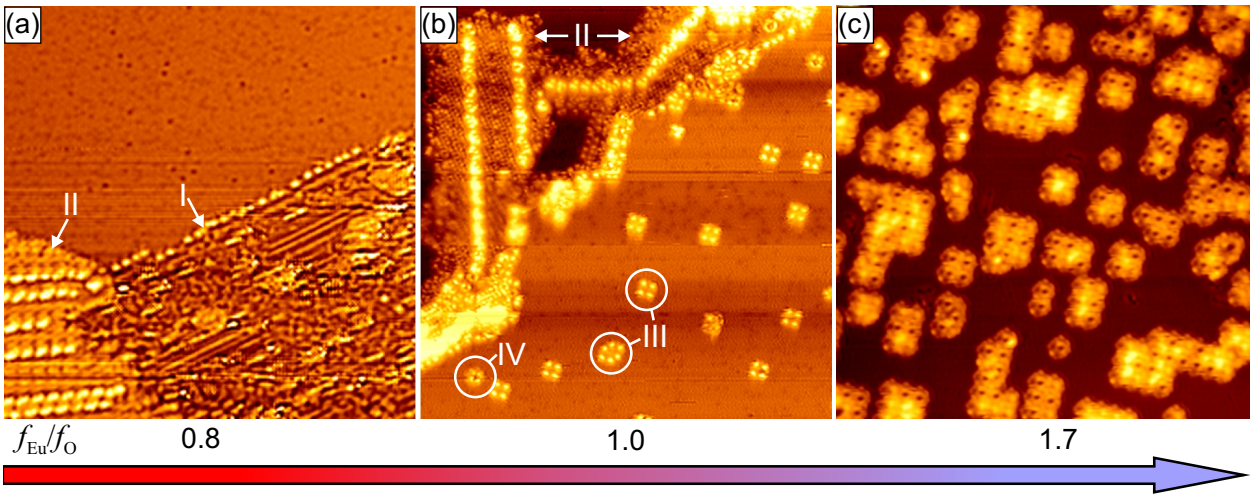

Figure 5.1: STM topographs of the distinct surface oxide phases for $0.8 \leq f_{Eu}/f_O \leq 1.7$, image dimensions 36 nm × 36 nm. All films were grown at $T_{growth} = 623$ K. **(a)** $f_{Eu}/f_O = 0.8$, $\Theta = 0.13$ MLE_{Ni} ($U_s = -2.5$ V, $I_t = 0.17$ nA). The dominant phase at this flux ratio is EuO(111), labelled **I**. Additionally, stripe islands (**II**) are present. **(b)** $f_{Eu}/f_O = 1.0$, $\Theta = 0.06$ MLE_{Ni} (−0.45 V, 2.0 nA). At the ascending Ni(100) step edge a stripe island (**II**) has grown. On the upper terrace clusters have grown which consist of two species, the 'magic' clusters (**III**) and the p(5×5) precursor clusters (**IV**), which are the building blocks of the p(5×5) superstructure shown in **(c)** $f_{Eu}/f_O = 1.7$, $\Theta = 0.2$ MLE_{Ni} (−1.0 V, 1.5 nA).

Figure 5.1 gives an overview of the Eu surface oxide phases which are analysed in this thesis. Already within a doubling of the O_2 pressure four different surface phases were found in the flux ratio range $0.8 \leq f_{Eu}/f_O \leq 1.7$ at $T_{growth} = 623$ K. These are the polar EuO(111) [Fig. 5.1(a), labelled I], complexer oxide islands which are decorated by stripes [Fig. 5.1(a) and (b), labelled II, in the following abbreviated as stripe islands], clusters of two different species [Fig. 5.1(b), labelled III and IV] and islands exhibiting a p(5×5) superstructure with respect to the Ni substrate [Fig. 5.1(c)]. One of the cluster species (IV) is a building block of the p(5×5) superstructure, which is therefore called p(5×5) precursor cluster. The other species exists in "magic" sizes only and is therefore named 'magic' cluster (III). While the 'magic' clusters only exist in a very narrow range around $f_{Eu}/f_O = 1.0$, the other phases fade gradually with increasing or decreasing f_{Eu}/f_O and a coexistence of the phases occurs. The stripe islands grow preferentially for $f_{Eu}/f_O = 1.0$ and at the step edges. Their quota is considerably reduced already for $f_{Eu}/f_O = 0.85$, where the polar phase [EuO(111)] is dominant. With increasing f_{Eu}/f_O the quota of the stripe islands is not reduced that fast and at $f_{Eu}/f_O = 1.2$ the majority of the atoms still builds stripe islands. For $f_{Eu}/f_O = 1.7$ only

small patches of stripe islands grow while nearly all of the material is incorporated into the p(5×5) superstructure phase. For a variation of f_{Eu}/f_O by a factor of two, three different two-dimensional Eu oxides were found which is comparable to the case of Mn oxide on Pd(100) at low O_2 pressures [108]. This leads to the conjecture that the complete Eu surface phase diagram on Ni(100) may be similarly manifold as that of Mn oxide on Pd(100).

In the following four sections detailed descriptions of the EuO(111) (Sec. 5.1.1), the stripe islands (Sec. 5.1.2), the clusters (Sec. 5.1.3), and the p(5×5) superstructure (Sec. 5.1.4) are given.

5.1.1 EuO(111)

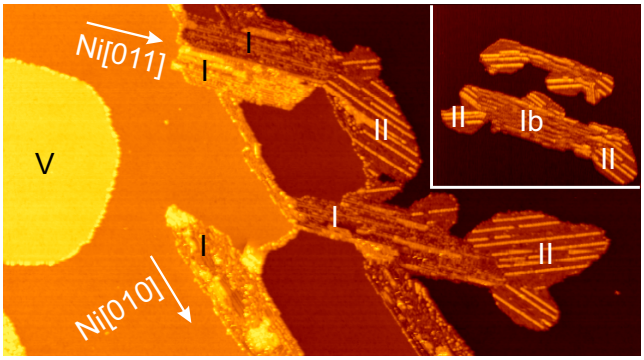

Figure 5.2: STM topographs ($U_s = -1.2$ V, $I_t = 32$ pA) of a film grown at $T_{growth} = 623$ K with $f_{Eu}/f_O = 0.85$ and $\Theta = 0.13$ MLE_{Ni}, image size 290 nm × 160 nm. The arrows show the Ni[011] and Ni[010] directions. Inset: same experiment, 170 nm × 150 nm. Indicated regions are: (I) polar ribbons grown at step edges, (Ib) polar ribbon grown on large terrace, (II) stripe island phase, (V) transported Ni.

Figure 5.2 shows an overview of a Eu oxide film grown with $f_{Eu}/f_O = 0.85$ at $T_{growth} = 623$ K with $\Theta = 0.13$ MLE_{Ni}. The labels are consistent with Fig. 5.1, i.e. I denotes EuO(111) and II stripe islands. Most of the Eu oxide nucleates at ascending step edges, whereby the polar phase adopts the shape of ribbons which orient either along Ni⟨011⟩ directions or along Ni⟨001⟩ directions and partially buries into the upper Ni terrace. This requires Ni mass transport which is consistent with the formation of Ni islands (V). Such islands are not present after the preparation of the Ni crystal as described in Sec. 4.1.1. Adjacent to the ribbon end on the lower terrace usually stripe island structures are found. As we will see in Sec. 5.1.2 it is very likely that all stripe islands are grown adjacent to EuO(111) (i.e., need a polar core to nucleate).

On terraces with lateral dimensions of 200 nm or more, one can occasionally find EuO(111) which is not adjacent to an ascending Ni step edge. This is the case for the structure labelled Ib in the inset of Fig. 5.2. Such separated EuO(111) islands also grow in ribbon shapes which are similarly aligned to the substrate as the ribbons at the step edges. Furthermore, stripe island structures are present at both ribbon ends.

Figure 5.3 shows details of two Eu oxide films grown with $f_{Eu}/f_O = 0.85$ at $T_{growth} = 623$ K, one with a deposited amount of $\Theta = 0.13$ MLE_{Ni} [Fig. 5.3(a)] and the other with about thrice of that [$\Theta = 0.42$ MLE_{Ni}, Fig. 5.3(b)]. As usual for $f_{Eu}/f_O = 0.85$, the EuO(111) covers a much

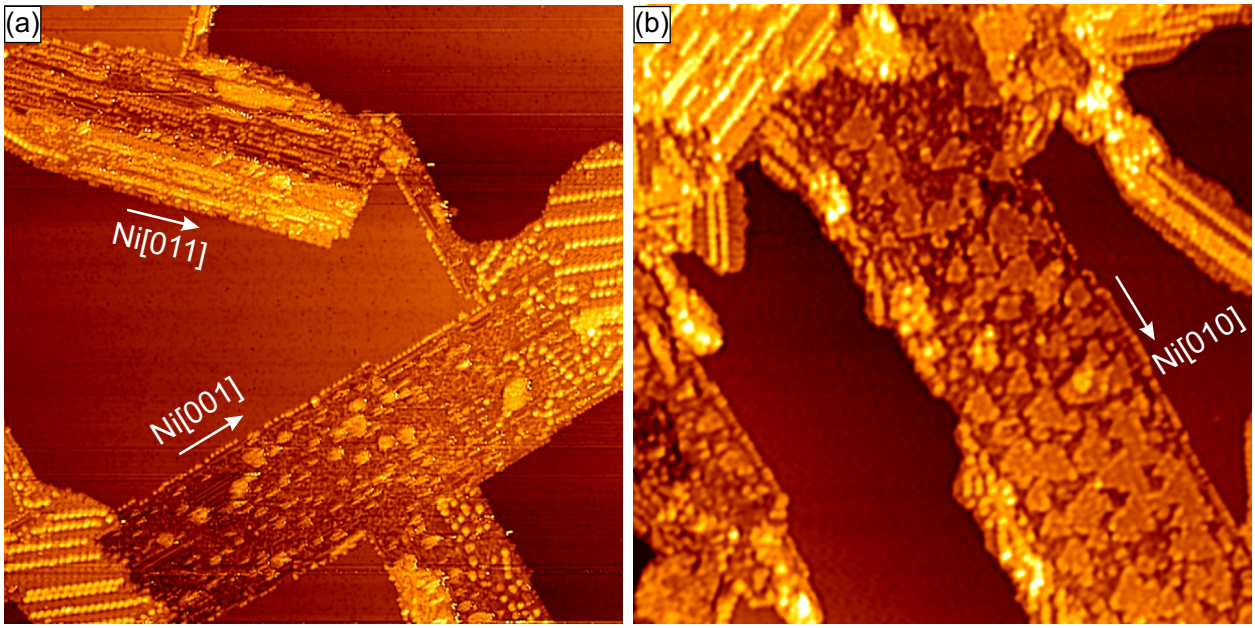

Figure 5.3: STM topographs of films grown with $f_{Eu}/f_O = 0.85$ at $T_{growth} = 623$ K, image dimensions 110 nm × 110 nm. The Ni[011] and Ni[001] lattice directions are indicated. **(a)** $\Theta = 0.13$ MLE_{Ni} ($U_s = -2.5$ V, $I_t = 0.17$ nA). **(b)** $\Theta = 0.42$ MLE_{Ni} (−1.3 V, 0.22 nA).

larger fraction of the substrate than the stripe islands.

As can be seen in Fig. 5.3(a) there are regular line patterns along the Ni[011] direction in the ribbon oriented along the same direction, whereas the structure on the ribbon oriented along the Ni[001] direction looks blurred, albeit it occasionally exhibits a weaker line pattern which is also parallel to the long edges. An eye-catching peculiarity in Fig. 5.3(a) is the position of the EuO(111) ribbon oriented along the Ni[001] direction which is widely enclosed by Ni terraces, emphasising the ribbon growth into the direction of the upper terrace and the subsequent necessity of Ni mass transport. On the right hand side of this ribbon the transition region from the EuO(111) to the stripe island structure can be seen. There is a mixing of adsorbates oriented along the Ni[001] direction and of adsorbates oriented along the stripe directions which deviate from low index Ni directions (for details see Sec. 5.1.2). This indicates a mixing of EuO(111) and stripe island structures in this transition region.

With increasing Θ, triangular structures evolve on the EuO(111) ribbons as can be seen in Fig. 5.3(b). The triangles are oriented such that one edge is parallel to the long edge of the ribbons which is the Ni[010] direction in this case.

For $f_{Eu}/f_O = 1.0$ mainly growth of stripe islands occurs, which preferentially nucleate at ascending step edges (compare Fig. 5.9(a)). This lead to the idea to first saturate the ascending step edges with stripe islands by depositing $\Theta = 0.19$ MLE_{Ni} with $f_{Eu}/f_O = 1.0$ and then lower f_{Eu}/f_O to 0.85 for additional $\Theta = 0.29$ MLE_{Ni}, a procedure which should reduce the growth of EuO(111) at ascending step edges and thus the Ni mass transport. The outcome of this experiment is shown in Fig. 5.4. Due to the complex arrangement of the oxide phases it was not possible to verify if

this method was successful in reducing the Ni mass transport.

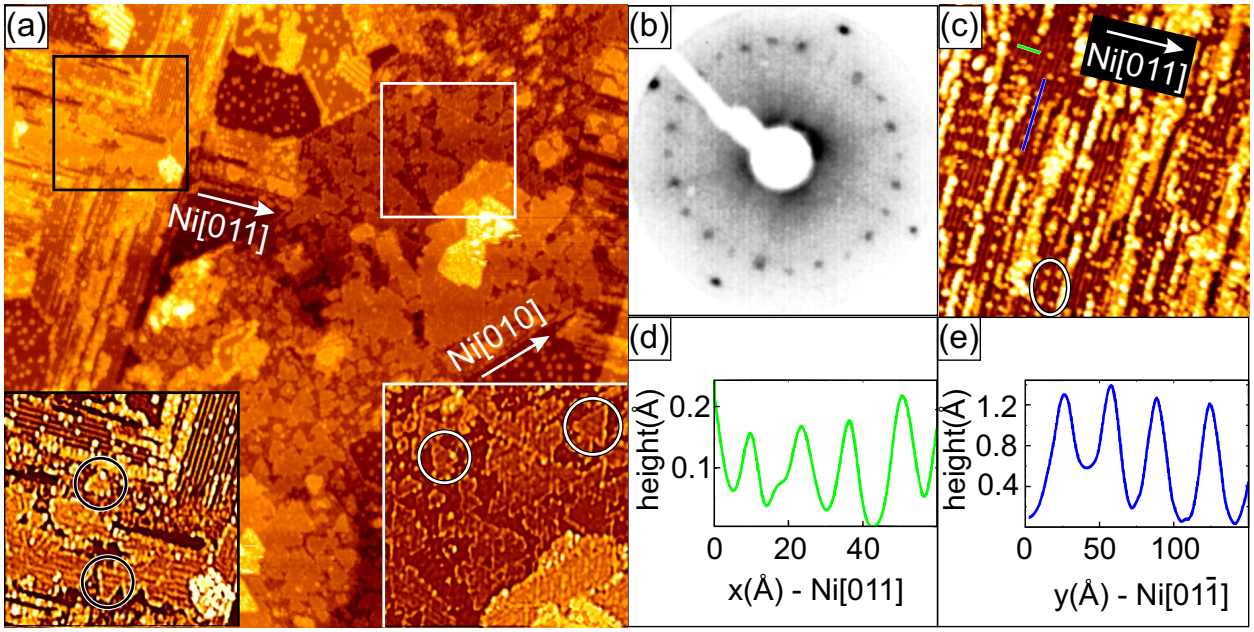

Figure 5.4: **(a)** STM topograph of a film after deposition of $\Theta = 0.19$ $\mathrm{MLE_{Ni}}$ with $f_{\mathrm{Eu}}/f_{\mathrm{O}} = 1.0$ and additional $\Theta = 0.29$ $\mathrm{MLE_{Ni}}$ with $f_{\mathrm{Eu}}/f_{\mathrm{O}} = 0.85$, giving in total $\Theta = 0.48$ $\mathrm{MLE_{Ni}}$ grown at $T_{\mathrm{growth}} = 623$ K. The Ni[001] and Ni[011] directions are indicated. Image size is 220 nm × 220 nm ($U_{\mathrm{s}} = -1.3$ V, $I_{\mathrm{t}} = 58$ pA). The insets (50 nm × 50 nm) in the lower edges show contrast enhanced zooms into the regions enclosed by the corresponding squares. The circles enclose regions with differently oriented triangles. **(b)** Inverted contrast LEED pattern of the film shown in (a) at a primary electron energy of 56 eV. The spots at the border of the field of view are {1,0} substrate spots. **(c)** Same experiment as (a), image size 68 nm × 68 nm (−1.3 V, 45 pA). The lines indicate the positions of the height profiles in (d) and (e). The oval encloses a region with a regular arrangement of adatoms. **(d)** Height profile in Ni[011] direction along the green line in (c). **(e)** Height profile in Ni[0$\bar{1}$1] direction along the blue line in (c).

The Ni surface in the STM topograph in Fig. 5.4(a) is covered by polar EuO(111) to a large extend. Only a few stripe islands are present and the remaining Ni surface is covered by clusters which have grown due to the initial use of $f_{\mathrm{Eu}}/f_{\mathrm{O}} = 1.0$. On the EuO(111) up to four layers of triangular structures have built. They have formed on both ribbon orientations, i.e. on ribbons oriented along Ni⟨011⟩ and Ni⟨001⟩ directions.

Figure 5.4(b) displays the LEED pattern of the film at a primary electron energy of 56 eV. At the border of the field of view four substrate spots can be seen which are most pronounced. Additionally, there are 24 spots arranged on a ring which belong to the two different orientations of the EuO(111). This can be explained as follows: For EuO(111) on Ni(100) with EuO$\langle 0\bar{1}1\rangle$ || Ni⟨011⟩ four domains [4 rotations of EuO(111) by 90°] are possible, two of which are mirror domains. Thus 12 LEED spots are expected in this case. The same is valid for EuO(111) on Ni(100) with EuO$\langle 0\bar{1}1\rangle$ || Ni⟨001⟩, whereby these 12 spots are rotated by 45° to the other 12. This gives in total 24 LEED spots as observed. Spots of the other surface oxide phases are not present.

The two insets in Fig. 5.4(a) show details of the two differently oriented triangular structures

which are indicated by the correspondingly coloured squares. Small, separated triangles are indicated by circles. The left hand side inset shows triangles aligned to the Ni[011] direction. For this orientation, there are faint line patterns visible inside the triangular structures. They are probably continuations of the more pronounced line patterns visible on the uncovered first bilayer of EuO(111), like those visible in the upper part of the inset. These line patterns are not present on the triangular structures aligned to the Ni[001] direction which can be seen in detail in the right hand side inset of Fig. 5.4(a).

Figure 5.4(c) displays details of the growth on the first bilayer of EuO(111). Before the triangular structures evolve, first single atoms adsorb along the line pattern which eventually coalesce to stripes. At regions with low atom density a preferred distance exists between the adsorbed atoms, indicating preferential adsorption sites. The oval in Fig. 5.4(c) encloses an example for such a region. One key factor for the adsorption behaviour is the line pattern on the first bilayer, the periodicity of which was measured by perpendicular height profiles. The green line indicates a position of such a profile which is plotted in Fig. 5.4(d). The distance between the lines is perfectly regular and is (12.5 ± 0.2) Å. The distances between the adsorbed atoms (or clusters) along the lines are density dependent, but in regions with a low density a characteristic separation width of (32.5 ± 0.5) Å can be found. This was also measured by height profiles, e.g. by that one which is indicated by the blue line and shown in Fig. 5.4(e).

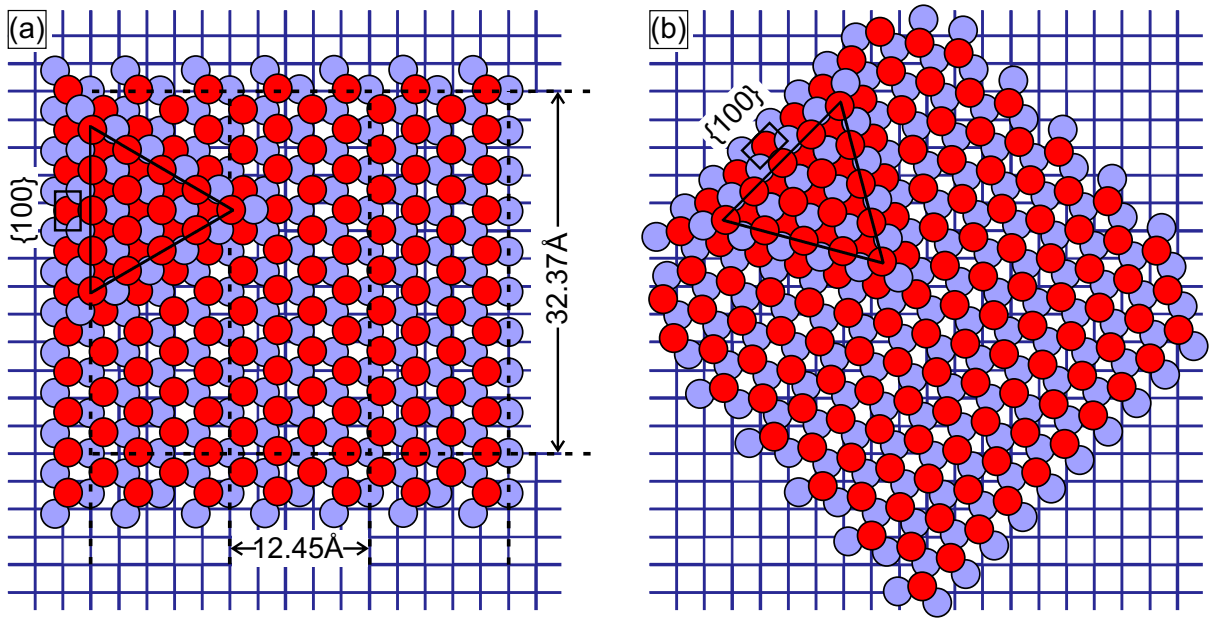

Figure 5.5: Top view ball models of one EuO(111) bilayer on Ni(100). Red circles represent O atoms, light blue circles Eu atoms, and the dark blue lines indicate the topmost substrate layer, with Ni atoms positioned at the crossing points. A triangular shaped part of a second bilayer with {100} micro facets at its borders is indicated. **(a)** EuO(111) oriented to the substrate with EuO[0$\bar{1}$1] || Ni[0$\bar{1}$1]. If the EuO lattice is compressed by 1.3% compared to its bulk value, a unidirectional coincidence with the substrate lattice occurs every 12.45Å or 5 Ni NN distances. In the perpendicular direction the coincidence would occur every 32.37Å or 13 Ni NN distances for a compression of 1.1%. **(b)** EuO(111) oriented to the substrate with EuO[0$\bar{1}$1] || Ni[001].

Several of the above observations can be explained by a simple ball model of slightly (1.3%) uniaxially compressed EuO(111) on Ni(100) which is presented in Fig. 5.5(a). It shows the EuO oriented with EuO$[0\bar{1}1]$ || Ni$[0\bar{1}1]$ and explains the line pattern with the periodicity of 12.5 Å on the first bilayer by a lattice coincidence after each fourth Eu row. Such coincidences can lead to an observable corrugation of topographic and/or electronic nature. The characteristic separation width of the adsorbates of ≈ 32.5 Å or 13 Ni nearest neighbour (NN) distances along the lines could also have a lattice coincidence as origin which would require a 1.1% smaller EuO lattice compared to the bulk value. Though it seems unlikely that a coincidence over such a relatively large distance is the origin for a lattice compression of 1.1%, it is possible that the lattice constant of a relaxed EuO(111) bilayer on Ni is slightly smaller than that in the bulk due to interface effects.

No lattice coincidences can be found in Fig. 5.5(b) which shows EuO(111) with EuO$[0\bar{1}1]$ || Ni[001]. This is consistent with the assignment of EuO$\langle 0\bar{1}1\rangle$ || Ni$\langle 001\rangle$ to the ribbons which exhibit no superstructure and are oriented along Ni$\langle 001\rangle$ directions. Correspondingly, the ribbons oriented along Ni$\langle 011\rangle$ directions consist of EuO(111) with EuO$\langle 0\bar{1}1\rangle$ || Ni$\langle 011\rangle$.

For both orientations in Fig. 5.5 a triangular patch of a second bilayer EuO(111) is shown. This visualises that triangular structures enable the formation of {100} micro facets and reduce the surface of the polar orientation. This growth mode is driven by the surface free energy difference between the neutral {100} and the polar {111} faces (see Sec. 2.3). With increasing film thickness this leads eventually to the formation of three-sided, {100} faceted pyramids and the evanescence of the polar surfaces (compare also Sec. 5.2.1).

In the ball models in Fig. 5.5 the bilayer EuO(111) is oriented such that the Eu is adjacent to the Ni and the O on top. This layer stacking was chosen because there exists evidence that it is indeed realised: The apparent height of the bilayer in the STM topographs is just similar to the height of a Ni step edge, i.e. 1.8 Å instead of the expected geometric height of 3.0 Å. This is consistent with a reduced apparent height due to a work function increase (see Sec. 4.3.3), an effect which is more pronounced for EuO(111) on Ir(111) as shown in Sec. 6.1.3. To increase the work function, an additional dipole pointing into the direction of the substrate is necessary which is consistent with the drawn layer stacking.

5.1.2 Stripe islands

Using a flux ratio of $f_{\mathrm{Eu}}/f_{\mathrm{O}} = 1.0$ the surface is covered by a mixture of clusters and islands, as shown in Fig. 5.1(b), 5.6, and 5.9(a). Most of these islands are decorated by stripes with a regular periodicity until the space in between the stripes is filled with increasing Θ. Independent of the type of decoration we will call islands of this phase stripe islands in the following. They preferentially grow at ascending step edges, as can be seen in Fig. 5.9(a), but form also at descending step edges and on larger terraces as shown in Fig. 5.6. There are several peculiarities of these islands, e.g., they grow preferentially in the direction of their stripes, thereby building ribbon-like branches. The stripe directions show manifold orientations, the majority of which can be described by a normal distribution with a standard deviation of 5°, centred around a direction which differs by $\pm(22 \pm 2)°$ from the Ni$\langle 011\rangle$-directions.

At least on the islands which nucleated on terraces one never finds one stripe orientation only,

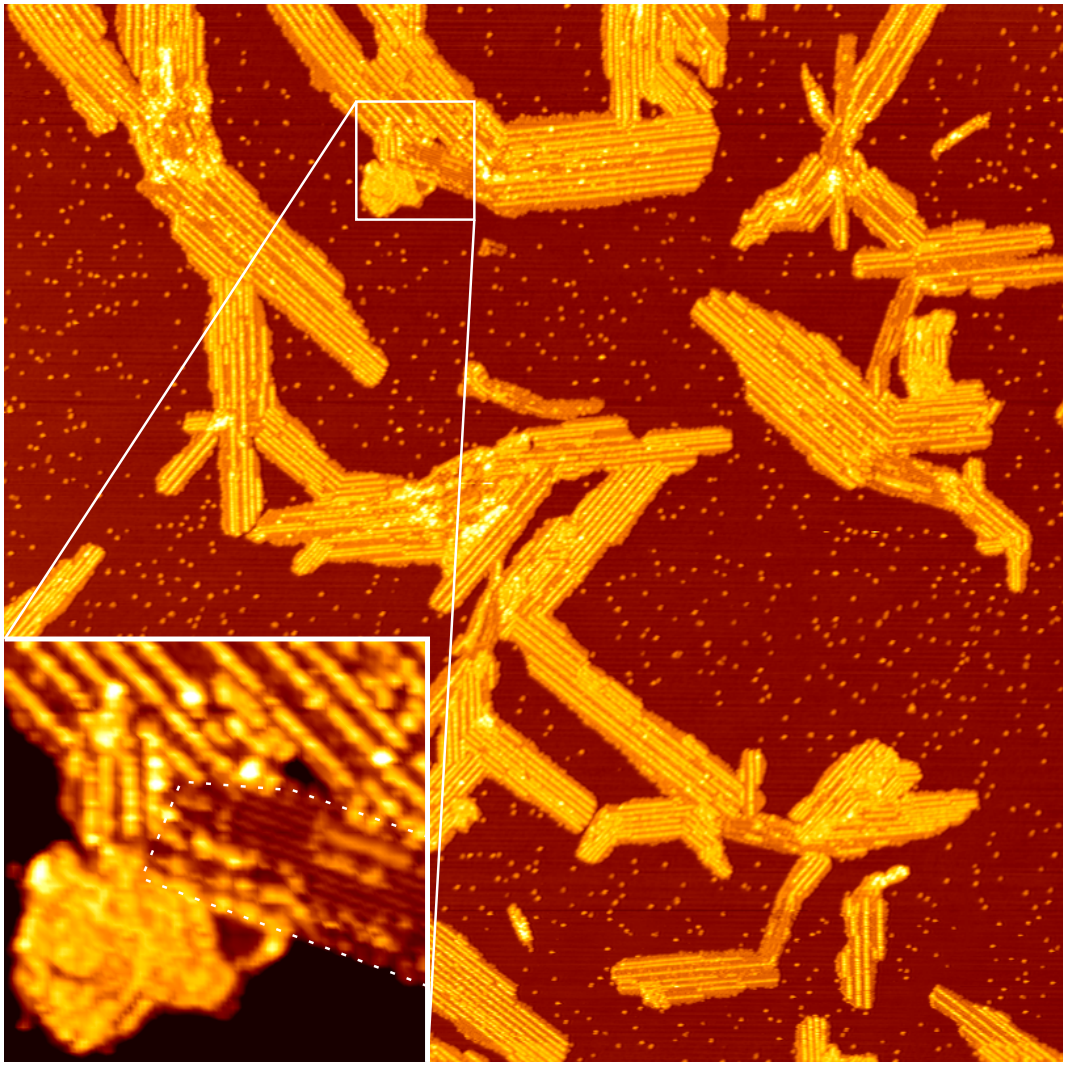

Figure 5.6: STM topograph (U_s = -1.6 V, I_t = 0.7 nA) showing a film grown at T_{growth} = 623 K with $f_{Eu}/f_O = 1.0$ and $\Theta = 0.13$ MLE_{Ni}, image size 500 nm × 500 nm. Inset: zoom (55 nm × 55 nm) into a larger EuO(111) region (enclosed by dashed line) between different stripe orientations.

but observes island parts with different stripe orientations. These parts are connected by a small region of a different structure, mostly placed near the centre of the island. These differently structured regions show unambiguous signs of the EuO(111) structure, as visible in the inset of Fig. 5.6. We assume these polar cores of the islands to be the nucleus for stripe island growth on terraces. The islands obviously have a high nucleation barrier as they need a part of the polar phase or a step edge to nucleate. Stripe islands grown close to step edges also nucleate at EuO(111). For growth at $f_{Eu}/f_O = 1.0$, parts of EuO(111) cannot be observed between the step edges and the stripe islands in most cases, probably because the size of the EuO(111) regions is too small to be identified. But, for $f_{Eu}/f_O = 0.85$, where the area of the polar phase is considerably increased, a polar part is always observed between the step edges and the stripe islands, as can be seen in the Figs. 5.3(a) and 5.2. Fig. 5.3(a) also shows that stripe islands can grow in the absence of clusters,

i.e. the presence of clusters is not mandatory for the formation of stripe islands.

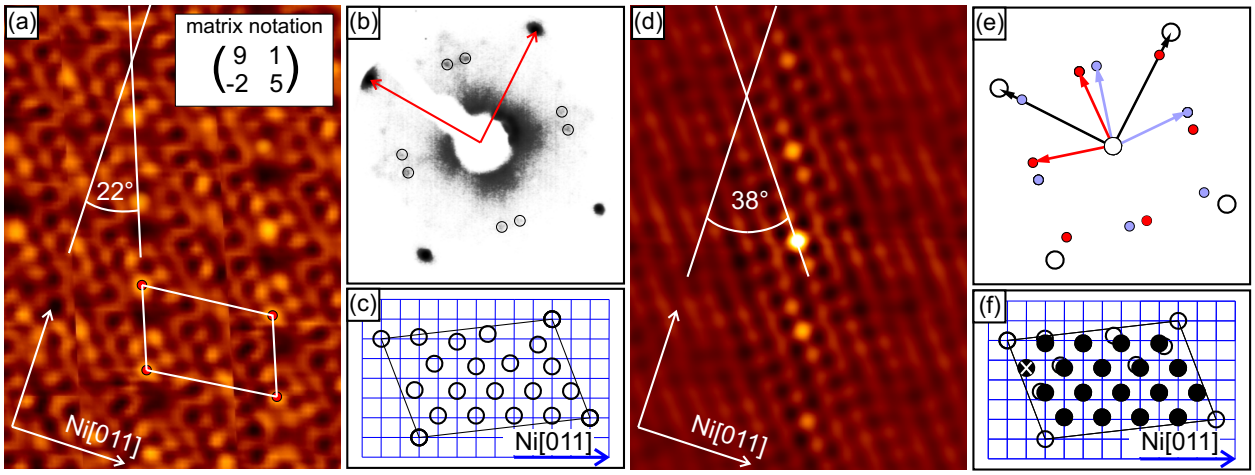

Figure 5.7: **(a)** Periodically repeated structure of the stripe island shown in the upper left part of Fig. 5.1(b). Substrate lattice directions, superstructure unit cell, and angle between stripe direction and Ni[0$\bar{1}$1] are indicated. Image size 7.8 nm × 5.7 nm. **(b)** Inverted contrast LEED pattern (50 eV) of the experiment shown in Fig. 5.6. Spots belonging to the stripe phase as well as the Ni(100) unit vectors are indicated. **(c)** Superstructure cell of (a) on Ni(100) lattice with circles positioned at bright spots in the STM topograph. **(d)** Self-correlation of (a), showing the undistorted periodicity of the stripe island. **(e)** Simulated LEED pattern of (d), unit vectors of two domains are coloured differently, Ni unit vectors indicated in black. **(f)** Same as (c), but additionally with filled circles positioned at bright spots in (d). The circle not present in (c) is marked by a ×.

Fig. 5.7(a) shows the inner structure of the stripe island in the upper left part of Fig. 5.1(b). The stripes on this island are rotated by 22° with respect to a Ni⟨011⟩-direction, making it an example for the most frequent island orientation. In order to visualise the full unit cell of the superstructure, the undecorated centre part between the stripes was copied and pasted after being shifted by the long unit vector of the superstructure cell. The stripes form by adsorption of atoms along virtual lines connecting the larger holes visible in STM topographs of undecorated island parts. These holes have the periodicity of the unit cell of the stripe islands, which is best described in matrix notation with respect to the Ni lattice as $\begin{pmatrix} 9 & 1 \\ -2 & 5 \end{pmatrix}$. This gives a periodicity of 13.4 Å within the stripes and a closest distance of 21.7 Å between different stripes. The periodicity within the stripes mostly appears as a dot pattern in the topographs. At higher resolution, as in Fig. 5.1(b), the inner structure of the dots can be seen. The structures inside adjacent dots look different which could indicate that the adsorption sites are not equivalent. In this case the unit cell of the stripe islands would be even larger. The reasons for the stripe formation and for the directional growth of the islands themselves cannot be extracted out of our data. As these structures consist of charged ions, electrostatic energy could play an important role.

Creation of a complete structure model for the stripe islands out of Fig. 5.7(a) alone is not possible, as STM topographs map the local density of states of the sample. Thus interpretation of

STM images of oxide structures is ambiguous since it is not clear what correlates to the contrast in a topograph when different chemical species are present. Bright dots mostly correlate to positions of atoms, but for the same tunnelling conditions only one atom sort of an oxide is preferentially imaged and one cannot know a priori whether this is the oxygen or the metal species [218]. For positive sample bias often only metal ions are seen [88; 218], but partially also both atom sorts [94; 95], while for negative sample bias oxygen ions could be imaged preferentially [218]. Additionally, different tip states can lead to a change between metal and oxygen mapping for otherwise similar tunnelling conditions [219].

It is quite reasonable to assume a rather stoichiometric composition, because the stripe islands preferentially form for a flux ratio $f_{\mathrm{Eu}}/f_{\mathrm{O}} \approx 1.0$. Then, the interpretation of the bright protrusions as approximate lattice points of an oxide with a two atom basis is consistent with the STM observations of oxides mentioned above. The protrusions in Fig. 5.7(a) principally run along lines which are rotated by $\pm 38°$ with respect to the Ni$[0\bar{1}1]$ direction, but with several shifts and distortions. Furthermore, at the position of the larger holes one protrusion is missing.

Fig. 5.7(d) shows a self-correlation of Fig. 5.7(a), which was applied in order to emphasise the undistorted lattice. The result is a centred rectangular lattice with unit vectors parallel to the Ni(100) surface lattice. The lengths of the unit vectors are 2 × and 2.5 × the Ni(100) unit vector. The simulated [220] LEED pattern of this lattice is shown in Fig. 5.7(e), whereby all rotational domains were considered for an easier comparison with the real LEED pattern of the experiment in Fig. 5.6. This was recorded at 50 eV primary electron energy and is shown in Fig. 5.7(b). There the 8 spots in between the Ni {1,0} spots are visible, while the 4 spots close to the Ni {1,0} spots are only visible at 82 eV, but even more faintly. In the real LEED pattern are additional faint spots with larger k values, which may belong to the parts of polar phase present in this film and/or to other structures not resolved by STM. The density of the clusters is far too low to give any intensity in LEED.

Fig. 5.7(c) shows the commensurate unit cell of the stripe island filled with circles representing the bright protrusions in 5.7(a). It is drawn onto a Ni(100) lattice to give a scale, whereby the exact position on the Ni substrate has no meaning in the drawing, as is not given by our data. Fig. 5.7(f) is the same as 5.7(c), but additionally with filled circles representing the structure of 5.7(d) to visualise the shifts of the protrusions out of the rectangular lattice. The circle without a counterpart in Fig. 5.7(c), i.e. the one close to the centre of the larger holes in the STM topograph, is marked by a ×.

One could easily get a full oxide structure with reasonable distances by using a basis of one Eu and one O atom per filled circle and shifting, e.g., the Eu atoms to the position of the open circles and the O atoms to reasonable positions in between. But, without aid and verification by density functional theory (DFT) calculations, development of a more detailed structure model is not meaningful. The undistorted lattice has a simple commensurate unit cell best described in matrix notation with respect to the Ni lattice as $\begin{pmatrix} 5 & 0 \\ 0 & 2 \end{pmatrix}$. The most probable reason for the deviations from the rectangular lattice is avoidance of unfavourable substrate positions. Subsequent buckling, deviations from stoichiometry and subsequent electronic changes could then explain the observed

topography.

The structures shown in Fig. 5.7 are only valid for the most common stripe directions which differ by ±22° from a Ni⟨011⟩ direction. Although we have no high resolution data of islands with stripe directions deviating from this angle, different arrangements of the larger holes in the islands and the corresponding changes of the distances between the stripes and of the periodicity within the stripes must be related to changes of the details of the structure while it seems probable that the underlying undistorted lattice is the same for all stripe islands.

5.1.3 Clusters

For films grown with a flux ratio of $f_{Eu}/f_O = 1.0$ and $\Theta \leq 0.52$ MLE_{Ni} are clusters with several different sizes on the substrate, beside the stripe islands described in section 5.1.2. An overview for a very low deposited amount of 0.06 MLE_{Ni} is given in Fig. 5.1(b), where three sizes of clusters are present, which all have edges aligned to the Ni⟨011⟩-directions. The largest cluster shows six bright dots at its corners, while the other ones have four of them. The apparent height of these dots is between 1.5 Å and 2.0 Å in all topographs, mainly depending on the tip state. Three of the 4-dot clusters in Fig. 5.1(b) are considerably smaller than the other 4-dot ones, and they are indeed a building block of continuous oxide islands with a p(5×5) superstructure, which are shown in Fig. 5.1(c) and 5.10. Therefore we call them p(5×5) precursor clusters and describe them later on in section 5.1.4 together with the p(5×5) superstructure itself.

The larger 4-dot clusters and the 6-dot ones belong to the same species, which forms also an 8-dot variant for higher Θ, e.g for 0.52 MLE_{Ni}, as shown in Fig. 5.8(a). The structure in the upper left side of this topograph is a part of a stripe island which already has an increased coverage in the second layer. The clusters have a comparatively high density without building larger structures than the 8-dot type. As this species builds three "magic" sizes of symmetric clusters we call them 'magic' clusters in the following. There exist also some clusters which appear to be 'magic' ones with attachments or missing parts, i.e. are not fully completed or in the state of transition to a larger size, which can be described as defective 'magic' clusters.

In the 0.52 MLE_{Ni} experiment the quota of p(5×5) precursor clusters is much lower compared to the 0.06 MLE_{Ni} experiment, despite the nominally same conditions. The reason is the extreme sensitivity of the cluster formation to the flux ratio f_{Eu}/f_O and the experimental difficulties to adjust exactly the same value again, although we achieved a reproducibility of f_{Eu}/f_O of better than 5%. For the examined growth temperature of 623 K the two different species of clusters are simultaneously present for a narrow range of flux ratios f_{Eu}/f_O only. For slightly higher O fluxes, using $f_{Eu}/f_O = 0.85$, no cluster formation could be observed at all, as shown in Fig. 5.2 and 5.3. For lower O fluxes the change is somewhat more gradually, but for $f_{Eu}/f_O = 1.25$ nearly all clusters are p(5×5) precursors or islands.

The bright dots at the corners of the 'magic' clusters are visible in the STM topographs for very low negative sample bias voltages and down to U_s = -1.5 V. For larger voltages or positive sample bias we did not achieve high resolution and stable imaging conditions simultaneously. We used these dots as starting points for the construction of the simple ball models of the different "magic" sizes shown in Fig. 5.8(b) through (d). The first step in building these models was to

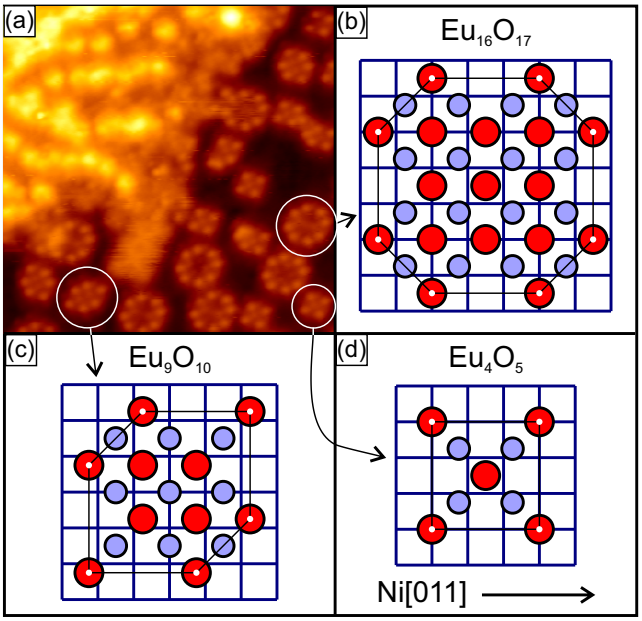

Figure 5.8: **(a)** STM topograph (U_s = -0.13 V, I_t = 4.9 nA) showing a film grown at T_{growth} = 623 K with f_{Eu}/f_O = 1.0 and Θ = 0.52 MLE_{Ni}, image size 27 nm × 27 nm. Beside the part of the stripe island there are several 'magic' clusters visible, three examples for the different sizes of them being indicated. **(b)** Model of the 8-dot 'magic' cluster, which has 8 dots visible in the topograph. **(c)** Model of the 6-dot 'magic' cluster and **(d)** of the 4-dot 'magic' cluster. Red circles represent O atoms, blue circles Eu atoms, and the lines indicate the topmost substrate layer, with Ni atoms positioned at the crossing points. Atoms positioned at the bright protrusions in the topograph are marked by a white dot.

determine the dot distances as precisely as possible. Therefore we used topographs where both 'magic' clusters and small p(5×5) islands [e.g., see 5.11(a)] were present. The latter ones gave a scale and enabled a correction of the image distortion. This gave 7.5 Å as nearest neighbour (NN) dot distance for the 4-dot cluster. The 6-dot and 8-dot type also have a shorter edge length, where a dot distance of 5.3 Å was measured. These shorter edges enclose angles of 45° or 135° with the longer ones, hence the shorter edge length is cos(45°) × the longer edge length due to the clusters' 4-fold symmetry with respect to the substrate lattice: While the 4-dot and 8-dot size are 4-fold symmetric themselves, the 6-dot size is 2-fold symmetric only, but exists in two different orientations, rotated by 90° to each other.

As already mentioned in section 5.1.2 the interpretation of protrusions in STM topographs is ambiguous. As the dots at the 'magic' clusters' corners are isolated and radial symmetric it is appropriate to assume that they correspond to positions of similar atoms. Hence we put atoms of the same sort in the measured dot distances and directions on a Ni(100) lattice and slightly shifted them such that they match exact substrate lattice points in the case of the 4-dot cluster. Thus we finally got a length of 7.48 Å (3 Ni NN distances) for the long edge and 5.29 Å (7.48 Å · $1/\sqrt{2}$) for the short edge. After that we put atoms of the other sort in between these NN dots, which gave a Eu-O distance of 2.65 Å, close to the distance in bulk EuO of 2.57 Å. To connect these edges

we used a quadratic lattice because of the 4-fold symmetry. Furthermore we avoided construction of polar edges, as these would be unfavourable due to the related electrostatic energy. Finally we have chosen O atoms to be at the dot positions for two reasons. First, the dots appear for negative sample bias, what could lead to preferential imaging of O atoms [218]. Second, our model for the p(5×5) superstructure has a slight excess of Eu with a Eu_8O_7 unit cell while growing preferentially at larger Eu excess. Hence a slight O excess, which results from choosing O atoms at the dot positions, seems to be more appropriate for the 'magic' clusters.

We note that the ball models in Fig. 5.8(b) through (d), which we got by this procedure, are just the simplest constructions which fit the measured dimensions and have reasonable Eu-O distances. Without DFT calculations it is not possible to verify or further improve these models. Nevertheless, due to the clusters' symmetry and the similarity between different "magic" sizes it was not possible to construct other models with a reasonable inner structure. Hence the basic structure seems to be appropriate while the details, especially that of the edges and the positioning of O atoms at the dots are relatively uncertain.

The bright imaging of the corner atoms could originate in their lower coordination number, as this is the main difference to their counterparts inside the cluster. An increased ionicity of the bonds as compensation for the missing Eu atom, which would be needed for full stoichiometry, is improbable, because the Eu-O distance is slightly enhanced compared to bulk EuO. Instead, a charge transfer from the substrate could occur, with the charge of the clusters localised at the corner atoms due to electrostatic repulsion. This would not necessarily lead to filling of pre-existing states only, but could also give rise to a substantial reorganisation of the LDOS and thus to the appearance of the corner atoms in STM topographs.

The reason for the formation of the "magic" sizes is not directly obvious. The clusters are mobile at the growth temperature, as we will show below; but coalescence of them would be kinetically hindered by electrostatic repulsion if the corner atoms are charged in the way one could expect by their electron affinity. Also attachment of an O atom would be unfavourable due to the formation of polar edges and attachment of a Eu atom would only be possible at a corner atom. The latter event has to be less probable than nucleation of a new cluster, as otherwise growth of continuous oxide layers would be expected. Additionally, as kinetic limitations only can explain the absence of continuous layers, there must be a reason for the symmetry of the clusters.

Annealing of the clusters leads to a considerable decrease of their density. Fig. 5.9(a) shows a film with $f_{Eu}/f_O = 1.0$ and $\Theta = 0.06$ MLE_{Ni}, which was immediately cooled down after ceasing the Eu and O fluxes. The total cluster density n, not distinguishing between different species, is 0.045 clusters nm^{-2}. Using the same growth parameters, but additionally leaving the sample at $T_{growth} = 623$ K for 10 s after ceasing the fluxes results in a decrease of n to 0.025 clusters nm^{-2}. Fig. 5.9(b) shows the film of (a) after annealing at 623 K for 600 s. Nearly all clusters have vanished, while several islands and smaller oxide patches are left on the terrace. This proves that the clusters are not stable at 623 K after shutting off the reagent fluxes. The material of the decayed clusters is either incorporated into or forming new stripe islands.

For further analysis we have grown a film with $f_{Eu}/f_O = 1.0$ and $\Theta = 0.13$ MLE_{Ni}, which was again cooled down immediately. Due to the higher deposited amount, n increased to 0.08 clus-

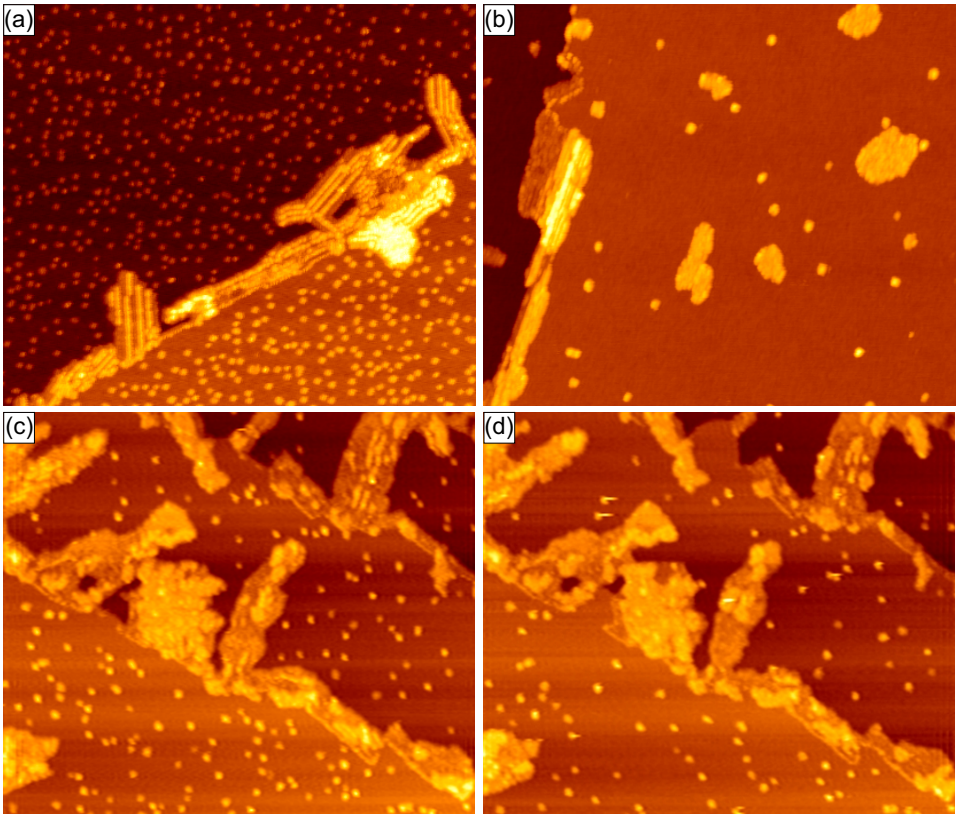

Figure 5.9: STM topographs with image size 160 nm × 135 nm: **(a)** Film grown at $T_{\mathrm{growth}} = 623$ K with $f_{\mathrm{Eu}}/f_{\mathrm{O}} = 1.0$ and $\Theta = 0.06$ $\mathrm{MLE_{Ni}}$, directly cooled down after growth (U_{s} = -0.23 V, $I_{\mathrm{t}} = 0.8$ nA). **(b)** same experiment as (a), additionally annealed at 623 K for 600 s (U_{s} = -0.23 V, $I_{\mathrm{t}} = 0.3$ nA). **(c)** Film grown at $T_{\mathrm{growth}} = 623$ K with $f_{\mathrm{Eu}}/f_{\mathrm{O}} = 1.0$ and $\Theta = 0.13$ $\mathrm{MLE_{Ni}}$, image taken at 558 K after an annealing time of 2090 s at this temperature **(d)** same film and position as in (c) after additional 2420 s of annealing at 558 K (U_{s} = -0.5 V, $I_{\mathrm{t}} = 1.0$ nA both).

ters nm^{-2}. After the measurement of these values, the film was annealed with stepwise increasing temperature and observed in-vivo with STM, whereby one topograph was recorded every 110 s. Changes, which happened in a reasonable time scale for STM, occurred at 558 K. Fig. 5.9(c) shows the film after 2090 s of annealing at this temperature. The cluster density already decreased to 0.02 clusters nm^{-2} and the stripe islands changed, as nearly all of the stripes are gone. Instead they are either undecorated or have partially a height of two layers. These changes originate not only in the inclusion of the additional material from the decayed clusters as there also occurs diffusion of atoms that were already part of the second stripe island layer.

Connecting the successive topographs to a video gives insight into the annealing behaviour of the clusters. Most of the clusters stay at the same position until the entire cluster begins to move or even vanishes within successive topographs. Hence the clusters do not just decay, but also diffuse as entity at 558 K and above. Interestingly, the hopping frequency of the clusters keeps considerably higher after the first displacement has taken place: Once their motion has started most of the clusters do not stop again and finally vanish, frequently in the vicinity of stripe islands.

The last topograph of the annealing sequence is shown in Fig. 5.9(d). During the additional 2420 s of annealing n further decreased to 0.009 clusters nm^{-2}. The dependence of n from the annealing time t can be described by an exponential decay law: $n = n_0 \exp(-t/\tau) + n_s$, with $n_0 = 0.073$ clusters nm^{-2} being the initial density of clusters which decay within the time constant $\tau = 1200$ s, and $n_s = 0.007$ clusters nm^{-2} the density of clusters which are stable at 558 K. It is most probable that all clusters, which decay with the same time constant, have the same size and belong to the same species. At $f_{Eu}/f_O = 1.0$ the vast majority of the clusters are 4-dot 'magic' clusters, although their quota varies between different experiments due to their high sensitivity to the flux ratio. Hence it is probable that n_0 is the density of 'magic' 4-dot clusters, although the resolution during the imaging at 558 K was not sufficient to distinguish between different cluster sizes and species. n_s would then be the combined density of larger 'magic' clusters and p(5×5) precursor clusters, as well as of slightly larger p(5×5) patches.

5.1.4 p(5×5) superstructure

As already mentioned, the cluster formation is very sensitive to the flux ratio f_{Eu}/f_O. For $f_{Eu}/f_O = 1.2$ the formation of 'magic' clusters is almost suppressed. Instead, the terraces are covered by p(5×5) clusters, or for larger Θ, by islands of the p(5×5) superstructure phase, as can be seen in Fig. 5.10(a) for $\Theta = 0.32$ MLE$_{Ni}$. For these growth parameters still a considerable quota of material was consumed by the growth of stripe islands, on which already some larger patches of the second layer are present and third layer adsorption has taken place, as shown in the inset of Fig. 5.10(a). The structures in this third layer have rectangular edges, which run along the Ni⟨011⟩-directions and display dots with a distance of 10 Å in the topographs, building a p(4×4) superstructure with respect to the Ni lattice, i.e. a c(4×4) superstructure with respect to a slightly compressed EuO(100) surface lattice [221]. Hence, this third layer could already be bulk like EuO where only one of eight atoms of the same sort is imaged by STM. This could be caused by inequivalent adsorption positions and related surface buckling and/or electronic differences. This p(4×4) superstructure was never observed by LEED as the total area of this structure is not large enough to give a signal that can be seen in the diffuse LEED intensity. Also, the p(4×4) was never observed by STM for fully coalesced films. It is probably covered by an additional layer, the fourth in total on the stripe phase, before the second layer on the terrace fully covers the p(5×5) structure.

Increasing f_{Eu}/f_O further to 1.7 fosters the growth of the p(5×5) oxide compared to the stripe islands, as can be seen in Fig. 5.10(b). Although Θ is lower than for the experiment of Fig. 5.10(a), the coverage of the terraces with the p(5×5) oxide is higher. This is caused by the reduction of stripe island growth and the corresponding lower quota of material condensed in the stripe phase. The ribbon-like branches, which are characteristic for this surface oxide at lower flux ratios, are absent. Instead it grows along the Ni step edges and is two layers high to a large extend. In between almost no stripes are left, i.e. these areas are widely undecorated and have a height of one layer, with a similar apparent height in STM as the Ni terrace. Thus, in large scale images, stripe phase areas are not easily distinguishable from the adjacent Ni terrace, which is covered by the p(5×5) superstructure. The black line in Fig. 5.10(b) indicates the approximate position of the border between the upper Ni terrace and the attached stripe phase oxide. This border does not resemble

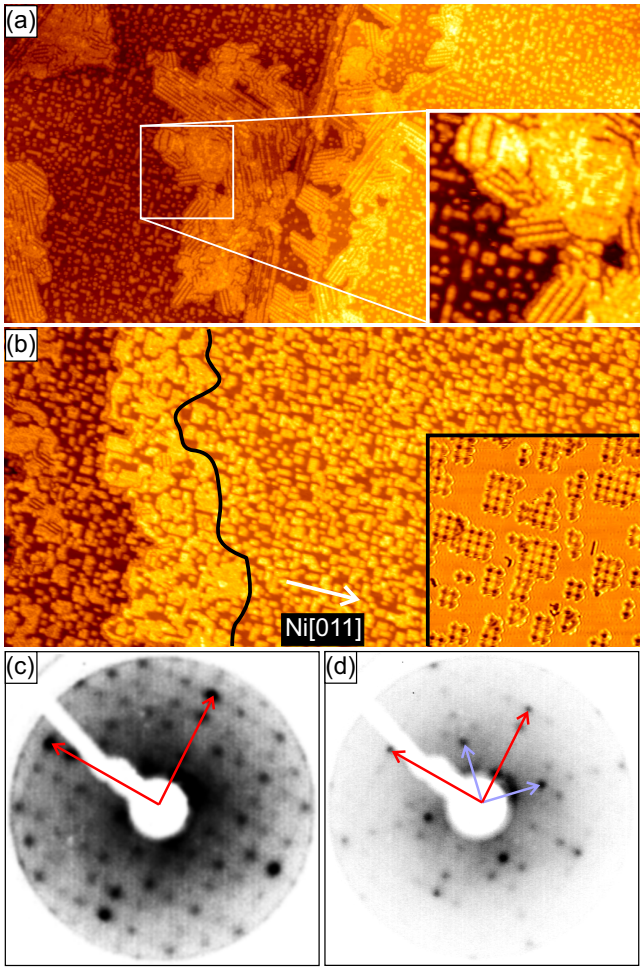

Figure 5.10: **(a)** STM topograph (U_s = -1.4 V, I_t = 0.2 nA) showing a film grown at T_{growth} = 623 K with f_{Eu}/f_O = 1.2 and Θ = 0.32 MLE_{Ni}, image size 320 nm × 160 nm. Inset: zoom into a stripe island with coalesced 2nd layer and 3rd layer adsorption, 45 nm × 45 nm. **(b)** STM topograph (U_s = -1.0 V, I_t = 0.6 nA) showing a film grown at T_{growth} = 623 K with f_{Eu}/f_O = 1.7 and Θ = 0.26 MLE_{Ni}, image size 320 nm × 160 nm. The black line indicates the approximate border of the upper Ni terrace, the Ni[011]-direction is indicated. Inset: same experiment, 30 nm × 30 nm (U_s = -1.0 V, I_t = 1.5 nA). **(c)** Inverted contrast LEED pattern of the film in (b), showing the p(5×5) superstructure (70 eV primary electron energy), the arrows represent the unit vectors of the Ni(100) surface. **(d)** LEED pattern of same film, but at 96 eV. The long arrows represent the unit vectors of the Ni(100) surface, the shorter ones those of the surface oxide.

the shape of a step edge on clean Ni(100) as the Ni step edges are influenced by the oxide growth.

As we will see in Sec. 5.2, the p(5×5) phase is the optimum foundation for the growth of high quality EuO(100) films. It is stable during annealing at 673 K for 300 s, but annealing at 873 K for 180 s destroys the superstructure and the LEED shows faint spots of pseudomorphic EuO. The p(5×5) surface oxide wets the Ni terraces smoothly, while at the ascending step edges stripe phase Eu oxide forms, on which the second and third layers evolve first upon continued growth.

The inset of Fig. 5.10(b) is a zoom into the p(5×5) phase, clearly showing a quadratic dot pattern with a periodicity of 12.5 Å. This is a p(5×5) superstructure with respect to the Ni lattice,

which is also present in the LEED pattern in Fig. 5.10(c). In the inset STM topograph one can additionally observe boundaries inside p(5×5) islands where a registry shift of the superstructure occurs. Hence, these are antiphase boundaries between translational domains, of which exist 25 for a p(5×5) superstructure. As registry shifts can be found even for a single building block, a precursor cluster, it is unlikely that these have a considerable mobility as entire unit at T_{growth}, because otherwise one would expect diffusion to a position where the precursor cluster fits to the adjacent lattice.

The p(5×5) surface oxide cannot be just a pseudomorphic, bulk-like EuO layer with missing atoms due to symmetry reasons: In this case the superstructure sites would be alternating Eu or O atoms, which would result in two distinct larger superstructure cells. Hence it must have a different lattice, which was also observed by LEED: For several primary electron energies spots [of the p(5×5) LEED pattern] are highly pronounced which belong to a quadratic structure that is rotated by 45° with respect to the Ni(100) lattice. The corresponding surface lattice constant of 4.4 Å is 21% larger than for bulk-like EuO(100). This is best seen in the LEED pattern in Fig. 5.10(d) which is taken from the same film as the pattern in Fig. 5.10(b), but recorded at 96 eV.

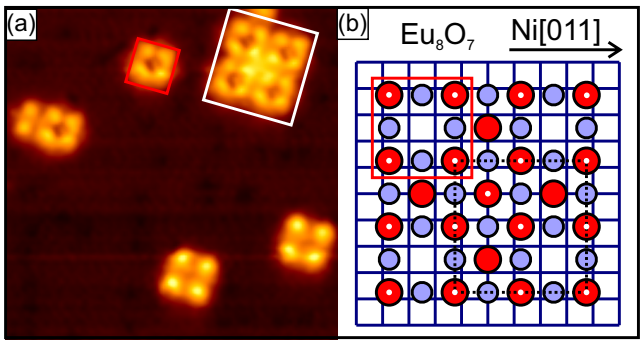

Figure 5.11: **(a)** STM topograph (U_{s} = -0.45 V, I_{t} = 2.0 nA) showing a film grown at T_{growth} = 623 K with $f_{\mathrm{Eu}}/f_{\mathrm{O}}$ = 1.0 and Θ = 0.06 $\mathrm{MLE_{Ni}}$, image size 10 nm × 10 nm. The structures in the upper half belong to the p(5×5) phase, below are two 'magic' clusters. The red square encloses a p(5×5) precursor cluster, the white square the p(5×5) patch that is modelled in **(b)**. The model uses the same colour code as Fig. 5.8. The red square in the upper left corner again encloses one precursor cluster. The larger, dashed square indicates a unit cell of the p(5×5) phase.

Fig. 5.11(a) is a small scale image of an experiment with $f_{\mathrm{Eu}}/f_{\mathrm{O}}$ = 1.0 and Θ = 0.06 $\mathrm{MLE_{Ni}}$. In the upper half are parts of the p(5×5) phase. Enclosed by a red square is a p(5×5) precursor cluster, which is the smallest entity of the p(5×5) structure and has a characteristic depression in its centre in STM topographs. Enclosed by the larger, white square is a quadratic p(5×5) island which contains 4 of the precursor units.

Fig. 5.11(b) shows a model of this island. It uses the enlarged EuO(100) lattice with a surface lattice constant of 4.4 Å and O vacancies positioned at the centres of the precursor units, resulting in a unit cell which contains 8 Eu and 7 O atoms. The assumption of O vacancies is justified by two reasons: The p(5×5) phase grows preferentially for Eu excess, and O atoms in a surface oxide commonly prefer on-top positions and avoid hollow positions on the metal substrate. This

principle is described for the oxidation of metal surfaces [89; 94], but may also be valid for the growth of an oxide of a different metal (see also Sec. 2.2). For the given lattice this principle is best fulfilled for the proposed model, where the used O vacancy pattern is the p(5×5) superstructure with respect to the substrate lattice. Enclosed by a red square in Fig. 5.11(b) is a p(5×5) precursor unit. It is obvious that coalescence of precursor clusters cannot build the p(5×5) phase: Between different precursor units the lattice is continued without vacancies. Similar to the models for the 'magic' clusters we note that this suggested p(5×5) model is just the simplest possible solution which complies with the STM and LEED data and requires verification by DFT calculations.

The O-O distance in the p(5×5) surface oxide is equal to the lattice constant of 4.4 Å. This is an unusually high value as the O-O distance of nearly all transition metal oxides is approximately 3 Å, in the bulk as well as for surface oxides [89]. An exception are oxygen induced structures on Ag, where the O-O distance is 4.1 Å, but these are not considered to be true surface oxides since they are characterised by metal-like Ag-Ag distances [89]. For bulk EuO the O-O distance of 3.64 Å is already larger than for the transitional metal oxides. But as the O-O distance in the 'magic' clusters of 3.75 Å is also quite close to the EuO bulk value, the p(5×5) of Eu_8O_7 on Ni(100) is probably no true surface oxide. This suggests a considerably reduced ionicity of the Eu-O bonds, what cannot be explained only by the 12.5% O vacancies as the O atoms are expected to have a charge of $2e^-$. Thus charge should also be provided by the Ni. This assumption is conform with the positions of the O atoms on the Ni substrate in the model, as the above described principle that O atoms in a surface oxide commonly prefer on-top positions and avoid hollow positions needs an ionic-like binding of the O to the substrate [89].

5.2 2.5 Monolayers and beyond

In this section high quality epitaxy of EuO(100) is developed. A careful adjusting of the initial growth parameters is decisive for the subsequent epitaxy of single phase EuO(100) films of excellent quality. Therefore, the EuO(100) growth was optimised by a LEED survey which is presented in Sec. 5.2.1. Appropriate annealing of films with up to 100 nm thickness generates sufficient conductivity for STM and electron spectroscopies. This procedure is described in Sec. 5.2.2. Ex-situ X-ray adsorption spectroscopy (XAS) and magneto-optical Kerr effect (MOKE) microscopy measurements of thicker films are consistent with stoichiometric single phase EuO with bulk properties which is shown in Sec. 5.2.3. A fast relaxation of the initial biaxial strain observed by LEED leaves little hope for an increase of the Curie temperature through epitaxial compression. The obtained diagram is plotted in Sec. 5.2.4.

XAS was performed on Al-capped films at the Dragon beamline at the National Synchrotron Radiation Research Center (NSRRC) in Taiwan. Eu $M_{4,5}$ XAS spectra were recorded in the total electron yield mode by measuring the sample drain current with a photon energy resolution of about 0.40 eV. The O K XAS spectra were collected by the bulk sensitive fluorescence yield mode with a photon energy resolution of about 0.20 eV.

MOKE microscopy was performed on Al-capped films with a self-developed setup [222] using an adapted Zeiss Axiotech® microscope. It is equipped with a high efficiency CCD camera and

a He flow cryostat allowing one sample temperature control down to a few K. Linearly polarised light from a halogen lamp reaches the sample surface almost normally, so that the Kerr rotation is sensitive to the magnetisation perpendicular to the plane of the surface (polar mode). The typical spatial resolution is 1 μm.

As we will see in the following, after the initial growth phase, EuO grows with its relaxed bulk lattice parameter. Therefore we measured the film thickness also in monolayers (ML), where 1 ML is defined with respect to the density of Eu and O atoms in one layer of EuO(100) with its bulk lattice constant, which is 1.51×10^{19} atoms m^{-2}. The films shown in this paper have a nominal thickness between 0.06 nm (0.25 ML) and 103 nm (400 ML) EuO(100). Typical fluxes used are $f_{\mathrm{Eu}} = 3.5 \times 10^{16}$ atoms m^{-2}s^{-1} (corresponding to a rate of 1.0 Å min^{-1} at the sample) and $f_{\mathrm{O}} = 2.5 \times 10^{16}$ atoms m^{-2}s^{-1} (4.6×10^{-9} mbar O_2-pressure), giving a ratio $f_{\mathrm{Eu}}/f_{\mathrm{O}} = 1.4$. We note that we used molecular oxygen and supposed $f_{\mathrm{O}} = 2f_{\mathrm{O_2}}$ for simplicity. Assuming a stoichiometric composition (i.e. excess Eu atoms re-evaporate) these fluxes give a growth rate of 0.18 ML/min; for the 100 nm thick film both fluxes were increased after the growth of 2.5 ML to achieve a growth rate of 0.53 ML/min and a ratio of $f_{\mathrm{Eu}}/f_{\mathrm{O}} = 1.6$.

5.2.1 Initial growth of EuO(100) films

In Sec. 5.1 we have seen surface oxide phases of hexagonal, square and even lower symmetry, which deviate in composition substantially from the known bulk stoichiometry of EuO. Even phases of clusters with "magic" (well defined) sizes are observed. As expected, we find that surface oxides of hexagonal symmetry foster growth of the polar EuO(111), while those of square symmetry foster the growth of EuO(100). The latter is the stable and desired growth orientation here.

To obtain single phase EuO(100) films, we tuned to the surface oxides of square symmetry by varying the flux ratio $f_{\mathrm{Eu}}/f_{\mathrm{O}}$ between 0.7 and 2.5 using characterisation with LEED. T_{growth} was varied between 563 K and 723 K, limited by the demand of being high enough to be at least at the onset of the distillation regime.

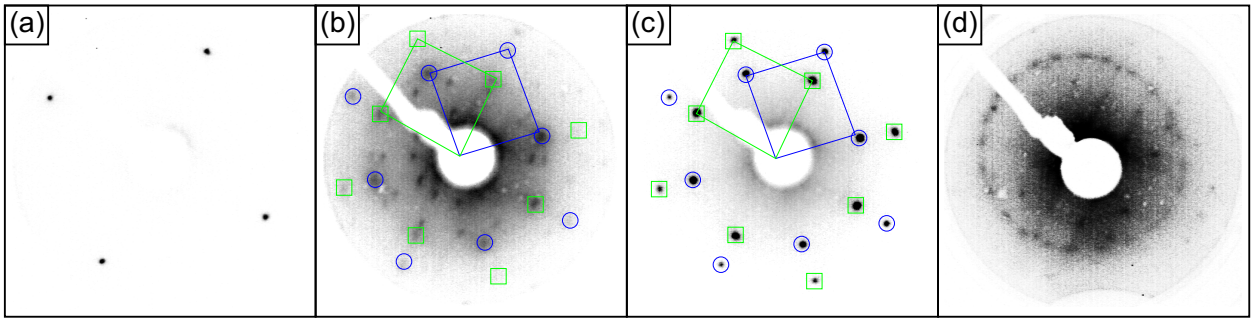

Figure 5.12: Inverted contrast LEED patterns. **(a)** Clean Ni(100) surface at 70 eV primary electron energy. **(b-d)** 2.5 ML thick EuO films on Ni(100) grown at 623 K with different flux ratios $f_{\mathrm{Eu}}/f_{\mathrm{O}}$ (63 eV primary electron energy): **(b)** $f_{\mathrm{Eu}}/f_{\mathrm{O}} = 2.5$, spots and unit cells belonging to two different EuO(100) domains are indicated; **(c)** $f_{\mathrm{Eu}}/f_{\mathrm{O}} = 1.4$, only spots of the two EuO(100) domains present; **(d)** $f_{\mathrm{Eu}}/f_{\mathrm{O}} = 0.7$ (image slightly distorted by magnetic field), ring belonging to EuO(111) with 24 spots in it, giving 4 preferential orientations.

Figures 5.12(b) through (d) show a sequence of LEED patterns for 2.5 ML thick films grown at 623 K with different flux ratios f_{Eu}/f_O. For $f_{Eu}/f_O = 2.5$, shown in Fig. 5.12(b), there is a mixture of square and hexagonal phases. The spots marked by blue circles belong to EuO(100) with EuO[001] ∥ Ni[011], as mentioned at the beginning of this chapter (in the following shortly pseudomorphic EuO), and the spots marked by green squares belong to EuO(100) with EuO[011] ∥ Ni[011], which is 45° rotated with respect to the pseudomorphic phase (in the following shortly 45° rotated EuO). Additionally there are three sets of spots with 12-fold symmetry. These sets are not fully visible in the image, two of them have their spots in the vicinity of the eight {1,0} spots of the EuO(100), the third set has about one half of the reciprocal length of the EuO {1,0} spots and is close to the electron gun. Their 12-fold symmetries represent two orientations of hexagonally structured grains, rotated by 90° with respect to each other. The set with the largest reciprocal lattice vector has a nearest neighbour (NN) distance of about 4 Å, very close to the NN distance of Eu metal of 3.99 Å. As our focus lies on the optimum conditions for EuO(100) growth, we spare further analysis of the hexagonal phases here. Figure 5.12(c) shows the pattern for $f_{Eu}/f_O = 1.4$, with spots of pseudomorphic and 45° rotated EuO only, and a drastically reduced diffuse LEED intensity. With decreasing flux ratio, there is the tendency to form EuO(111), as seen in STM and LEED for experiments with sub-ML coverage and for thicker films, like in Fig. 5.12(d) for $f_{Eu}/f_O = 0.7$. The ring pattern contains 24 spots, corresponding to four preferential orientations of EuO(111) (compare with Fig. 5.4(b)), being rotated 45° with respect to each other.

The absence of spots with hexagonal symmetry in LEED does not guarantee the absence of EuO(111) grains as the observation of LEED spots requires a sufficient total surface area of the corresponding structures. As was pointed out in Sec. 5.1, the different surface phases of Eu oxide on Ni(100) coexist in a certain range of f_{Eu}/f_O. This lead, for example, to the inclusion of small EuO(111) grains in EuO(100) films grown at $T_{growth} = 623$ K with $f_{Eu}/f_O = 1.3$, the LEED pattern of which showed no spots of EuO(111). If such a film of 6 ML thickness is annealed at 673 K in Eu vapour, a method which improves the quality and the conductivity of EuO(100) films and which is described in more detail in Sec. 5.2.2, these EuO(111) grains build pyramids with a height that is one order of magnitude higher than that of the EuO(100) grains. Figure 5.13 shows this film and the details of a pyramid.

In Fig. 5.13(a) an exceptional high number of pyramids can by seen. They are not evenly distributed but appear to be stringed which is most probably caused by the preferential nucleation of EuO(111) at pre-existing Ni(100) step edges (compare Sec. 5.1.1). A 3D representation of such a pyramid as shown in Fig. 5.13(b) enables a better visualisation as the two dimensional, colour coded representation usually used for STM topographs. The height profile of this pyramid in Fig. 5.13(c) demonstrates two properties. Firstly, the pyramid is 10 nm higher than the surrounding EuO(100) which itself has a thickness of 1.5 nm only. Secondly, the sides of the pyramids and their bases enclose an angle of $\alpha = 54° \pm 2°$ and the edges of the pyramids and their bases enclose an angle of $\beta = 34° \pm 2°$, which both match the theoretical values of 54.7° between {111} and {100} planes and 35.3° between {111} planes and ⟨100⟩ edges, respectively. This proves that these pyramids are indeed {100}-faceted. The reason for the formation of such three-sided, {100}-faceted pyramids is the avoidance of the polar catastrophe and the low free surface energy of the {100}-faces of rock-salt

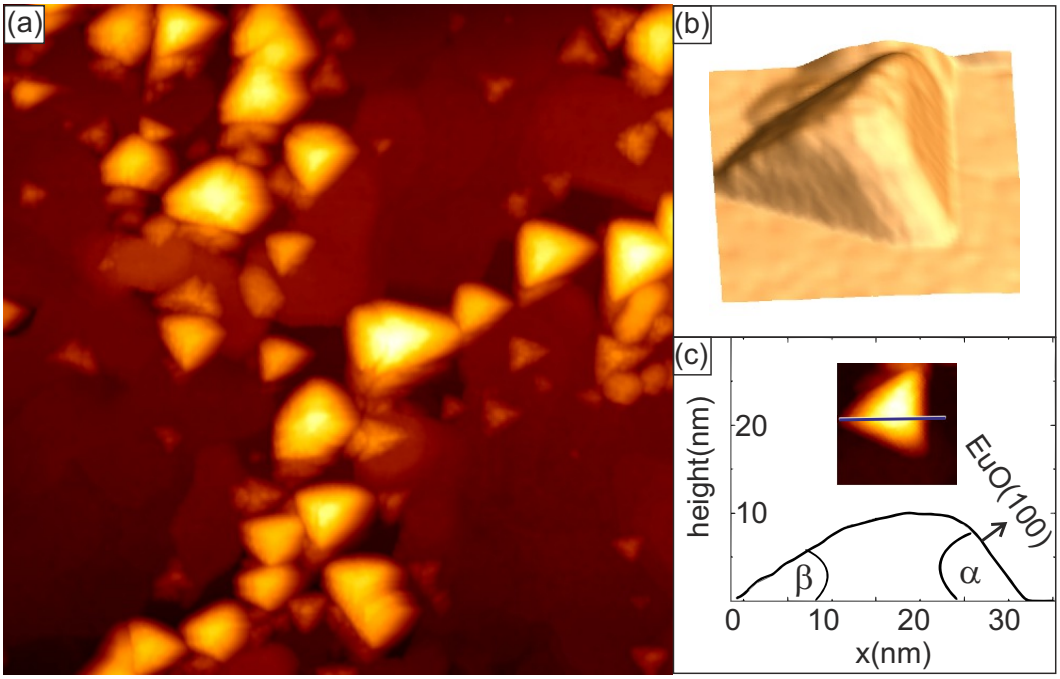

Figure 5.13: **(a)** STM topograph of a 6 ML (1.5 nm) film grown at T_{growth} = 623 K with $f_{\mathrm{Eu}}/f_{\mathrm{O}}$ = 1.3 after annealing for 3600 s at 673 K with applied Eu pressure of 1.3 × 10^{-8} mbar, image size 320 nm × 320 nm (U_{s} = −1.9 V, I_{t} = 53 pA). **(b)** STM Image of a pyramid in three dimensional illustration, 42 nm × 42 nm × 10 nm. **(c)** Height profile across the pyramid of (b) as indicated in the 2D-inset (42 nm × 42 nm).

oxides (see Sec. 2.3). Such pyramids were already observed for other systems, e.g. for MnO on Pd(100) [126].

The minimisation of patches of the polar EuO(111) surface in the growing film is very important for STM and STS because films containing such grains are difficult to image, probably due to the polarity of the surface, which considerably increases the work function. For films in the ML range, EuO(111) surfaces induced continuously tip changes when tunnelling parameters suitable for EuO(100) surfaces were used, and for annealed films like in Fig 5.13 the high pyramids complicate the STM measurements, especially on samples with low conductivity. Due to their geometry, the surface area of the pyramids reduces with increasing film thickness until they are eventually overgrown by EuO(100) grains. The film thickness at which the pyramids are overgrown depends on their base length and thus on the size of the EuO(111) bilayer adjacent to the substrate. This stresses the importance of the initial growth conditions for the quality of EuO(100) films on Ni(100).

Varying T_{growth} changes the patterns mainly by a reduction of diffuse LEED intensity, that is, the intensity which is highest around the shadow of the electron source and belongs to electrons scattered out of the discrete beams that characterise diffraction from an ordered surface [223]. Additionally the spot sharpness increases with temperature. The flux ratio $f_{\mathrm{Eu}}/f_{\mathrm{O}}$ = 1.4 is the optimum for growing single phase EuO(100) films in the tested temperature range between 563 and 723 K. Therefore we restricted further experiments to $f_{\mathrm{Eu}}/f_{\mathrm{O}}$ = 1.4 for the initial growth, which are the parameters leading to the growth of the p(5×5) surface oxide (see Sec. 5.1.4). After the

EuO film is fully coalesced and covers the Ni substrate, a higher Eu excess can be used (e.g., when the growth of Eu-rich EuO is required).

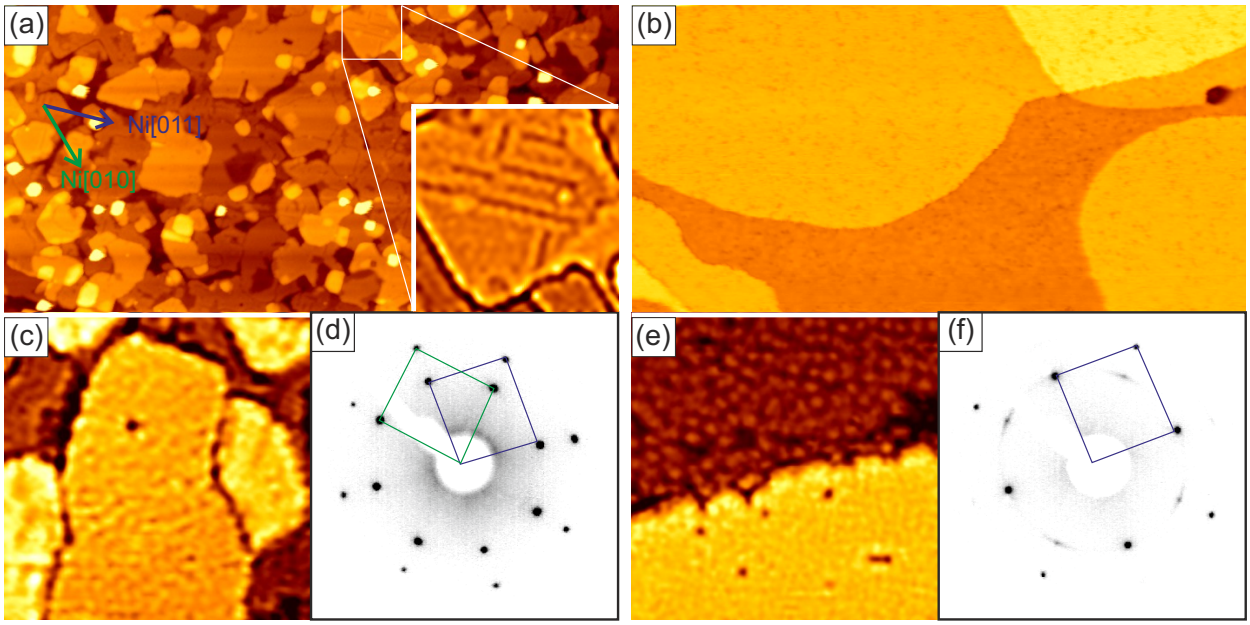

Figure 5.14: 2.5 ML EuO on Ni(100). **(a)** STM topograph (U_s = +1.3 V, I_t = 42 pA) of a film grown at 623 K, image size 320 nm × 160 nm. The inset is a zoom into the indicated grain with enhanced edge contrast, size 30 nm × 30 nm; **(b)** STM topograph (U_s = -1.3 V, I_t = 24 pA) of a film grown at 723 K, image size 320 nm × 160 nm; **(c)** same film as in (a), image size 30 nm × 30 nm, high contrast, (U_s = -1.6 V, I_t = 44 pA); **(d)** inverted contrast LEED pattern of film in (a) at 63 eV primary electron energy, the unit cells of the two EuO(100) domains are indicated. **(e)** same film as in (b), image size 30 nm × 30 nm, high contrast, (U_s = -1.6 V, I_t = 24 pA); **(f)** inverted contrast LEED pattern of film in (b) at 63 eV primary electron energy, the unit cell of the pseudomorphic EuO(100) domain is indicated.

Figure 5.14 shows STM topographs and LEED patterns of two films of 2.5 ML thickness. Both films were grown with $f_{Eu}/f_O = 1.4$, one at 623 K and the other at 723 K, to compare the effect of the growth temperature on the EuO films. The LEED pattern in Fig. 5.14(d) displays spots of the two orientations of EuO(100) in nearly equal intensity, indicating that both orientations cover the substrate in a similar amount. Lattice constant measurements revealed that the pseudomorphic EuO is compressed somewhat more than 3%, thus being indeed pseudomorphic to the Ni(100) substrate.

The 45° rotated EuO is compressed about 7%, indicating that the epitaxial relation, where the EuO lattice coincides the Ni lattice in a relation of 3:4 is realised. The other relation mentioned in the introduction, where the EuO lattice coincides the Ni lattice in a relation of 2:3 would require a contracted EuO(100), which was never found. Suspended monolayers of rock-salt compositions (e.g., NiO [224] or NaCl [225]), are predicted to have a considerably smaller lattice constant compared to their bulk layers due to a finite size effect. This is probably also the case for EuO and would explain the preference of the 3:4 relation. An additional reason may by found in the details

of the first oxide layer.

The LEED pattern of the film grown at 723 K [Fig. 5.14(f)] shows even sharper spots for the pseudomorphic EuO(100) orientation, while the diffuse LEED intensity is further reduced. The data of Figs. 5.14(d) and (f) were recorded with the same electron beam current and the same contrast enhancement was applied to the images, thus the intensities are directly comparable. In Fig. 5.14(f) the spots of the 45° rotated EuO(100) are less intense, and their arc-like elongation indicates some rotational scatter of the grains. Thus the higher growth temperature not only reduces the amount of 45° rotated EuO, but also enables rotation of this highly compressed EuO out of the epitaxial direction, which results in strain relaxation.

The similar intensities of the LEED spots of the 45° rotated EuO and of the pseudomorphic EuO at $T_{\mathrm{growth}} = 623$ K indicate a nearly equal area of both orientations. As the total area of the stripe phase is much less than 50%, nucleation of the rotated EuO is more likely related to the inhomogeneities of the p(5×5) layer at the boundaries between the translational domains. Another reason could be a restructuring of the p(5×5) layer during the growth of the bulk-like second layer, which could give rise to the nucleation of two differently rotated EuO(100) islands. Whether the p(5×5) surface oxide is lifted during the growth of the second layer cannot be unambiguously answered on the basis of our data. However, the small penetration depth of electrons in LEED and complete absence of p(5×5) superstructure reflections in the LEED data of the 2.5 ML films make it plausible that indeed the reconstruction is removed.

In Fig. 5.14(a) the film surface has relatively smooth terraces with 90° or 45° angles between the step edges, which, according to the LEED data, have to be compressed bulk like EuO(100) surfaces of the two epitaxial relations. For negative sample bias [e.g., -1.6 V as in Fig. 5.14(c)], an inner structure is visible on the grains, which is much more pronounced for grains having an edge oriented along Ni⟨110⟩ directions. As larger grain edges follow EuO⟨100⟩ directions to avoid polar edges, these grains are the pseudomorphic ones. This inner structure lacks any recognisable order and has a corrugation of less than ±30 pm, hence it is expected to be of electronic origin only. On the highly strained 45° rotated EuO grains depressions are visible, typically in the form of stripes oriented along the EuO⟨110⟩ directions, which coincide with the Ni⟨110⟩ directions for these grains. The stripes therefore enclose an angle of 45° with the grains' edges. They can be seen on several grains in Fig. 5.14(a) (e.g., on the indicated one and in the region below it). The crystallographic directions of the Ni substrate are indicated by the arrows.

For the growth at 723 K the outcome is very different. The STM topograph in Fig. 5.14(b) has the same dimensions like that in Fig. 5.14(a). Due to the 100 K higher T_{growth} the grains are much larger and have usually flat terraces on their top with a lateral dimension of more than 100 nanometres, thus the step density is drastically decreased compared to the growth at 623 K. The root mean square (RMS) roughness is below 0.2 nm for both temperatures, similar to that of the substrate. A further striking difference is the absence of straight step edges at $T_{\mathrm{growth}} = 723$ K, all steps are rounded. Figure 5.14(e) shows the inner structure in the terraces of the 723 K experiment. While the structure on the grain at the bottom of the image is comparable to that in Fig. 5.14(c) regarding size and apparent height, it is different for the grain in the upper part of the image. There not only the apparent height is twice as large, but the whole structure is more coarse. As

the straight step edges are missing, it is in this case not distinguishable which one of the structures belongs to pseudomorphic EuO and which one belongs to the 45° rotated EuO.

Also visible on most grains are some larger dark disks with a diameter in the range between 1 nm and 2 nm and an apparent depth of about 1.5 Å [e.g., one on the centre grain in Fig. 5.14(c) or six on the grain at the bottom of Fig. 5.14(e)]. On the grain in the upper part of this figure these features are also existent, but not that clearly visible due to the coarse inner structure. These features are most likely vacancies, probably O vacancies. This assumption is justified by the fact that we closed the shutter of the Eu effusion cell 10 s after closing the valve of the O supply, which is a short step of the annealing procedure described in the following paragraph. This procedure was executed for every film with a thickness above 2 ML, then the film was kept at T_{growth} for another 10 s to re-evaporate excess Eu, and cooled down afterwards. This final 10 s evaporation of Eu without O slightly improves the quality of the films, e.g., reduces the step density and increases the intensity of the LEED spots compared to the diffuse intensity. This evaporating of Eu only at 673 K was tested as longer annealing procedure for a 10 ML thick EuO film grown at 623 K.

5.2.2 Annealing in Eu vapour

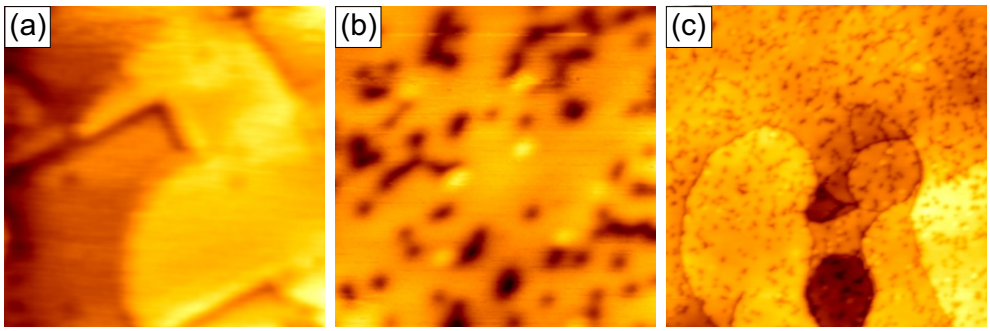

Figure 5.15: 10 ML thick EuO(100) film grown at 623 K. **(a)** STM topograph (U_{s} = -3.0 V, I_{t} = 28 pA) of film as grown, image size 30 nm × 30 nm; **(b)** STM topograph ($U_{\mathrm{s}} = -2.2$ V, I_{t} = 40 pA) after annealing for 3600 s at 673 K with applied Eu pressure, same image size. **(c)** same as (b), 120 nm × 120 nm (-2.2 V, 40 pA).

Figure 5.15(a) shows a 10 ML thick film prior and Figs. 5.15(b) and (c) after annealing for 3600 s at 673 K in front of the Eu effusion cell. The Eu flux at the sample was 1.00 Å/min., corresponding to a Eu pressure of 1.3×10^{-8} mbar. The differences are striking. First, the imaging conditions before annealing were more difficult. Frequent tip changes in nearly all of the images indicated a too small tip sample distance, even for $I_t < 10$ pA and $|U_s| > 2$ V. After annealing steady imaging was possible in all tested sample areas. We assume that the improvement of the tunnelling conditions relies on an increased conductivity of the sample. Second, the annealed film has a drastically increased density of the dark disks described previously, several of them being coalesced to larger structures. Third, the structural quality has improved. Due to the annealing the grain size increased and the step density decreased; also the step edge shapes became round. Consistent with the improved crystal quality the intensity to background ratio of the LEED spots

increased considerably. These effects intensify with increasing annealing temperature. However, annealing between 623 K and 723 K without applying Eu pressure leaves the EuO films nearly unchanged.

This annealing behaviour is probably dominated by the diffusion of Eu atoms on the EuO surface and at grain boundaries. A well studied system for such diffusion mechanisms is NiO on Ni. There the diffusion coefficients of Ni [226] and of O [227] were determined for both bulk and grain boundaries by successive usage of different Ni or O isotopes. The grain boundary diffusion turned out to be the dominant part and it seems likely that this might also be the case for Eu diffusion in EuO: Eu-rich single crystals can be generated by annealing of stoichiometric ones at 1673 K in Eu vapour, followed by a very slow process of diffusion [39]. Further diffusion paths may be located at dislocations [228], which form during EuO growth on Ni(100) within the first 40 ML to release the epitaxial strain, as will be shown in Sec. 5.2.4; hence Eu atoms may diffuse to deeper layers along grain boundaries and dislocations during the annealing procedure, despite low mobility in the bulk at 673 K. The structural improvement due to the presence of diffusing Eu during annealing could be explained by formation of EuO dimers, detaching at step edges or at grain boundaries, subsequently leading to a restructuring of the film.

The conductivity of EuO at room temperature changes drastically from 3×10^{-8} Ω^{-1} cm^{-1} for stoichiometric EuO over 5×10^{-5} Ω^{-1} cm^{-1} for 0.3% O vacancies to metallic conductance with 27 Ω^{-1} cm^{-1} for 0.5% O vacancies [75]. In insulating Eu-rich EuO each O vacancy traps two electrons above T_C, of which at least one becomes itinerant during the MIT. Above T_C these electrons may become thermally exited with an activation energy of about 0.3 eV, typical for an ordinary semiconductor [47]. Because of this strong dependence of the conductivity on the O vacancy concentration, the overall out-of-plane conductivity of a EuO film may be enhanced by O vacancy formation in the vicinity of grain boundaries and dislocations only, and, for a film of 10 ML thickness, also by O vacancy formation in the topmost layer(s).

Because a higher conductivity is a veritable explanation for the observed improvement of the STM imaging conditions, it is plausible to assume the formation of O vacancies by the annealing in Eu atmosphere. Hence the dark disks in the STM topographs in Figs. 5.15(b), (c) (3600 s annealing at 673 K), and Fig. 5.14(e) (10 s annealing at 723 K) should be mostly O vacancies. Their density in the annealed 10 ML film is inhomogeneous and varies between 0.25% and 1% of the O density in the top EuO layer for several images of a size of (30 nm)^2. O vacancies may influence the local density of states (LDOS), which is in fact imaged by the STM, on a larger area than one surface unit cell of EuO occupies. In the images, the area affected by one feature ranges between 3 and 12 times the area of a EuO unit cell, only slightly depending on the sample bias. Possibly the smaller features are vacancies in the second layer, which influence the LDOS of the Eu atom on-top. Assuming vacancies in the centre of the features, coalescence of them, as seen in the Figs. 5.15(b) and (c), is possible while maintaining the EuO rock-salt lattice.

5.2.3 100 nm thick EuO(100) films

A major concern in EuO thin film growth is the control of the film stoichiometry. Even since 1994, when the interest in EuO films was renewed after two decades of progress in film preparation and

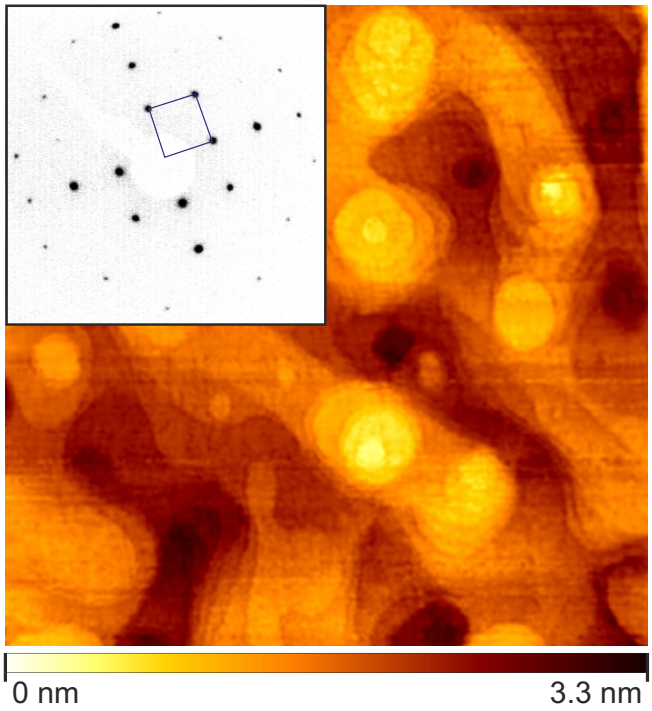

Figure 5.16: STM topograph ($U_s = +4.4$ V, $I_t = 0.5$ nA) of a 100 nm EuO film grown at 593 K and annealed at 873 K for 1200 s. Image size 600 nm × 600 nm, imaged at 35 K. The palette at the bottom correlates the colours with the topographic height and spans 3.3 nm. The inset shows the LEED pattern (inverted contrast) at a primary electron energy of 223 eV, the EuO(100) unit cell is indicated.

analysis methods, many of the films characterised contained Eu metal, Eu_3O_4 or Eu_2O_3 grains [8; 9; 13; 20; 25; 56; 82; 229]. Therefore we decided to grow a film with a thickness of about 100 nm in order to perform ex-situ XAS on an Al-capped EuO film and thereby determine the oxidation state of the Eu.

For full film characterisation we performed in-situ LEED and STM first. Especially for the latter method an appreciable conductivity is necessary for a film of this thickness. After growing a 2.5 ML thick EuO basis with the same parameters as used for the film shown in Fig. 5.14(b), we lowered T_{growth} to 593 K and increased f_{Eu}/f_O to 1.6. The reduced temperature, decreasing the Eu re-evaporation rate, and the increased Eu excess shifted the EuO stoichiometry slightly to the Eu-rich side. We then performed STM below T_C at 35 K. Although it was possible to establish a tunnelling contact for $U_s > +2$ V, meaningful STM was initially not possible. We then applied the annealing procedure described for the 10 ML film in Fig. 5.15, but for 1200 s with an increased temperature of 873 K and an increased Eu pressure of 4.7×10^{-8} mbar as compensation for the 40 times greater film thickness.

STM was still difficult, but at $U_s = +4.4$ V it was possible to resolve the film morphology as shown in Fig. 5.16. The film has large terraces with a lateral width in the order of 100 nm, and has rounded step edges comparable to thinner films grown at 723 K or annealed at 673 K under Eu pressure. Despite the relatively poor resolution, the presence of dark dots, i.e. O vacancies, is

discernible, with a density comparable to that in Figs. 5.15(b) and (c). It still was not possible to establish a tunnelling contact for -1.2 V< U_s < +2 V at 35 K, thus the film behaved not metallic below T_C. To create films with a sufficiently high O vacancy density, a further reduction of T_{growth} could be applied, but this would risk the high crystalline quality of the films. Another possibility would be to increase the Eu excess until the resulting films show an MIT.

The total height difference in the image in Fig. 5.16 with a size of 0.6 μm × 0.6 μm is 2.7 nm, corresponding to 10 ML EuO(100). On an image of this scale the Ni substrate typically displays seven monatomic steps, resulting in a total height difference of about 1.2 nm. The smoothness of the EuO film is also expressed by the RMS roughness of about 0.5 nm, a factor of 2.5 larger than the substrate roughness of 0.2 nm. This smooth and well defined surface is accompanied by a high crystalline quality seen by LEED, with spots as sharp as for the Ni(100) substrate and low diffuse intensity up to very high electron energies. A LEED pattern for 223 eV is shown in the inset in Fig. 5.16. Only spots of the pseudomorphic EuO orientation are present in this thick film.

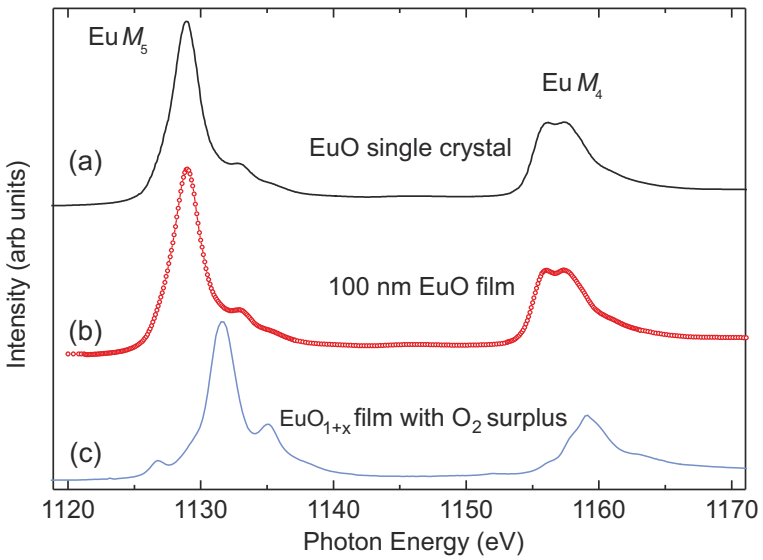

Figure 5.17: Eu $M_{4,5}$ (3d→4f) XAS spectra of **(a)** a EuO single crystal, **(b)** the 100 nm EuO film, and **(c)** a EuO_{1+x} film grown with O_2 surplus.

After finishing the in-situ analysis the EuO film was capped with a 4 nm thick Al film, which formed a stable Al_2O_3 protection layer when exposed to air.

To check the Eu valence and the stoichiometry, we have studied the Eu $M_{4,5}$ and O K XAS of the EuO film. Figure 5.17 shows the Eu $M_{4,5}$ XAS spectra of the 100 nm EuO film [Fig. 5.17(b)] together with one for a EuO single crystal [Fig. 5.17(a)] for comparison. The stoichiometric single crystal (T_C = 69.5 K) was grown by a solution sintering process [230] and in-situ cleaved under UHV conditions at 100 K. The very similar multiplet spectral structure and energy position of our EuO film and of the EuO single crystal indicate a divalent state of Eu. In Fig. 5.17(c) we present a thick EuO_{1+x} film grown with high oxygen pressure (2×10^{-7} mbar). One can see that the energy shift with respect to the EuO single crystal and the multiplet structure of the EuO_{1+x} film are in good agreement with the theoretical Eu^{3+} spectrum obtained by Thole *et al.* [231]. For the

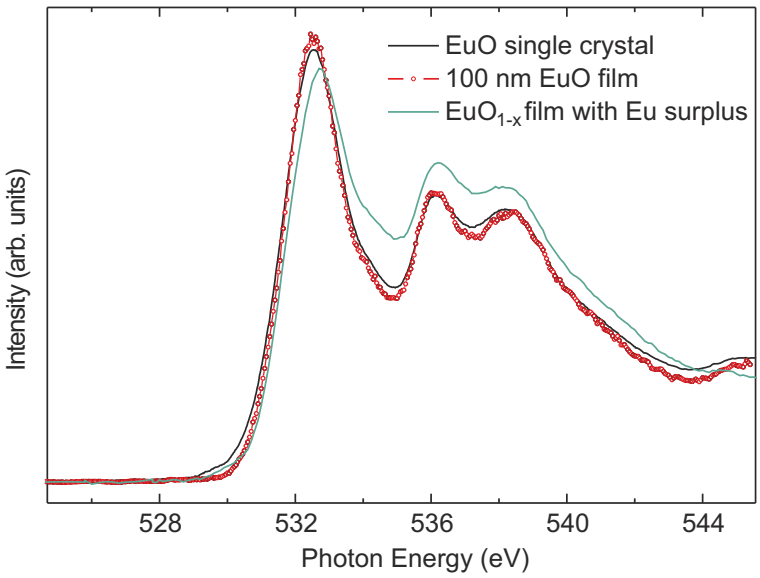

Figure 5.18: O K XAS spectra of a EuO single crystal (black line), the 100 nm EuO film (dashed red line with circles), and a EuO_{1-x} film grown with Eu surplus (green line).

EuO_{1+x} film with O surplus, namely large Eu deficiency, we found a spectral structure at the main peak of the Eu^{3+} spectrum (1131.7 eV), where there is a dip in the Eu^{2+} spectrum. Thus, we have confirmed that our 100 nm EuO film is free from Eu^{3+} content.

Since Eu metal is divalent, the Eu surplus cannot be detected in the Eu $M_{4,5}$ spectrum; thus we investigated the O K XAS spectrum to further confirm that there is no Eu surplus. Fig. 5.18 shows the O K XAS spectra of the 100 nm EuO thin film, of the EuO single crystal, and of a EuO_{1-x} film with Eu surplus for comparison. One can see that the overall spectral feature of our 100 nm EuO film is very similar to that of the EuO single crystal, while in the EuO_{1-x} film with large O deficiency the first peak at 532.5 eV, originated from Eu 5d-O2p hybridisation, has a relative weak spectral weight [4].

Figure 5.19 displays MOKE images of the sample under zero-magnetic field, at 70 K [5.19(a)] and 40 K [5.19(b)]. The pattern visible at low temperature is characterized by two sub-structures: (i) parallel lines, typically aligned to a $\langle 011 \rangle$ direction of Ni, separated by $\simeq 30$ μm, running through the width of the figure, and (ii) in between the lines, a structure with a typical length scale of a few micrometers. The onset for the formation of this pattern upon cooling and heating the sample was found at (69±1) K. The pattern morphology and formation temperature were found identical in a series of temperature cycles.

The shape anisotropy for the thin EuO film is expected to result in in-plane magnetisation. The corresponding magnetic domains themselves should therefore not be detectable with polar MOKE. We therefore assume the observed pattern to be created by magnetic domain walls with perpendicular magnetisation (Bloch walls) [1]. In this view the (69±1) K onset temperature is the

[1]A possible MIT of EuO at T_C would decrease the transmittivity for lower temperatures by free carrier absorption. Therefore the transition would not unveil the magnetic pattern of the Ni underneath. Hence the pattern must have its origin in the EuO film.

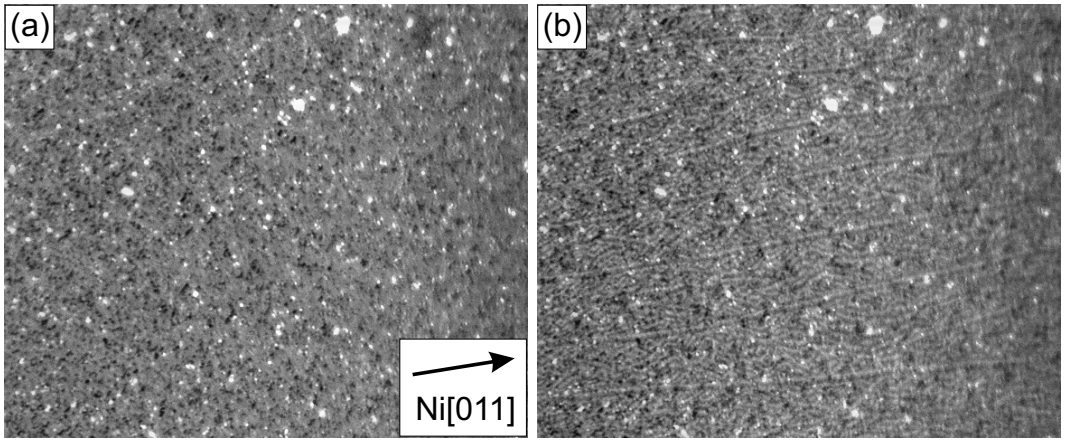

Figure 5.19: MOKE microscopy images of the 100 nm EuO film, image sizes 370 μm $\times$ 310 μm. **(a)** recorded at 70 K and **(b)** recorded at 40 K. The additional pattern at 40 K is related to domain walls in the EuO film which orient along the $\langle 011 \rangle$ directions of the Ni substrate (direction indicated). The bright spots showing no magnetic contrast are dust particles.

Curie temperature (T_C) of the films. Within the limit of experimental uncertainties, this value corresponds to that for bulk stoichiometric crystals. No changes of the Ni magnetic structure are expected in the explored temperature range ($[25 - 300]$ K) well below the Curie temperature of Ni. As an explanation for the well-defined orientation of the magnetic pattern of EuO in all measurements, we propose a coupling of the magnetic structure of EuO to the one of Ni due to magnetic interactions between EuO and Ni. We note that the easy magnetisation axes in Ni are along $\langle 111 \rangle$ directions [i.e., they form an angle of 45° with respect to the surface of the Ni(100) single-crystal]. The projection of these directions in the plane of the EuO film are $\langle 011 \rangle$ and correspond to the observed pattern orientation. Such directions are, as one may expect, off the hard axis ones for EuO (i.e. $\langle 001 \rangle$) [232].

5.2.4 Epitaxial strain

As mentioned in the introduction, the Curie temperature of EuO is expected to increase with compressive biaxial strain [17], which is a very interesting point for applications. This could give the opportunity to tune T_C by the selection of a substrate with an appropriate lattice mismatch. For the growth on the Ni(100) substrate we have seen two epitaxial relations realised for the growth at 623 K. At a film thickness of 2.5 ML the pseudomorphic EuO(100) is strained by 3.1% at room temperature, while for the 45° rotated EuO the strain is about 7%, already somewhat lower than the theoretical value of 8.7% for a lattice coincidence in a 3:4 relation.

The simultaneous growth of the two epitaxial relations with different strains at $T_{\text{growth}} = 623$ K gave us the opportunity to analyse the relaxation of two different strains within the same films by a sequence of EuO films of different thicknesses. The lattice constants were measured by LEED, hence the results shown in Fig. 5.20 represent the topmost layers only. The lattice constant of the pseudomorphic EuO increases gradually and reaches the EuO bulk value at a thickness of about

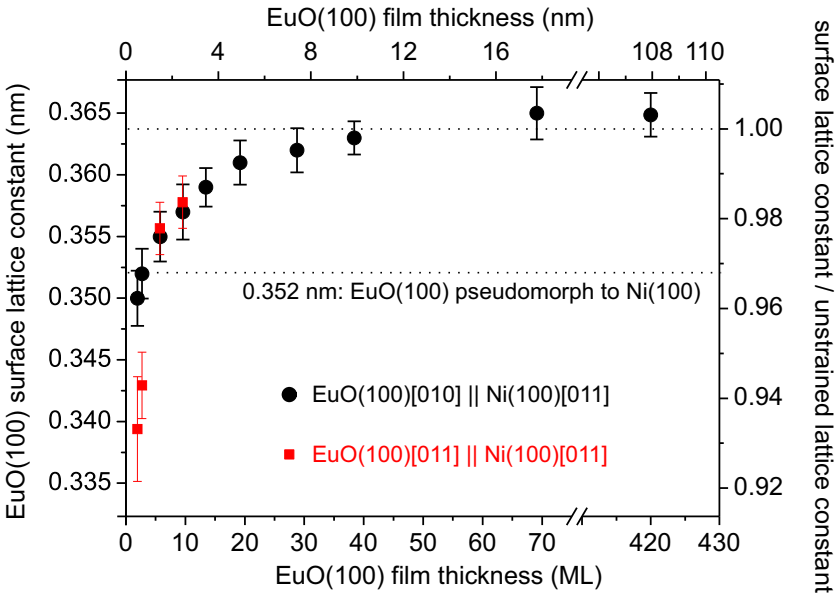

Figure 5.20: Evolution of the EuO surface lattice constant with film thickness, measured by LEED. Black circles belong to pseudomorphic EuO(100), red squares to the 45° rotated EuO.

30 ML or 8 nm. Similar gradual strain relaxations for oxide growth on metallic substrates was also observed for other oxide systems [e.g., for NiO on Pd(100) [233], MnO on Ag(001) [234], and MgO on Ag(100) [235]]. The strain relaxation for the 45° rotated EuO occurs even earlier, reaching the same strain value as the pseudomorphic orientation just above 5 ML. Further measurements for this phase were not possible, as the corresponding LEED spots broadened, while their intensity faded with increasing film thickness. For the pseudomorphic orientation a broadening of the spots occurred when growing films thicker than 3 ML, but the spots became sharp again for the 18 nm thick film. The broadening of the spots simultaneously with the strain relaxation is explainable by misfit dislocations, which release the stress in the film.

The relaxation of the lattice constant is nearly completed at a film thickness of 5 nm, hence it is unlikely that a substantial increase in T_C can be achieved by tuning the lattice mismatch. This is emphasised by the fact that the relaxation is even faster for stronger compressions of the first layer. Additionally a decrease of T_C for film thicknesses of a few ML is expected due to finite size effects [69]. The situation becomes even more complicated on metallic substrates, where the finite size effects are counteracted by image charge screening at the metal interface [86; 87]. A detailed analysis of this combined effects on T_C could be addressed by in-situ surface sensitive MOKE measurements, which we plan for future experiments.

5.3 Summary

Europium oxide growth on Ni(100) shows a variety of different surface phases, dependent on the growth temperature and the flux ratio of Eu to O. These phases include polar EuO(111), clusters which occur in three "magic" sizes, islands with a centred rectangular lattice which are decorated by stripes, and a EuO(100) like surface oxide with increased lattice constant and O vacancies arranged in a p(5×5) superstructure with respect to the Ni substrate. The latter structure is the optimum base for growing EuO(100). Epitaxial EuO(100) pseudomorph to the Ni(100) forms for thicknesses between 2 ML and 3 ML at $T_{\mathrm{growth}} = 723$ K and $f_{\mathrm{Eu}}/f_{\mathrm{O}} = 1.4$; hence this EuO is oriented with its [001] direction parallel to Ni[011] and compressively strained by 3.1%. For thicknesses above 3 ML the strained lattice relaxes to that of bulk EuO within the first 30 ML deposited. As comparable strain relaxations were also observed for other oxide films on metal substrates [233–235] this is probably a general behaviour and rejects the idea of increasing T_{C} by epitaxial strain.

After creation of a fully coalesced film of 2.5 ML thickness the growth parameters may be changed, as long as they comply with the MBE distillation technique [27]. Even at $T_{\mathrm{growth}} = 593$ K and $f_{\mathrm{Eu}}/f_{\mathrm{O}} = 1.6$ (i.e., at an increased probability to introduce O vacancies into the EuO lattice) the films are stoichiometric within the detection limits of XAS and show no metallic behaviour in STM at 35 K. The Curie temperature, as determined by MOKE, is about 70 K for a 100 nm thick film, comparable to bulk EuO. Annealing at 673 K in Eu vapour (using the same Eu flux as during growth) generates sufficient conductivity to enable STM imaging even for the 100 nm thick film. This annealing introduces O vacancies into the film with a concentration of less than 1% at the surface as imaged by STM. Creation of O vacancies without annealing could be possible by lowering the growth temperature even further, which may result in a poor crystalline quality, or by considerably increasing the Eu excess, i.e. the ratio $f_{\mathrm{Eu}}/f_{\mathrm{O}}$.

Typical terrace widths in the order of 100 nm and a RMS roughness below 0.5 nm, together with the sharp LEED patterns with low diffuse intensity indicate the high crystalline quality of the films. The single crystal quality of our films together with their smooth surface and the possibility to introduce oxygen vacancies by annealing makes them well suited for temperature and thickness dependent studies of EuO by scanning tunnelling spectroscopy.

6 EuO on Iridium

The complicated surface oxides which form upon EuO growth on Ni(100) require a highly precise parameter regulation in the initial growth phase to achieve high quality EuO films. Furthermore the ferromagnetism of the substrate substantially complicates magnetic measurements of the EuO film on top. This lead to the decision to test EuO growth on other substrates than Ni(100) despite the high quality achieved.

Ir was selected as substrate material because it has several advantages compared to Ni. It is a noble metal[1] and cannot be oxidised under the EuO growth conditions. It is not ferromagnetic and therefore does not disturb magnetic measurements. Ir has a cohesive energy of 6.9 eV [237] which is significantly higher than for Ni (4.4eV[238]), leading to a considerable reduction of substrate atom diffusion during EuO growth. Thus, mass transport as observed for Ni (see Sec. 5.1) is less probable.

The Ir surface lattice constant of 2.715 Å enables, for certain orientations, epitaxial growth of EuO in a relation of 3:4 with a compressive strain of $\approx 0.5\%$, hence highly oriented films with a low defect density can be expected. In this chapter the growth of EuO on two different Ir surfaces is described, which are the (111) surface (Sec. 6.1) and the (100) surface (Sec. 6.2).

6.1 EuO on Ir(111)

The hexagonal symmetry of the fcc(111) surface prevents growth of large EuO(100) domains because of three possible epitaxial orientations which are rotated by 120° to each other. But, since the (111) surface is the (electronically) least corrugated of an fcc metal, it has a high potential for the growth of high quality oxide films, even if the film does not coincide the substrate lattice.

The EuO growth was performed in the temperature range $623 \leq T_{\mathrm{growth}} \leq 723\,\mathrm{K}$ and for flux ratios $0.8 < f_{\mathrm{Eu}}/f_{\mathrm{O}} < 1.8$. For low coverages of the substrate just formation of a bilayer (BL) EuO(111) was observed (1 BL is here defined as 1 ML of Eu ions plus 1 ML of O ions), whereby T_{growth} and $f_{\mathrm{Eu}}/f_{\mathrm{O}}$ changed structural details only. For higher coverages formation of EuO(100) occurred and, for sufficiently high Eu excess, also formation of Eu metal islands. Contrary to the case of Ni(100) no special surface oxides were found on Ir(111), hence it is suitable to express the deposited amount of Eu and O with respect to EuO. As there exists no single ML of EuO(111), the deposited Eu amount (Θ) is expressed in $\mathrm{MLE_{EuO}}$, whereby $1\,\mathrm{MLE_{EuO}}$ is the amount of Eu atoms equal to their density in one layer of EuO(100) with its bulk lattice constant, which is $7.55 \times 10^{18}\,\mathrm{Eu\ atoms\ m^{-2}}$. The Eu atom density in 1 BL EuO(111) is $8.75 \times 10^{18}\,\mathrm{Eu\ atoms\ m^{-2}}$, thus 1 BL EuO(111) requires $1.16\,\mathrm{MLE_{EuO}}$ of Eu atoms. Together, Θ, $f_{\mathrm{Eu}}/f_{\mathrm{O}}$, and T_{growth} fully define the properties of the grown film.

[1] The chemical nobility of Ir is similar to Pt (both have a standard electrode potential of 1.2 V) and only excelled by Au (standard potential 1.5 V) ([236], p. 8-28).

For the used parameter range the most obvious changes in the EuO films occurred in dependence of Θ. Thus, the description of EuO growth on Ir(111) starts with the film thickness dependence in the following section. In Sec. 6.1.2 the flux ratio dependence is explained and in Sec. 6.1.4 the temperature dependence. Work function measurements of a BL EuO(111), which are very interesting in the context of the polarity of the EuO(111), are analysed in Sec. 6.1.3.

6.1.1 Film thickness dependence

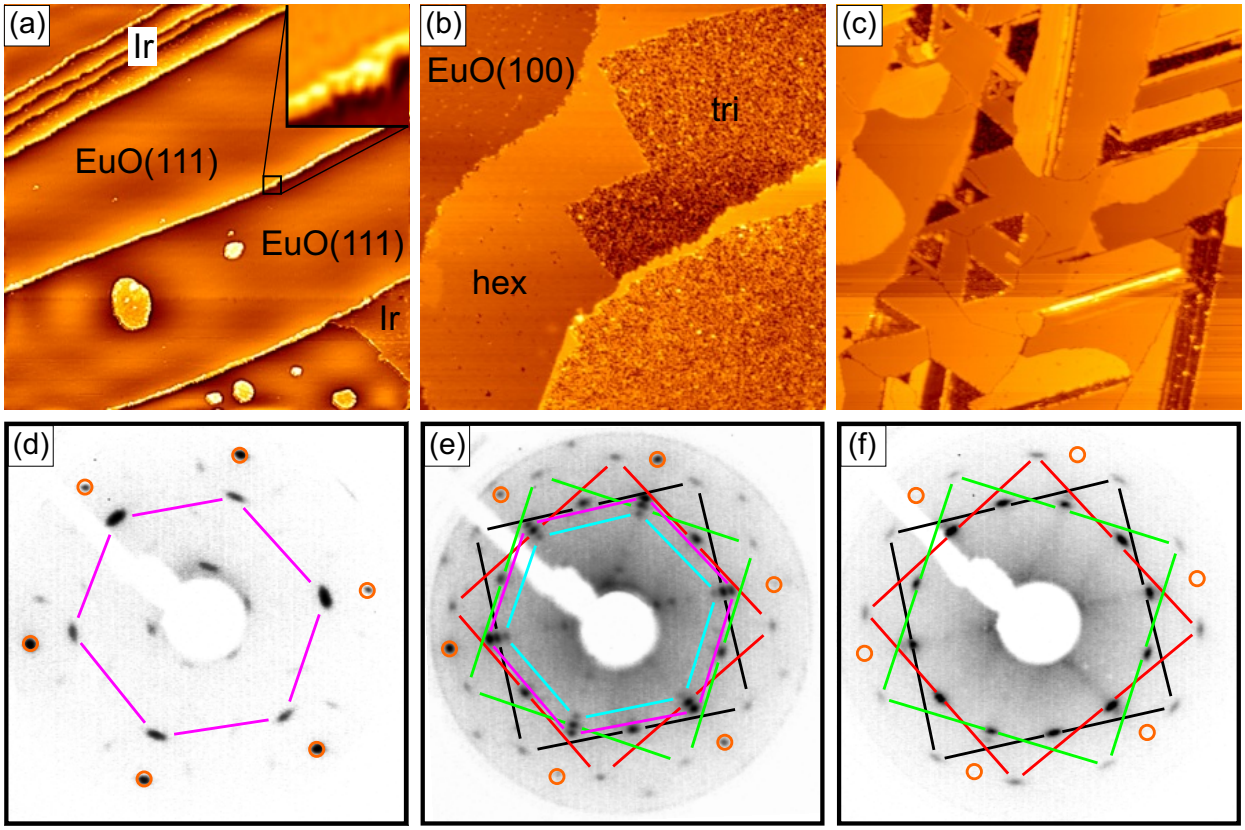

Figure 6.1: **(a-c)** STM topographs of EuO films grown at $T_{\mathrm{growth}} = 723\,\mathrm{K}$, image size $230\,\mathrm{nm} \times 230\,\mathrm{nm}$. **(a)** $\Theta = 0.46\,\mathrm{MLE_{EuO}}$, $f_{\mathrm{Eu}}/f_{\mathrm{O}} = 1.7$ ($U_{\mathrm{s}} = -0.61$ V, $I_{\mathrm{t}} = 0.86$ nA). Inset: zoom into the indicated region, $10\,\mathrm{nm} \times 10\,\mathrm{nm}$. **(b)** $\Theta = 1.0\,\mathrm{MLE_{EuO}}$, $f_{\mathrm{Eu}}/f_{\mathrm{O}} = 1.7$ (+0.22 V, 4.0 nA). **(c)** $\Theta = 3.7\,\mathrm{MLE_{EuO}}$, $f_{\mathrm{Eu}}/f_{\mathrm{O}} =$ (0.84 for the first 540 s, 1.12 for the last 240 s) (−1.3 V, 25 pA). **(d-f)** Inverted contrast LEED patterns at a primary electron energy of 67 eV, each corresponding to the STM image above. Positions of Ir spots [absent in (f)] are indicated by orange circles, spots belonging to EuO(100) domains are connected by black, red, and green squares. Spots belonging to EuO(111) are connected by magenta coloured hexagons and those belonging to metallic Eu by a cyan coloured hexagon. In (d) also superstructure spots are present, which have the highest intensity in the vicinity of shadow of the electron gun.

Figure 6.1 shows the film thickness dependence of the EuO structures on Ir(111). The $\Theta = 0.46\,\mathrm{MLE_{EuO}}$ film in Fig. 6.1(a) mainly consists of EuO(111) of BL thickness. This topograph was flattened to yield sufficient contrast for the relevant structures despite the high corrugation of

several Ir(111) steps. This flattening lead to a buckled appearance of the otherwise flat terraces. The EuO(111) grows adjacent to the ascending step edges but stays away a few nanometres from the descending step edges which can be better seen in the inset of Fig. 6.1(a)[1]. This indicates an interaction of the polar EuO(111) with the step edge dipole of the Ir(111) as shown in Fig. 6.2. Such step edge dipoles occur due to a smoothening effect of the electron density at steps [239]. Hence the O ions terminate the BL EuO(111) to the vacuum. O terminated bilayers of (111) oriented oxides with rock-salt structure on noble metal substrates grow also for other material combinations, e.g., in the case of FeO on Pt(111) [99].

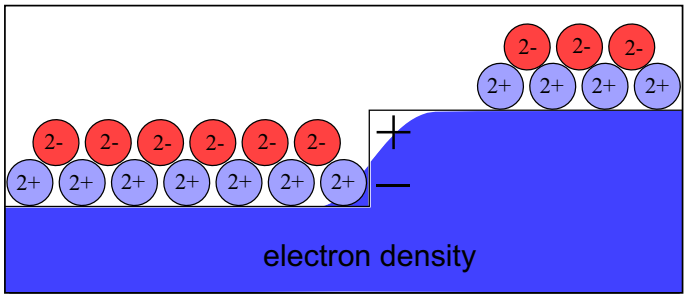

Figure 6.2: Side view ball model of one EuO(111) bilayer at a substrate step. Red circles represent O atoms, light blue circles Eu atoms. The indicated charges correspond to the idealised oxidation states in bulk EuO. The electron density of the substrate (indicated in dark blue) is smoothed at the step edge, leading to the step edge dipole which attracts the EuO(111) at the ascending step edge and repels it at the descending step edge.

Occasionally islands have formed on top of the BL EuO, which are probably the third layer EuO(111). The small Ir terraces are not covered by EuO as well as a part in the lower right hand side part of Fig. 6.1(a). Surprisingly, this Ir terrace part has a larger apparent height than the adjacently grown EuO(111) which is on top of this terrace. This is connected to a considerable work function difference generated by the polar EuO(111) and will be discussed in Secs. 6.1.2 and 6.1.3. The shapes of the Ir step edges are not influenced by the EuO growth, contrary to the case of Ni, where mass transport was observed already for growth at 623 K (see Sec. 5.1.1).

Figure 6.1(d) shows the LEED pattern for the $\Theta = 0.46\,\mathrm{MLE_{EuO}}$ film. It consists of spots with sixfold symmetry only, whereby the Ir spots are indicated by orange coloured circles and the EuO(111) spots are connected by a magenta coloured hexagon. Additional spots, which are poorly visible at 67 eV, appear at first sight as p(3×3) superstructure of the EuO which is expected due to the epitaxial relation to the Ir substrate of 3:4. This is demonstrated by the ball model in Fig. 6.3. But this situation is only approximately realised for growth at 623 K as will be shown in Sec. 6.1.4. For 723 K growth there is a rotational misalignment, leading to an elongation of the EuO and its superstructure spots in Fig. 6.1(d). The Figs. 6.4(a) and (b) show STM topographs of the superstructure and the corresponding atom positions of the BL EuO(111). The different positions of the brightest atoms with respect to the superstructure corrugation already indicate a rotational misalignment. This can be quantitatively analysed by the Fourier transform of Fig. 6.4(b), which

[1]We note that the Ir is imaged brighter than the BL EuO(111) on top which will be discussed in the following.

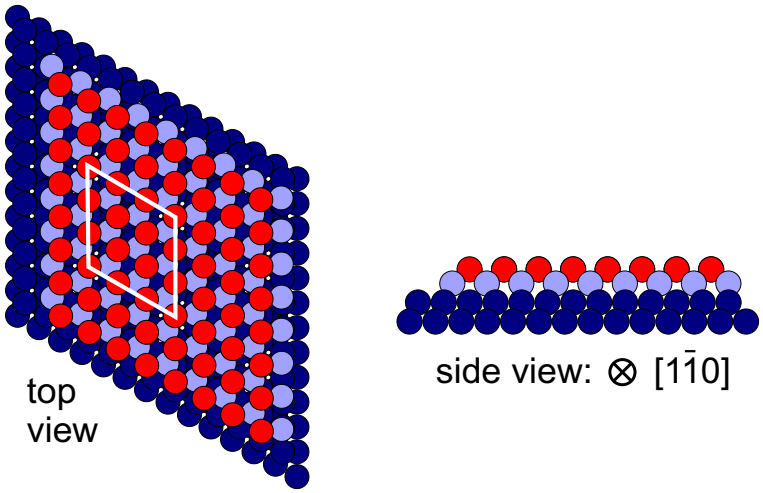

Figure 6.3: Top and side view of a simple ball model of a BL EuO(111) on Ir(111) with the Ir $[1\bar{1}0]$ direction aligned to EuO $[1\bar{1}0]$. In this case the EuO coincides the Ir lattice in a 3:4 ratio for 0.7% compressive strain, thereby leading to a p(3×3) superstructure of the EuO. Colour scheme: Ir dark blue, Eu light blue, and O red.

is shown in Fig. 6.4(c). The outer peaks correspond to the atomic lattice of 3.7 Å periodicity, while the innermost ones belong to the superstructure. The rotational misalignment of $\approx 7°$ between the atomic and the superstructure lattice is already noticeable. More details of the BL EuO(111) will be given in Secs. 6.1.2 and 6.1.4.

Figure 6.1(b) shows a similar experiment with $\Theta = 1.0\,\mathrm{MLE_{EuO}}$. The appearance is completely different. No Ir substrate could be observed and the surface is fully covered by three different structures. This is consistent with the LEED pattern in Fig. 6.1(e) which shows additional spots compared to Fig. 6.1(d). These are spots of three domains of EuO(100), 120° rotated to each other, with a surface lattice constant of 3.3 Å (connected by differently coloured squares) and spots with sixfold symmetry (connected by a cyan coloured hexagon) and a relatively large lattice constant of 4.2Å. This is close to the value one would expect for hexagonally arranged Eu metal (see Sec. 8.2.2). The ML EuO(100) is compressed by $\approx 8\%$, a similar value as was found for the thinnest EuO(100) films on Ni(100) (see Sec. 5.2.1). As no epitaxial reason could be found for this lattice contraction it confirms the tendency of rock-salt crystals towards smaller lattices due to finite size effects ([224], [225]).

Additionally, there are two sets of hexagonal spots in Fig. 6.1(e). Their surface lattice constants of 6.9Å and 9.6Å could not be accurately determined due to the proximity to the shadow of the electron gun and may have an error of $\approx 10\%$. Because of the large values of the lattice constants these spots must belong to superstructures, either of the EuO(111) or of the other hexagonal phase.

Figure 6.1(c) shows an experiment with $\Theta = 3.7\,\mathrm{MLE_{EuO}}$ which fits not directly into the sequence of Fig. 6.1(a-c), as a different $f_{\mathrm{Eu}}/f_{\mathrm{O}}$ was used. Furthermore $f_{\mathrm{Eu}}/f_{\mathrm{O}}$ was not kept constant, but was 0.84 for the first 540 s and 1.12 for the last 240 s of the experiment. This procedure was used as a lower initial $f_{\mathrm{Eu}}/f_{\mathrm{O}}$ resulted in a larger ratio of EuO(100)/EuO(111) as found out by LEED measurements. The subsequent increase of $f_{\mathrm{Eu}}/f_{\mathrm{O}}$ was carried out to avoid a possible Eu

deficiency and the subsequent formation of Eu^{3+}. The LEED pattern belonging to Fig. 6.1(c) is shown in Fig. 6.1(f). The intensity of the EuO(111) spots is barely visible at 67 eV and thus considerably lower than that of the EuO(100), the surface lattice constant of which did increase to 3.5 Å at this film thickness. No other structures are present. This is consistent with the corresponding STM topograph, where the EuO(111) can be identified by the noisy appearance. It often has triangular borders and its quota of the surface area is considerably lower than in Fig. 6.1(b). After 3.7 MLE_{EuO} Eu exposure the EuO(111) is already difficult to image. For this reason, no topographs with a lower areal ratio of EuO(100)/EuO(111) were recorded at this film thickness and an experiment with f_{Eu}/f_O different from 1.7 was chosen for this film thickness sequence.

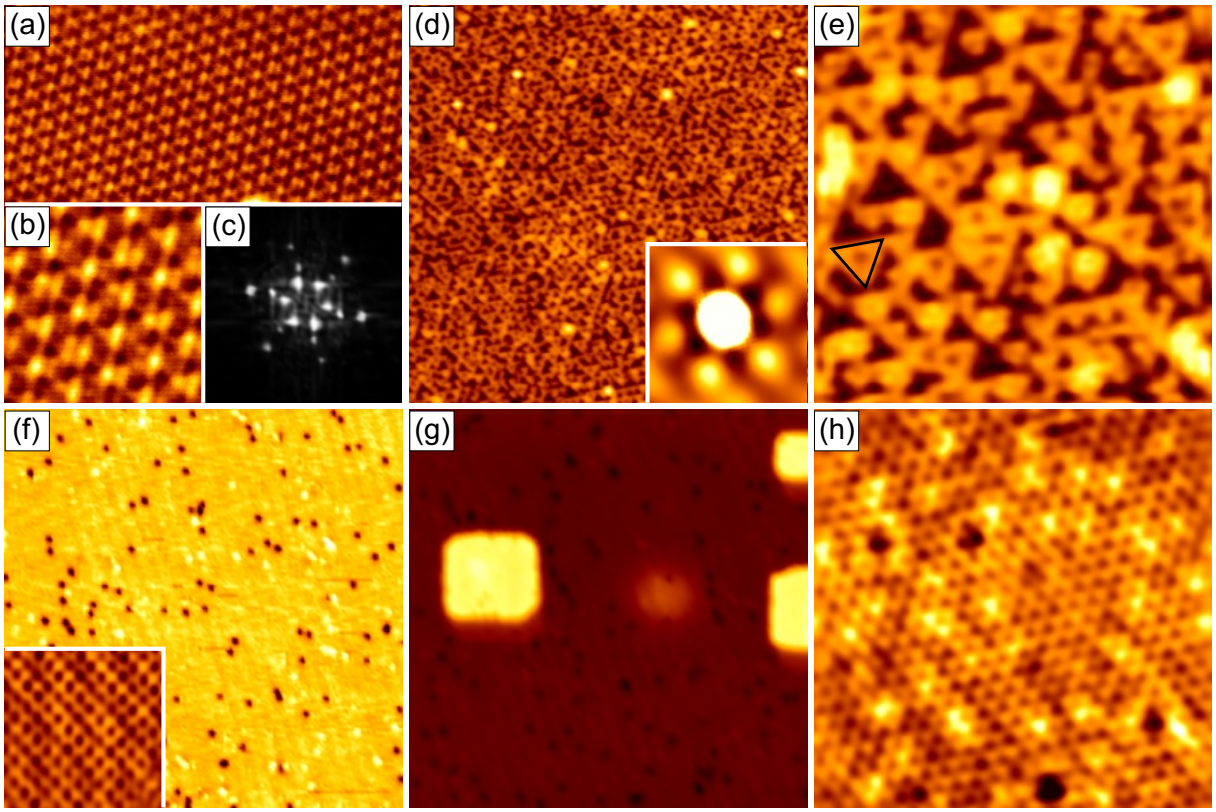

Figure 6.4: STM topographs showing the different structures of Figs. 6.1(a) and (b) in higher resolution. **(a)** BL of EuO(111) as shown in Fig. 6.1(a), image size 20 nm × 10 nm (U_s = +0.13 V, I_t = 9.3 nA). **(b)** Same as (a), 5 nm × 5 nm. **(c)** Fourier transform of (b). **(d)** Structure labelled as 'tri' in 6.1(b) (70 nm × 70 nm, −1.0 V, 0.46 nA) Inset: Self-correlation. **(e)** Same as (d), 20 nm × 20 nm. One of the most common triangles is indicated. **(f)** EuO(100) structure of Fig. 6.1(b) (80 nm × 80 nm, +0.94 V, 0.14 nA). Inset: Zoom into defect-free area, 3.5 nm × 3.5 nm (−1.0 mV, 83 nA). **(g)** Same structure and parameters as in (f). **(h)** Structure labelled as 'hex' in 6.1(b) (20 nm × 20 nm, −0.54 V, 1.5 nA).

As already mentioned, the three different phases in Fig. 6.1(b) fully cover the Ir surface. Although the Eu amount of 1 MLE_{EuO} would be sufficient for one ML EuO(100), the amount of oxygen is only ≈ 60% of that. Thus, there is not enough O to fully cover the substrate by a mixture of EuO(100) and EuO(111). The only reasonable explanation for the full coverage of the Ir is the

presence of Eu islands as third phase, especially because of the presence of the LEED spots which correspond to hexagonally arranged Eu metal. This suggests that the bonding between Eu and Ir is sufficient to suppress re-evaporation at 723 K.

The absence of such islands for the $\Theta = 0.46\,\mathrm{MLE_{EuO}}$ experiment [Fig. 6.1(a)] does not contradict this interpretation. If the average Eu atom density on the Ir surface is not higher than 14% of the surface atom density of Ir(111), the Eu only forms a $(\sqrt{7} \times \sqrt{7})$R19.1° superstructure which appears just as a noisy Ir terrace when imaged at 300 K due to the high mobility of the Eu. Only for higher coverages metallic Eu islands form (see App. A). While for the $\Theta = 0.46$ $\mathrm{MLE_{EuO}}$ experiment the amount of oxygen should be sufficient to cover 22% of the substrate with BL EuO(111), the excess Eu corresponds to $\approx$ 12% of the remaining Ir(111) surface atoms if no re-evaporation has taken place, i.e. the Eu atom density is lower than for the $(\sqrt{7} \times \sqrt{7})$R19.1° superstructure. Thus, no island formation is expected.

For the $\Theta = 1.0\,\mathrm{MLE_{EuO}}$ experiment the situation has changed. While the amount of excess Eu is increased to $0.43\,\mathrm{MLE_{EuO}}$, the Ir surface which is not covered by EuO is decreased to less than 50%. Thus, the Eu atom density on the Ir is increased considerably, but a quantitative estimate as above is not possible because not all excess Eu is located on the Ir terraces. This is deduced from the observation of the 'tri' structure for $\Theta = 1.0\,\mathrm{MLE_{EuO}}$ [Figs. 6.4(d) and (e)] instead of the atomically resolved BL EuO(111) structure [Figs. 6.4(a) and (b)]. This means that a part of the excess Eu did already start to build the third layer of EuO(111). However, the Eu atom density on the Ir is obviously sufficient to build large islands.

The assignment of the three structures in Fig. 6.1(b) to the corresponding lattices observed in the LEED pattern [Fig. 6.1(e)] is possible even for large scale images due to their characteristic appearance. The structure labelled 'tri' in Fig. 6.1(b) has a rough appearance when compared to the atomically flat terraces of the EuO(100) and the structure labelled 'hex', making it easily distinguishable. The Figs. 6.4(d) and (e) show higher resolved topographs of the 'tri' structure, which one can interpret either as triangular depressions or protrusions on an otherwise flat surface. Such triangular motifs are often found in surface reconstructions which occur to avoid the high electrostatic potential of polar surfaces (see Sec. 2.3). Thus it is highly probable that the 'tri' structure is EuO(111) where a reconstructed third layer has grown. The edges of the triangles are aligned to the EuO-$\langle 1\bar{1}0 \rangle$-directions. The NN distance of the dots in the self-correlation of Fig. 6.4(d), which is shown in the inset, is $\approx$ 2.2 nm. This would correspond to a p(6×6) superstructure of the EuO(111), but as the size of the triangles is obviously not homogeneous there exists no superstructure with a long range order. The 2.2 nm are slightly more than the length of the largest triangles, one of which is indicated in 6.4(e). These show a depression at their centre and give the impression that they consist of three smaller triangles at their corners. Thus the large triangles are probably no own structure but appear when three small triangles have formed in the closest possible distance to each other. Hence the 2.2 nm should be the shortest repetition distance of the small triangles. Due to a lack of resolution further details of this structure cannot be determined.

The EuO(100) phase can be unambiguously identified by dark disks, which can be seen in the Figs. 6.4(f) and (g). The dark disks remind one to the oxygen vacancies in EuO(100) on Ni after annealing in Eu vapour [Figs. 5.15(b), (c), and Fig. 5.14(e)]. The incorporation of O vacancies

is likely due to the Eu excess of 70%. The proof that this structure is EuO(100) is given by two evidences: Firstly, the inset in Fig. 6.4(f) shows atomic resolution (only one ion sort is imaged as bright protrusions) at a position where no O vacancy is present. Secondly, in Fig. 6.4(g) are small second layer islands with 90° angles between the edges.

The structure labelled 'hex' in Fig. 6.1(b) is shown in higher resolution in Fig. 6.4(h). As mentioned above, the presence of metallic Eu on the Ir is probable. Because the EuO(100) can be identified unambiguously and the 'tri' structure is most probably a reconstruction of the polar EuO(111) this remaining phase should be the expected metallic Eu. The hexagonal pattern in Fig. 6.4(h) has a NN distance of ≈ 10Å and therefore has to be a superstructure. This distance corresponds to the (9.6 ± 1) Å found for the inner LEED spots in Fig. 6.1(e), but no simple connection to the 4.23 Å which were found by LEED and are expected for the metallic Eu can be found. The $\langle 1\bar{1}0 \rangle$-directions of all structures are aligned to another, thus a superstructure should be given by a factor which is an integer number. Also characteristic for the 'hex' phase is a high amount of adsorbates, which is an additional argument for the presence of highly reactive metallic Eu. Additionally, in this structure often larger depressions are found which are most probably oxidised parts. These dark areas are typically larger than the dark disks (representing the oxygen vacancies) on the EuO(100) and thus make it possible to distinguish this 'hex' phase from the EuO(100) on large scale images.

6.1.2 Flux ratio dependence

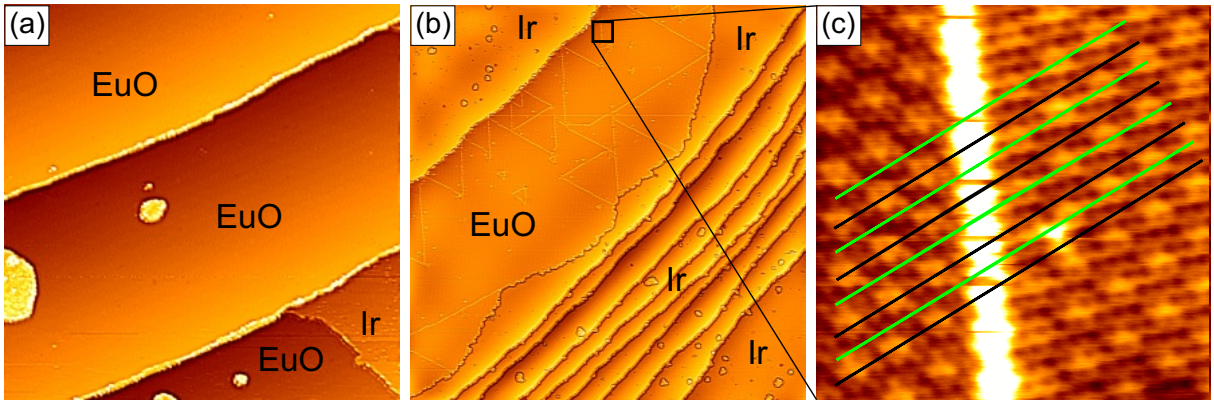

Figure 6.5: STM topographs of EuO(111) on Ir. **(a)** Same topograph as in Fig. 6.1(a) for comparison [image size 160 nm × 160 nm, $\Theta = 0.46\,\mathrm{MLE_{EuO}}$, $f_{\mathrm{Eu}}/f_{\mathrm{O}} = 1.7$, $T_{\mathrm{growth}} = 723$ K ($U_{\mathrm{s}} = -0.61$ V, $I_{\mathrm{t}} = 0.86$ nA)]. **(b)** $\Theta = 0.23\,\mathrm{MLE_{EuO}}$ Eu grown with $f_{\mathrm{Eu}}/f_{\mathrm{O}} = 0.85$ at $T_{\mathrm{growth}} = 723$ K (160 nm × 160 nm, −1.0 V, 0.82 nA). **(c)** Zoom into (b), 8 nm × 8 nm, same parameters. The green and black lines indicate dense packed rows of the superstructure on the right hand side and on the left hand side of the bright stripe, respectively.

As lower values of $f_{\mathrm{Eu}}/f_{\mathrm{O}}$ lead to preferential growth of EuO(100) for $\Theta = 3.7\,\mathrm{MLE_{EuO}}$, submonolayer growth with different flux ratios should give a hint to the underlying mechanism.

Figure 6.5 shows a comparison between the growth for $f_{\mathrm{Eu}}/f_{\mathrm{O}} = 1.7$ and $f_{\mathrm{Eu}}/f_{\mathrm{O}} = 0.85$. Figure 6.5(a) is part of the same topograph as in Fig. 6.1(a), but without flattening applied. This allows

one to better perceive the lower apparent height of the EuO(111) compared to the Ir terrace on which it has grown. Also the small ridges of free Ir at the descending step edges are better visible.

The topograph in Fig. 6.5(b) had to be flattened to give contrast to features of the EuO film despite the high amount of Ir(111) steps. For this experiment the O_2 exposure was kept constant while only half of the Eu was deposited. Due to the Eu deficiency ($f_{Eu}/f_O < 1$) now all Eu was incorporated into the EuO film. Thus, the EuO coverage is nominally 85% of the film with $\Theta = 0.46\,\mathrm{MLE_{EuO}}$ - $f_{Eu}/f_O = 1.7$ and both films have a similar coverage and are thus suitable for a comparison of the flux ratio dependence. If just f_{Eu}/f_O would have been reduced and not Θ, the nominal coverage would have been 70% higher than for the $\Theta = 0.46\,\mathrm{MLE_{EuO}}$ experiment.

In Fig. 6.5(b) again only EuO(111) islands are present, but additionally there are small clusters on the Ir terraces which are probably also an Eu oxide. Thus, for coverages up to $\approx 25\%$ BL EuO(111) larger islands consists only of polar EuO for $0.85 \leq f_{Eu}/f_O \leq 1.7$ and the decisive influence of f_{Eu}/f_O leading to the preferential growth of EuO(100) for $\Theta = 3.7\,\mathrm{MLE_{EuO}}$ must occur in a later growth stage.

Figure 6.5(b) shows three major differences compared to Fig. 6.5(a): (I) no islands are present in the third layer, (II) bright stripes are present in the EuO, and (III) the apparent height of the EuO is larger than of adjacent Ir.

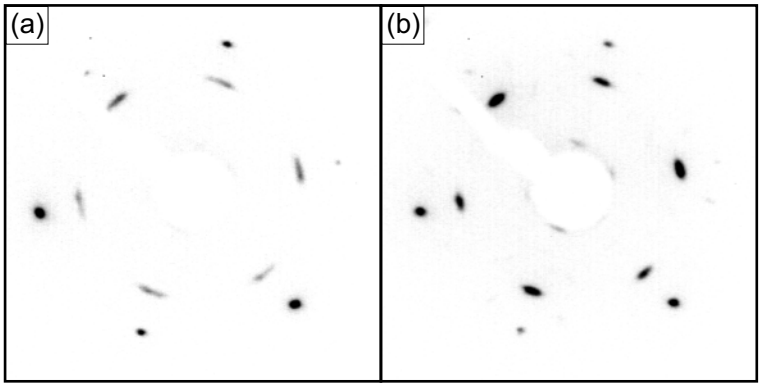

Figure 6.6: Inverted contrast LEED patterns of sub-ML EuO(111) grown at $T_{growth} = 723\,\mathrm{K}$. Primary electron energy 78 eV. **(a)** $\Theta = 0.23\,\mathrm{MLE_{EuO}}$, $f_{Eu}/f_O = 0.85$. **(b)** $\Theta = 0.46\,\mathrm{MLE_{EuO}}$, $f_{Eu}/f_O = 1.7$. The EuO spots are arc-like elongated, contrary to the Ir spots.

(I) is a consequence of the lack of Eu. As the film was grown Eu deficient there is not enough Eu present to form the third EuO(111) layer. (II) The bright stripes are anti-phase domain boundaries. If two EuO(111) islands grow together it is improbable that their superstructures fit together. In such a case a line type defect is expected, at which a registry shift of the superstructures occurs. This can be seen in Fig. 6.5(c), which is a zoom into the area indicated by a square in Fig. 6.5(b). There, green lines are on top of dense packed rows of superstructure protrusions at the right hand side of the bright stripes and the black lines are on top of the corresponding superstructure rows on the left hand side of the bright stripe. Green and black lines are both not on top of superstructure protrusions on the other sides of the bright stripe, thereby confirming that these stripes are anti-phase domain boundaries. For $f_{Eu}/f_O = 1.7$ no such domain boundaries were found, so the higher

O chemical potential influences the growth kinetics towards formation of smaller domains.

The influence on the growth kinetics is also seen by LEED, where the arc-like elongation of the EuO(111) is increased for the Eu deficient conditions as can be seen in Fig. 6.6. For both f_{Eu}/f_O the six EuO(111) spots are arc-like elongated, contrary to the Ir(111) spots which are radially symmetric. But, for $f_{Eu}/f_O = 0.85$ [Fig. 6.6(a)] the FWHMs of spot profiles along the azimuthal direction are (17.5 ± 1) %SBZ[1] while for $f_{Eu}/f_O = 1.7$ [Fig. 6.6(b)] the FWHMs are (13 ± 0.5) %SBZ only. Due to a a lack of intensity of higher order spots the standard deviation angle could not be determined for $f_{Eu}/f_O = 0.85$. For $f_{Eu}/f_O = 1.7$ the standard deviation from the EuO[$1\bar{1}0$]-Ir[$1\bar{1}0$] alignment is $\pm 2.3°$ as will be shown in Sec. 6.1.4.

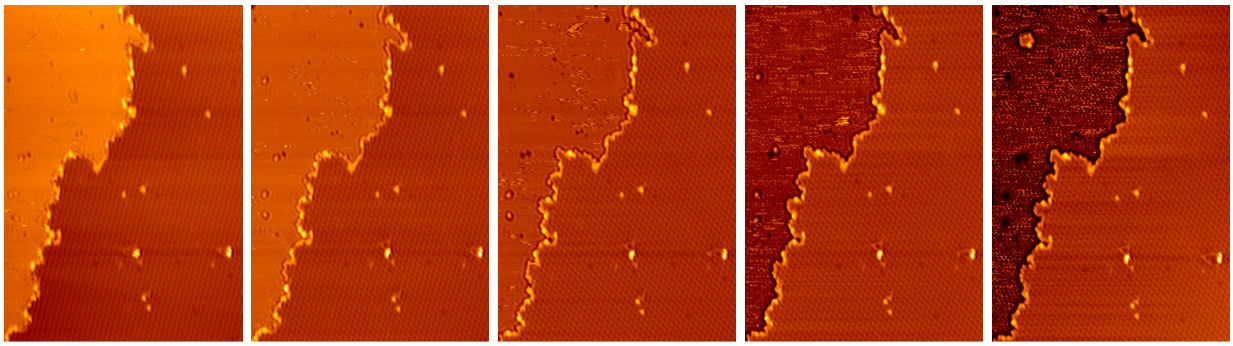

(a) 0 L (b) 0.3 L (c) 0.5 L (d) 0.8 L (e) 1.0 L

Figure 6.7: STM topographs of a film with 0.46 MLE_{EuO} Eu exposure, grown with $f_{Eu}/f_O = 1.7$ at $T_{growth} = 723$ K. All images are 40 nm × 60 nm in size and tunnelled at $U_s = -0.54$ V and $I_t = 0.74$ nA. At the left hand side they show Ir(111) and at the right hand side EuO(111). During tunnelling the sample was exposed to an O_2-pressure of $7,3 \cdot 10^{-10}$ mbar at 300 K. The O_2 exposure increases from the left to the right and is given in langmuir. The contrast is similar in all images and the brightness is adjusted to the EuO.

(III) For Eu rich growth conditions, the EuO(111) has a larger apparent height than the underlying Ir terrace. For Eu deficient conditions this is not the case. As turned out after some testing, this phenomenon is related to work function changes on the Ir terrace due to the presence of adsorbed O. This was proven by O_2 adsorption experiments carried out for EuO which was grown under Eu rich conditions. Figure 6.7 shows a sequence of O adsorption where a total of 1 L O_2 was adsorbed at 300 K. Before O_2 adsorption [Fig. 6.7(a)] the EuO (at the right hand side) appears lower than the Ir. With increasing O_2 exposure the brightness of the Ir terrace decreases while the noise level increases. So for films grown with O_2 excess, mobile O remains on the Ir surface and gives rise to the differences in the apparent height.

Figure 6.7 additionally demonstrates that the EuO is not influenced by the O_2 exposure as there is not the smallest sign of adsorbed O or structural changes on the EuO island. Because Eu^{2+} is still highly reactive this can only be explained by O termination of the EuO to the vacuum side. This is consistent with the step edge dipole interaction as explained above and also with the work function increase of the EuO(111) which leads to the low apparent height.

[1]Thereby, 1 SBZ is defined as the diameter of the unreconstructed EuO(111) surface Brillouin zone in Γ-M-direction (i.e., 100 %SBZ = 2.76 nm^{-1}).

6.1.3 Work function of the polar EuO(111)

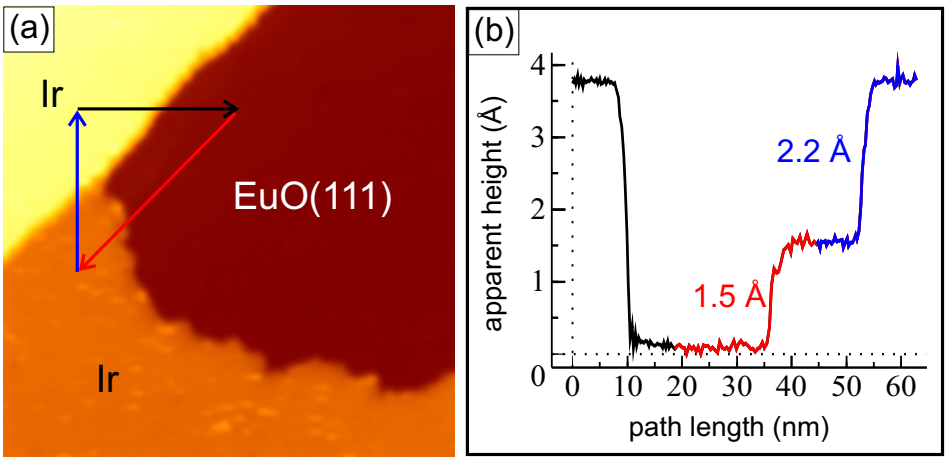

Figure 6.8: **(a)** STM topograph of a BL EuO(111) on Ir. $\Theta = 0.46\,\mathrm{MLE_{EuO}}$, $f_{\mathrm{Eu}}/f_{\mathrm{O}} = 1.7$ (Image size $50\,\mathrm{nm} \times 50\,\mathrm{nm}$, $U_{\mathrm{s}} = -0.61$ V, $I_{\mathrm{t}} = 0.86$ nA). **(b)** Profile of the apparent height along the path indicated in (a) in different colours.

The decrease of the apparent height of the EuO(111) due to its polarity is considerable as demonstrated in Fig. 6.8. The STM topograph shows two Ir terraces, the lower of which is partially covered by EuO(111). Arrows in different colours indicate the path of the apparent height profile in Fig. 6.8(b). The step height between the Ir terraces is 2.2 Å and corresponds to the topographic height. The step along the red arrow is 1.5 Å with the EuO being lower than the Ir. The geometrical height of a BL EuO(111) should be 2.97 Å ($5.14\,\text{Å}/\sqrt{3}$), thus the apparent height of the BL EuO(111) is ≈ 4.5 Å lower than the geometrical height.

To measure the work function differences between the Ir(111) and the EuO(111) field emission resonance (FER, see Sec. 4.3.3) measurements were performed. The spectra shown in Fig. 6.9(a) were taken between $0.5\,\mathrm{V} < U_{\mathrm{b}} < 10\,\mathrm{V}$ for both Ir and EuO whereby U was modulated by 50 mV with a frequency of 433 Hz. The feedback loop was tuned to slow response, keeping $I_{\mathrm{t}} = 1.0$ nA. The recording time for each spectrum was 100 s. The spectrum on the Ir surface is relatively noisy, probably caused by mobile adsorbates on the surface.

The numbers above the oscillation indicate their order. The peak at $U_{\mathrm{b}} \approx 3\,\mathrm{V}$ on the EuO(111) is not a FER because it does not fit to the distances between the different FER orders, the peak positions of which are given by

$$U_{\mathrm{peak}} = U_0 + U_1 \cdot (n+1)^{2/3}, \tag{6.1}$$

whereby n is the order of the oscillation and U_0 and U_1 are offset and slope constants, respectively. Instead the first peak on EuO is assumed to be an interface state [240].

In Fig. 6.9(b) the peak positions and their shift between EuO and Ir are plotted for the first 7 orders. The 0 order peak positions do not coincide with the fits given by Eq. 6.1 due to the influence of the image potential (see Sec. 4.3.3). For the orders ≥ 1 the shift is constant within the

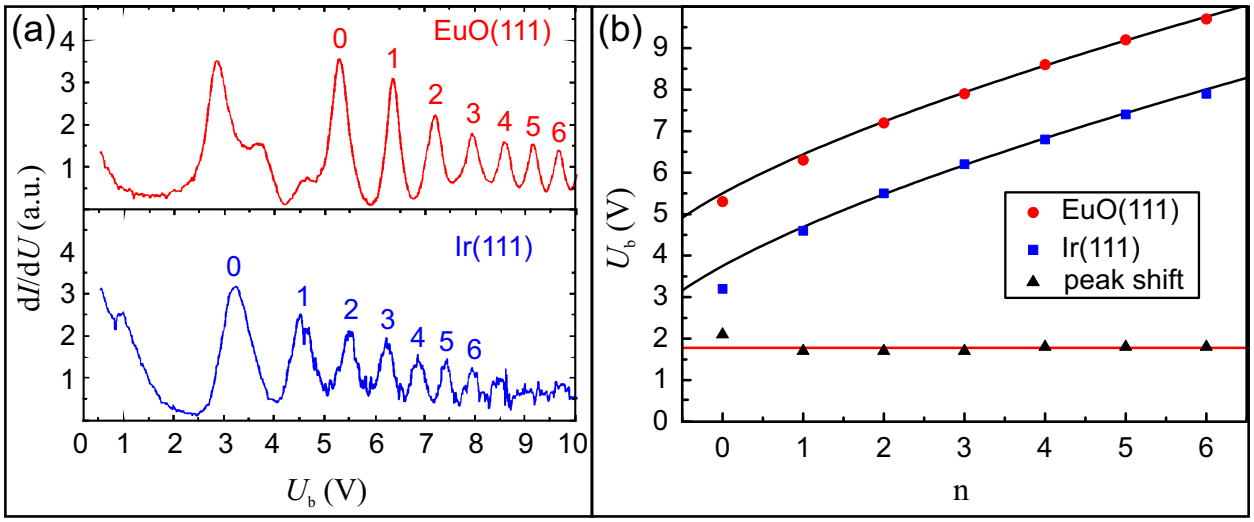

Figure 6.9: **(a)** FERs measured above EuO(111) (red) and above Ir(111) (blue). The order of the oscillation is indicated at the corresponding maximum. **(b)** Peak positions of the FERs plotted in dependence of the oscillation order n for EuO (red dots) and for Ir (blue squares). The black lines are fits using Eq. 6.1 with $U_0 = 3.9\,\mathrm{V}$ (EuO), $U_0 = 2.1\,\mathrm{V}$ (Ir) and $U_1 = 1.6\,\mathrm{V}$. The black triangles represent the shifts between the EuO and the Ir peak positions of the same order. For orders ≥ 1 the shift is constant as given by the red line.

given error and corresponds to the work function difference. The average of several measurements gives a work function difference of

$$\Delta\Phi = \Phi_{\mathrm{EuO}} - \Phi_{\mathrm{Ir}} = (1.77 \pm 0.02)\,\mathrm{eV}.$$

Using $\Phi_{\mathrm{Ir}} = 5.76\,\mathrm{eV}$ [241] the work function of the polar EuO(111) is $\Phi_{\mathrm{EuO}} = (7.53 \pm 0.02)\,\mathrm{eV}$.

This value is considerable higher than the work function of EuO(100), which is less than 2 eV [242]. This large difference of $\approx 6\,\mathrm{eV}$ demonstrates the large dipole moment connected with the polar orientation of the Eu(111). Using a naive model of a plate capacitor, where the voltage is $U_{\mathrm{BL}} = \sigma \cdot d_{111}/\varepsilon_0$ (see Sec. 2.3), a value of $U_{\mathrm{BL}} = 46.9\,\mathrm{V}$ would be expected using $d_{111} = 1.48\,\text{Å}$ and calculating σ by assuming Eu^{2+} and O^{2-} ions. Although this naive model overestimates the dipole moment by neglecting the discrete nature of the charge distribution it is about one order of magnitude higher than the measured work function increase. Thus a partial compensation of the polarity by a mechanism described in Sec. 2.3 is likely.

As at least the in-plane positions of the atoms are not changed, as proved by STM and LEED, a severe reconstruction of the BL EuO(111) can be ruled out. Due to the low pressure in the UHV chamber the presence of adsorbates on the EuO is unlikely. Thus direct electronic modifications are the most probable polarity compensation mechanism. Furthermore, work function shifts of ultra thin oxide films on metals occur due to metal-induced gap states which arise from penetration of metal electron wave functions into the oxide overlayer and from chemical bonds between metal and oxide [240]. This may also considerably effect the measured work function of the BL EuO(111).

6.1.4 Temperature dependence

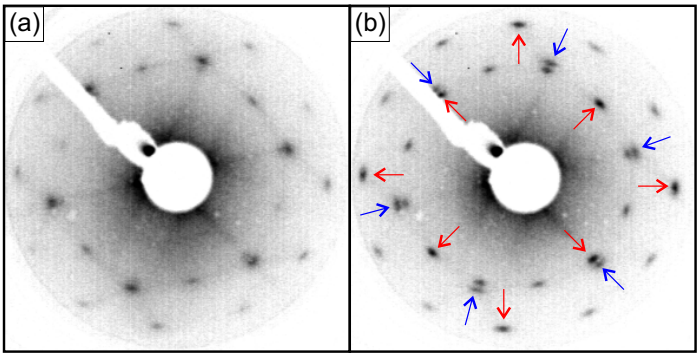

Figure 6.10: Inverted contrast LEED patterns of EuO films with $\Theta = 3.4\,\mathrm{MLE_{EuO}}$ and $f_{\mathrm{Eu}}/f_{\mathrm{O}} = 0.85$, primary electron energy 57 eV. **(a)** $T_{\mathrm{growth}} = 623\,\mathrm{K}$. **(b)** $T_{\mathrm{growth}} = 723\,\mathrm{K}$. Blue arrows indicate EuO(111) spots and red arrows one domain of EuO(100).

Up to now all results were given on a basis of EuO films grown at 723 K. The selection of this growth temperature was based on the results of the EuO growth on Ni(100) (Chap. 5) and LEED measurements of two films grown with $\Theta = 3.4\,\mathrm{MLE_{EuO}}$ and $f_{\mathrm{Eu}}/f_{\mathrm{O}} = 0.85$ at 623 K and at 723 K which are shown in Fig. 6.10. For $T_{\mathrm{growth}} = 623\,\mathrm{K}$ [Fig. 6.10(a)] the most pronounced spots are the hexagonal ones of the EuO(111). Additional spots belong to the three domains of EuO(100), but these have a considerably lower intensity.

For $T_{\mathrm{growth}} = 723\,\mathrm{K}$ [Fig. 6.10(b)] the EuO(111) spots (indicated by blue arrows) did not noticeably change in intensity but are elongated in azimuthal direction, indicating an increase of in-plane misorientation of the EuO(111). The EuO(100) spot intensity is increased and surpasses the intensity of the EuO(111). Eight of the EuO(100) spots (i.e. one domain), which are indicated by red arrows, have a higher intensity than the other EuO(100) spots. Thus one EuO(100) domain has grown preferentially, which could be related to the small miscut ($< 0.1°$) of the (111) plane of the Ir crystal.

The principal difference between the growth temperatures 623 K and 723 K is thus a considerable increase of the EuO(100) LEED spot intensity of $\Theta = 3.4\,\mathrm{MLE_{EuO}}$ films for $T_{\mathrm{growth}} = 723\,\mathrm{K}$. Additionally, the lower growth temperature lead to a reduction of the arc-like elongation of the EuO(111) LEED spots. Therefore, the impact of the growth temperature on EuO(111) was analysed further for sub-monolayer coverage, i.e. BL EuO(111) structures. The results are shown in Fig. 6.11.

In both topographs in Figs. 6.11(a) and (d) the BL EuO(111) looks similar and has a lower apparent height than the adjacent Ir terrace as expected for $f_{\mathrm{Eu}}/f_{\mathrm{O}} = 1.7$. In both EuO layers bright stripes can be seen, which were identified as boundaries of translational domains in Sec. 6.1.1. Contrary to the case for Eu deficient growth these stripes form fewer and only very small triangles, thus their total length per area is much lower. Between $T_{\mathrm{growth}} = 623\,\mathrm{K}$ and $T_{\mathrm{growth}} = 723\,\mathrm{K}$ no significant change of the areal density of anti-phase domain boundaries could be found.

But an influence of T_{growth} was found for another defect, which appears as ‘missing superstruc-

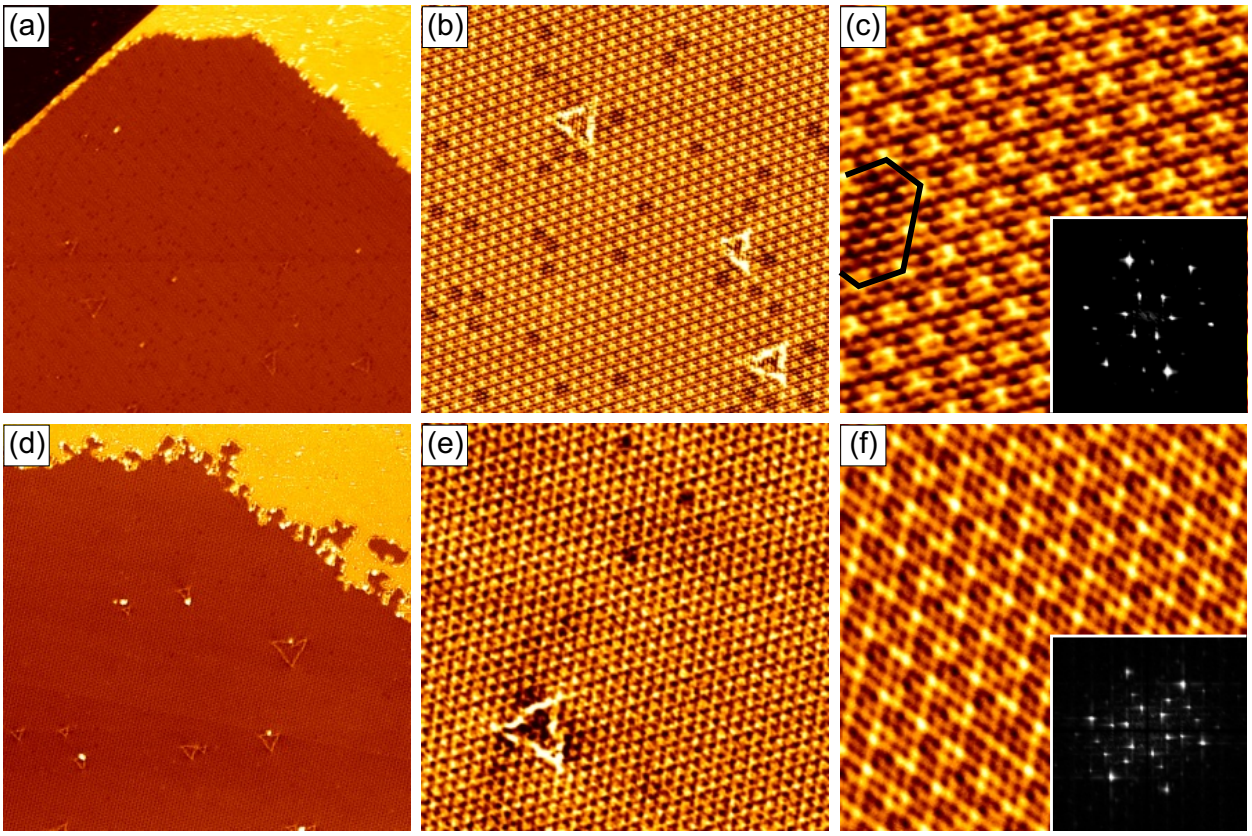

Figure 6.11: STM topographs of BL EuO(111) ($\Theta = 0.46\,\mathrm{MLE_{EuO}}$) grown with $f_{\mathrm{Eu}}/f_{\mathrm{O}} = 1.7$ at $T_{\mathrm{growth}} = 623\,\mathrm{K}$ (a-c) and at $T_{\mathrm{growth}} = 723\,\mathrm{K}$ (d-f). **(a)** Image size $100\,\mathrm{nm} \times 100\,\mathrm{nm}$ ($U_{\mathrm{s}} = -0.61\,\mathrm{V}$, $I_{\mathrm{t}} = 0.32\,\mathrm{nA}$). **(b)** $30\,\mathrm{nm} \times 30\,\mathrm{nm}$, $-21\,\mathrm{mV}$, $1.4\,\mathrm{nA}$. **(c)** $9\,\mathrm{nm} \times 9\,\mathrm{nm}$, $-21\,\mathrm{mV}$, $1.4\,\mathrm{nA}$. The black hexagon surrounds 2 defects. Inset: Fourier transform. **(d)** $100\,\mathrm{nm} \times 100\,\mathrm{nm}$, $-1.2\,\mathrm{V}$, $0.47\,\mathrm{nA}$. **(e)** $30\,\mathrm{nm} \times 30\,\mathrm{nm}$, $-0.49\,\mathrm{V}$, $0.37\,\mathrm{nA}$. **(f)** $9\,\mathrm{nm} \times 9\,\mathrm{nm}$, $-0.75\,\mathrm{V}$, $2.8\,\mathrm{nA}$. Inset: Fourier transform.

ture protrusion'. These defects have a much higher areal density for $T_{\mathrm{growth}} = 623\,\mathrm{K}$ than for $T_{\mathrm{growth}} = 723\,\mathrm{K}$, which is better visible on the higher resolved topographs in Figs. 6.11(b) and (e).

In Fig. 6.11(c) two adjacent of such defects are enclosed by a black hexagon. As this topograph is atomically resolved one can see that the atomic rows run through these defects without defects, i.e. there seem to be no missing or shifted atoms. Possibly, such superstructure defects mark missing atoms below the top layer which would be Eu vacancies. Another explanation could be adsorbates. This cannot be be clarified without knowledge of the nature of the superstructure. Its periodicity is given by the epitaxial relation between the oxide film and the substrate, but the low corrugation of the Ir(111) surface makes a purely topographic origin improbable. Thus at least an electronic contribution has to be considered. If the origin of the superstructure defects lies not in the (for STM invisible) Eu layer beneath, another explanation for the unchanged atomic rows at the defects could be that the superstructure consists of Eu atoms on top of the BL (i.e., in the third EuO layer). Possibly, such a periodic Eu adsorption may be required for the stabilisation of the polar BL EuO(111).

Beside this superstructure defects the difference between both growth temperatures lies in the

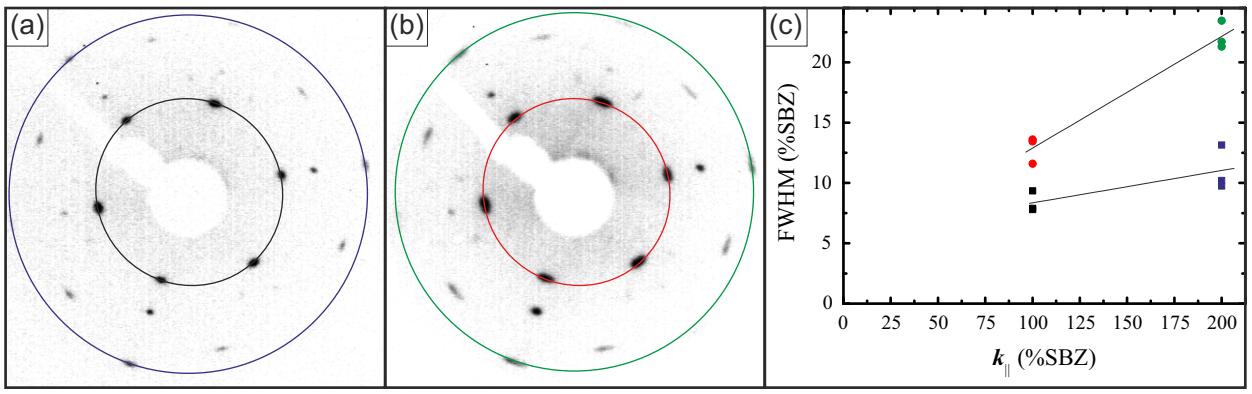

Figure 6.12: Inverted contrast LEED patterns of BL EuO(111) ($\Theta = 0.46\,\mathrm{MLE_{EuO}}$, $f_{\mathrm{Eu}}/f_{\mathrm{O}} = 1.7$) at a primary electron energy of 72 eV grown at **(a)** $T_{\mathrm{growth}} = 623\,\mathrm{K}$ and **(b)** $T_{\mathrm{growth}} = 723\,\mathrm{K}$. The circles indicate the paths along which the spot profiles were taken. **(c)** Plots of FWHMs of three equivalent EuO(111) spots. Black squares: first order, $T_{\mathrm{growth}} = 623\,\mathrm{K}$; red circles: first order, $T_{\mathrm{growth}} = 723\,\mathrm{K}$; blue squares: third order, $T_{\mathrm{growth}} = 623\,\mathrm{K}$; green circles: third order, $T_{\mathrm{growth}} = 723\,\mathrm{K}$. 1 SBZ is here defined as the diameter of the unreconstructed EuO(111) surface Brillouin zone in Γ-M-direction (i.e., 100 %SBZ = $2.76\,\mathrm{nm}^{-1}$).

degree of misorientation of the EuO. This has also an impact on the superstructure as can be seen in Figs. 6.11(c) and (f), which are both atomically resolved. The angle between the superstructure and the dense packed EuO rows ($\phi_{\mathrm{EuO,super}}$) is amplified, compared to the angle between the dense packed EuO and Ir rows ($\phi_{\mathrm{EuO,Ir}}$), similar to the case of the graphene moiré in Sec. 2.4.2. This amplification and the subsequent superstructure misorientation result in a considerable deviation from the p(3×3) superstructure. Due to the smaller superstructure unit cell the amplification is smaller than for the graphene moiré. For small angles [i.e. $\sin(\phi_{\mathrm{EuO,Ir}}) \approx \phi_{\mathrm{EuO,Ir}}$] the amplification is ≈ 4 and $\phi_{\mathrm{EuO,Ir}}$ can be calculated by:

$$\phi_{\mathrm{EuO,Ir}} = \left(\frac{k_{\mathrm{Ir}} - k_{\mathrm{EuO}}}{k_{\mathrm{Ir}}} \right) \sin\left(\phi_{\mathrm{EuO,super}}\right). \tag{6.2}$$

The angles $\phi_{\mathrm{EuO,super}}$ can be measured in the Fourier transforms of the topographs which are shown in the insets of Figs. 6.11(c) and (f). There, the superstructure is represented by the inner hexagonal spots and the EuO atoms by the outer hexagonal spots. The angles $\phi_{\mathrm{EuO,super}}$ are given by the angles between the hexagons and are $\phi_{\mathrm{EuO,super}}$(Fig. 6.11(c)) $\approx 2°$ and $\phi_{\mathrm{EuO,super}}$(Fig. 6.11(f)) $\approx 4.5°$. Using Eq. 6.2 and the surface lattice constants $a_{\mathrm{EuO}} = 3.7$Å and $a_{\mathrm{Ir}} = 2.71$Å the angles $\phi_{\mathrm{EuO,Ir}}$ are $\phi_{\mathrm{EuO,Ir}}$(Fig. 6.11(c)) $= 0.5°$ and $\phi_{\mathrm{EuO,Ir}}$(Fig. 6.11(f)) $= 1.2°$.

These misalignment angles of the EuO are only local examples. To determine the average misorientation the azimuthal elongation of the LEED spots can be used, similar as for the graphene moiré in Sec. 4.1.4. Figure 6.12(a) shows the LEED pattern of the BL EuO(111) film grown at $T_{\mathrm{growth}} = 623\,\mathrm{K}$ and Fig. 6.12(b) the LEED pattern of the BL EuO(111) film grown at $T_{\mathrm{growth}} = 723\,\mathrm{K}$. The FWHMs of azimuthal profiles of three equivalent first and third order spots are plotted for both temperatures in Fig. 6.12(c).

Although the FWHMs of the equivalent spots of the same temperature vary between each other,

the increase with the spot order is clearly visible. The fits [solid lines in Fig. 6.12(c)] have a slope of 2.7% for $T_{\text{growth}} = 623\,\text{K}$ and of 9.3% for $T_{\text{growth}} = 723\,\text{K}$. Thus, the the standard deviation from the EuO[$1\bar{1}0$]-Ir[$1\bar{1}0$] alignment is $\pm 0.7°$ for $T_{\text{growth}} = 623\,\text{K}$ and $\pm 2.3°$ for $T_{\text{growth}} = 723\,\text{K}$.

The misalignment the EuO(111) could result from a slight increase of the surface lattice constant ($a_{\text{EuO(111)}} = 3.7\,\text{Å}$) compared to the bulk value. This lattice expansion is a completely different behaviour than for the ML EuO(100) and could be a consequence of the polarity: An increase of the in-plane lattice constant reduces the surface electron density and thus decreases the electrostatic energy of the polar EuO(111). An increase of the surface lattice constant was also found for other polar oxides on metal substrates, e.g., MgO(111) on Ag(111) [113] or FeO(111) on Pt(111) [243].

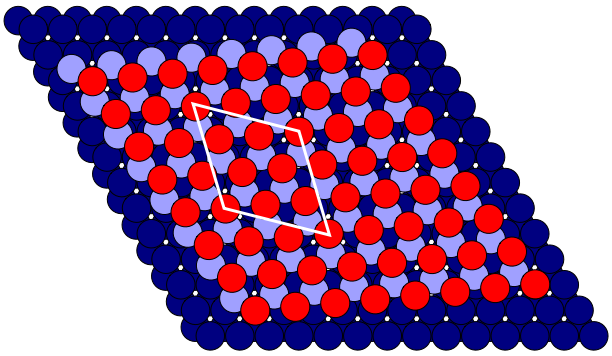

Figure 6.13: Top view of a ball model of a BL EuO(111) on Ir(111) with an angle of 5.2° between the Ir-$[1\bar{1}0]$ and the EuO-$[1\bar{1}0]$. For a slightly expanded EuO lattice ($a_{\text{EuO(111)}} = 3.7\,\text{Å}$) the EuO builds a $(\sqrt{7} \times \sqrt{7})$R19.1° superstructure. Colour scheme: Ir dark blue, Eu light blue, and O red.

EuO(111) with a surface lattice constant of $a_{\text{EuO(111)}} = 3.7\,\text{Å}$ coincides the Ir(111) lattice in a $(\sqrt{7} \times \sqrt{7})$R19.1° superstructure and requires a misalignment of the Ir-$[1\bar{1}0]$ and EuO-$[1\bar{1}0]$-directions of 5.2°. This case is drawn as ball model in Fig. 6.13. If the lattice expansion is really connected to a reduction of the electrostatic energy, it should increase with the size of the oxide island. Then the temperature dependence of the misalignment could be explained by the necessity to rotate EuO islands of a certain size, which requires a sufficient temperature.

6.2 EuO on Ir(100)

Contrary to Ni(100), on Ir(111) no surface oxides were observed and directly rock-salt structured EuO has grown. The intention of EuO growth on Ir(100) was to combine these advantages with the fourfold symmetry of a (100) surface for the growth of EuO(100).

As starting point for the growth on Ir(100) the optimum values for EuO(100) growth on Ni(100) were chosen, i.e. $f_{\text{Eu}}/f_{\text{O}} = 1.4$ and $T_{\text{growth}} = 723\,\text{K}$. Under these conditions, growth of a $\Theta = 3.8\,\text{MLE}_{\text{EuO}}$ film lead to the presence of facet reflexes, i.e. spots which run to the border of the field of view with increasing electron energy. Simultaneously EuO(100) spots of two different domains are present, the first order spots of which are connected by a red or green square in Fig. 6.14(a). These domains are rotated by $\pm 12°$ out of an EuO[001] ∥ Ir[011] alignment, and have a surface lattice constant of ≈ 3.6Å, i.e. as expected for bulk like EuO(100).

The presence of the facet reflexes indicates a large amount of EuO(111) grains which grow in pyramidal shape with {100}-facets to minimise the surface free energy, similar to the observations for the growth on Ni(100) (see Sec. 5.1.1). Thus, both (100) and (111) oriented grains form under Eu rich conditions, similar as for the (111) face of Ir. There, Eu deficiency during the initial growth phase ($\Theta \leq 2.5\,\mathrm{MLE_{EuO}}$) considerably increased the ratio of EuO(100)/EuO(111). Hence, initial Eu deficient growth was also tested for Ir(100). The easiest way to achieve this was to leave out the removal of the p(2 × 1)-O adsorbate layer, which was used to lift the p(5 × 1) reconstruction of the Ir(100) (see Sec. 4.1.2).

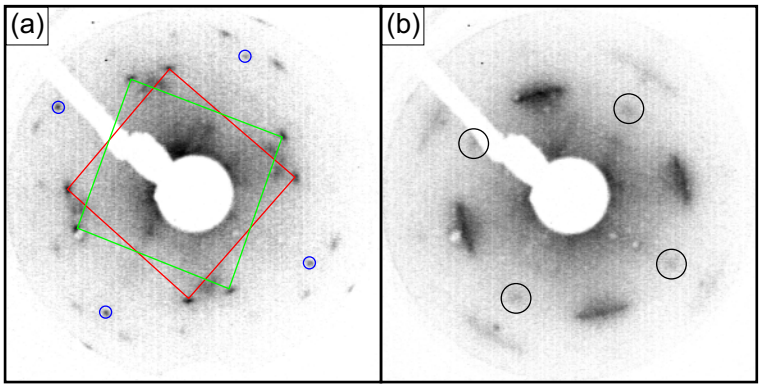

Figure 6.14: Inverted contrast LEED patterns of EuO films grown with $\Theta = 3.8\,\mathrm{MLE_{EuO}}$ and $f_{\mathrm{Eu}}/f_{\mathrm{O}} = 1.4$ at $T_{\mathrm{growth}} = 723\,\mathrm{K}$. Primary electron energy 62 eV. **(a)** Film grown on clean surface. The Ir(100) spots are enclosed by blue circles, the red or green squares connect first order spots of two EuO(100) domains. Adjacent to these first order spots are facet reflexes of EuO(111). **(b)** Film grown on surface with a p(2 × 1)-O adlayer. The intensity enclosed by black circles belongs to EuO(100) spots with EuO[011] ∥ Ir[011].

Figure 6.14(b) shows the LEED pattern of a EuO film grown on Ir(100) with an p(2 × 1)-O adlayer. All growth parameters of the film are the same as for the film represented by Fig. 6.14(a). Still facet reflexes were observed for LEED of this film but with reduced intensity. Thus, similar to the Ir(111) substrate, Eu deficiency during the initial growth phase increased the ratio of EuO(100)/EuO(111). The EuO with ≈ EuO[001] ∥ Ir[011] is represented by elongated spots instead of two sharp, but rotated spots. This means that the full range of angles between the ±12° deviation of EuO[001] ∥ Ir[011] alignment is realised. Therefore, similar to the (111) surface, O surplus leads to an increase of the misalignment of the EuO films (see Sec. 6.1.2).

For EuO(111) films on Ir(111) grown at $T_{\mathrm{growth}} = 623\,\mathrm{K}$ the elongation of the LEED spots was reduced compared to films grown at $T_{\mathrm{growth}} = 723\,\mathrm{K}$. Thus, a reduction of the growth temperature could also improve the degree of orientation of the EuO(100) on Ir(100), but in the ideal case this should result in the two rotated domains which are present in Fig. 6.14(a). Possibly the quota of EuO(111) could be reduced by further decreasing $f_{\mathrm{Eu}}/f_{\mathrm{O}}$, but this would increase the probability of incorporating Eu^{3+}-ions. Hence the performed experiments give no hint towards a recipe for single phase EuO(100) on Ir(100).

6.3 Summary

EuO grows on Ir(111) without formation of surface oxides which have no structural counterpart in bulk EuO, contrary to the case of the Ni(100) substrate. This is probably related to the low chemical reactivity of the noble metal Ir which primarily acts as a screening surface for the oxide growth. Initially, a BL of Eu(111) forms for $\Theta = 0.46\,\mathrm{MLE_{EuO}}$, $0.85 \leq f_{\mathrm{Eu}}/f_{\mathrm{O}} \leq 1.7$, and $623\,\mathrm{K} \leq T_{\mathrm{growth}} \leq 723\,\mathrm{K}$. The work function of the BL EuO(111) is increased by $\approx 6\,\mathrm{eV}$ compared to the (100) surface of a EuO single crystal, whereby the additional surface dipole is created by the polarity of the rock-salt (111) surface. This proves that this BL is terminated by a negatively charged layer, i.e. O-ions.

For $\Theta = 1.0\,\mathrm{MLE_{EuO}}$ the Ir is additionally covered by three rotational domains of a rock-salt structured ML of EuO(100), which has a contracted lattice with $a_{\mathrm{EuO}} = 4.8$Å(i.e. 7% compression). This is similar to the BL EuO(100) on Ni(100), which is also compressed up to 7%, and is probably related to finite size effects. In contrast, the BL EuO(111) has a bulk-like or even slightly expanded lattice which enables a reduction of the surface electron density and thus a reduction of the polarity. The characteristic superstructures of the BL EuO(111), ranging from a $\mathrm{p}(3 \times 3)$ to a $(\sqrt{7} \times \sqrt{7})\mathrm{R}19.1°$, are no longer present for $\Theta = 1.0\,\mathrm{MLE_{EuO}}$, indicating that the third layer of EuO(111) already reconstructs to lower the electrostatic potential. At least for $f_{\mathrm{Eu}}/f_{\mathrm{O}} = 1.7$ also a third phase is present for $\Theta = 1.0\,\mathrm{MLE_{EuO}}$, which consists most probably of metallic Eu islands.

For $\Theta = 3.7\,\mathrm{MLE_{EuO}}$ the film consists of EuO(100) and EuO(111) grains, whereby the ratio of EuO(100)/EuO(111) can be increased by initial usage of lower $f_{\mathrm{Eu}}/f_{\mathrm{O}}$. This is also true for EuO films of this thickness grown on Ir(100). There, the misalignment between EuO(100) and substrate is high as can be seen by the very long LEED spot elongation.

In total, Ir is the ideal substrate to analyse ML EuO(100) and BL EuO(111). It will also be suitable to analyse the reconstruction of the third layer of EuO(111). For STM analysis of thicker films it is less suitable as no method to grow single-phase EuO(100) or EuO(111) films was found. The inclusion of (111)-oriented grains makes crash-free STM difficult for thicker films. To enable growth of thicker films on a non-magnetic substrate, EuO growth on graphene on Ir(111) was tested, as will be shown in the next chapter.

7 EuO on graphene on Ir(111)

In Sec. 5.2 we have seen that it is possible to grow single-phase EuO(100) films on Ni(100). As Ni has the disadvantage of being ferromagnetic and thus of disturbing magnetic measurements, Ir was tested as a substrate. This was described in the previous chapter. Contrary to Ni, on Ir it was possible to grow ML thick EuO(100) in rock salt structure as no complex surface oxides form. On Ir no single phase EuO could be achieved for film thicknesses of more than 1 ML.

For rock-salt crystals like EuO the (100) surface has the lowest surface energy (see Sec. 2.2) because of (I) the atom density is the highest for this plane and (II) the electrostatic neutrality of this surface. Thus, the driving force for the growth of other orientations, like the polar EuO(111), is the strong interaction with the metal substrate in the initial growth stage. To suppress the growth of other orientations than (100), a substrate which only slightly interacts with EuO should be chosen. As the substrate still had to be conductive to perform STM and STS, graphene on Ir(111) was considered to be a good choice.

Graphene is comparatively inert and has a very low surface energy ($\approx 0.3\,\mathrm{eV\,nm^{-2}}$, see Sec. 2.4) compared to Ni(100) or Ir(111) ($\approx 15\,\mathrm{eV\,nm^{-2}}$ and $\approx 19\,\mathrm{eV\,nm^{-2}}$, respectively [244; 245]). Thus, the interaction of graphene with EuO is expected to be considerably reduced compared to these metal substrates. Furthermore, graphene can be easily grown in high quality on the already present Ir(111) crystal, which made this substrate choice even more apparent.

After the experience with the Ni and Ir substrates, the intention was to initially analyse the growth of sub-monolayer films. Thereby no EuO was found, but the Eu was intercalated between the graphene and the Ir. These results are described in Sec. 8.1 in a separate chapter. In the following section films of multilayer thickness are analysed which consist of only partially coalesced and typically {100}-faceted grains. Therefore, it is useful to give the film thickness, similar to Sec. 5.2, in ML, whereby 1 ML is defined with respect to the density of Eu and O atoms in one layer of EuO(100) with its bulk lattice constant, which is 1.51×10^{19} atoms $\mathrm{m^{-2}}$. As all films were grown with O deficiency, the O exposure is assumed to be the limiting factor for the film thickness, i.e. it is assumed that excess Eu re-evaporates (or intercalates, see Sec. 8.1). In Sec. 7.2 two typical $\mathrm{d}I/\mathrm{d}U$ spectra taken on the grains' surfaces are discussed.

7.1 Morphology of the EuO grains

All experiments presented in this chapter were grown on closed TPG+CVD graphene films which were grown as described in Sec. 4.1.4. For the initial experiments the parameters $T_{\mathrm{growth}} = 723\,\mathrm{K}$ and $f_{\mathrm{Eu}}/f_{\mathrm{O}} = 1.4$ were used because they were expected to result in high quality films, based on the experiences with the growth of EuO(100) films on Ni(100) (see Sec. 5.2). A corresponding film of 3.2 ML thickness is shown in the STM topograph in Fig. 7.1(a). It consists mainly of {100}-faceted grains, which are only partially coalesced and surrounded by uncovered graphene. Thus, the EuO

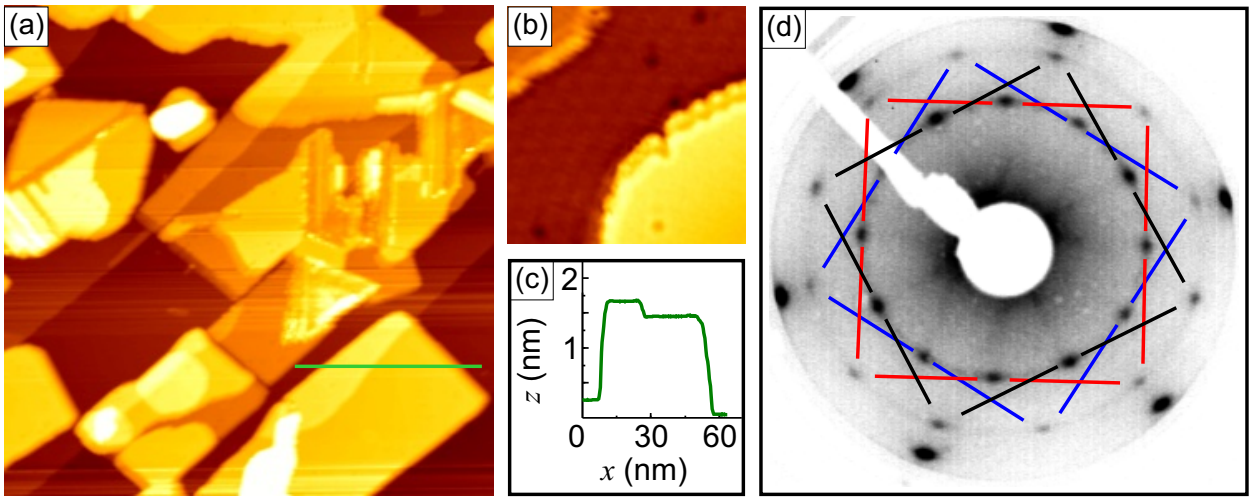

Figure 7.1: **(a)** STM topograph of EuO grains grown at $T_{\mathrm{growth}} = 723\,\mathrm{K}$ with $f_{\mathrm{Eu}}/f_{\mathrm{O}} = 1.4$. Film thickness 3.2 ML, image size $160\,\mathrm{nm} \times 160\,\mathrm{nm}$ ($U_{\mathrm{s}} = -2.2\,\mathrm{V}$, $I_{\mathrm{t}} = 31\,\mathrm{pA}$). **(b)** Zoom on grain surface, $25\,\mathrm{nm} \times 25\,\mathrm{nm}$ ($-1.7\,\mathrm{V}$, 31 pA). **(c)** Height profile along the line in (a). **(d)** Inverted contrast LEED pattern at a primary electron energy of 64 eV. The spots of the three rotational EuO(100) domains are connected by differently coloured squares.

does not wet this substrate as it was expectable due to the low surface energy of graphene. Above the green line, which indicates the profile in Fig. 7.1(c), a triangular structure is present, which is probably (111) oriented EuO. This indicates that growth of polar EuO is not totally suppressed for this parameters, while the vast majority of the grains are (100) oriented.

Figure 7.1(b) shows a higher resolved topograph of a grain surface. It contains some of the dark discs which are typical for Eu rich growth conditions and were identified as O vacancies in Sec. 5.2. Their low concentration is indicative of a low charge carrier concentration, which is consistent with the experienced difficulties in STM imaging. Stable imaging was only possible for very low tunnelling currents of $\approx 30\,\mathrm{pA}$, but even then the topographs were streaky, indicating frequent tip-sample interactions.

Figure 7.1(c) is a profile of a grain with a height of $\approx 1.5\mathrm{nm}$, a typical value for the grains of this experiment, the surface area of which is in the order of $5000\,\mathrm{nm}^2$. This is somewhat less than the double of the average film height of 0.8 nm (or 3.2 ML), which was calculated assuming the O exposure as limiting factor. The steep sides of the grain, which enclose an angle of 90° with the top surface (the slight deviation from the perpendicular is given by the tip apex), prove that these grains are fully {100}-faceted.

As already visible in the STM topograph in Fig. 7.1(a), the EuO grains have a preferred in-plane orientation. This is quantitatively shown in the LEED pattern in Fig. 7.1(d), which contains spots of three EuO(100) domains, which are connected by differently coloured squares. At the border of the field of view the six graphene spots can be seen. These were used to determine the lattice constant of the EuO as described in Sec. 4.4. To minimise the effect of distortions the second order spots of the EuO were used which are relatively close to the graphene spots. This gave a surface lattice constant of $a_{\mathrm{EuO(100)}} = (3.5 \pm 0.05)\,\text{Å}$, i.e. a by 4% contracted lattice compared to the EuO

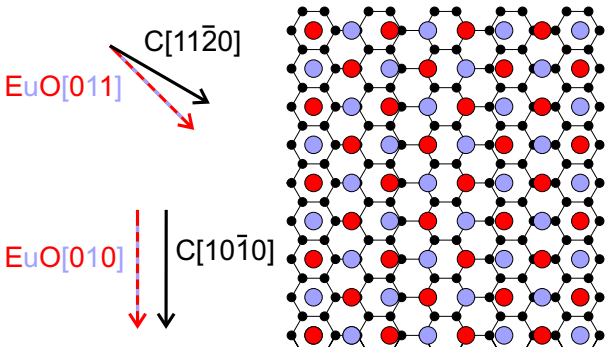

Figure 7.2: A compressed EuO(100) lattice ($a_{\mathrm{EuO}(100)} = 3.47\,\text{Å}$) on graphene, corresponding to Fig. 7.1(d). The EuO[011]-direction is rotated by 15° with respect to the C[11$\bar{2}$0]-direction, thus EuO[010] is aligned to C[10$\bar{1}$0] and coincides with the C lattice in a 1:2 relation. Colour scheme: O red, Eu blue, C black.

bulk value.

This could be a consequence of the typical grain thickness of 6 EuO(100) layers and related finite size effects. We have seen in Sec. 6.1.1 that one ML of EuO(100) on Ir(111) has a surface lattice constant of only 3.3 Å without any apparent epitaxial reason, which increased to 3.5Å for 4 ML thickness. Thus, a similar effect is likely on graphene as the interaction strength with the substrate is probably too low to achieve such a high compression. Nevertheless, the substrate could support this lattice contraction as, for EuO(100) with a surface lattice constant of 3.47 Å and with a EuO⟨010⟩ direction aligned to a C⟨11$\bar{2}$0⟩ direction, a lattice coincidence with a ratio of 1:2 exists as shown in Fig. 7.2. In this model the dense packed lattice directions of EuO and graphene enclose an angle of 15° which is consistent with the angle between the first order spots of EuO and graphene in the LEED pattern. Slightly dilating this 3.47 Å surface lattice by 1% would result in a lattice coincidence in the perpendicular direction with a ratio of $6{:}7\sqrt{3}$, but there exist several other 'long range' coincidences for slight variations of the lattice constant which could be realised upon dilatation of the grains during growth.

The perpendicular side walls of the grains are a considerable handicap for STM. In order to prevent tip sample contacts the scanning speed has to be very low. Furthermore, one needs to invest a lot of time for tip preparation as this surface topography is very prone to tip artefacts. The dewetting of the substrate is driven by minimisation of the free energy of the system and clearly indicates that the surface free energy of the graphene is lower than that of the EuO. Thus, the EuO surface is reduced at the cost of leaving graphene surface uncovered. To build lower EuO grains with larger lateral dimensions T_{growth} should be reduced.

A test with $T_{\mathrm{growth}} = 300\,\text{K}$ did result in a film which showed no LEED spots and even annealing up to 600 s at 873 K lead only to faint spots at the graphene positions in the otherwise diffuse LEED intensity. In Sec. 5.2.2 we have seen that annealing of EuO films on Ni(100) in Eu vapour is much more efficient in creating smooth EuO surfaces. Furthermore, the Eu chemical potential gives rise to the formation of O vacancies, thereby improving the conductivity. Thus, the film was annealed again, but now for 600 s at 723 K with an applied Eu pressure of $p_{\mathrm{Eu}} = 1.3 \times 10^{-8}\,\text{mbar}$. The

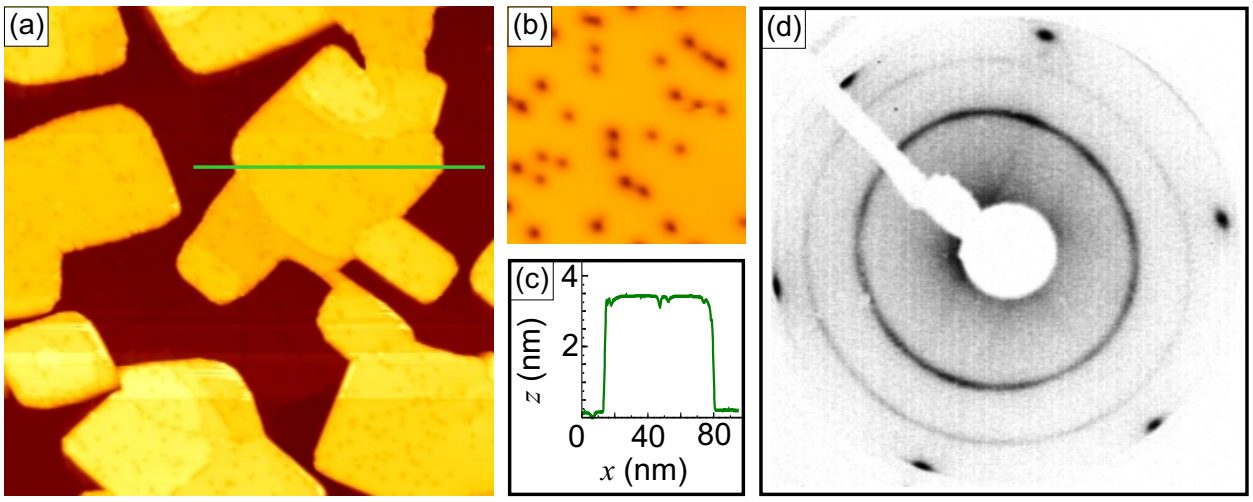

Figure 7.3: **(a)** STM topograph of EuO grains grown at $T_{\mathrm{growth}} = 300\,\mathrm{K}$ with $f_{\mathrm{Eu}}/f_{\mathrm{O}} = 1.4$ after annealing. Film thickness 3.2 ML, image size $160\,\mathrm{nm} \times 160\,\mathrm{nm}$ ($U_{\mathrm{s}} = -2.0\,\mathrm{V}$, $I_{\mathrm{t}} = 83\,\mathrm{pA}$). **(b)** Zoom on grain surface, $25\,\mathrm{nm} \times 25\,\mathrm{nm}$ ($-2.0\,\mathrm{V}$, 83 pA). **(c)** Height profile along the line in (a). **(d)** Inverted contrast LEED pattern at a primary electron energy of 64 eV. The EuO(100) has no in-plane orientation.

results are shown in Fig. 7.3.

As can be seen in the topograph in Fig. 7.3(a) the grains are even more compact than these for $T_{\mathrm{growth}} = 723\,\mathrm{K}$ and the overall quality is improved. No polar EuO was found during STM and the grains' conductivity had improved, enabling higher tunnelling currents. It was also possible to record reproducible $\mathrm{d}I/\mathrm{d}U$ spectra which will be discussed in Sec. 7.2. Figure 7.3(b) shows a higher resolved topograph of a grain surface which exhibits a higher density of oxygen vacancies [$0.03\,\mathrm{nm}^{-2}$ or 0.4% on average in Fig. 7.3(a)] than the grain surface in Fig. 7.1(b). This is consistent with the observed enhancement of the conductivity and is also typical for this annealing procedure (compare with Sec. 5.2.2).

The height profile in Fig. 7.1(c) was taken along the green line in Fig. 7.1(a). This grain is slightly higher than 3 nm (a very common height for the grains of this film). While the grains are more uniform in size than for $T_{\mathrm{growth}} = 723\,\mathrm{K}$ with a surface area in the order of $2500\,\mathrm{nm}^2$, the orientation of the grains is lost. This is already visible in the topograph in Fig. 7.3(a), but even more obvious in the LEED pattern in Fig. 7.3(d), where the electrons diffracted by the EuO(100) are imaged as two rings. Thus, the in-plane orientation of the grains is absolutely random. Lattice constant measurements on the outer EuO ring with LEED at the positions of the spots of the oriented EuO in Fig. 7.1(d), revealed a EuO surface lattice constant of (3.6 ± 0.05) Å. This is close to the bulk value of 3.64 Å. Assuming an average grain height of slightly more than 3 nm this is consistent with the relaxation behaviour shown in Fig. 5.20 for EuO on Ni(100). Due to the low EuO-substrate interaction and due to the absence of epitaxial orientation it is likely that the grains dilate as a whole with increasing height.

Compared to the film grown at $T_{\mathrm{growth}} = 723\,\mathrm{K}$, the annealed film was an improvement with respect to the tunnelling conditions because of the higher conductivity. But this was partially coun-

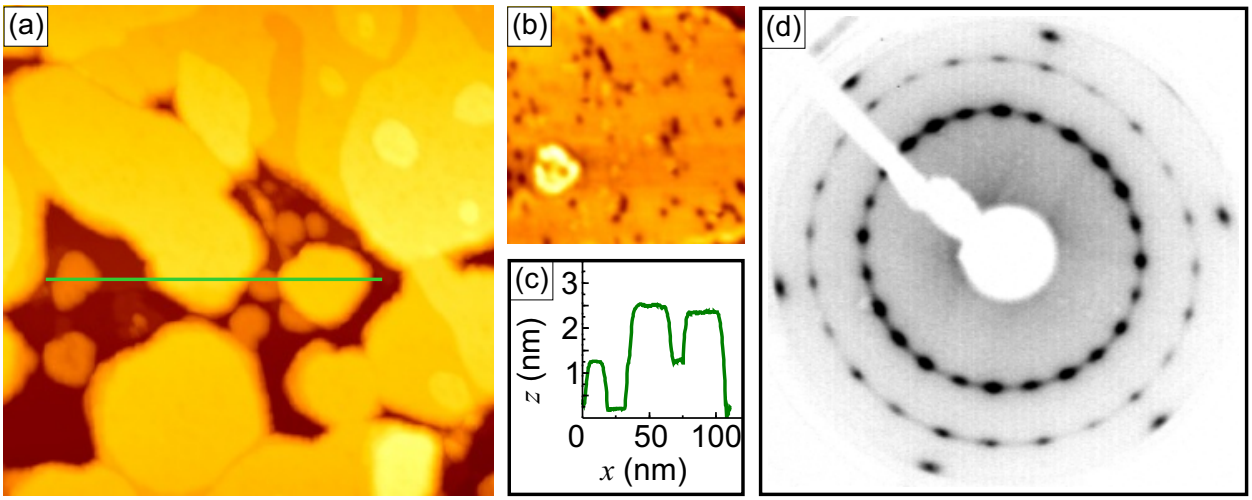

Figure 7.4: **(a)** STM topograph of EuO grains grown at $T_{\mathrm{growth}} = 553\,\mathrm{K}$ with $f_{\mathrm{Eu}}/f_{\mathrm{O}} = 2.4$ after annealing, imaged at 35 K. Film thickness 2.7 ML, image size 160 nm × 160 nm ($U_{\mathrm{s}} = +1.3\,\mathrm{V}$, $I_{\mathrm{t}} = 0.35\,\mathrm{nA}$). **(b)** Zoom on grain surface, 25 nm × 25 nm (+1.3 V, 0.35 nA). **(c)** Height profile along the line in (a). **(d)** Inverted contrast LEED pattern at a primary electron energy of 64 eV.

teracted by the increased grain height which made imaging even more prone to tip artefacts. Thus, for the next experiment a lower annealing temperature of 673 K (600 s with $p_{\mathrm{Eu}} = 1.3 \times 10^{-8}$ mbar) was selected to achieve flatter grains. To avoid the risk of rough grain surfaces, T_{growth} was increased again to 553 K. Additionally, it was intended to image metallic EuO at 35 K and, as T_{C} is expected to be lowered for films of less than 20 layers (5 nm) thickness [85], the flux ratio was increased to $f_{\mathrm{Eu}}/f_{\mathrm{O}} = 2.4$ and 1.7% Gd was co-evaporated. Assuming re-evaporation of excess Eu, but no re-evaporation of Gd (the vapour pressure of Gd at 673 K is neglectable), a substitution of 4% of the Eu atoms with Gd is expected. The aim is to further enhance the grains' conductivity due to the additional 5d electron of Gd compared to Eu and also to increase T_{C}. For bulk EuO such a Gd concentration enhances T_{C} to 125 K [28], thus the grains are expected to exhibit a considerable magnetisation despite possible finite size effects. The resulting film was characterised at 35 K and is shown in Fig. 7.4.

The topograph in Fig. 7.4(a) demonstrates considerable differences to both EuO films described above, e.g., the grain size is spread over a wide range. Lateral grain dimensions between 5 nm and 250 nm were found and the grains' heights vary between 0.25 nm [i.e. 1 ML EuO(100)] and ≈ 3 nm, whereby the largest terraces are usually lower than 2 nm in height. Figure 7.4(c) shows a characteristic height profile taken along the green line in Fig. 7.4(a).

The higher resolved topograph in Fig. 7.4(b) displays again the dark disks assumed to be oxygen vacancies. Although the appearance of a Gd impurity in an STM topograph is unknown, it is unlikely that a Gd impurity is imaged in the same way as an O vacancy. The concentration of the dark discs [$0.07\,\mathrm{nm}^{-2}$ on average in Fig. 7.4(a), i.e. 0.9% O vacancies] is about twice as high as in Fig. 7.3(b), which is probably a result of the lower annealing temperature and the increased Eu surplus during growth. Due to the increased O vacancy concentration, together with the Gd

doping of 4%, all grains of this film are expected to be metallic at the imaging temperature of 35 K.

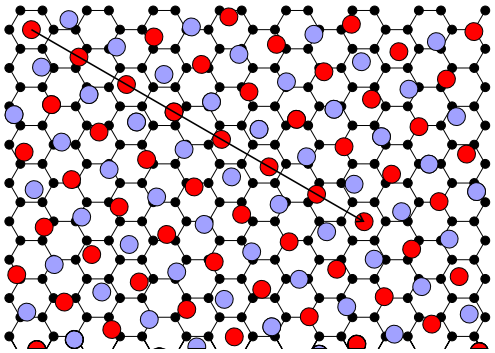

Figure 7.5: A compressed EuO(100) lattice ($a_{\mathrm{EuO}(100)} = 3.52\,\text{Å}$) on graphene with the EuO[011]-direction aligned to C[11$\bar{2}$0]. The arrow indicates a unit vector of the superstructure cell, with a surface lattice coincidence ratio of 7:10. Colour scheme: O red, Eu blue, C black.

The in-plane orientation of the grains cannot be estimated by their topography as they are roundly shaped and lack the rectangular terraces that are present in Figs. 7.1(a) and 7.3(a). From the LEED pattern in Fig. 7.4(d) we learn that the degree of orientation lies in between the annealed film grown at 300 K and the film grown at 723 K. While there is also some ring-like intensity, 48 spots are present in this pattern, belonging to six different domains of EuO(100). This means that there exists an additional substrate orientation compared to $T_{\mathrm{growth}} = 723\,\mathrm{K}$ with the EuO$\langle 011\rangle$ direction aligned to a C$\langle 11\bar{2}0\rangle$. This is shown in Fig. 7.5 for a EuO surface lattice constant of $a_{\mathrm{EuO}(100)} = 3.52\,\text{Å}$ as determined by LEED, which results in a lattice coincidence ratio of 7:10. This ratio crucially depends on the value of $a_{\mathrm{EuO}(100)}$ and varies for the error $\Delta a_{\mathrm{EuO}(100)} = 0.07\,\text{Å}$ between 5:7 and 9:13 and it is also possible that the lattices are indeed incommensurate. This emphasises that the smaller EuO lattice is caused by finite size effects and not by epitaxial strain. As the lattice constant was determined by LEED it represents the average grain height of $\approx 2\,\mathrm{nm}$, which again is consistent with the lattice constant evolution in Fig. 5.20.

7.2 Spectroscopy

The distinct EuO grains on graphene appear as optimal system to perform STS of EuO(100) with defined properties for different, precisely determined grain thicknesses. Therefore some test spectra were taken on larger grains of the films grown at $T_{\mathrm{growth}} = 300\,\mathrm{K}$ (Fig. 7.3) and at $T_{\mathrm{growth}} = 553\,\mathrm{K}$ (Fig. 7.4). Although these tests were only of rudimentary nature, one interesting feature was discovered. The corresponding plots can be seen in Fig. 7.6.

Spectra of the $T_{\mathrm{growth}} = 300\,\mathrm{K}$ film were taken at room temperature on a large grain of 4 nm [16 ML EuO(100)] height in the voltage range $3.0\,\mathrm{V} \geq U_{\mathrm{s}} \geq -3.0\,\mathrm{V}$. An extract of such a spectrum is shown in Fig. 7.6(a). Although a lateral drift compensation was established it was not possible to fully suppress the drift and thus the tip was not kept at the same lateral position. It is assumed that this is not an issue because of the lack of resolution of the used tip which did not resolve any structure on the EuO terraces (except in the vicinity of the vacancies) in topographs. This

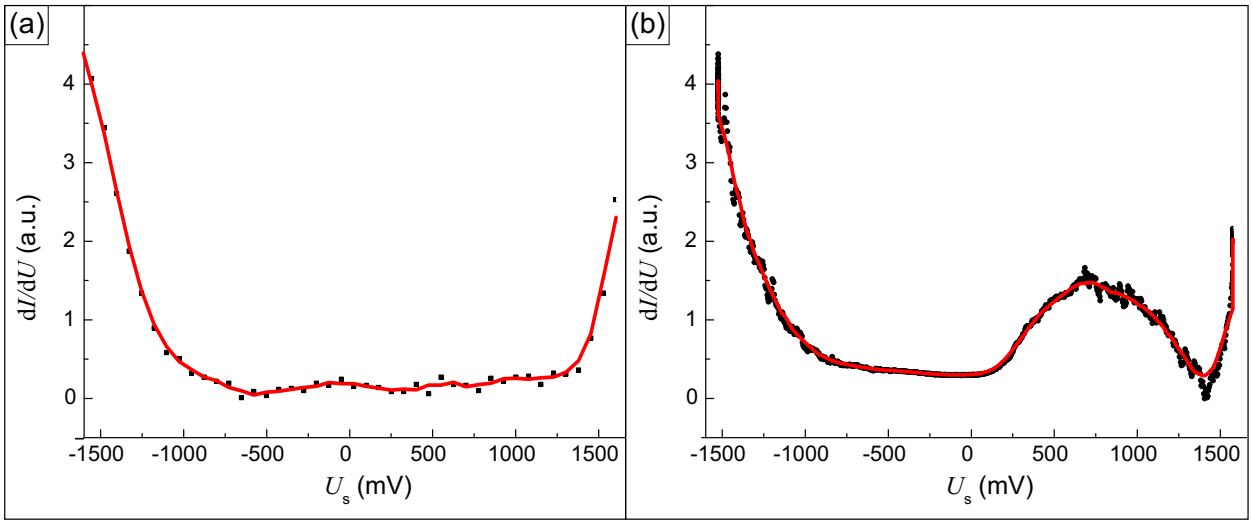

Figure 7.6: **(a)** dI/dU spectrum on a grain surface of Fig. 7.3 taken at 300 K. **(b)** dI/dU spectrum on a grain surface of Fig. 7.4 taken at 35 K.

indicates that the tip was not sensitive to a specific position above non-defective EuO. Additionally, the course of the above spectrum was reproducible at different locations.

The stabilisation current was set to 0.4 nA at $U_s = +3.0$ V, leading to a very small current of < 10 pA for $|U_s| < 1.6$ V and subsequently to a low signal-to-noise ratio. In order to improve the signal-to-noise ratio, a modulation of $\delta U = 30$ mV (frequency $\nu = 433\,\mathrm{s}^{-1}$) was used and the averaging time at the lock-in was set to 300 ms, resulting in few data points only. Despite this fact, for dI/d$U \leq 0.5$ a.u. the course of the spectrum is determined by the noise and the small corrugation between $1.3\,\mathrm{V} \geq U_s \geq -1.0$ V has no physical meaning. The spectrum is determined by the tunnelling transmission probability (T) and no other significant contributions are observable. A possibility to extract weaker LDOS features out of the spectrum would be the normalisation with the tunnelling transmission probability T (see Sec. 4.3.2), but here it makes no sense due to the high noise level.

Spectra of the $T_{\mathrm{growth}} = 553$ K film were taken at 35 K on a grain of 2.5 nm [10 ML EuO(100)] height in the voltage range $1.6\,\mathrm{V} \geq U_s \geq -1.5$ V. The starting current of 2.0 nA was stabilised at +1.6 V and I_t remained well above the noise level, except for the region $0.2\,\mathrm{V} \geq U_s \geq -0.3$ V. A modulation of $\delta U = 10$ mV ($\nu = 433\,\mathrm{s}^{-1}$) and an averaging time of 30 ms were used. Again, the spectra were highly reproducible and contain a broad peak centred around 750 mV which can be seen in Fig. 7.6(b). This peak is the only obvious difference to Fig. 7.6(a).

For a better interpretation of this spectrum a normalisation is desirable. As the tunnelling current was recorded simultaneously with the dI/dU signal the normalisation by I/U (see Sec. 4.3.2) could be directly calculated. To avoid artefacts at regions with low currents, an offset of 5 pA was added to I_t which had otherwise no significant influence on the course of the normalised curve. The result is plotted in Fig. 7.7(a). The main differences to the unnormalised curve are the shift of the position of the broad peak and the approximately linear increase of dI/dU/(I/U) for $U < 0$.

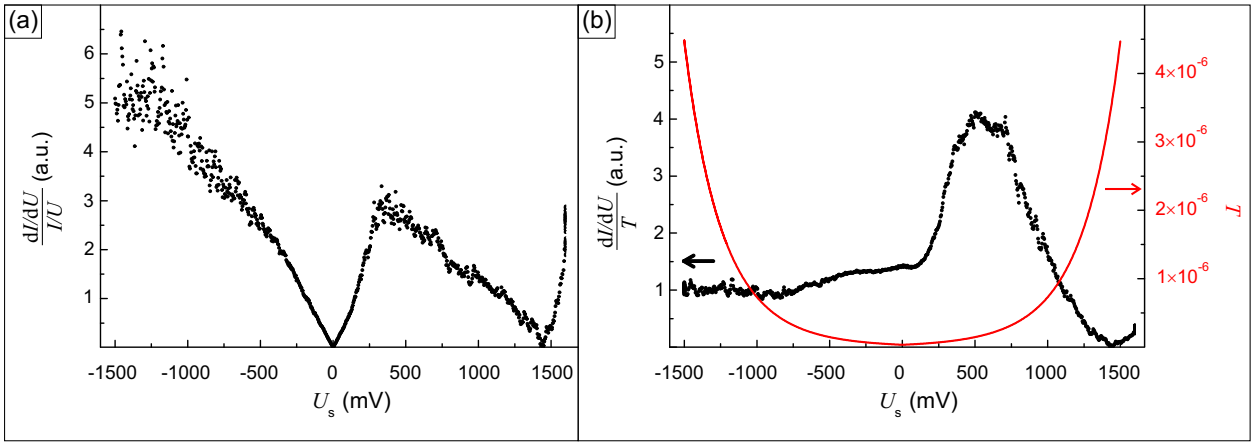

Figure 7.7: **(a)** $\mathrm{d}I/\mathrm{d}U$ spectrum of Fig. 7.6(b) normalised by $I_\mathrm{t} + 5\,\mathrm{pA}/U_\mathrm{s}$. **(b)** $\mathrm{d}I/\mathrm{d}U$ spectrum of Fig. 7.6(b) normalised by T (4.9) with s=9.9 Å and $\overline{\Phi} = 3.2\,\mathrm{eV}$.

A more sophisticated approach is the normalisation by the tunnelling transmission probability T. Therefore, first a fit for T as described by Eq. 4.9 had to be found. As T has to be symmetric and the peak at $U = 750\,\mathrm{meV}$ complicated the fitting procedure, only the branch with $U < 0$ was used for the fitting. The best fit was obtained for a tip-sample distance of $s = 9.9\,\text{Å}$ and an average work function $\overline{\Phi} = 3.2\,\mathrm{eV}$ (which both are reasonable values). Figure 7.7(b) contains the plot of T as well as the normalised spectrum. Contrary to the I/U normalisation there is no increase of $\mathrm{d}I/\mathrm{d}U/T$ for $U < 0$, which was somehow expectable as the fitting of T was done using the branch with $U < 0$. To conclude, the only significant feature in the spectrum is the peak which has its maximum positioned at $U_\mathrm{s} = 750\,\mathrm{mV}$ in Fig. 7.6(b), at $U_\mathrm{s} = 350\,\mathrm{mV}$ in Fig. 7.7(a) and at $U_\mathrm{s} = 500\,\mathrm{mV}$ in Fig. 7.7(b), whereby the latter should be the most reasonable approximation of the sample LDOS. Apart from this peak, the spectrum in Fig. 7.7(b) is featureless, suggesting the lack of narrow bands with a high LDOS contributing to the tunnelling current.

Tunnelling spectra recorded at 5 K during recent experiments of a follow-up project show that this peak is also present on Eu rich EuO without Gd doping, thus it is not connected to Gd states. During these recent measurements this peak changed in dependence of the distance to the O vacancies: While the peak height at 500 mV is highest in the surrounding close to the vacancy, the intensity is increased and shifted towards $\approx 1000\,\mathrm{mV}$ inside the vacancy [246]. Possibly this peak is linked to the metallic state of the EuO but the vanishing tunnelling current for $0.2\,\mathrm{V} \geq U_\mathrm{s} \geq -0.3\,\mathrm{V}$ impedes any information about a possible extension of the lower peak edge down to E_F.

Another possible origin of the peak could be the theoretically predicted surface state [48] (see Sec. 2.1.3). The spin-down part of the surface state shown in Fig. 2.4 coincides with the lower edge of the spin-up part of the conduction band which both will be much closer to the Fermi level in Eu-rich EuO as depicted in Fig. 2.4 due to the n doping. But, the dependence of the peak intensity on the distance to O vacancies suggests that the origin of this peak lies in the presence of the O vacancies and not in a surface state predicted for defect free EuO(100).

7.3 Summary

On graphene on Ir(111), EuO can be grown as thin films of distinct, {100}-faceted grains. Depending on T_{growth}, the grains orient with EuO$\langle 010\rangle$ $\parallel$ C$\langle 11\bar{2}0\rangle$ (for both $T_{\mathrm{growth}} = 723\,\mathrm{K}$ and $T_{\mathrm{growth}} = 553\,\mathrm{K}$) and EuO$\langle 011\rangle$ $\parallel$ C$\langle 11\bar{2}0\rangle$ (for $T_{\mathrm{growth}} = 553\,\mathrm{K}$ only). For $T_{\mathrm{growth}} = 300\,\mathrm{K}$ no in-plane orientation of the grains was found, even after annealing to 873 K.

The morphology of the grains for a given film thickness is mainly determined by T_{growth} and by the annealing procedure. For films with a nominal thickness of about 3 ML (7.7 Å) the typical grain size varies from 1.5 nm in height and a surface area in the order of $5000\,\mathrm{nm}^2$ for a non annealed film grown at $T_{\mathrm{growth}} = 723\,\mathrm{K}$ to 3 nm in height and a surface area in the order of $2500\,\mathrm{nm}^2$ for a film grown at $T_{\mathrm{growth}} = 300\,\mathrm{K}$ and annealed up to 873 K for 600 s. The grain's height influences its surface lattice constant which is $a_{\mathrm{EuO(100)}} = (3.5 \pm 0.05)$ Å for 1.5 nm grain height and increases to 3.6 Å (i.e. almost to the bulk value) for 3 nm high grains. These values are similar to those found for the relaxation behaviour of EuO(100) on Ni(100) shown in Fig. 5.20.

The EuO grains on graphene appear as suitable model system for scanning tunnelling spectroscopy of EuO(100) as one can analyse distinct grains of precisely measurable dimensions, and the O vacancy concentration can be controlled by annealing in Eu vapour (i.e. by the method already described for the EuO films on Ni(100) in Sec. 5.2.2) and by choosing an appropriate Eu surplus and growth temperature. The first recorded tunnelling spectra of EuO(100) with 1% O vacancies in the topmost layer exhibit states about 500 meV above the Fermi level which are most probably related to O vacancies.

8 Eu on and intercalated under graphene on Ir(111)

Figure 8.1: Topograph of Fig. 7.3(a) [$T_{\mathrm{growth}} = 300\,\mathrm{K}$, annealed to 723 K, $f_{\mathrm{Eu}}/f_{\mathrm{O}} = 1.4$, $\Theta = 180\%\,\mathrm{ML}$, image size $160\,\mathrm{nm} \times 160\,\mathrm{nm}$, $U_{\mathrm{s}} = -2.0\,\mathrm{V}$, $I_{\mathrm{t}} = 83\,\mathrm{pA}$] with derivative filter applied to the substrate level.

This chapter deals with Eu on and intercalated under graphene on Ir(111). At first, the experiments presented here were motivated by the observation of patterns at the substrate level during the growth of EuO on graphene. Figure 8.1 is a modified version of the topograph in Fig. 7.3(a) where a derivative filter was applied to the substrate level. This gives enough contrast to the graphene to see the moiré pattern and additional trenches which are not present in pure graphene on Ir(111). Subsequent experiments at $T_{\mathrm{growth}} = 723\,\mathrm{K}$ revealed that these lines are connected to Eu intercalation which is elucidated in Sec. 8.1.

Further experiments were performed at lower T_{growth} to get a more complete overview of Eu adsorption on graphene. The reason for this extended study was a fundamental interest in this adsorbate system, as the large magnetic moment of Eu could bestow graphene with magnetic properties without destroying the graphene's π-electronic system (see Sec. 2.4.3). For $T_{\mathrm{growth}} \leq 400\,\mathrm{K}$ Eu intercalates - under closed graphene layers - only in very small quantities and instead forms clusters and/or islands on top which are described in Sec. 8.2. Especially remarkable, at 300 K and in an intermediate coverage range Eu adsorption results in a phase of uniformly distributed Eu clusters (size 10-20 atoms) coexisting in two dimensional equilibrium with large Eu-islands in a $(\sqrt{3} \times \sqrt{3})\mathrm{R}30^\circ$ structure.

To use a consistent deposition quantity independent of the actual structure, in this chapter

the deposited Eu amount (Θ) is given in %ML, whereby 100 %ML correspond to a Eu density of 1Eu/2C, i.e. one Eu atom per graphene unit cell or 1.91×10^{19} atoms m^{-2}.

A first-principles description of the Eu adsorption on graphene on Ir(111) is achieved by means of density functional theory (DFT) calculations within the generalised gradient approximation (GGA) [247]. We consider, both, non spin-polarised calculations with the Eu 4f-shell frozen to f^7 configurations as well as spin-polarised calculations including the Eu 4f-shell, where we account for the strong local Coulomb interactions of the Eu 4f-electrons within the GGA+U approach. Here, we use the Coulomb parameters of $U = 7\,\text{eV}$ and $J = 1\,\text{eV}$ which have been established to be well suited to describe the spectral properties of rare earth systems [248; 249].

To simulate different Eu coverages, we consider hexagonal graphene supercells with sizes between $(\sqrt{3} \times \sqrt{3})\text{R}30°$ supercells (6 C-atoms) and 6×6 supercells (72 C-atoms) containing different amounts of adsorbed Eu. Using the Vienna Ab Initio Simulation Package (VASP) [250] with the projector augmented wave (PAW) [251; 252] basis sets, we obtain relaxed adsorption geometries and calculate electronic properties including the local density of states (LDOS), work functions, and dipole moments. In all calculations, the carbon atoms and Eu atoms were relaxed until forces were below $0.02\,\text{eV}\,\text{Å}^{-1}$. In the calculations with Ir substrate [4 layer Ir(111) slabs], the Ir(111) slabs were forced to a perfect lattice with lattice constant 3.5 Å to avoid computationally very expensive calculations involving supercells with lateral extent corresponding to the full moiré structure. Hence, the Ir substrate has the same surface lattice constant as graphene (2.46 Å) in the calculations.

Angular resolved photoemission spectroscopy (ARPES) measurements were done in another UHV system which had a base pressures in the 10^{-9} mbar range. For substrate cleaning, fabrication of closed graphene layers, and film growth, the same procedures were used as described in chapter 4. ARPES spectra were taken at 60 K by a Scienta SES-100 hemispherical electron analyser with an energy resolution of ~25 meV using 21.22 eV photons from a helium discharge source with a beam spot diameter of about 2 mm. For the parallel momentum scan the polar angle ranged from 40° to 70°. The azimuthal angle, φ, was changed by a wobble stick and roughly checked by the LEED spot orientation. For a range of azimuths within a few degrees around the Γ-K-M direction, the absolute value of φ can be determined to a precision better than 0.5° when the measured dispersion is fitted by the tight-binding approximation bands of graphene [167; 253]. For additional experiments with Cs intercalation an SAES alkali metal dispenser [254] was used. The Cs evaporation rate remained undetermined, whereby a dispenser current between 6.5 A and 7 A lead to recognisable Cs amounts on the sample after evaporation times in the order of minutes.

8.1 Eu intercalate patterns oriented along the graphene moiré

All experiments presented in this section were grown on closed TPG+CVD graphene films. Figure 8.2 shows a large scale topograph of $\Theta = 18\%$ ML Eu deposited at $T_{\text{growth}} = 723\,\text{K}$ with $f_{\text{Eu}}/f_{\text{O}} = 1.4$ (i.e., grown similarly as the experiment of Fig. 8.1 but with only 1/10 of the deposited amount). While the EuO grains are completely absent, the deposit has built stripes and hexagonal islands with an apparent height of ≈ 2 Å. The lines and island edges are aligned to each other and thus have to be oriented along certain substrate directions. These directions are not the same on the whole

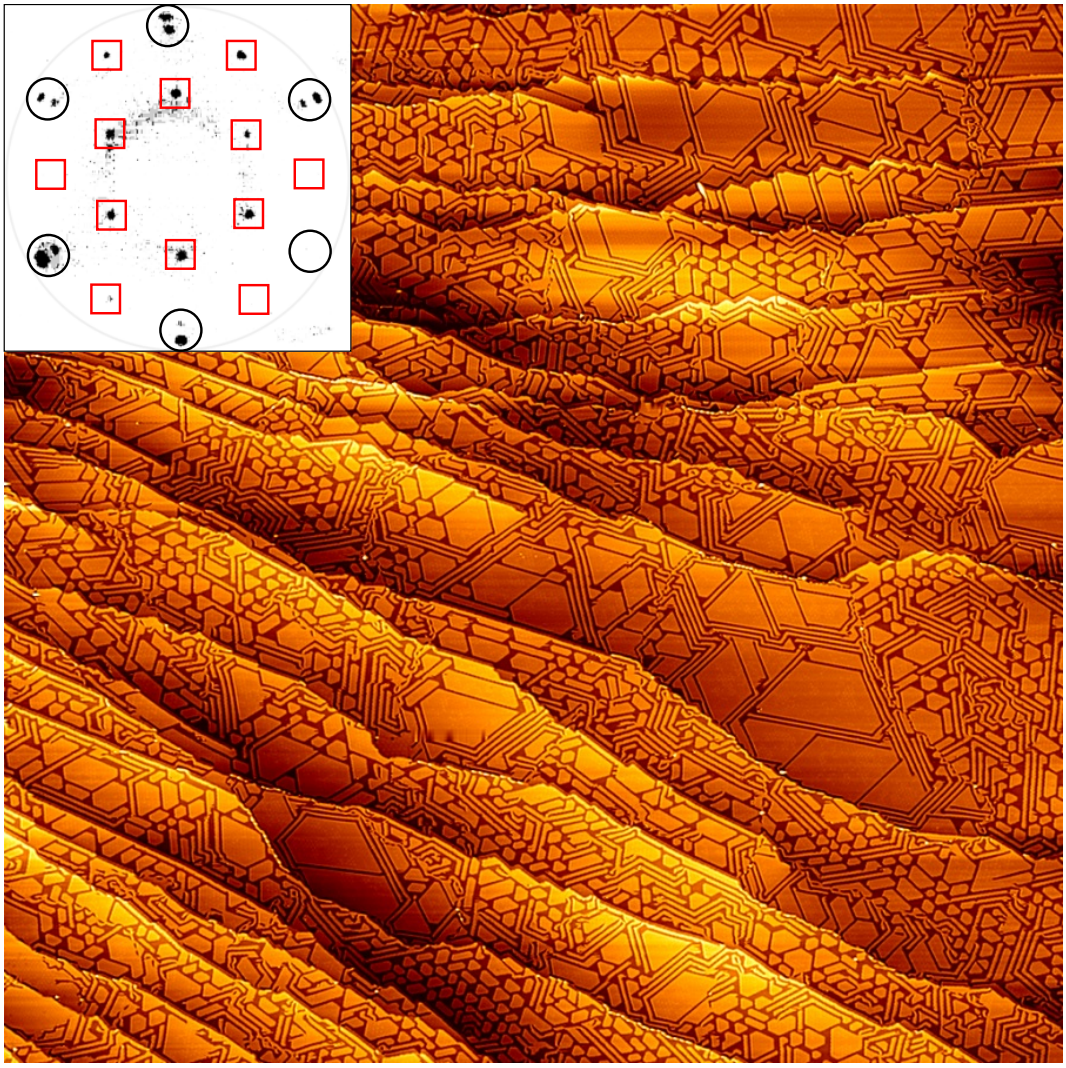

Figure 8.2: STM topograph of $\Theta = 18\%$ ML Eu deposited at $T_{\mathrm{growth}} = 723\,\mathrm{K}$ with $f_{\mathrm{Eu}}/f_{\mathrm{O}} = 1.4$ (image size $600\,\mathrm{nm} \times 600\,\mathrm{nm}$, $U_{\mathrm{s}} = -1.5\,\mathrm{V}$, $I_{\mathrm{t}} = 54\,\mathrm{pA}$). There are several pre-existing Ir step edges and some dislocations in this image. Inset: Corresponding LEED pattern at 48 eV primary electron energy. Black circles enclose C and Ir spots, red squares the additional Eu spots.

substrate but can differ considerably, whereby the change occurs at graphene grain boundaries. Also the size distribution of the islands is rather inhomogeneous. The details of this patterns will be discussed in Sec. 8.1.3.

As can be seen in the LEED pattern which is shown as inset in Fig. 8.2, the spots of the grown film are at the position of a p(2×2) superstructure with respect to graphene. As we will see in the following, these spots belong to pure (i.e., non oxidised) Eu which is intercalated between the graphene and the Ir(111).

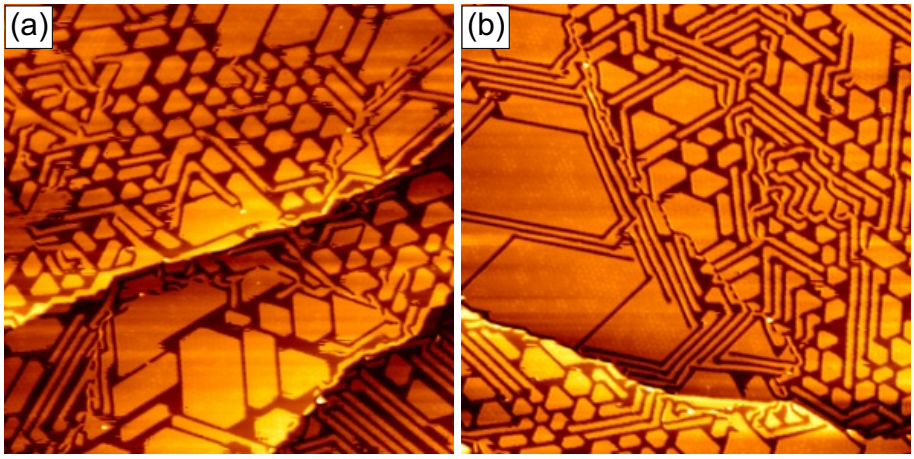

Figure 8.3: STM topographs of films grown at 723 K, size 160 nm × 160 nm, imaged at 300 K. **(a)** $\Theta = 18\%$ ML Eu deposited ($U_s = -1.5$ V, $I_t = 110$ pA) **(b)** $\Theta = 18\%$ ML Eu deposited with with simultaneous O_2 supply with a flux ratio of $f_{Eu}/f_O = 1.4$ (−1.5 V, 54 pA).

8.1.1 Chemical stability of intercalated Eu

The first indication of Eu intercalation was that the observed structures are independent of O_2 exposure. Figure 8.3 shows a comparison of two $\Theta = 18\%$ ML films grown at 723 K, one of which was exposed to O_2 with $f_{Eu}/f_O = 1.4$ during growth [Fig. 8.3(b)] while the other was not [Fig. 8.3(a)]. In both cases the same topography of stripes and hexagonal islands has formed. Thus it is reasonable to assume that these structures do not contain any O atoms and the Eu is not oxidised. This is very astonishing because of the high reactivity of the Eu and was further tested by in-vivo STM during O_2 exposure at 300 K. While no changes were observed for O_2 amounts of several Langmuir, structural changes of the stripes and islands could be observed independent of the O_2 exposure, indicating a high lateral mobility of the Eu atoms even at room temperature. As turned out later, the intercalated Eu is even not affected by sample transport through air. After several days in air and mild annealing to 700 K to clean the graphene surface, LEED showed spots of graphene and still these of the intercalated Eu [255].

8.1.2 Intercalate structures

The atomic structure of the intercalate could not be resolved by STM at 300 K due to the mobility of the Eu. Although islands were formed, they have no stable shape. This can be seen in Fig. 8.4 which contains three exemplary topographs out of a sequence of several frames taken every 84 s at 300 K. In each topograph streaks are present at several locations which are not caused by tip changes but by the mobility of the Eu. This becomes obvious by comparing the topographs taken at different points in time, where not only the island shapes have changed but also coalescence and separation of islands has taken place. These changes suggest that the evolved patterns are equilibrium structures, especially as the film was grown at 723 K. Further structural details were analysed by imaging at 35 K.

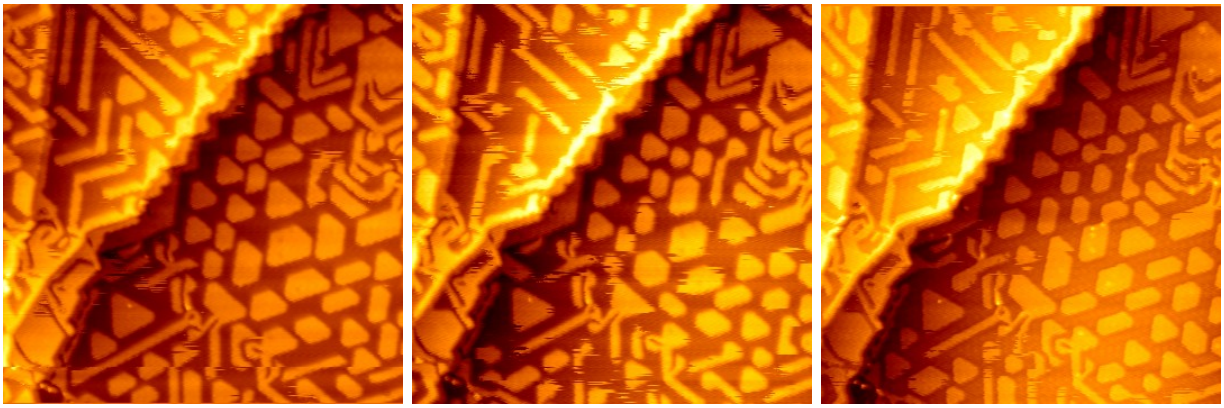

(a) t = 0 (b) t = 924 s (c) t = 1344 s

Figure 8.4: STM topographs of a film grown at 723 K and imaged at 300 K. Θ = 18% ML Eu, image size 120 nm × 120 nm ($U_s = -1.4$ V, $I_t = 0.1$ nA). **(b)** was taken 924 s after **(a)** and **(c)** was taken further 420 s later.

Figure 8.5(a) shows a 10 nm × 10 nm part of 12% ML Eu adsorbed at 720 K. Three Eu islands step edges can be seen, the appearance of which is characteristic for the islands of intercalated Eu. The steps have no sharp border, but the height increases or decreases stepwise over three to four atomic rows. This is demonstrated by the height profile in Fig. 8.5(a) (indicated by the red line) and displayed in the inset. The stepwise height change at the Eu edges resembles the appearance of Ir step edges in the pure graphene on Ir(111) system, where the graphene grows in a carpet like mode over the step edges [161]. This similarity further indicates that the graphene is the top layer (i.e., that the Eu is intercalated).

The shape of the step edges is not always similar. There exist two different types of Eu island step edge shapes, which are both present in Fig. 8.5(a). The step edge in the lower part of this topograph runs completely straight while the lower step of the upper Eu island is curved, showing an undulated shape with the same periodicity as the graphene moiré. As will be shown in Sec. 8.1.3, this undulation is related to differences in the binding energy between C and Ir within the moiré unit cell.

Figure 8.5(b) is a flattened version of Fig. 8.5(b). After the removal of the high corrugation at the islands step edges one can observe the lattice patterns on pure graphene and on the islands with intercalated Eu simultaneously. The C lattice can be seen everywhere while on the Eu islands additional corrugation exists. This gives the opportunity to measure the Eu lattice using the C lattice as a scale.

This was done for Fig 8.5(c), which is a zoom into an intercalated Eu island with sufficient resolution. As was already known from the LEED pattern (inset of Fig. 8.2), the Eu is arranged in a p(2×2) superstructure with respect to the graphene. This is better visible in the self-correlation image in Fig. 8.5(d). A profile of the self-correlation image along a dense packed atom row is shown in Fig. 8.5(e). This profile unambiguously shows the existence of two periodicities, one with the graphene lattice constant of 2.46 Å and a small corrugation, and the other with the doubled periodicity and a considerably higher corrugation.

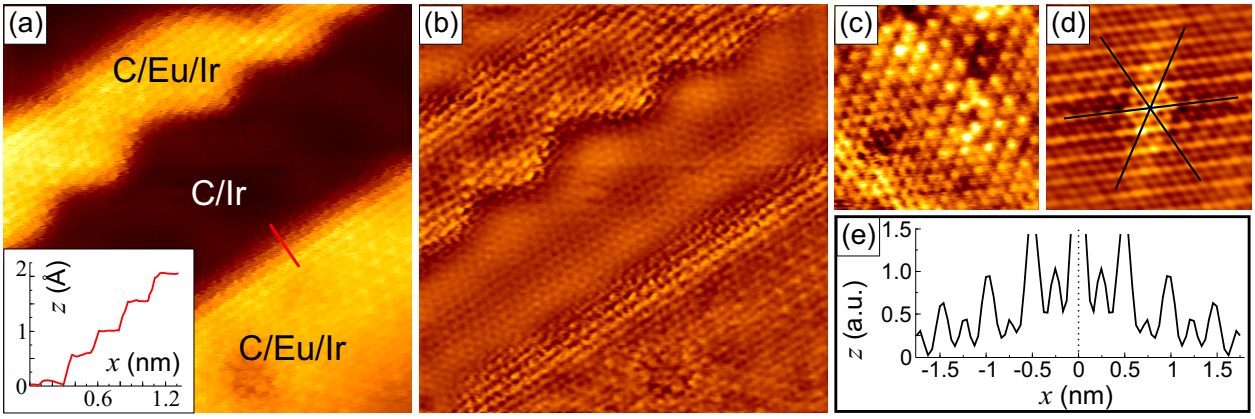

Figure 8.5: **(a-c)** STM topographs of 12% ML Eu deposited at 723 K, imaged at 35 K. **(a)** $U_s = -0.29$ V, $I_t = 0.73$ nA, size 10 nm × 10 nm. Bright areas are islands of intercalated Eu. Inset: Height profile along the red line. **(b)** Same as (a) after image flattening. **(c)** +0.15 V, 1.6 nA, 4.3 nm × 4.3 nm. **(d)** Self-correlation of (c), the line indicates the position of the height profile shown in **(e)**.

The crystallographic structure of the intercalated Eu in dependence of Θ was analysed in more detail by LEED. As turned out, denser Eu structures appeared after exposition of more Eu than was needed to saturate the Eu p(2×2) layer. The evolution of the LEED pattern with increasing Θ is shown in Fig. 8.6 (a-c).

With increasing Θ, first the LEED spots of the intercalated Eu become considerably more pronounced. Figure 8.6(a) shows the pattern for a nearly saturated p(2×2) layer at Θ ≈ 24% ML. For higher Θ the LEED pattern changes. In Fig. 8.6(b), for Θ ≈ 29% ML, the intensity of the p(2×2) spots has decreased while additional spots have emerged, which correspond to a $(\sqrt{3} \times \sqrt{3})$R30° superstructure with respect to Ir(111). Both sets of spots have a nearly equal intensity, indicating a mixed system where islands of both superstructures coexist and allocate a similar total area. For Θ > 33% ML only LEED spots of the $(\sqrt{3} \times \sqrt{3})$R30° superstructure are left [Fig. 8.6(c)], but now with a 10% larger reciprocal length (i.e., with respect to the graphene lattice). This is the densest Eu intercalation structure we have found, which is consistent with the saturation structure for Eu intercalation into graphite (see Sec. 2.4.4).

The Figs. 8.6(d-f) show ball models of the different Eu structures beneath the graphene and the corresponding adsorption energies per Eu atom which were determined by the DFT calculations. Additionally, the saturation coverages (Θ_{sat}) for the structures are given. In all models the graphene honeycomb is represented by black balls and lines and the Eu atoms are coloured differently, depending on the structure. Thereby the same colour code was used as for the indication in the LEED patterns in the Figs. 8.6(a-c): Red for the p(2×2), grey for the $(\sqrt{3} \times \sqrt{3})$R30° with respect to Ir(111), and green for the $(\sqrt{3} \times \sqrt{3})$R30° with respect to the graphene lattice.

The change from the p(2×2) to the $(\sqrt{3} \times \sqrt{3})$R30° structures can be understood by comparing the adsorption energy per Eu atom (E_{ad}) and the atom densities, which are 10% and 1/3 higher for the two $(\sqrt{3} \times \sqrt{3})$R30° structures. As comes out of the DFT calculations, $E_{ad} = -3.8$ eV is lowest for the intercalated p(2×2) structure. But the large energy difference of 2 eV between the

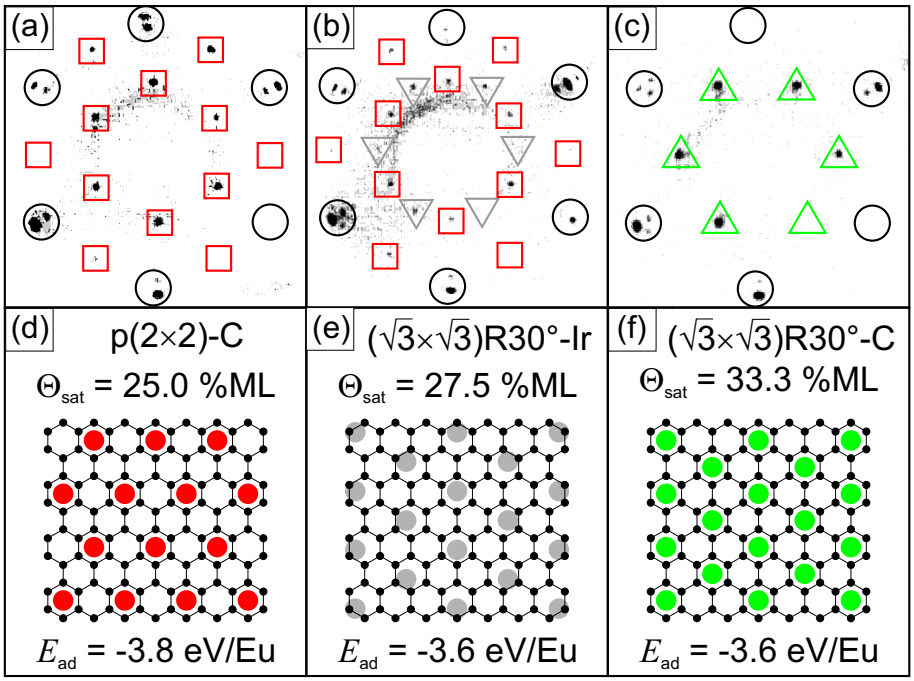

Figure 8.6: **(a-c)** Inverted contrast LEED patterns of Eu intercalated between graphene and Ir(111) at a primary electron energy of 48 eV. Spots belonging to the graphene on Ir(111) system are enclosed by a black circle. **(a)** Eu p(2×2) superstructure with respect to graphene (spots enclosed by red squares); **(b)** Mixed system: simultaneous presence of the p(2×2) superstructure as in (a) and of a $(\sqrt{3} \times \sqrt{3})$R30° superstructure with respect to Ir(111) (spots enclosed by grey, downward pointing triangles); **(c)** Eu $(\sqrt{3} \times \sqrt{3})$R30° superstructure with respect to graphene (spots enclosed by green, upward pointing triangles). **(d)-(f)** Ball models of the different Eu structures. The colours of the Eu atoms correspond to the indication of the LEED spots in the Figs. (a-c). The graphene is represented by the black honeycomb structures.

intercalated $(\sqrt{3} \times \sqrt{3})$R30° structure ($E_{\mathrm{ad}} = -3.6\,\mathrm{eV\,atom^{-1}}$) and the most favourable structure on top, also a $(\sqrt{3} \times \sqrt{3})$R30° ($E_{\mathrm{ad}} = -1.6\,\mathrm{eV\,atom^{-1}}$), leads to intercalation of more Eu than fits into a p(2×2) lattice, thus making a transformation into the denser $(\sqrt{3} \times \sqrt{3})$R30° structures necessary. The intermediate formation of the $(\sqrt{3}\times\sqrt{3})$R30° superstructure with respect to Ir(111) indicates that E_{ad} is lower for this structure compared to the $(\sqrt{3} \times \sqrt{3})$R30° superstructure with respect to graphene. This could not be clarified by the DFT calculations as the Ir lattice was shrinked such that it had the same surface lattice constant as the graphene. This means, that the structures in Fig. 8.6(e) and (f) were equal in the DFT calculations.

It is possible to change the system back to the p(2×2) structure by annealing. For example, annealing at 1120 K for 60 s lead again to a mixed LEED pattern like in Fig. 8.6(b) and further annealing at 1170 K for 60 s to a pure p(2×2) system. As was shown by thermal desorption spectroscopy measurements of K intercalated between graphene and Ir(111) ([179], see Sec. 2.4.4), this loss of Eu may be caused by evaporation which at first requires a deintercalation step and therefore a much higher activation energy than usual. But, also a dissolution into the bulk of the Ir crystal could be a plausible explanation.

8.1.3 Intercalate patterns

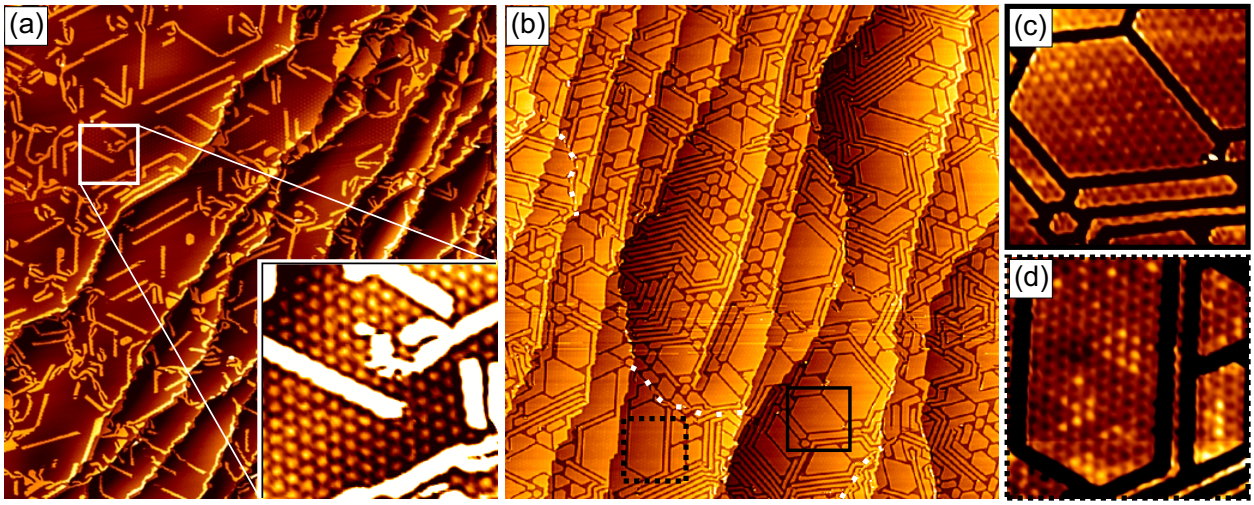

Figure 8.7: **(a)**, **(b)** STM topographs after Eu deposition on graphene/Ir(111) at 720 K, imaged at 300 K. **(a)** $\Theta = 4\%$ ML, image size 320 nm × 320 nm ($U_s = -2.5$ V, $I_t = 30$ pA). Inset: Zoom into the indicated region with enhanced contrast to show the graphene moiré, 38 nm × 38 nm. **(b)** $\Theta = 18\%$ ML, 320 nm × 320 nm (−1.2 V, 98 pA). The white dots indicate positions of grain boundaries in the graphene. The black squares indicate the regions of the zoom-ins. **(c)** Contrast enhanced zoom (40 nm × 40 nm) into the region indicated by the continuous square in (b). **(d)** Contrast enhanced zoom (40 nm × 40 nm) into the region indicated by the dotted square in (b).

Very interesting are the unique patterns of the intercalated Eu, which were already shown in Fig. 8.2. More details can be seen in Fig. 8.7 for different Eu coverages deposited at 720 K.

For $\Theta = 4\%$ ML [Fig. 8.7(a)] the Eu tends to one dimensional growth, thereby decorating the Ir step edges - from both sides. While this is obvious for the upper terrace, it is more difficult to see at the lower terrace because the apparent height of the intercalated Eu is similar to that of an Ir(111) step. On the terraces the Eu stripes mostly grow oriented in three different directions which enclose angles of 60° or 120°. As can be seen in the inset of Fig. 8.7(a), these directions coincide with those of the graphene moiré. And not only the orientation depends on the moiré, but also the width of the stripes: Most of the stripes have the same width and allocate two of the bright moiré rows which usually indicate *ontop* regions (see Sec. 2.4.2). Occasionally, already at $\Theta = 4\%$ ML some smaller islands are present, while the island formation becomes dominant for higher coverages.

Figure 8.7(b) shows the variety of patterns which exist for $\Theta = 18\%$ ML. Although the layer is already quite full and covers $\approx 75\%$ of the Ir, there exist regions where still stripes are preferred. For example, bunches of stripes are preferentially located at ascending local Ir double steps, of which three are present in this topograph. Thus, the one dimensional structures are still favourable under certain conditions.

The white dots in Fig. 8.7(b) indicate positions of grain boundaries in the graphene layer. They can be easily identified by a rotation of the moiré direction between the adjacent regions: While

the rotational misalignment of the $\langle 11\bar{2}0 \rangle_C$-directions is quite small, the misalignment of the moiré patterns is amplified by a factor of 10.7 (see Sec. 2.4.2), leading to considerable differences in the moiré orientations.

Figure 8.7(c) and (d) are contrast-enhanced zooms into regions with different moiré orientations, whereby the moiré in (d) is not oriented along the C lattice. The graphene moiré on Ir(111) is clearly visible above the intercalated Eu islands and its periodicity remains, just the corrugation is reduced. Thus, the moiré is barely perceptible above the intercalated Eu at normal contrast levels. For both orientations in the Figs. 8.7(c) and (d) the Eu step edges are aligned to the moiré. This means that the Eu island step edges in Fig. 8.7(d) are not aligned to the C lattice as its orientation differs considerably from that of the moiré due to the above mentioned angular amplification factor of 10.7. A further peculiarity of the intercalated Eu patterns was found by comparing the lengths between different stripes or islands: While their absolute length cannot be precisely determined due to the convolution with the tip geometry (i.e., STM exaggerates lateral dimensions dependent on the tip sharpness), the length differences between stripes or islands along the moiré direction can be measured accurately. They are not arbitrary but are multiples of the unit length of the graphene moiré on Ir(111), which is 25.3 Å. Thus, not only the orientation of the Eu structures depends on the moiré, but also their widths and lengths.

Another feature of the Eu structures are the undulated step edges. While there exist also some straight step edges, most of them are undulated with the moiré periodicity. This can be seen in Fig. 8.7(d) where the moiré contrast on the Eu structures is very high, and is also partially visible in Fig. 8.7(c) and in the inset of Fig. 8.7(a). Choosing an appropriate contrast as in Fig. 8.8(a), the undulation of the stripes can be seen even better. Obviously, it is in phase for the long edges.

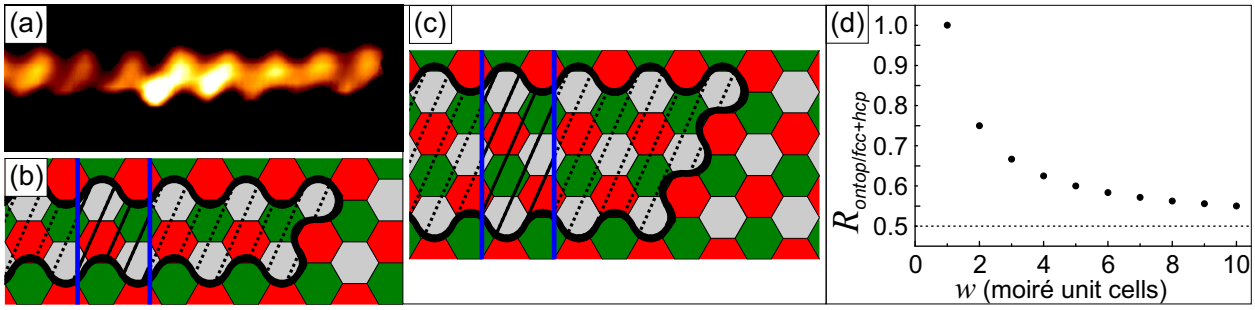

Figure 8.8: **(a)** Contrast enhanced zoom into Fig. 8.7(a) showing a stripe of intercalated Eu. **(b)** Top view model of an intercalated Eu stripe. The system graphene on Ir(111) is represented by hexagons which are differently coloured depending on the position within the moiré cell (*fcc* green, *hcp* red, and *ontop* grey). The hatching indicates the area where the Eu is intercalated and the thick black lines represent its undulated borders. The space in between the blue lines (continuous hatching) corresponds to one unit length of the stripe. **(c)** Model similar to (b), but for a stripe with a width of two moiré cells. **(d)** Plot of the ratio $R_{ontop/fcc+hcp}$ in dependence of the stripe width w. The dotted line indicates the convergence value of $R_{ontop/fcc+hcp} = 1/2$ for $w \to \infty$.

The complexity of the Eu intercalate patterns and the discrete distribution of their lengths and widths, which change in multiples of the moiré unit cell (25.3 Å), can only be understood by

taking the peculiarities of the system graphene/Ir(111) into account. The most important one is the inhomogeneous binding between C and Ir within one moiré unit cell [172; 256], which was already described in Sec. 2.4.2. As already mentioned in Sec. 8.1.2, the patterns are equilibrium structures. Thus, it is suitable to consider an energetic model.

An ansatz to achieve a qualitative understanding is the extended area model of Fig. 2.9(c). For simplicity, the loss of binding energy between C and Ir upon Eu intercalation can be assumed as ≈ 0 within the *ontop* regions. For *fcc* regions the loss of binding energy per region is finite and about the same as for *hcp* regions. Taking only this moiré model into account, the intercalated Eu would only be located at *ontop* regions for low coverages like the 4% ML in Fig. 8.7(a). This case is not realised due to other energy contributions which will be discussed later on. Let us consider now that these additional contributions just lead to the requirement that a distinct patch of intercalated Eu must have an area of one moiré cell or more. Then the loss of binding energy between C and Ir is minimised by building continuous structures which maximise the ratio $R_{ontop/fcc+hcp} = N_{ontop}/(N_{fcc} + N_{hcp})$, with N being the numbers of the corresponding regions where Eu is located.

Figure 8.8(b) shows a model of a structure which maximises $R_{ontop/fcc+hcp}$. The Eu is located in the hatched area between the black lines. The latter are undulated to fully make use of the *ontop* areas while simultaneously minimising the *fcc* and *hcp* area allocated by the Eu. This intercalate structure resembles the shape of the the stripe in Fig. 8.8(a) (i.e., has undulated borders which are in phase) and also allocates two rows of *ontop* regions as do the real structures. Per unit length of the stripe (indicated by the continuous hatching) two *ontop* and one *fcc* plus one *hcp* region are allocated, resulting in $R_{ontop/fcc+hcp} = 1$.

Increasing the width of this optimum stripe would just increase the allocated area of *fcc* and *hcp* regions until the next *ontop* regions are reached. In this case the stripe width increases by one moiré cell, but now with the undulation of the long edges being in an antiphase condition. The corresponding stripe is shown in Fig. 8.8(c). Increasing the stripe width w by one moiré cell adds one *ontop*, one *fcc*, and one *hcp* region per unit length, resulting in $R_{ontop/fcc+hcp} = 3/4$. This sequence continues by increasing N_{ontop} by one and $N_{fcc} + N_{hcp}$ by two for increasing the width by one moiré cell and finally converges to $R_{ontop/fcc+hcp} = 1/2$ for an infinite area. In Fig. 8.8(d) $R_{ontop/fcc+hcp}$ is plotted for stripes width from $w = 1$ to $w = 10$. The considerable decrease from $R_{ontop/fcc+hcp} = 1$ for $w = 1$ to $R_{ontop/fcc+hcp} = 3/4$ already for $w = 2$ is the strongest in the sequence and explains why most of the stripes in Fig. 8.7(a) have a width of $w = 1$.

The model presented above explains several peculiarities of the intercalate patterns like the undulated edges and the discrete size changes in moiré unit cells, but fails to give a complete explanation of the pattern formation. It is obvious that larger Eu islands must built with increasing exposure, at the latest, when the maximum possible stripe density is exceeded. The realised Eu distribution in Fig. 8.7(b) shows large local differences in the structure sizes. Despite the high coverage still regions with stripe structures are present. They are preferentially located around ascending local Ir double steps which are expected to create elastic stress in the graphene. This indicates the importance of graphene's elastic energy for the pattern formation. Additional energetic contributions come from the step edge free energies of Eu and graphene. The relevance of the different contributions will be discussed in the following.

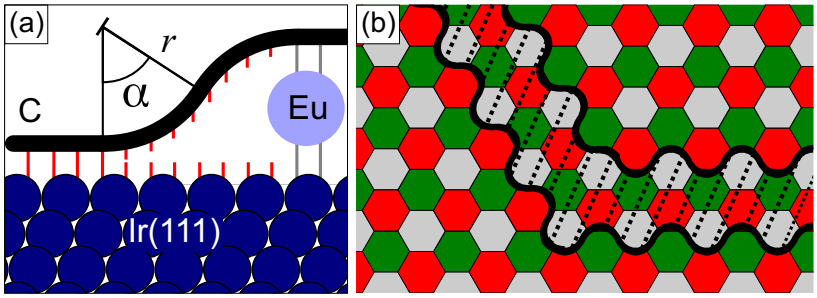

Figure 8.9: **(a)** Side view sketch of a graphene layer (represented by the thick black line) which is bent at the edge of an intercalated Eu structure. The curvature at the bending is approximated by two arcs of a circle with radius r and opening angle α. The red lines symbolise the binding between graphene and Ir which is reduced at the bending. **(b)** Top view sketch [similar to Figs. 8.8(b) and (c)] of a Eu stripe with a kink of 120°.

- **Pre-existing compressive strain**

  Due to the large difference in the thermal expansion coefficients of graphene and Ir(111), which is on average $7.15 \times 10^{-6}\,\mathrm{K}$ [163], the graphene is compressively strained upon cooling down from the growth temperature of 1100 K. This should lead to a compression of the graphene lattice of 0.64% at 300 K, but the corresponding elastic energy is partially relieved by the formation of wrinkles. Still, an average compressive strain of 0.2% remains [163] (roughly $0.3 \times 0.64\%$ for the 1D continuum model in Fig. 5 of this reference). This strain, which is part of the system graphene on Ir(111), can be partially relieved by the presence of the intercalated Eu. For every step at a Eu structure the graphene has to bend over the edge which enables an increase in length of the graphene layer. This is shown in Fig. 8.9(a), where the bending is approximated as two arcs of a circle with radius r and opening angle α, similar to reference [163]. The required extra length of graphene Δ is then $\Delta = 2r\alpha - 2r\sin(\alpha)$ per bending.

  This length change causes a shift of the moiré pattern, i.e. the distances between the moiré rows is reduced if a bending is in between. This was confirmed by comparative measurements of moiré row distances on larger intercalate islands and between stripes. Thereby, the moiré row repeat distance along the $\langle 1\bar{1}00\rangle$-directions is shortened by (2.8±0.2) Å per bending. The shift of the graphene lattice is then given after division by the moiré amplification factor of 10.3 and is therefore (0.27±0.02) Å per bending. This is 0.43 Å less than the the 0.7 Å which were found for Ir steps [161].

  The graphene lengthening of 0.27 Å per Eu step edge would require a stripe density (ρ_{stripe}) of $1/27\,\mathrm{nm}^{-1}$ (2 steps per stripe) to compensate a residual compressive strain of 0.2% in graphene. As the wrinkle formation is reversible when the strain is released [163] it could be possible that the full strain of 0.64% determines ρ_{stripe}[1]. This would lead to an optimum

[1]Though still wrinkles were found after Eu intercalation their number was smaller than without intercalated Eu.

ρ_{stripe} of $1/8.5\,\text{nm}^{-1}$. The maximum achievable ρ_{stripe} is one stripe per distance of two moiré rows[1] (i.e., $1/4.4\,\text{nm}^{-1}$). This is about twice the stripe density which is required to release the full pre-existing strain of 0.64%. That $\rho_{\text{stripe}} = 1/4.4\,\text{nm}^{-1}$ is indeed realised at certain locations requires that the graphene is partially under tensile strain. This is only understandable by additional important contributions which tend to increase ρ_{stripe}. These are the binding energy differences within the moiré unit cell which are already responsible for the stripe formation. The local differences in ρ_{stripe} indicate local differences in the pre-existing graphene compression which in some cases seem to be related to structural features of the substrate [e.g., at the ascending double steps in Fig. 8.7(b)].

- **Graphene deformation at Eu kinks**
  The model presented in Fig. 8.8(b) explains the width of the Eu stripes but not their straight growth. As can be seen in Fig. 8.9(b), $R_{ontop/fcc+hcp} = 1$ if the stripe has a kink of 120°. Even a zigzag course would be compatible with this model. Thus, it is assumed that elastic energy which is created by the deformation of the graphene at such kinks is responsible for the straight Eu edges.

- **Graphene bending at Eu edges**
  The bending of the graphene as shown in Fig. 8.9(a) contributes also to its elastic energy. This contribution makes a decrease of the step density favourable.

- **C-Ir binding energy**
  This contribution has two parts. One is the gain of binding energy between C and Ir due to the model in Fig. 8.8(b) while the other is the loss of binding energy in the region of the bending as illustrated in Fig. 8.9(a) by the broken bonds (red lines). The magnitude of the latter part depends on the length $2r\sin(\alpha)$ of the bending region.

- **Eu step free energy**
  The formation of the stripe patterns creates a very long total length of Eu step edges and thus a considerable step free energy. This contribution makes a decrease of the step density favourable.

- **Long range electronic interaction**
  As will be shown in Sec. 8.1.4, the Eu n-dopes the graphene, thereby becoming positively charged. For a similar situation, in the system Eu on graphene a long range repulsive interaction between the Eu exists (see Sec. 8.2). For example, this leads after deposition of 3.3% ML Eu at 300 K to clusters with an average size of 14 atoms and an average separation distance of approximately two moiré unit cells. This distance is similar to the closest possible between two intercalate stripes. Thus, such a long range interaction could also contribute to the pattern formation.

[1] The distance between the moiré rows in $\langle 1\bar{1}00\rangle$-direction is $2.53\,\text{nm}\cdot\cos(30°) = 2.19\,\text{nm}$.

8.1.4 Graphene doping

In order to determine the influence of the intercalated Eu on the graphene's band structure, ARPES measurements were performed for the p(2×2) Eu structure and for the $(\sqrt{3}\times\sqrt{3})$R30° Eu structure with respect to graphene. Fig. 8.10 shows the results of the corresponding scans approximately along the Γ-K-M-direction. Due to mechanical difficulties in the angular adjustment, the azimuthal angle deviated by $\Delta\varphi = 1.5°\pm0.5°$ from the Γ-K-M-direction for the scan of the intercalated p(2×2) Eu [Fig. 8.10(a)]. Thus, only a conic section of the Dirac cone is imaged, leading to the impression of an apparent band gap. For the scan of the $(\sqrt{3}\times\sqrt{3})$R30° Eu structure [Fig. 8.10(b)] it was possible to reduce the deviation to $\Delta\varphi = 1.0°\pm0.5°$.

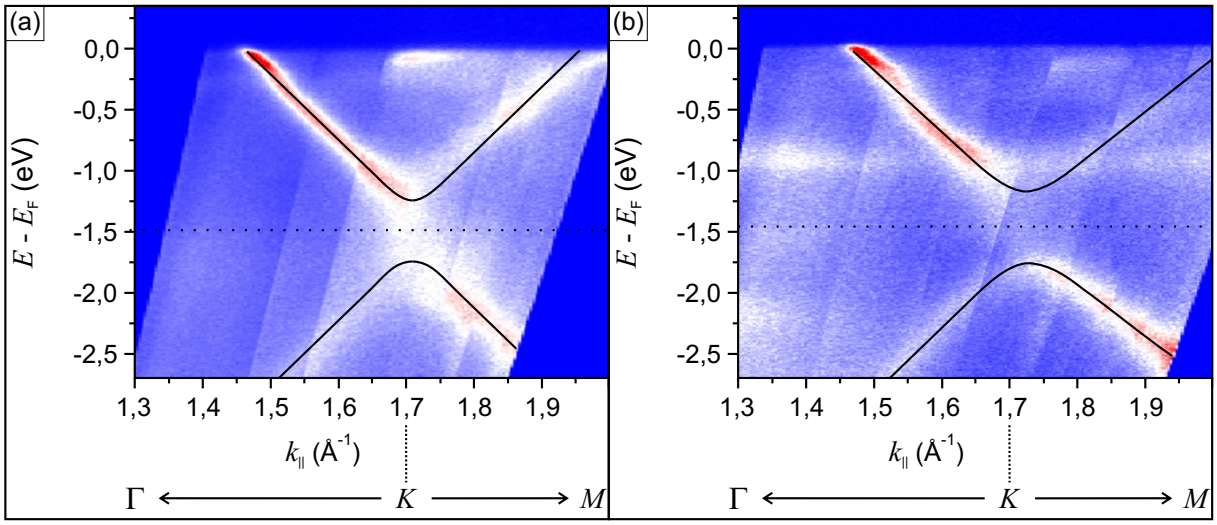

Figure 8.10: ARPES spectra of graphene/Ir(111) with intercalated Eu, showing primarily a section of the Dirac cone. The azimuth angle φ differs by $\Delta\varphi$ from the Γ-K-M-direction, leading to apparent band gaps. The approximate positions of the conic sections are given by the black lines. The dotted black lines indicate the positions E_D of the virtual Dirac points. **(a)** Full layer of Eu with p(2×2) structure. $\Delta\varphi = 1.5°$. **(b)** Full layer of Eu with $(\sqrt{3}\times\sqrt{3})$R30° structure. $\Delta\varphi = 1°$.

The main feature in the ARPES data is the Dirac cone, whereby an anisotropic intensity of the cone branches is noticeable. This anisotropy is a manifestation of electronic chirality which has its origin in the two inequivalent lattice sites in the graphene unit cell [257]. Because the cones are not fully visible due to the anisotropic intensity, black lines were added to all ARPES figures to emphasise the positions of the conic sections.

In both cases, for the p(2×2) and for the $(\sqrt{3}\times\sqrt{3})$R30° Eu structure, the virtual Dirac point[1] is positioned at $E_D \approx -1.5\,\text{eV}$. Thus, the Eu induces a considerable n-doping of the graphene while it preserves the Dirac cone to a far extend. The apparent band gaps are $\sim 0.5\,\text{eV}$ for the p(2×2) and $\sim 0.6\,\text{eV}$ for the $(\sqrt{3}\times\sqrt{3})$R30° structure. To account for the azimuth offset, the absolute value of E_{gap} was determined after fitting the measured dispersion to the tight-binding approximation bands of graphene. For the p(2×2) structure, the gap part from the azimuth mismatch is 0.5 eV

[1]Although there is an apparent band gap and the Dirac is not imaged, it is convenient to express the doping by a virtual Dirac point in the middle of the apparent gap.

(i.e., the same as the apparent band gap), thus the real gap is $E_{\mathrm{gap}} \approx 0$. For the $(\sqrt{3} \times \sqrt{3})$R30° structure, the gap part from the azimuth mismatch is 0.35 eV, thus the apparent gap includes a real gap of $E_{\mathrm{gap}} \approx 0.25$ eV. The opening of band gaps in graphene in coincidence with doping was already observed for other dopants (e.g., for K adsorbed on graphene/SiC [154]).

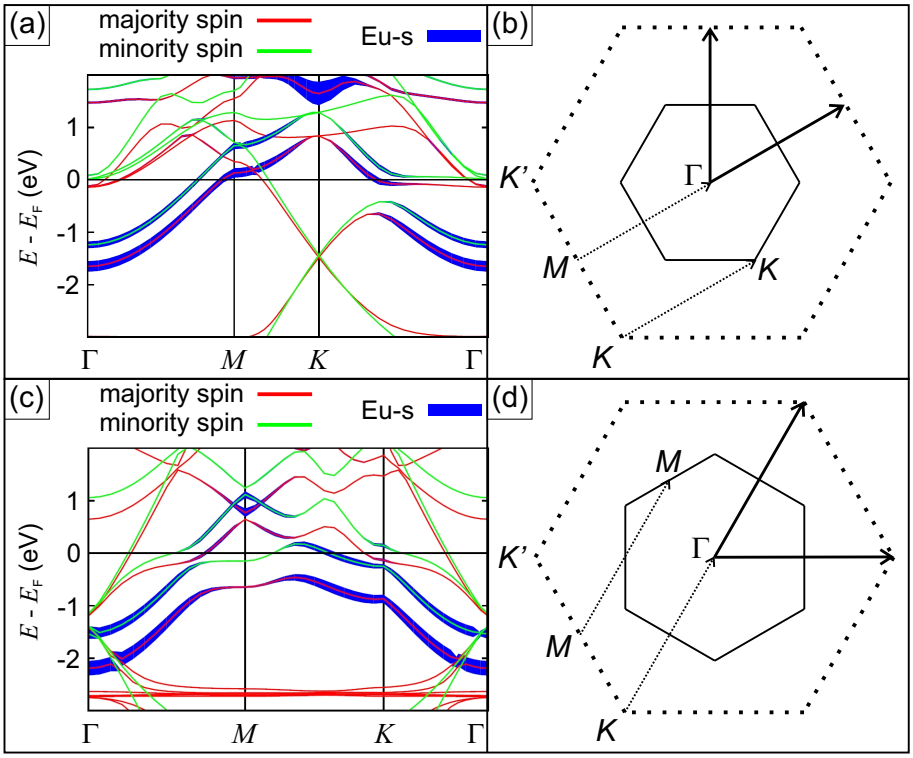

Figure 8.11: **(a)** Spin resolved band structure (calculated by DFT) of the p(2×2) Eu phase on free-standing graphene reduced to the superstructure Brillouin zone (BZ). The different polarisations are coloured in red and green, respectively. Contributions from Eu-*s* states are marked as blue fatbands. **(b)** BZs of graphene (dotted edges) and of the p(2×2) Eu superstructure (continuous edges). The unit vectors of the reciprocal superstructure lattice are indicated. The M and K points of the original graphene BZ are folded to the Γ and K points of the superstructure BZ, respectively. **(c)** Spin resolved band structure (calculated by DFT) of the $(\sqrt{3} \times \sqrt{3})$R30° Eu phase on free-standing graphene reduced to the superstructure BZ. The different polarisations are coloured in red and green, respectively. Contributions from Eu-*s* states are marked as blue fatbands. **(d)** BZs of graphene (dotted edges) and of the $(\sqrt{3} \times \sqrt{3})$R30° Eu superstructure (continuous edges). The unit vectors of the reciprocal superstructure lattice are indicated. The M and K points of the original graphene BZ are folded to the M and Γ points of the superstructure BZ, respectively.

Figure 8.11(a) shows the spin resolved band structure of the p(2×2) Eu phase on free-standing graphene as calculated by DFT. As demonstrated in Fig. 8.11(b) the Dirac cone remains at the K point of the superstructure BZ. Consistent with the ARPES measurements E_{D} is shifted to ~ -1.5 eV and the Dirac cone is left intact (i.e., no band gap opens). The calculations show also a spin splitting of ~ 50 meV at E_{D} which cannot be seen in the ARPES data due to a lack of resolution.

Figure 8.11(c) shows the spin resolved DFT band structure of the $(\sqrt{3} \times \sqrt{3})$R30° Eu phase on

free-standing graphene. As demonstrated in Fig. 8.11(d) the Dirac cone is folded to the Γ point of the superstructure BZ. The Dirac cone is modified and a band gap of $E_{\mathrm{gap}} \approx 0.25\,\mathrm{eV}$ has opened, consistent with the ARPES results. The cone shift is slightly reduced with $E_{\mathrm{D}} \approx -1.3\,\mathrm{eV}$, which is slightly less than found by the ARPES measurements.

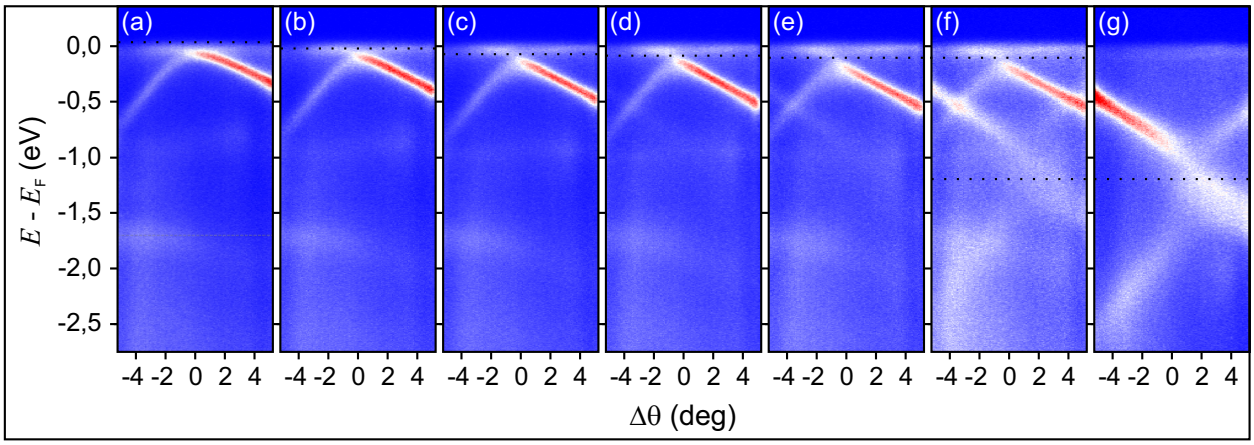

Figure 8.12: ARPES spectra around the K point of graphene on Ir(111) after deposition of different amounts of Cs at 300 K. The dotted black lines indicate the positions E_{D} of the (virtual) Dirac points. **(a)** 240 s deposition at 6.0 A dispenser current. **(b)** Additional 240 s deposition at 6.5 A. **(c)** Additional 240 s at 6.5 A. **(d)** Additional 420 s at 6.5 A. **(e)** Additional 420 s at 6.5 A. **(f)** Additional 1020 s at 6.5 A. **(g)** Additional 720 s deposition at 7.0 A.

Very interesting results with respect to the electron distribution in graphene in the vicinity of dopants were found by Cs adsorption experiments at 300 K. Figure 8.12 shows the surrounding of the Dirac cone of graphene on Ir(111) in a sequence with increasing amounts of deposited Cs. The approximate position of E_{D} is indicated by the dotted lines. Due to the uncalibrated Cs dispenser only evaporation time and dispenser current are given for each ARPES plot. The Figs. 8.12(a) through (d) clearly show a gradual shift of E_{D} with increasing Cs adsorption and in Fig. 8.12(d) already the onset of a second Dirac cone is recognisable. While the intensity of this second cone increases with further Cs deposition as can be seen in the Figs. 8.12(e) and (f), the intensity of the original cone slowly diminishes and its shifting ceases to increase. After a further considerable increase in deposited Cs only the second cone remains [Fig. 8.12(g)].

The existence of two distinct Dirac cones as shown in the Figs. 8.12(d) through (f) requires the coexistence of two different Cs phases. This was confirmed by STM measurements of this system which show a phase mixture of adatoms with (local) hexagonal arrangement and dense islands of intercalated Cs in a p(2×2) structure [258]. Upon further Cs adsorption a full layer of intercalated p(2×2) Cs builds and finally a denser $(\sqrt{3}\times\sqrt{3})$R30° Cs layer [258], similar to the Eu intercalation. These Cs phases correspond to those found for Cs adsorption on graphite at 80 K [259]. There, domains of hexagonal Cs arrays with no orientational ordering with respect to the substrate were found for low coverages. Upon further deposition denser phases of Cs on graphite form, which include the p(2×2) and the $(\sqrt{3}\times\sqrt{3})$R30°, whereby intercalation is probably inhibited by the low adsorption temperature. Apparently, the Cs atoms overcome the intercalation barrier of graphene

on Ir(111) at 300 K after the adatom phase has reached a certain density.

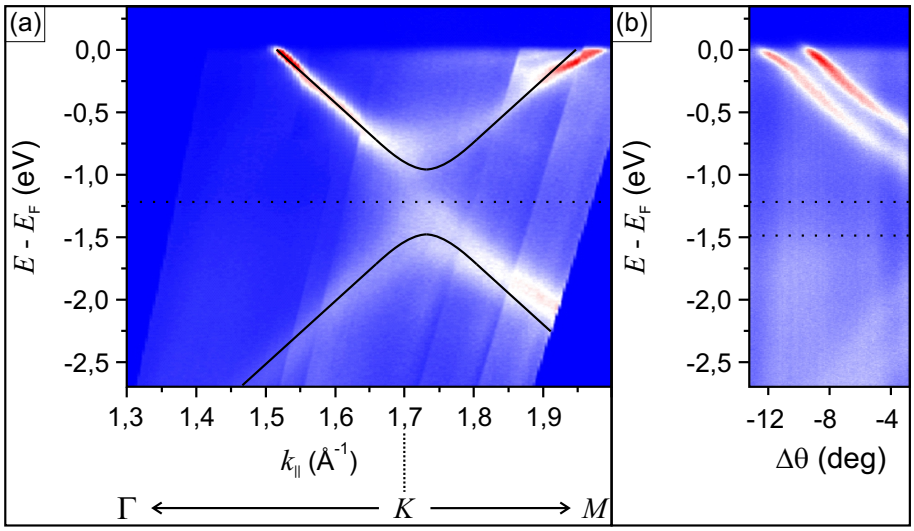

Figure 8.13: **(a)** ARPES spectrum of graphene on Ir(111) with a full layer of intercalated Cs in the p(2×2) structure. The azimuth angle φ differs slightly from the Γ-K-M-direction, leading to an apparent band gap. The whole intensity belongs to a section of the Dirac cone, the approximate position of which is given by the black lines. The dotted black line indicates the position E_D of the virtual Dirac point. **(b)** ARPES spectrum approximately between 1.45 Å^{-1} and 1.65 Å^{-1} of the film shown in (a) after additional deposition of 12% ML Eu at 473 K an annealing to 723 K for 60 s. The branches of two distinct Dirac cones of nearly equal intensity can be seen. The dotted black lines indicate the positions E_D of the virtual Dirac points.

Figure 8.13(a) shows the Dirac cone of graphene/Ir(111) with Cs intercalated in the p(2×2) structure [a part of this cone is already displayed in Fig. 8.12(g)]. The virtual Dirac point is positioned at $E_\mathrm{D} \approx -1.2$ eV and the apparent band gap is ~ 0.5 eV. Additional deposition of 12% ML Eu [i.e. half of the saturation coverage of the p(2×2) phase] at 473 K onto this sample and subsequent annealing to 723 K for 60 s again lead to the existence of two Dirac cones, the intense upper branches of which can be seen in Fig. 8.13(b). These two cones have nearly equal intensity and their virtual Dirac points are at $E_\mathrm{D} \approx -1.2$ eV and $E_\mathrm{D} \approx -1.5$ eV. The latter value belongs to intercalated Eu as shown in Fig. 8.10, thus the Eu has squeezed out the intercalated Cs [1]. The corresponding LEED pattern shows, additionally to the spots of graphene/Ir(111), only spots of a p(2×2) superstructure. Hence, probably both Cs and Eu coexist as intercalated islands in the p(2×2) structure.

The existence of the two distinct Dirac cones indicates that the electrons with which the graphene is doped by the intercalated metals are confined to the vicinity of the different dopants. If there would be a larger area required for the equilibration of the doping levels one would expect more intensity between the branches of the two different cones in Fig. 8.13(b). On the other hand the electrons must distribute to a certain extend as otherwise the shifting of the Dirac cone in the

[1] For Eu on top of graphene, the Dirac cone was not visible in the ARPES data. Thus, the presence of this cone proofs indeed the intercalation of the Eu and its high intensity indicates that most of the 12% ML Eu is intercalated.

Figs. 8.12(a) through (d) cannot be explained. To estimate this extend, consider an amount of 0.5% ML Cs deposited, which is a reasonable guess for the case of Fig. 8.12(a). In a hexagonal arrangement of Cs atoms this would lead to an adatom distance of $\approx 3.5\,\mathrm{nm}$. Thus, the electrons must distribute in an area around the adatoms with a radius of at least half of that value (i.e. $\sim 2\,\mathrm{nm}$) to achieve a homogeneous doping level as observed in Fig. 8.12(a).

8.2 Eu on Graphene

Due to the (almost complete) absence of intercalation for $35\,\mathrm{K} \leq T_{\mathrm{growth}} \leq 400\,\mathrm{K}$, the results of the experiments in this temperature range differ completely from those presented in Sec. 8.1 for $T_{\mathrm{growth}} = 723\,\mathrm{K}$. Hence, Eu adsorption at room temperature and below is analysed in this separate section.

For Eu growth at room temperature or annealing of Eu films from low to room temperature closed TPG+CVD films (see Sec. 4.1.4) were necessary, otherwise intercalation of Eu underneath graphene takes place. TPG+CVD films were used for the experiments represented by Figs. 8.14(d) and (g), Fig. 8.16, Fig. 8.17 and Fig. 8.18. For Eu growth at low temperature TPG graphene was used. The flakes provided sufficiently large areas for structure formation and allowed us at the same time the observation of Eu on Ir(111). This was helpful for precise coverage calibration, as for small coverages Eu forms on Ir(111) only phases of separated, single adatoms (see App. A). Thereby, for the experiments shown in Figs. 8.14(c), (e), (f) and (h) the deposited amount of Eu was precisely evaluated by counting adatoms on STM topographs of Ir terraces adjacent to graphene flakes.

8.2.1 Eu adsorption at 35 K

To ease the presentation and discussion of the low temperature Eu adsorption experiments, some properties of graphene on Ir(111) (see Sec. 2.4.2) are shortly repeated. Fig. 8.14(a) displays a graphene flake on Ir(111) as obtained by the TPG method. The graphene is well oriented with respect to the substrate such that the $\langle 1\bar{1}0\rangle$-directions of Ir(111) and the $\langle 10\bar{1}0\rangle$-directions of graphene coincide with an angular scatter of $(0.00 \pm 0.25)^\circ$. The periodicity visible is the moiré resulting from the mismatch of the 2.461 Å of the graphene unit cell and the 2.715 Å of the Ir(111) surface unit cell, giving rise to an incommensurate 10.3×10.3 superstructure with respect to the graphene lattice [9.3×9.3 with respect to Ir(111)] and a pitch of 25.3 Å. The relation of the moiré to the graphene lattice is visualised by the inset of Fig. 8.14(a). In a recent calculation using the van der Waals density functional (vdW-DF) the height modulation resulting from the moiré was estimated to be 35 pm [165]. The graphene is physisorbed, but with a slight chemical modulation of binding to the substrate. Fig. 8.14(b) displays the corresponding LEED pattern, where the first order Ir and graphene spots are surrounded by moiré reflections.

The sequence of STM topographs in Figs. 8.14(c) - (h) visualises the evolution of the surface morphology with deposited amount Θ of Eu. In Fig. 8.14(c) a graphene flake extends through the central part of the image from top to bottom. Its borders are indicated by white lines. After a dose of $\Theta = 0.8\%$ ML Eu, dots with a rather non-uniform distribution are visible. We recalculate the Eu dot number density ρ to their separation in an ideal hexagonal arrangement as $d = (\rho \cos 30^\circ)^{-1/2}$

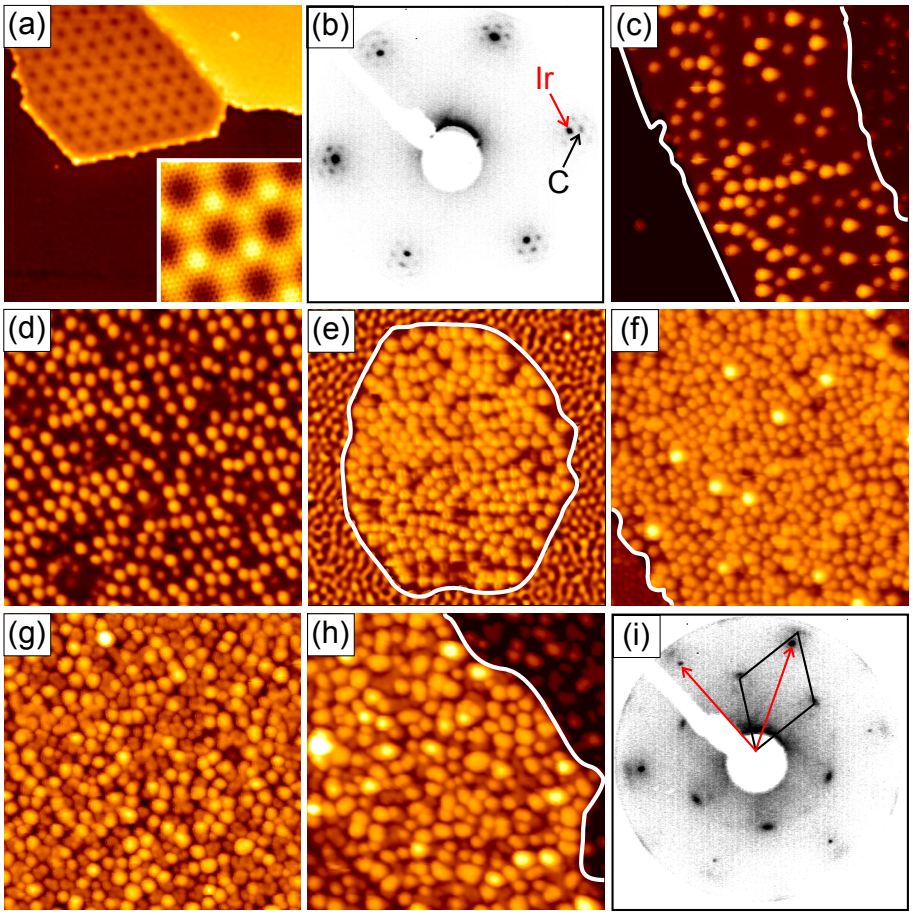

Figure 8.14: **(a)** STM topograph of a graphene flake grown on Ir(111) by temperature programmed growth. The moiré corrugation is visible in the flake. The inset (4.1 nm×4.1 nm) displays the moiré together with the atomically resolved graphene lattice. **(b)** Inverted contrast LEED pattern of Ir(111) partially covered with TPG graphene flakes at a primary electron energy of 78 eV. Red and black arrows highlight first order Ir and graphene reflections, respectively. **(c)** - **(h)** STM topographs after Eu adsorption at 35 K. White lines indicate boundaries of graphene flakes. **(c)** 0.8% ML Eu ($U_s = -1.8$ V, $I_t = 14$ pA). **(d)** 1.8% ML Eu (−0.67 V, 11 pA). **(e)** 3.3% ML Eu (−1.8 V, 50 pA). **(f)** 5% ML Eu (−2.1 V, 25 pA). **(g)** 15% ML Eu (−1.5 V, 86 pA). **(h)** 25% ML Eu (−0.65 V, 93 pA). **(i)** Inverted contrast LEED pattern of the 25% ML experiment at a primary electron energy of 78 eV. Black lines indicate unit cell of the $(\sqrt{3} \times \sqrt{3})$R30°-superstructure with respect to the graphene lattice. Red arrows indicate the primitive translations of the Ir(111) surface unit cell. The STM topograph size is always 40 nm × 40 nm.

in order to specify their average spacing. In the topograph of Fig. 8.14(c) we find $d = 13.8$ graphene unit cell repeat distances $a_C = 2.461$ Å. The dots display two distinct brightnesses with apparent heights of 3 Å and 5 Å, respectively. As about 60% of the dots are the brighter ones and as the average atom number s_{av} in each dot is 1.6 atoms we infer that the brighter dots correspond to Eu dimers and the lower ones to single adatoms.

After deposition of $\Theta = 1.8$% ML Eu in Fig. 8.14(d), the density of dots ρ has roughly doubled and the dot separations are almost uniform with some local hexagonal order. Comparison to

Fig. 8.14(a) shows that the Eu adsorbates have locked in orientation to the graphene moiré. Indeed, we measure $d = 9.8\,a_C$, which is very close to the moiré repeat distance of $10.3\,a_C$. Compared to Fig. 8.14(a) the average dot size increased only slightly to $s_{av} = 1.75$ atoms. This again corresponds to the proportions of brighter and darker dots assuming them to consist of dimers and monomers, respectively.

For $\Theta = 3.3\%$ ML in Fig. 8.14(e), the dot density has increased by about 65% compared to Fig. 8.14(d), corresponding to a decrease in d to $7.7\,a_C$. While the dots still display short range order, the apparent hexagonal order of Fig. 8.14(d) is lost. In contrast to the significant decrease in d, s_{av} increased only slightly to $s_{av} = 1.9$ atoms. Based on the average dot size and the proportions of brighter and darker dots we again identify them as dimers and single adatoms, respectively.

After deposition of $\Theta = 5\%$ ML Eu in Fig. 8.14(f), the dot density and d remained almost constant compared to Fig. 8.14(e) with $d = 7.3\,a_C$. In contrast, s_{av} increased significantly to $s_{av} = 2.6$ atoms. Apparently, when a critical dot separation of $d \approx 7.5\,a_C$ is approached, new dimers are no more formed. The atoms deposited additionally are integrated into existing clusters. This leads to a size increase, i.e. an increase in s_{av}. Adatoms are absent in Fig. 8.14(f), most clusters are still dimers and probably also some trimers are present, displaying the same brightness as dimers. A few dots in Fig. 8.14(f) display a new height level of 8 Å. It is plausible that this level corresponds to the smallest possible two-layer clusters, a tetrahedral arrangement of Eu atoms in a tetramer.

Increasing the deposited amount to $\Theta = 15\%$ ML leaves the dot density and d almost unchanged at $d = 7.9\,a_C$, whereas the average cluster size increases to $s_{av} = 9.3$ atoms as shown in Fig. 8.14(g). Two height levels can clearly be distinguished in Fig. 8.14(g) which are of 5 Å and 8 Å height.

For $\Theta = 25\%$ ML in Fig. 8.14(h), the cluster density has again decreased slightly through coalescence of the clusters, while they grew strongly in size compared to Fig. 8.14(g). The clusters positioning is again influenced by the moiré periodicity signified by their hexagonal arrangement and $d = 9.8\,a_C$. However, their size distribution is less uniform than in Fig. 8.14(d). Their average size is $s_{av} = 24$ atoms. The atoms are arranged in a $(\sqrt{3} \times \sqrt{3})$R30° structure with respect to the graphene lattice, as visible in the LEED pattern shown in Fig. 8.14(i).

Fig. 8.15 summarises the evolution of d and s_{av} with Θ. It is apparent that when the minimum cluster separation of $d \approx 7.5\,a_C$ is approached, cluster formation ceases and the clusters start to grow in size. When reaching the minimum separation d with increasing Θ, the dimer appears to be the preferred, "magic" cluster size, to which aggregation of additional atoms appears to be unfavourable. Noteworthy, for the same coverages on Ir(111) Eu monomers form as preferred entities. Eu monomers on Ir(111) are for instance visible in the surrounding of the graphene flake in Fig. 8.14(e).

For the $\theta = 1.8\%$ ML, $\theta = 3.3\%$ ML and $\theta = 5\%$ ML also the most probable cluster separation d_{prop} as obtained from the image self-correlation is indicated in Fig. 8.15. The values of d and d_{prop} agree rather well. From this agreement and with the minimal d and d_{prop} being considerably smaller then the moiré pitch we conclude that the latter is not essential for the minimal cluster separation. However, when d comes close to the moiré pitch the orientation order is enhanced and turned hexagonal. The observed behaviour would be consistent with a short range attractive

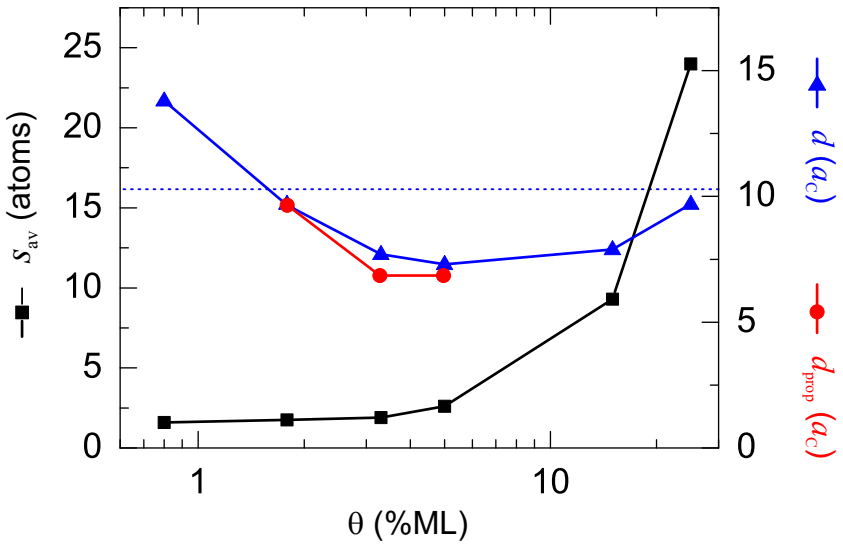

Figure 8.15: Average cluster size s_{av} in atoms (black squares), average cluster separation d (blue triangles), and most probable cluster separation d_{prop} (red dots) versus deposited amount θ. Both distances are given in graphene unit lengths $a_C = 2.461$ Å. The dashed line marks the moiré repeat distance. Lines to guide the eye.

interaction of Eu monomers with clusters, resulting in the observed cluster growth with coverage. Moreover, the apparent initial inhibition of cluster growth beyond the dimer size and the observed short range order indicate the presence and relevance of a repulsive interaction between adatoms and dimers. While the separation of the Eu atoms in the clusters can not be determined directly, the observation of the $(\sqrt{3} \times \sqrt{3})$R30° structure in the larger clusters of Fig. 8.14(h) makes it plausible that Eu atoms in clusters, beginning with the dimer size, possess a characteristic distance close to the one of this structure.

A remark on the height evolution of the cluster is in place here. According to our measurements the first layer of Eu on graphene has an apparent height of 5 Åand the second layer an apparent height of 3 Å, giving rise to 8 Å high two layer clusters. Due to the rapid decay of the peaked local density of states of adatoms, their apparent height is considerably lower, similar to what is known for adatoms on metal surfaces. This explains the 3 Å apparent height of adatoms on graphene [compare Fig. 8.14(f)].

8.2.2 Room temperature Eu adsorption

Fig. 8.16 displays the evolution of the surface morphology with increasing Θ if deposited at 300 K on TPG+CVD graphene. Similar to $\Theta = 3.3\%$ ML Eu deposited at 35 K, after deposition of the same amount at 300 K the sample is covered with small dispersed clusters as shown in Fig. 8.16(a). Distinct to the low temperature situation, the clusters are larger with $s_{av} = 14.4$ atoms instead of $s_{av} = 1.9$ atoms. Correspondingly, the average cluster separation increased from $d = 7.7\,a_C$ to $d = 21\,a_C$. Based on the self-correlation of the topograph shown as inset in the lower right of Fig. 8.16(a), we conclude on a local hexagonal order, despite the apparent inhomogeneities in

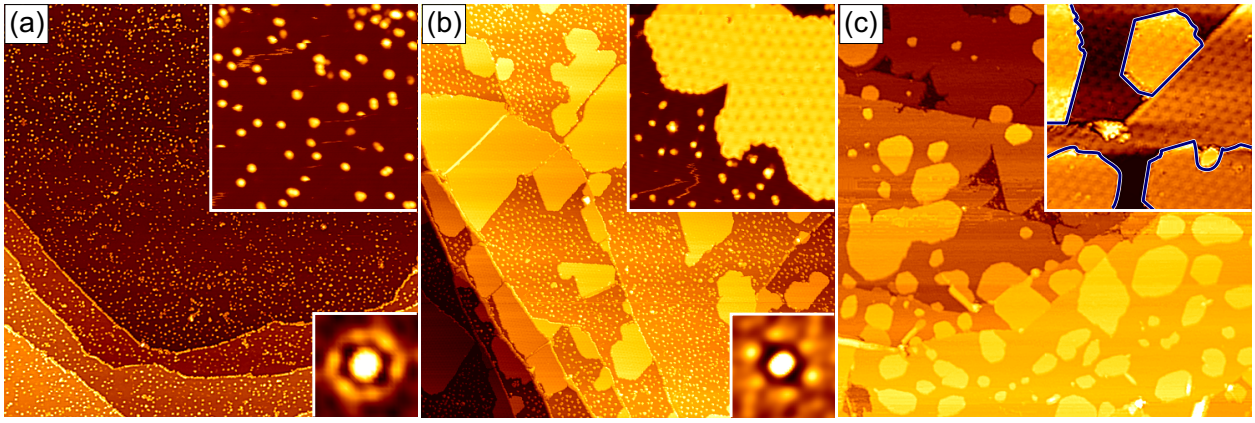

Figure 8.16: STM topographs after Eu deposition at 300 K on TPG+CVD graphene on Ir(111). **(a)** 3.3% ML Eu ($U_s = -1.0\,\mathrm{V}$, $I_t = 9.6\,\mathrm{pA}$, same for upper right inset). Inset at lower right: two dimensional self-correlation of a 200 nm × 200 nm image part. **(b)** 12% ML (−0.83 V, 87 pA, upper right inset: −0.63 V, 4.9 pA). Inset at lower right: two dimensional self-correlation of a 60 nm × 60 nm image part covered by clusters only. **(c)** 40% ML (−0.56 V, 0.11 nA, same for inset). The inset is filtered to enhance the moiré contrast. Second layer islands are encircled with blue lines. Image sizes for (a)-(c) are 320 nm × 320 nm and for the upper right insets 40 nm × 40 nm.

cluster distribution. Note also, that substrate steps (more precise: locations where the graphene film bends over them) are decorated by a rim of clusters.

Upon increase of Θ to 12% ML only a slight decrease of d is possible while at the same time a condensed island phase is squeezed out as visible in Fig. 8.16(b). The separation of clusters in the disperse phase has dropped to $d = 17\,a_C$. The clusters appear larger than for $\Theta = 3.3\%$ ML, but a quantitative statement is impossible due to the phase coexistence and the large scale of the structures involved. The clusters are more regularly positioned than for $\Theta = 3.3\%$ ML and based on the self-correlation in the lower right of Fig. 8.16(b), we conclude on a hexagonal short range order. Again, the substrate steps are decorated by Eu with a stripe width corresponding to the typical cluster diameter. Assuming the distance $d = 17\,a_C$ to be the minimal distance of clusters achievable and assuming the clusters to possess the size observed in Fig. 8.16(a) after deposition of 3.3% ML, we estimate that beyond $\Theta = 5\%$ ML the formation of the condensed phase sets in.

The islands of the condensed phase as well as the clusters have an apparent step height of 5 Å, consistent with our assignment for the height of the first Eu layer of clusters in the previous section. The Eu islands reflect the corrugation of the graphene moiré with Ir(111) as visible in the topographic insets of Figs. 8.16(b) and (c). While for STM imaging of graphene on Ir(111) the moiré contrast and the apparent corrugation depend strongly on tunnelling conditions, this is not the case for STM imaging of the Eu islands resting on graphene/Ir(111). We find a corrugation of $(38 \pm 2)\,\mathrm{pm}$ for the voltage range $-1.6\,\mathrm{V} \leq U_s \leq +0.4\,\mathrm{V}$ for $I_t \approx 100\,\mathrm{pA}$. This insensitivity to the tunnelling voltage indicates that the geometric, rather than the electronic corrugation is measured. At least, the agreement of our result with the vdW-DF study is remarkable, which yields a corrugation of 35 pm for the graphene moiré [165].

After deposition of $\Theta = 40\%$ ML Eu, the first Eu layer is almost perfectly closed and islands of

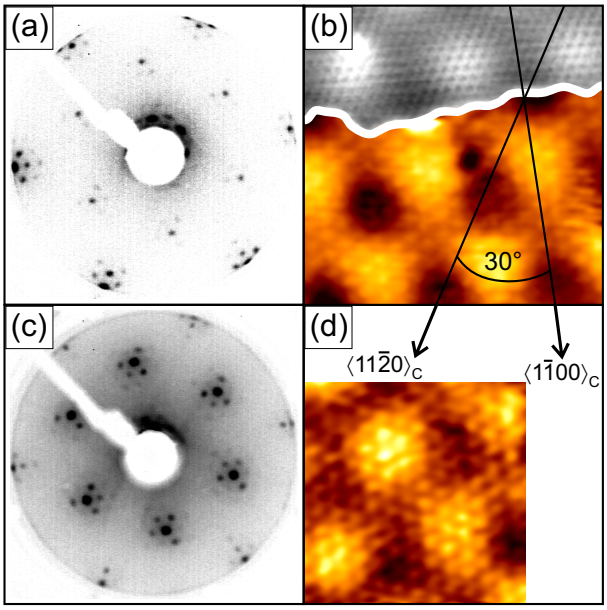

Figure 8.17: **(a)** Inverted contrast LEED pattern of the 12% ML experiment at a primary electron energy of 58 eV. **(b)** Corresponding STM topograph (6.6 nm × 6.6 nm, $U_s = -0.63$ V, $I_t = 18$ nA) at an Eu island edge. The white line indicates the edge of the Eu island (coloured) grown on graphene on Ir(111) (grey). The image contrast is adjusted, such that the graphene and the island level are visible simultaneously. The angle between the dense packed rows of Eu and graphene is 30°. **(c)** Inverted contrast LEED pattern of the 40% ML experiment at a primary electron energy of 58 eV. **(d)** Corresponding STM topograph (4.9 nm × 4.9 nm, −0.04 V, 6.7 nA) showing atomic and moiré contrast of a second layer island. The indicated $\langle 1\bar{1}00\rangle$ and $\langle 11\bar{2}0\rangle$ directions of the graphene lattice are also valid for (b).

the second layer nucleated on top as shown in Fig. 8.16(c). The apparent height of the second layer islands is about 3.4 Å, close to the expected height for a step on the dense packed ⟨110⟩ terrace of *bcc* Eu. The observed height is consistent, but slightly larger than what we inferred in the previous section for the apparent height of the second layer in clusters.

The crystallographic structure of the first and second layer of condensed Eu on graphene remains to be determined. Fig. 8.17(a) shows the LEED pattern of the 12% ML experiment. At the borders of the LEED screen the graphene spots are present, while further inside $(\sqrt{3}\times\sqrt{3})$R30° reflections with respect to these graphene reflections are visible, together with faint moiré spots. Fig. 8.17(b) shows an STM topograph of the same experiment, taken at the edge of an Eu island. In the upper image part graphene on Ir(111) is visible (grey), while in the lower part the Eu island grown on graphene is imaged (coloured). The angle of 30° between the dense packed atomic rows of graphene and of the Eu islands is highlighted by thin black lines. Comparing the atomically resolved structures in the two image parts makes the larger unit cell within the Eu adsorbate layer obvious. We conclude that the first layer Eu islands on graphene possess a $(\sqrt{3}\times\sqrt{3})$R30° structure. The nearest neighbour distance of the Eu atoms in this hexagonal layer is 4.26 Å. This value is just in between the two Eu-Eu distances found for a (110) plane of bulk Eu, which is quasi-hexagonal with atomic distances of 3.97 Å and 4.58 Å along and across the ⟨001⟩-chains, respectively.

The crystallographic structure of the second layer islands is identical to that of the first layer, i.e. Eu still does not form its *bcc* bulk structure but is a two layer *hcp* or *fcc* crystal. This is consistent with the LEED pattern in Fig. 8.17(c) after deposition of 40% ML Eu. The $(\sqrt{3} \times \sqrt{3})$R30° spots together with the corresponding moiré ones are intense, while other reflections are absent. The atomically resolved topograph of a second layer island in Fig. 8.17(d) is a direct proof for the $(\sqrt{3} \times \sqrt{3})$R30° structure and nicely displays the persistence of the moiré corrugation up to the second Eu layer.

8.2.3 Annealing

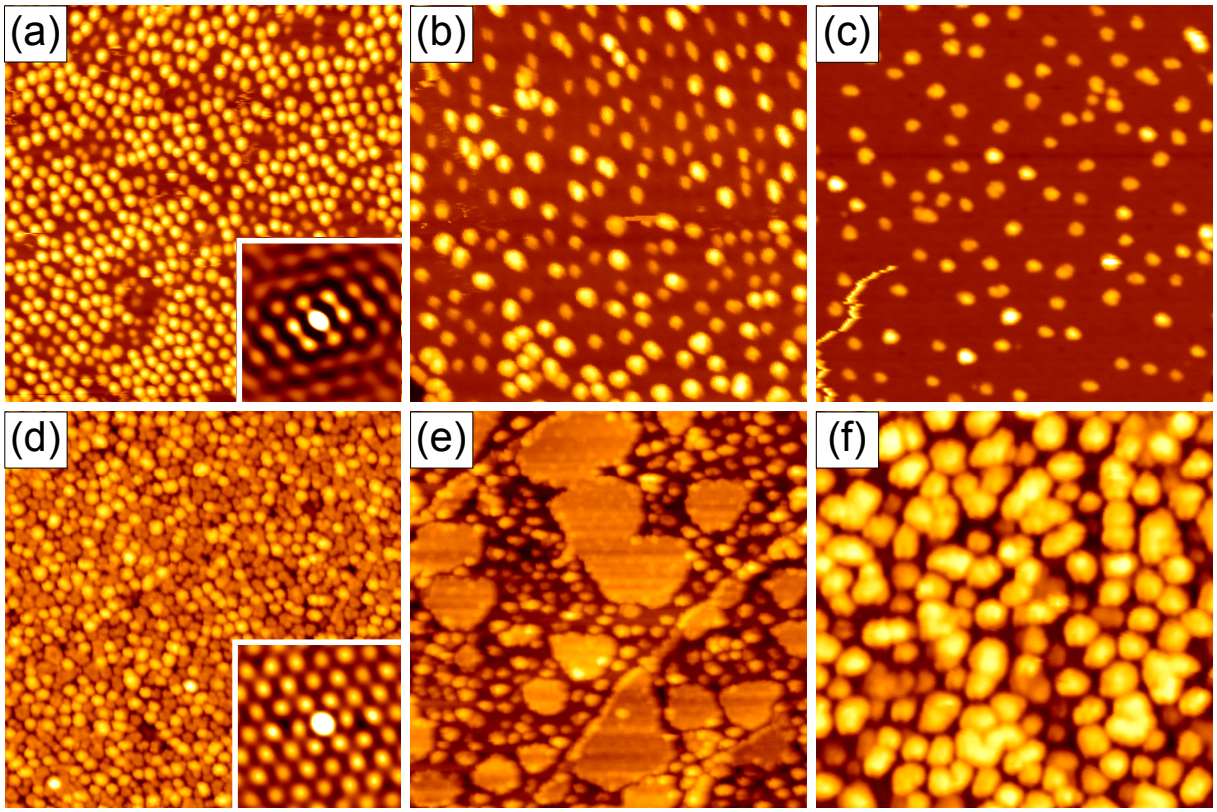

Figure 8.18: STM topographs of annealing sequences after deposition of 1.8% ML [**(a)-(c)**] and 15%ML [**(d)-(f)**] Eu at 35 K on graphene/Ir(111). **(a)** 1.8% ML Eu as grown ($U_s = -0.67$ V, $I_t = 11$ pA). **(b)** As (a), but additionally annealed to 200 K for 60 s (−2.4 V, 0.16 nA). **(c)** As (b), but additionally annealed to 300 K for 60 s (−0.75 V, 62 pA). **(d)** 15% ML Eu as grown ($U_s = -0.79$ V, $I_t = 15$ pA). **(e)** As (d), but additionally annealed to 300 K for 120 s (−1.98 V, 7 pA). **(f)** As (e), but additionally annealed to 400 K for 120 s (−1.55 V, 83 pA). The insets in (a) and (d) display the two dimensional self-correlation of the respective images. Topograph size is always 60 nm × 60 nm.

In order to obtain insight into the relative importance of energetic versus kinetic effects for the observed morphologies we conducted two sets of annealing experiments. Figs. 8.18(a) - (c) represent STM topographs after deposition of 1.8% ML Eu at 35 K. Fig. 8.18(a) displays the starting configuration, while Figs. 8.18(b) and (c) are topographs after additional annealing intervals of 60 s

at 200 K and 300 K, respectively. As highlighted by the image self-correlation shown in the inset of Fig. 8.18(a), the starting configuration is hexagonally ordered due to the close match of $d = 9.8\,a_C$ with the moiré periodicity. Through annealing the cluster density decreases considerably resulting in an increase of the cluster separation starting from $d = 9.8\,a_C$ at 35 K to $d = 18\,a_C$ and $d = 26\,a_C$ after annealing to 200 K and 300 K, respectively. The average cluster size increases from $s_{av} = 1.75$ atoms at 35 K via $s_{av} = 5.9$ atoms at 200 K to $s_{av} = 12$ atoms at 300 K. We assume that the cluster separation after annealing to 300 K is close to the one that would result from direct deposition at 300 K. Though the precisely matching experiment is missing, after deposition of 3.3% ML at 300 K as in Fig. 8.16(a) we found $s_{av} = 14.4$ and $d = 21\,a_C$, which is in line with the values for 1.8% ML given above.

Figs. 8.18(d) - (f) represent STM topographs after deposition of 15% ML Eu at 35 K. Fig. 8.18(d) displays the starting configuration, while Figs. 8.18(e) and (f) are topographs after additional annealing intervals of 120 s at 300 K and 400 K, respectively. Similar to the previous annealing sequence, the image self-correlation shown in the inset of Fig. 8.18(d) underlines the hexagonal order of the brighter clusters in the starting configuration. In the initial configuration the average cluster spacing is $d = 7.9\,a_C$. Upon annealing to 300 K the uniform cluster phase decomposes into a phase of large, compact $(\sqrt{3} \times \sqrt{3})$R30° Eu islands which is embedded into a phase of disperse clusters with a rather uniform spacing of monolayer height. Quantitative analysis results in $d = 12\,a_C$, a separation somewhat smaller than the one of phase coexistence after deposition at 300 K without additional annealing [see Fig. 8.16(b)], which is $d = 17\,a_C$. Upon further annealing to 400 K the coexistence of islands and clusters is destroyed. A uniform cluster phase with $d = 21\,a_C$ and $s_{av} = 57$ atoms is re-established. The clusters display a much larger average height of $h_{av} = 1.2$ nm compared to what we discussed up to now (in the following briefly: 3D clusters). Given the apparent heights of 5 Å for the first Eu layer and 3 - 3.4 Å for the second Eu layer we conclude that the 3D clusters are at least three atomic layers high. Very few remainders of $(\sqrt{3} \times \sqrt{3})$R30° Eu islands are left which are bounded by 3D clusters. We take this as an indication for dewetting of the monolayer $(\sqrt{3} \times \sqrt{3})$R30° Eu islands from graphene. If the Eu is directly deposited at 400 K (not shown here) such large clusters are formed without any sign of $(\sqrt{3} \times \sqrt{3})$R30° islands. LEED conducted after annealing the 15% ML sample to 400 K displays no diffraction spots other than the Ir(111) and the graphene moiré ones. Heating from 300 K to 400 K apparently destroys the $(\sqrt{3} \times \sqrt{3})$R30° structure of islands and clusters. The 3D clusters are likely to be present in **bcc** crystal structure of bulk Eu without a single specific orientation with respect to graphene.

8.2.4 DFT Results

Using a supercell containing 32 C atoms and one Eu atom (corresponding to $\Theta = 6.3\%$ ML), we obtain relaxed structures for starting configurations with Eu at different high-symmetry sites. We find the lowest energy configuration for Eu positioned 2.5 Å above the middle of a carbon hexagon (h-site). Eu on top of a carbon atom (t-site) or above a bridge site (b-site) is higher in energy by 0.12 eV and 0.11 eV, respectively.

The LDOS of an Eu adatom in its minimum energy configuration depicted in Fig. 8.19 shows that Eu is in $4f^7$-configuration with the 6s-orbital being singly occupied. With the s- and the

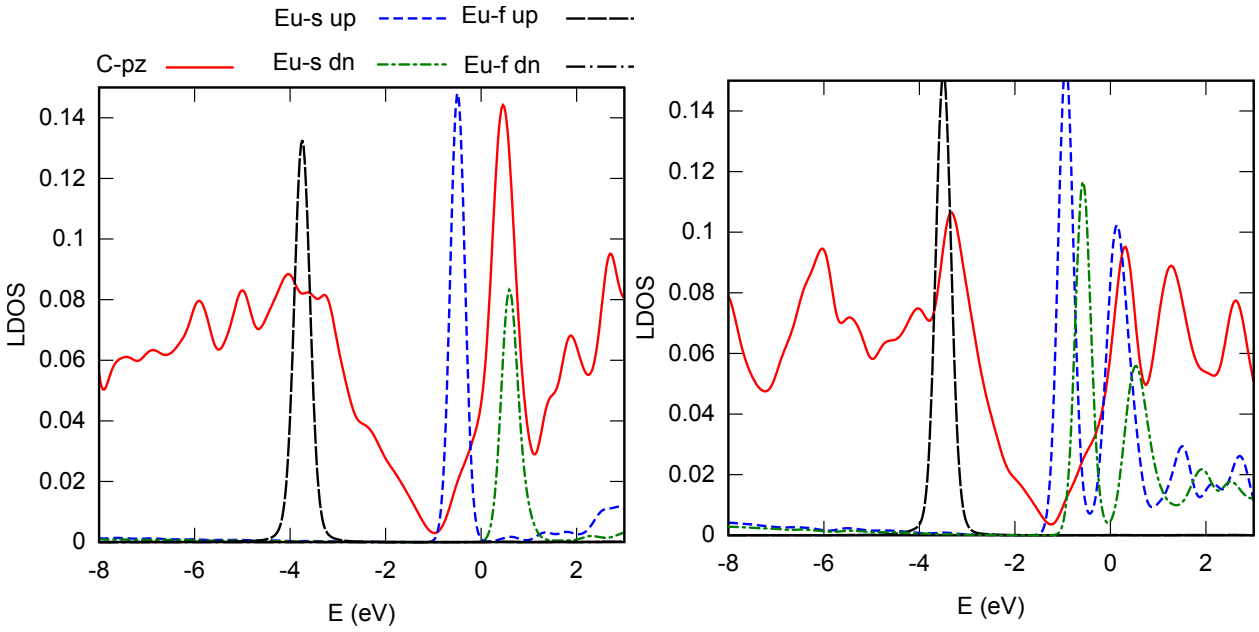

Figure 8.19: Spin and orbitally resolved local density of states (LDOS) of an Eu adatom (left) and Eu dimer (right) on graphene. The spin-down Eu 4f-LDOS is outside the energy range shown here.

f-electron spins coupling ferromagnetically this leads to a total spin of $S = 4$ of Eu. Both, the Eu s- and f-LDOS consist of one peak which is characteristic for ionically bonded impurities on graphene [152]. The Eu LDOS suggests that the adatoms have approximately 8 valence electrons. Hence, our calculations yield ionic bonding between Eu and graphene with Eu carrying a charge on the order of $+1e$. The LDOS at the carbon sites shows that the Dirac point is at $-0.95\,\mathrm{eV}$ for $\Theta = 6.3\%\,\mathrm{ML}$ (see below). In a rigid band model, this shift corresponds to doping of the graphene bands by $-0.85e$, which is well in line with Eu having 8 valence electrons.

The Eu adsorption energies shown in Fig. 8.20 depend strikingly on the Eu coverage[1]. We use the convention that the adsorption energy is a negative quantity, i.e. the decrease of system free energy upon adsorption at 0 K. At a coverage of 6.3% ML the adsorption energy exhibits a maximum. The dense $(\sqrt{3} \times \sqrt{3})\mathrm{R}30°$ superstructure yields the lowest adsorption energy $E_{\mathrm{ad}} = -1.53\,\mathrm{eV}$.

At a growth temperature of 35 K and for $\Theta \leq 5\%\,\mathrm{ML}$ our STM experiments suggest that Eu dimers are formed preferentially. For Eu dimers adsorbed on graphene, our calculations yield the coverage dependent adsorption energies shown in Fig. 8.20. At low coverages ($\Theta < 12.5\%\,\mathrm{ML}$) dimer formation is energetically favoured compared to having a hexagonal lattice of isolated adatoms. In the dimers, the Eu-Eu distance is $4.0\,\text{Å} \approx 1.6\,a_C$, which is slightly smaller but similar to the Eu-Eu distance of $\sqrt{3}a_C \approx 4.3\,\text{Å}$ in the $(\sqrt{3} \times \sqrt{3})\mathrm{R}30°$ superstructure. Similar to the $(\sqrt{3} \times \sqrt{3})\mathrm{R}30°$ structure, the dimer atoms are located close to h-sites, but with a small shift towards each other.

The electronic structure of the Eu dimers on graphene differs from the one of the Eu monomers

[1]These adsorption energies differ from those mentioned in Sec. 8.1.2 because the Ir substrate is neglected for the values in Fig. 8.20.

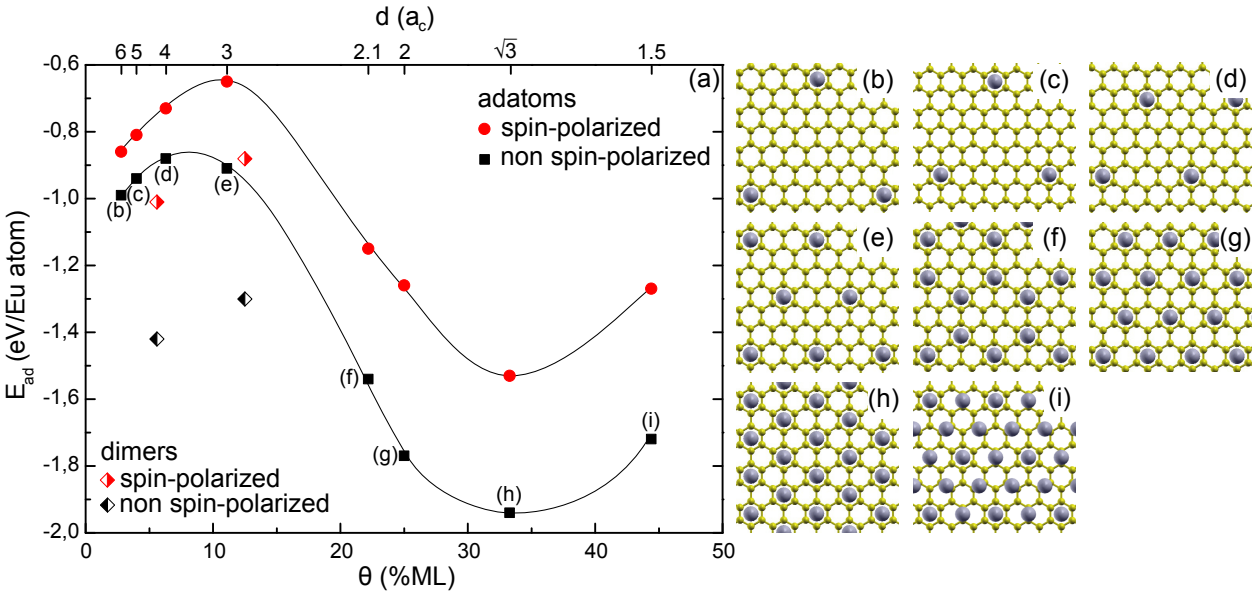

Figure 8.20: **(a)** Adsorption energy E_{ad} per Eu atom adsorbed to h-sites depending on the coverage Θ. Adsorption energies for regular superstructures of Eu adatoms as well as for Eu dimers on graphene are shown. The upper non-linear axis marks the corresponding Eu nearest neighbour distances d in the hexagonal Eu superlattice structures. For Eu the honeycomb lattice at $\Theta = 22.2\%$ ML as well as for the Eu dimers d is recalculated to the Eu separation in an ideal hexagonal arrangement with the same density. Results from non spin-polarised calculations with frozen Eu 4f-shell (black squares) as well as more accurate spin-polarised calculations including the Eu 4f-shell (red dots) are shown. Lines to guide the eye. **(b) - (i)** Calculated Eu (gray) superstructures on graphene (yellow) for coverages of 2.8% ML, 4.0% ML, 6.3% ML, 11.1% ML, 22.2% ML, 25.0% ML 33.3% ML, and 44.4%.

(Fig. 8.19) mainly in the Eu s-orbitals: In the case of the dimer, the Eu s-orbitals split into bonding and antibonding molecular orbitals (MO) visible as two peaks in the Eu s-LDOS. The bonding-antibonding splitting of the Eu 6s-orbitals ($\sim 1\,\mathrm{eV}$) is larger than the spin-splitting ($\sim 0.5\,\mathrm{eV}$). While the bonding Eu 6s-MO is always fully occupied, the occupation of the antibonding Eu 6s-MO is concentration dependent: At $\Theta = 5.6\%\,\mathrm{ML}$ it is virtually empty but becomes slightly occupied at a coverage of 12.5% ML (Fig. 8.19). From the shift of the Dirac point we obtain nominal charges for the dimers of $+0.76e$ and $+0.66e$ per Eu atom at coverages of $5.6\%\,\mathrm{ML}$ and $12.5\%\,\mathrm{ML}$, respectively.

This trend continues to the dense Eu superstructures on graphene: For the p(2×2) and ($\sqrt{3} \times \sqrt{3}$)R30° superstructures on graphene (Fig. 8.21) the LDOS of the Eu 6s-orbitals broadens indicating that these orbitals further delocalise due to band formation within the Eu layer. Furthermore the Eu 6s-orbitals are not fully spin-polarised which results in a reduction of the magnetic moment to $7.3\,\mu_B$ and $7.5\,\mu_B$ for the p(2×2) and ($\sqrt{3}\times\sqrt{3}$)R30° superstructure, respectively. In both cases graphene is n-doped by Eu. The Dirac point appears at $-1.5\,\mathrm{eV}$ and $-1.3\,\mathrm{eV}$ for the p(2×2) and the ($\sqrt{3} \times \sqrt{3}$)R30° corresponding to a charge transfer of $0.6e$ and $0.3e$ per Eu atom, respectively.

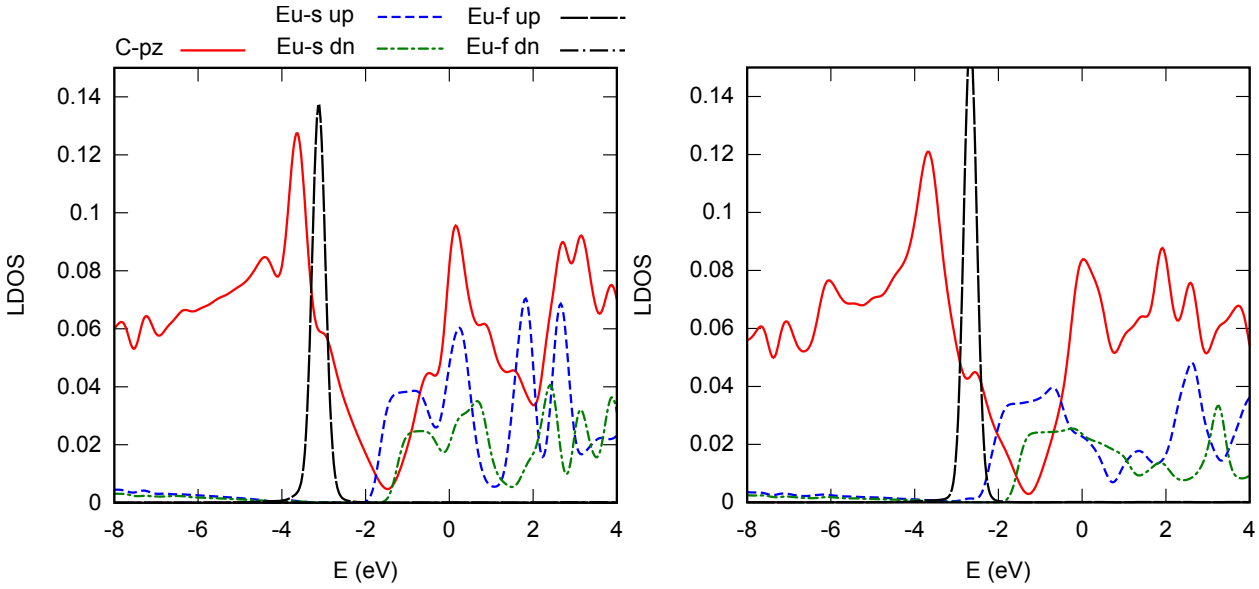

Figure 8.21: Spin and orbitally resolved local density of states (LDOS) of Eu p(2×2) (left) and $(\sqrt{3} \times \sqrt{3})$R30° superstructures (right) on graphene. The spin-down Eu 4f-LDOS is outside the energy range shown here.

In going from the lowest calculated coverage of $\Theta = 2.8\%$ ML to the experimentally observed $(\sqrt{3} \times \sqrt{3})$R30° superstructure at $\Theta = 33\%$ ML the charge transfer per Eu atom decreases by about a factor of three, from $0.85e$ to $0.3e$, while the magnitude of adsorption energy more than doubles. This finding can be rationalised by stating that with increasing coverage the Eu bonding shifts from a purely ionic one between the Eu adatom and the graphene substrate, to more metallic bonding dominated by bonds within the Eu-layer. This metallic bonding is signalled by the formation of a partly occupied s-band in the $(\sqrt{3} \times \sqrt{3})$R30° superstructure [compare Fig. 8.21, right panel].

An estimate for the relative strength of the two contributions to bonding is obtained by the following considerations. Linear interpolation of the low coverage data of Fig. 8.20 to zero allows one to estimate the ionic bond strength of an isolated Eu atom to graphene to be ≈ -1 eV (spin polarised data). At zero coverage the charge transfer will be about $1e$. For $\Theta = 33\%$ ML according to our calculations the charge transfer per Eu atom has reduced to $0.3e$. Assuming for simplicity a linear correlation between charge transfer and bond strength, the ionic contribution to the -1.5 eV binding energy (spin polarised data) at $\Theta = 33\%$ ML is therefore -0.3 eV, leaving a metallic Eu-Eu binding energy of about ≈ -1.2 eV per atom.

There is another important feature in Fig. 8.20, yet unexplained: with increasing coverage from $\Theta = 0$ to $\Theta \approx 10\%$ ML the Eu adatoms are less and less strongly bound. This decrease in bond strength takes place in the coverage regime where due to their large separation metallic bonds between Eu adatoms are still absent. We identify two contributions to this decrease in the magnitude of adsorption energy. (i) As pointed out by Ishida and Palmer [260], due to the small density of states of graphene, charge transfer to graphene causes an upward shift of the Fermi level. As the band energy increases with Θ, the charge transfer per Eu atom is reduced. Consequently,

the ionic bond strength is diminished. (ii) As charge transfer lifts neutrality, with increasing Θ an increasing Coulomb energy penalty has to be paid resulting from electron-electron repulsion in the graphene layer and from ion-ion repulsion, which counteract the attraction between positively charged Eu ions and the negatively charged screening clouds.

Both effects not only diminish the bond strength with increasing Θ (as long as direct Eu-Eu bonding is absent), but also cause a net long range repulsive interaction between Eu ions. For illustration, assume a homogeneous adatom distribution to be replaced by a homogeneous adatom distribution with double density, but covering only half of the graphene substrate. The band energy as well as the Coulomb repulsion will increase to the values corresponding to doubled coverage and the total system energy increases. In consequence, a force results, which tends to disperse the adatom distribution into the empty graphene area.

8.2.5 Discussion

In order to bring some light into the puzzle of Eu adsorption on graphene we first analyse the room temperature adsorption and annealing experiments to establish the thermodynamic equilibrium Eu phases on graphene. We will then investigate the mechanism for the coexistence of two phases, the $(\sqrt{3}\times\sqrt{3})$R30° structure and a phase of well separated clusters of about 15 atoms. Finally, we will analyse in more detail the low temperature experiments, in which kinetic limitations complicate the interpretation, and compare our results with alkali metal adsorption.

8.2.5.1 Equilibrium phases

As shown in Fig. 8.18(f), after annealing to 400 K we observe 3D Eu clusters on graphene, distributed uniformly. The Eu bulk cohesive energy is -1.86 eV [261], while the largest DFT calculated spin-polarised adsorption energy of Eu on graphene is -1.53 eV for the $(\sqrt{3}\times\sqrt{3})$R30° structure. These numbers suggest that Eu prefers to bind to Eu rather than to graphene. Therefore in thermodynamic equilibrium and without any kinetic restrictions we assume Eu to grow as 3D islands. In our data we have no evidence for a specific epitaxial relation of the clusters with respect to graphene, but this could change for longer or higher annealing temperatures.

At temperatures below 400 K formation of 3D structures is kinetically inhibited. Constraining thermodynamic considerations to two dimensions, we may analyse the resulting two dimensional equilibrium phases. For $\Theta \leq 5\%$ ML we obtain at 300 K monolayer high Eu clusters uniformly distributed over the sample. For 3.3% ML deposited typical separations are $d \approx 21\, a_C$ and $s_{av} \approx 14$ atoms. It is plausible that increasing Θ up to 5% ML will decrease d to a minimum value [compare Fig. 8.16(a)] and s_{av} to a maximum value, but both values will be of similar magnitude as the numbers mentioned above. This disperse cluster phase is realised for a given Θ at 300 K, irrespective of the kinetic pathway: either by direct deposition at 300 K [compare Fig. 8.16(a)] or by low temperature deposition and subsequent annealing to 300 K [compare Figs. 8.18(a) - (c)]. From this independence of the kinetic pathway we conclude that the disperse cluster phase is an equilibrium surface phase at 300 K.

Several arguments lead to the conclusions that each cluster is built from Eu atoms in a $(\sqrt{3}\times$

$\sqrt{3}$)R30° structure. First, our DFT calculations show that this structure has the lowest energy and already single dimers prefer a geometric configuration and a distance $1.6\,a_C$ consistent with a relaxed ($\sqrt{3}\times\sqrt{3}$)R30° arrangement. Second, we find experimentally at all temperatures the cluster height (except for the single adatom) to be similar to the height measured for large ($\sqrt{3}\times\sqrt{3}$)R30° Eu islands. Finally, at low temperature and for large clusters with $s_{\mathrm{av}} = 24$ atoms we observe a ($\sqrt{3}\times\sqrt{3}$)R30° LEED pattern as shown in Fig. 8.14(h). These facts leave little doubt, that all two dimensional clusters observed - and specifically the clusters of the disperse cluster phase observed after 300 K deposition - possess internally a structure close to the ($\sqrt{3}\times\sqrt{3}$)R30° one.

For 5% ML $\leq \Theta \leq$ 33% ML we observe coexistence of monolayer high Eu clusters uniformly distributed over the sample with compact ($\sqrt{3}\times\sqrt{3}$)R30° Eu islands. This situation is realised for a given Θ at 300 K, again irrespective of the kinetic pathway: either by direct deposition at 300 K [compare Fig. 8.16(b)] or by low temperature deposition and subsequent annealing to 300 K [compare Figs. 8.18(d) and (e)]. The slight differences in cluster densities and sizes as well as island densities and sizes realised on the two pathways indicate that kinetic limitations are not fully lifted. Nevertheless, we conclude that the disperse cluster phase is in thermodynamic equilibrium with the ($\sqrt{3}\times\sqrt{3}$)R30° island phase. The phase diagram is shown in Fig. 8.22 and discussed in more detail in the following section, Sec. 8.2.5.2.

Since the ($\sqrt{3}\times\sqrt{3}$)R30° island phase is an equilibrium phase it should fully cover graphene for $\Theta = 33.3\%$ ML. As Fig. 8.16(c) shows, even after deposition of 40% ML still small patches of the disperse cluster phase are left, while ($\sqrt{3}\times\sqrt{3}$)R30° second layer islands nucleated. The nucleation of second layer islands prior to the closure of the first layer is a typical behaviour in epitaxial growth, even if step edge barriers are negligible [262]. Therefore we may conclude that under the constraints of a closed ($\sqrt{3}\times\sqrt{3}$)R30° Eu layer on graphene and only two dimensional phase formation also for the second layer ($\sqrt{3}\times\sqrt{3}$)R30° islands are the thermodynamic equilibrium phase. Note that for the second layer no disperse cluster phase is formed. This underlines the specificity of the disperse cluster phase for Eu adsorption on *graphene*. In conclusion we find four equilibrium or quasi-equilibrium phases as a function of coverage and temperature: (i) the 3D cluster phase at 400 K; (ii) the disperse cluster phase at 300 K and for small coverages; (iii) the ($\sqrt{3}\times\sqrt{3}$)R30° island phase, which has an extended coexistence range with the disperse cluster phase and is phase pure only for $\Theta = 33.3\%$ ML at 300 K; (iv) eventually again a ($\sqrt{3}\times\sqrt{3}$)R30° island phase, which is the only stable condensed phase in second Eu layer at 300 K.

8.2.5.2 Phase coexistence of clusters and ($\sqrt{3}\times\sqrt{3}$)R30° islands

The most striking observation reported here is probably the disperse cluster phase at low coverage and, especially, its coexistence with the ($\sqrt{3}\times\sqrt{3}$)R30° island phase at room temperature for larger coverages.

Phase coexistence implies that the free energy $F = E - TS$ plotted as a function of coverage (or composition) must be concave in the phase coexistence range. Due to the large number N_{Eu} of atoms per cluster, the entropic contribution to the free energy TS per Eu atom arising from the possibility to distribute the clusters across the plane (estimated as $\frac{k_B T}{N_{\mathrm{Eu}}} \ln 1/\Theta \ll 0.01\,\mathrm{eV}$ with k_b being the Boltzmann constant) is even at room temperature small compared to all other

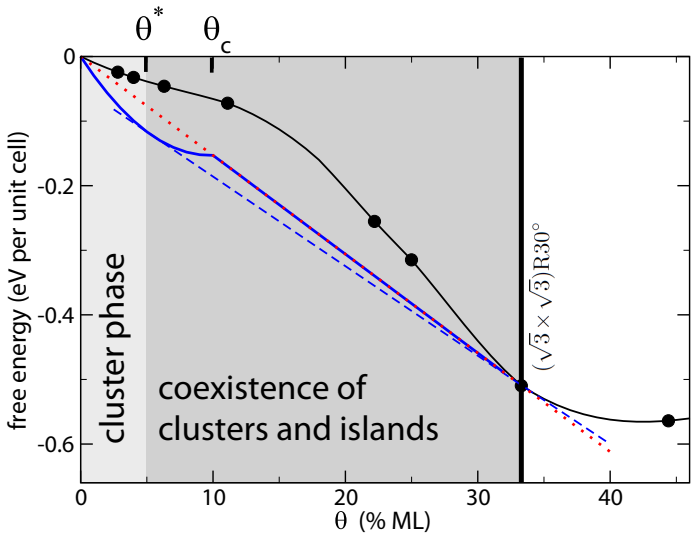

Figure 8.22: Equilibrium phase diagram and schematic plot of the change of the free energy per graphene unit cell due to the adsorption of Eu as a function of the Eu coverage Θ. Full black dots: Adsorption energy from spin-polarised DFT calculations assuming uniform coverage (same data as in Fig. 8.20). The average free energy can be lowered down to the red dotted line for $\Theta < 1/3$ by putting all Eu atoms into one large island with a $(\sqrt{3}\times\sqrt{3})$R30° structure ($\Theta = 1/3$). For $\Theta < \Theta_c$ the system can, however, gain even more energy by breaking the large island into smaller clusters (solid blue line, the corresponding energy gain is exaggerated in the schematic figure). While for $\Theta < \Theta^*$ the disperse cluster phase is stable, one can lower the energy down to the blue dashed line for $\Theta^* < \Theta < 1/3$ due to the coexistence of the cluster phase with $\Theta = \Theta^*$ and of an island with the $(\sqrt{3}\times\sqrt{3})$R30° structure.

contributions (see below) and will therefore be neglected in the following. Consequently, we can use our DFT result for the adsorption energy per Eu atom to estimate the energy (per graphene unit cell) as a function of the coverage Θ (dots in Fig. 8.22). The concave DFT curve clearly predicts that one big $(\sqrt{3}\times\sqrt{3})$R30° island should form. A large metallic $(\sqrt{3}\times\sqrt{3})$R30° island is preferred in the DFT calculation to isolated adatoms (and also compared to the dimer phase) by the dominant contribution of metallic Eu-Eu binding to the total adsorption energy. Here it is important to take into account that the DFT calculation assumed an *uniform* coverage and does, by construction, not allow for cluster formation. While Eu atoms form indeed *locally* a $(\sqrt{3}\times\sqrt{3})$R30° structure (as predicted by DFT), our experiments show that for low coverage extra energy can be gained by breaking up the big island into clusters.

When forming uniformly distributed clusters out of the single $(\sqrt{3}\times\sqrt{3})$R30° island, the breaking of Eu-Eu bonds will the cost edge energy E_{edge} per Eu atom. The electrons can, however, *lower* their kinetic energy by moving away from the Eu clusters into areas where graphene is not covered by Eu. In the limit of vanishing coverage and small charge transfer δn per Eu atom, the energy gain per Eu atom can be estimated from the difference of the work function of the $(\sqrt{3}\times\sqrt{3})$R30° structure and pure graphene, $\Delta E_\Phi \approx -\delta n(4.3 - 2.9)\,\text{eV} = -\delta n\,1.4\,\text{eV}$ (see Sec. 8.3, table 8.1). The redistribution of charge, however, is associated with a Coulomb energy penalty arising from

the charging of the clusters. It is the interplay of these three contributions to the total energy that determines the phase diagram and leads to cluster formation: First, the edge energy E_{edge} of the cluster arises because the Eu atoms locally prefer the $(\sqrt{3}\times\sqrt{3})$R30° phase where metallic binding to neighbouring Eu atoms is possible. Second, electrons gain energy by lowering their kinetic energy when moving away from the cluster, thereby building up a charge imbalance which, third, costs Coulomb energy. The fact that this Coulomb energy penalty (which limits the gain of kinetic energy) can be reduced by forming clusters is in our opinion the main driving mechanism for the formation of the disperse cluster phase. Ultimately, optimising the energy by choosing the optimal cluster size allows to maximise the energy gain, thus lowering the total energy by forming clusters instead of one large $(\sqrt{3}\times\sqrt{3})$R30° island.

For an estimate of the Coulomb energy the screening from the underlying Ir substrate plays an important quantitative role. However, to get a qualitative understanding of the physics, we neglect for the following argument the underlying Ir substrate. We consider a grossly oversimplified model which mimics screening only by a relative permittivity $\epsilon_r > 1$ (valid only for insulating substrates) and also assumes that the electrons distribute uniformly on the part of graphene not covered by Eu. Approximating furthermore the Eu island by a uniformly charged disk one obtains for a single island (i.e. in the limit $\Theta \to 0$) an energy cost per Eu of $E_c \approx \frac{(\delta n)^2}{\epsilon_r}\sqrt{N_{\text{Eu}}}\cdot 5.5$ eV. The Coulomb energy grows rapidly with increasing number of Eu atoms per cluster N_{Eu} implying that $\delta n = 0$ for an infinite size cluster.

Minimising $E_c + \Delta E_\Phi$ we obtain an energy gain per Eu of approximately $E_{\text{gain}} = -\frac{\epsilon_r}{\sqrt{N_{\text{Eu}}}}\cdot 0.1\,\text{eV}$. For a magic cluster with $N_{\text{Eu}} = 19$ Eu atoms (two shells around a central atom) one has 15 broken Eu-Eu bonds (compared to 19 atoms in an infinite $(\sqrt{3}\times\sqrt{3})$R30° structure) and therefore the energy gain per broken bond is only $\epsilon_r \cdot 0.03\,\text{eV}$. This approximation can only serve as an order of magnitude estimate. In reality the energy gain will be bigger as the Coulomb energy can be considerably reduced by employing a non-uniform distribution of the electrons around the cluster. Furthermore, screening will also lead to a substantial increase of the energy gain as can be seen from the linear dependence of E_{gain} on ϵ_r. In this approximation the two opposing energy contributions – E_{gain} favouring small clusters and E_{edge} favouring large islands – are both proportional to $\frac{1}{\sqrt{N_{\text{Eu}}}}$. Therefore our toy model does not predict an optimal cluster size.

To obtain the phase diagram and an optimal cluster size two more effects have to be taken into account. First, for small N_{Eu} when $\delta n \propto 1/\sqrt{N_{\text{Eu}}}$ becomes larger, non-linear effects have to be taken into account. Probably the most important effect is that the binding of Eu to graphene becomes more ionic (according to our DFT results an Eu atom in the $(\sqrt{3}\times\sqrt{3})$R30° phase loses ~ 0.3 electrons compared to ~ 1 electron for a single Eu atom). If this reduces the Eu-Eu binding energy, it could explain the existence of an optimal cluster size for small Θ. Furthermore, for increasing coverage Θ, the gain in potential energy due to cluster formation is reduced both by the Coulomb repulsion of neighbouring clusters approaching each other and by the doping of the pristine graphene which lowers the gain of kinetic energy by Pauli blocking. It has been argued by Ishida and Palmer [260] that this effect is especially important in graphene, where due to the peculiar low density of states the Fermi energy rapidly rises with doping. As in the limit $\Theta \to 1/3$ the gain in energy vanishes completely, there will necessarily be a critical coverage θ_c such that the

cluster phase is not locally stable for $\Theta > \theta_c$.

Fig. 8.22 displays schematically the resulting free energy as a function of the coverage Θ which is consistent with the experimental results and the theoretical arguments described above. The blue solid line describes the free energy for a phase of clusters where for each value of Θ the (average) number of atoms per cluster N_{Eu} has been optimised. For $\Theta > \theta_c$ this optimisation leads to $N_{\mathrm{Eu}} = \infty$ and therefore to an energy which can be obtained by the usual linear interpolation of the energies at $\Theta = 0$ and $\Theta = 1/3$. For $\Theta < \theta_c$ the optimal clusters have a finite size and the energy is lower. As shown and discussed in Fig. 8.22 this leads to phase separation in the regime $\Theta^* < \Theta < 1/3$, where a cluster phase with coverage Θ^* coexists with big $(\sqrt{3} \times \sqrt{3})\mathrm{R}30°$ islands. While for $\Theta \to \theta_c$ the size of the optimal cluster nominally diverges, it is finite at Θ^*.

A full ab-initio calculation of the energy of the cluster phase would certainly be highly desirable. But a direct simulation appears to be impossible at present due to the large unit cells required.

8.2.5.3 Kinetically limited growth at low T

All morphologies fabricated at 300 K or annealed to a temperature well above 35 K were cooled down to 35 K to freeze their high mobility for imaging. These morphologies are quite different from the ones grown and imaged at 35 K, even if one compares similar coverages. Therefore the 35 K morphologies represent to a good extent the kinetic limitations of the growth process. One might argue that part of the difference in appearance is due to the different relevance of entropy at 35 K and 300 K, However, the arrangement of small clusters with $s_{\mathrm{av}} = 1.9$ obtained after deposition of 3.3% ML [compare Fig. 8.14(e)] has certainly a larger entropy than the arrangement of clusters with $s_{\mathrm{av}} = 14.4$ obtained for the same Θ at 300 K [compare Fig. 8.16(a)]. Thus the entropy argument goes into the wrong direction and appears to be largely irrelevant (consistent with the estimates given above). In the following we analyse the 35 K data represented Fig. 8.14 under the viewpoint of kinetic limitations and put them into relation to our DFT calculations.

Imaging at 35 K makes obvious that the morphology is frozen at 35 K. It is plausible that the entity with the highest mobility is the monomer, for which we calculate an activation energy $E_a = 0.11\,\mathrm{eV}$. This value is a lower bound approximation based on the difference in adsorption energy between the h-site and b-site. Assuming a standard attempt frequency $\nu_0 = 1 \times 10^{12}\,\mathrm{Hz}$ we obtained at 35 K a hopping rate $\nu = \nu_0 e^{E_a/k_b T} = 1.4 \times 10^{-4}\,\mathrm{Hz}$. The resulting hopping period of the order of an hour is consistent with the observed frozen morphology, thereby keeping experiment and DFT calculation consistent.

With increasing coverage up to about $\Theta \approx 5\%$ ML the 35 K data display a decreasing, but eventually rather uniform cluster-cluster separation down to a minimum value of $d = 7.3\,a_{\mathrm{C}}$, while the average cluster size is pinned to the dimer. This behaviour is a clear expression for the relevance of repulsive interactions that were discussed already in Sect. 8.2.4 and are manifested in Fig. 8.20. These are repulsive Coulomb interactions between the Eu ions and between their screening clouds in graphene. In addition we have Pauli repulsion of the electrons in the screening clouds: Due to the low density of states an overlapping of the screening clouds will cause a local upward shift of the Fermi energy, i.e. an increase of band energy [260]. Therefore, the screening clouds pinned to the Eu-ions will avoid to come close and thus keep the Eu ions apart. A likely explanation

of the observed features is that upon deposition the transient mobility of adatoms is sufficient to overcome the long range repulsive Coulomb interactions to another adatom. In consequence a dimer is formed. Our DFT calculations are consistent with this scenario, as the dimer is energetically preferred compared to two adatoms (compare Sect. 8.2.4) The energetic preference results from the large energy gain caused by the Eu-Eu bond formation. For low coverages at 35 K, the long-distance repulsion of single adatoms and dimers is too large for single adatoms to come sufficiently close to a dimer to form trimers. Apparently, this must also be the case for the long-distance repulsion between dimers as no tetramers were found for $\Theta \leq 3.3\%$ ML.

Through continued deposition therefore more and more dimers will be formed until their concentration reaches a maximum, where the screening clouds substantially overlap. At this point cluster growth (allowing formation of more Eu-Eu bonds) takes place rather than the formation of new dimers. If our speculation is proper, the minimum dimer distance of $d \approx 7a_C$ is an estimate for the extension of the delocalised screening cloud around dimers resulting from the charge transfer of Eu s-electrons to graphene. Subsequent aggregation may also be eased by the reduced charge transfer of the newly arriving adatoms after the Fermi-level has already shifted by about 1 eV through the already existing clusters. The reduced charge transfer implies a reduced repulsive interaction of the adatom with the existing clusters.

The 35 K and the 300 K data display a striking similarity. In both cases initially the graphene is covered rather uniformly by a single phase of disperse and similar sized clusters, until beyond $\Theta \approx 5\%$ ML the morphology becomes more heterogeneous with varying cluster sizes or the onset of the $(\sqrt{3} \times \sqrt{3})$R30° islands. However, the selected cluster sizes and distances for the same coverage differ significantly for the same Θ due to the presence of repulsive interactions, which cause kinetic growth limitations at low temperature. Both values, s_{av} and d are much larger at 300 K.

8.2.5.4 Comparison to alkali metal adsorption

The adsorption of Eu on graphene bears certain similarities to the adsorption of alkali metals on graphite and metal surfaces. The basis of these similarities is the fact that in the low coverage limit an adsorbed Eu adatom donates an s-electron to the substrate, as it is observed for alkali metal adsorption. Still the best studied system of an alkali metal on graphite is the adsorption of potassium [260; 263–267]. Upon adsorption at 90 K a disperse adatom phase was observed, giving rise to a LEED ring, which compresses continuously upon adsorption until at a critical coverage a (2x2) K overlayer forms. Alkali adsorption on metals usually leads through a sequence of adatom phases with increasing density till a dense ordered phase is formed. However, the coexistence of phases differing in density as much as for K on graphite or here for Eu on graphene has not been observed on metals [268; 269]. In a theoretical study [260] Ishida and Palmer emphasise that for a semimetallic substrate with a low density of states like graphene, the band energy changes significantly with coverage. These authors propose that this strong band energy change may give rise to the phase coexistence of adatoms and a condensed phase of K on graphite.

In distinction to all reported alkali adsorption cases on metals or graphite, for Eu adsorption on graphene we find coexistence of a low density phase of uniformly distributed clusters with a condensed phase of high density. The low density phase is formed by clusters, which combine

already at low coverage aspects of ionic and metallic bonding. The phase separation is understood here as resulting from the requirement to donate charge to graphene as rapidly and uniformly as possible in order to lower the electron kinetic energy of the system under the constraint of minimal repulsive Coulomb and band energy effects, while maintaining as much Eu-Eu bonding as possible.

For K on graphite, the adsorption energies of adatoms, dimers and (2×2) monolayer structures have been compared in Ref. [265]. The adsorption energies of a K adatom and a dimer in a 4×4 graphite supercell are $-0.99\,\mathrm{eV}$/K-atom and $-0.74\,\mathrm{eV}$/K-atom, respectively. For the K monolayer an adsorption energy of $-0.81\,\mathrm{eV}$/K-atom has been found. This is qualitatively different from the adsorption energies obtained for Eu on graphene, where we find that isolated adatoms gain generally less energy by adsorption than dimers or adsorbed monolayers [$(\sqrt{3}\times\sqrt{3})$R30° structure]. Eu adatoms on graphene thus seem to form stronger adsorbate-adsorbate bonds than K adatoms. This can be understood in two limiting cases: In the dilute limit, K on graphene or graphite has a completely empty $4s$ orbital, in contrast to the half-filled $6s$-orbital of Eu on graphene. Thus, only for Eu but not for K the outer s-orbital can lead to a strong metallic adsorbate-adsorbate bond. At higher coverage, the difference between the K adsorption on graphite and Eu adsorption on graphene may also be in part be due to the larger cohesive energy of Eu, making adsorbate-adsorbate bonding more important compared to adsorbate-substrate bonding.

8.3 Work function comparisons

As it was described in Sec. 4.3.4, differences in work functions can be determined by comparative $I_\mathrm{t}(s)$ measurements. Therefore, we conducted sets of $I_\mathrm{t}(s)$ spectra in adjacent sample areas of different structure, but with identical tip (no tip changes) and identical bias voltages. In the Figs. 8.23 and 8.24 typical $I_\mathrm{t}(s)$ curves obtained by this method can be seen for the comparisons of TPG graphene on Ir(111) with Ir(111) [Fig. 8.23(a)], of $(\sqrt{3} \times \sqrt{3})$R30° Eu islands on graphene with graphene on Ir(111) [Fig. 8.23(b)], and of graphene on Ir(111) with and without intercalated Eu in the p(2×2) structure (Fig. 8.24).

Averaging over many pairs of $I_\mathrm{t}(s)$ curves as shown in the Figs. 8.23 and 8.24 results in apparent work function differences $\Delta\Phi_{\mathrm{Ir-Ir/C}} = (1.1 \pm 0.3)\,\mathrm{eV}$, $\Delta\Phi_{\mathrm{Ir/C-Ir/C/Eu}} = (1.4 \pm 0.3)\,\mathrm{eV}$, and $\Delta\Phi_{\mathrm{Ir/C-Ir/Eu/C}} = (1.5 \pm 0.2)\,\mathrm{eV}$. Thereby, the work function is highest for pure Ir and lowest with adsorbed or intercalated Eu.

The experimentally measured work function changes upon Eu adsorption or intercalation can serve as a fingerprint of charge doping and additional surface dipoles due to the Eu. Calculating these work function changes theoretically can further corroborate the experimental observations of the Eu structures.

To this end, we modelled the Ir(111) surface in DFT calculations by a slab consisting of 4 atomic Ir layers which was covered with graphene and Eu on one side and ≈ 25 Å of vacuum between the periodic images of the slabs. The work functions were then obtained by comparing the Fermi level to the vacuum levels. In the calculations with adsorbed Eu, we employed dipole corrections according to Ref. [270]. The calculated work functions are shown in Table 8.1.

The work function of the Ir(111) surface is 5.4 eV for the relaxed surface and 5.6 eV when Ir

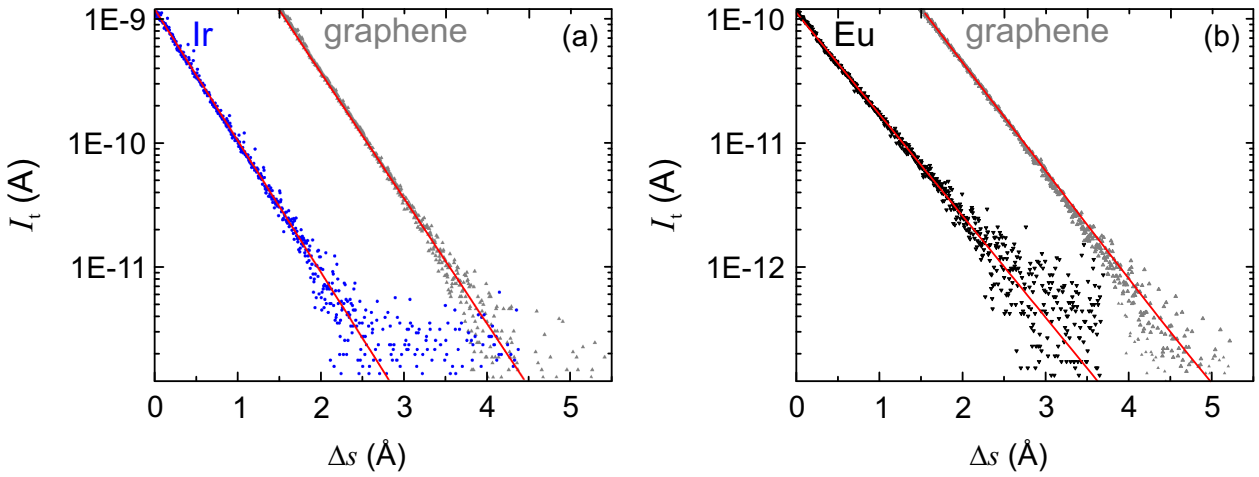

Figure 8.23: **(a)** $I_t(s)$ measurements for Ir(111) (blue dots) and TPG graphene on Ir(111) (grey triangles) taken with the same tip at $U_s = -0.5\,\mathrm{V}$. **(b)** $I_t(s)$ measurements for graphene on Ir(111) (grey triangles) and $(\sqrt{3}\times\sqrt{3})$R30° Eu islands on graphene on Ir(111) (black, downward pointing triangles) taken with the same tip at $U_s = -1.0\,\mathrm{V}$. In both cases the graphene data are shifted by 1.5 Å for better visibility; red lines indicate fits to the data.

is forced to a perfect fcc lattice with a lattice constant of 3.5 Å. As the calculation of graphene on Ir(111) was performed for the latter geometry, we expect a theoretical error margin on the order of 0.2 eV. Previous experimental values for the Ir(111) work function are 5.70 eV and 5.76 eV [241; 271], in reasonable agreement with our results.

For graphene on Ir(111) our calculations find a work function of 4.3 eV. It is 1.3 eV lower than for Ir alone, in good agreement with the 1.1 eV found in our experiments. A recent LEEM study finds the Ir(111) work function to be lowered by 0.8 - 0.9 eV due to graphene adsorption [168], in reasonable agreement with our findings.

Upon Eu adsorption, both, theory and experiment find a reduction of the work function by 1.4-1.5 eV. This is well in line with the observation of charge being transferred from the Eu-s orbital to the graphene bands and corresponding dipoles being formed. We find Eu adatoms on graphene causing dipole moments of 0.07eÅ in the $(\sqrt{3}\times\sqrt{3})$R30° superstructure. When decreasing the Eu concentration the dipole moment per atom increases reaching $0.36e$Å for $\Theta = 6.3\%$ ML.

adsorbate	substrate	DFT Φ_{ads} (eV)	DFT Φ_{sub} (eV)	DFT $\Delta\Phi$ (eV)	experiment $\Delta\Phi$ (eV)
graphene on Ir(111)	Ir(111)	4.3	5.6	1.3	1.1 ± 0.3
$(\sqrt{3}\times\sqrt{3})$R30° Eu islands on graphene on Ir(111)	graphene on Ir(111)	2.8	4.3	1.5	1.4 ± 0.3
p(2×2) Eu intercalated between graphene and Ir(111)	graphene on Ir(111)	3.5	4.3	0.8	1.5 ± 0.2

Table 8.1: Comparison of the work function values measured by $I_t(s)$ spectroscopy and calculated by DFT.

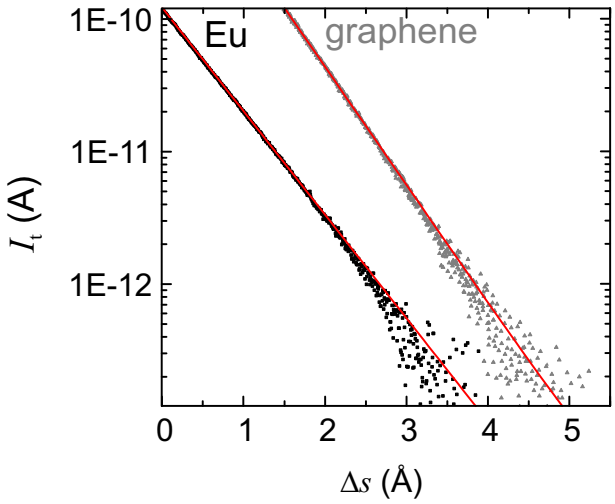

Figure 8.24: $I_t(s)$ measurements for p(2×2) Eu intercalated between graphene and Ir(111) (black squares) and graphene on Ir(111) (grey triangles) taken with the same tip at $U_s = -0.5\,\mathrm{V}$. The graphene data are shifted by 1.5 Å for better visibility; red lines indicate fits to the data.

For the case of Eu intercalation the work function determined by theory is 3.5 eV which is only 0.8 eV lower than that of graphene on Ir(111). The STM measurements find a reduction of 1.5 eV in regions with intercalated Eu, which is similar to that of the Eu islands on graphene. As the calculated n-doping of 1.3 eV for graphene with intercalated p(2×2) Eu is smaller than the 1.5 eV measured by ARPES (see Sec. 8.1.4), the theoretical calculations probably exaggerate the work function somewhat, but this alone cannot explain the discrepancy of 0.7 eV between theory and experiment in this case. Another possible reason for the discrepancy could be that the assumptions made for determining the work function by $I_t(s)$ measurements are not fulfilled. While the trapezoidal barrier is certainly an oversimplification to an actual tunnelling barrier, to first order the errors involved (e.g. image potential effects) cancel in $\Delta\Phi$. The apparent barrier height $\bar{\Phi}$ was found to be distance dependent in several experiments [213], but usually for small tip-sample distances of less than 6 Å which are not expected for the tunnelling conditions used above.

Possibly of more significance for the discrepancy is the structure of the sample. Dependent on Θ, there are either only small areas of free graphene between intercalated Eu or only small stripes of Eu for the measurements. We have chosen $\Theta = 12\%$ ML, i.e. half of a saturated p(2×2) Eu layer as compromise. This allowed us to measure above relatively big Eu islands (of ≈ 15 nm diameter) and to keep a distance of ≈ 3 nm to the next Eu structure for the measurements of the graphene. At this distance the graphene could still be influenced (e.g. n-doped) by the Eu. N-doping decreases the work function, which would lead to a decrease of the work function difference compared to the theory values, contrary to our results. Hence, the structure size should not contribute to the discrepancy.

The high corrugation of the intercalated Eu atoms in the STM data is more pronounced than that of the C atoms of the graphene layer on top (see Fig. 8.5), which indicates another possible

origin for the discrepancy: The tunnelling could possibly occur not only between the tip and C atoms but also between the tip and Eu atoms which would create an ambiguous situation for the $I_t(s)$ measurements. Hence $I_t(s)$ measurements may be unsuitable to determine the work function of the intercalated Eu structures.

The reduction of the work function above the adsorbed $(\sqrt{3}\times\sqrt{3})$R30° Eu islands has a direct relevance for STM image interpretation. Due to the lower tunnelling barrier compared to graphene, the tip will be in a larger distance from the Eu compared to the graphene to draw the same current in constant current mode imaging. Therefore, the 5 Å apparent height of the first Eu layer is a convolution of the structural height and the lower work function. As the first and the second Eu layer display to first order the same work functions, the apparent height of 3 - 3.4 Å measured for the second layer can be considered to be much closer to the structural height (compare Sec. 8.2.2).

8.4 Summary

Upon the deposition of Eu on graphene/Ir(111) many different structures occur in dependence of the deposition temperature (T_{growth}) and the deposited amount (Θ), an overview of which is given in the diagram in Fig. 8.25. The most striking difference between the structures originates in the intercalation of the Eu between graphene and Ir(111) which becomes relevant above 400 K.

In the lower temperature regime ($T_{\text{growth}} \leq 400$ K) and for closed TPG+CVD graphene films the Eu stays on top of the graphene and preferentially builds clusters, the sizes of which increase with both T_{growth} and Θ. The formation of the clusters is driven by the interplay of three effects: First, the metallic Eu-Eu binding leads to the local stability of $(\sqrt{3}\times\sqrt{3})$R30° structures. Second, electrons lower their kinetic energy by leaving the Eu *clusters*, thereby doping the graphene. Third, the Coulomb energy penalty associated with the charge transfer from Eu to graphene is strongly reduced for smaller clusters. These combined effects together with kinetic limitations lead to the preferential growth of dimers at 35 K in a local hexagonal arrangement until a cluster distance of $d \approx 14$ graphene unit cell repeat distances ($a_C = 2.461$ Å) is reached for $\Theta \approx 3.5\%$ ML and the clusters grow in size. This size increase leads, again due to the kinetic limitations, to formation of *2D clusters*, the height of which exceeds two monolayers only occasionally for Θ up to 25% ML. At this coverage, for coalesced *2D clusters*, LEED shows a $(\sqrt{3}\times\sqrt{3})$R30° pattern with respect to the graphene, demonstrating the epitaxial growth growth of the clusters.

With increasing T_{growth} the *2D clusters* grow in size and keep a larger distance between them while their local hexagonal order is maintained even for separations $\sim 20\,a_C$ (5 nm). Especially remarkable is the phase coexistence - in an intermediate coverage range at 300 K - of *2D clusters* (10-20 atoms in size) in two dimensional equilibrium with large, monolayer high Eu-islands in the $(\sqrt{3}\times\sqrt{3})$R30° structure [denoted as $\sqrt{3}$ *ML* in Fig. 8.25]. Shortly before the saturation coverage of these $\sqrt{3}$ *ML* islands is reached, island formation in the second Eu layer sets in [denoted as $\sqrt{3}$ *2.ML* in Fig. 8.25]. The structure of the $\sqrt{3}$ *2.ML* islands remains the same as of the first layer instead of building the bulk *bcc* structure of Eu. At 400 K the kinetic limitations for Eu growth are almost lifted and *3D clusters* form instead of the above mentioned phase equilibrium. These *3D clusters* have a typical height of three layers or more.

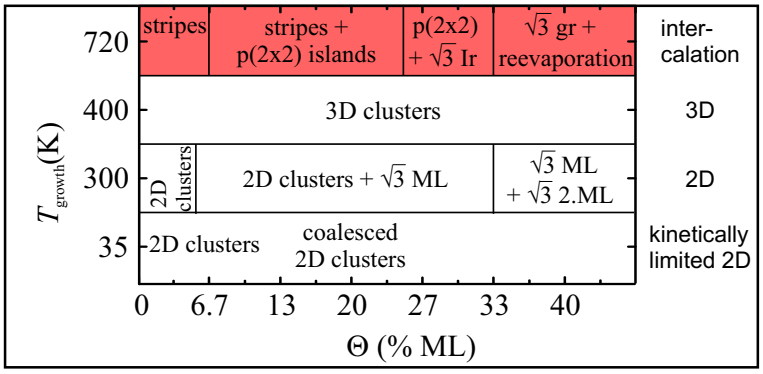

Figure 8.25: Diagram summarising the Eu structures on graphene/Ir(111) for different T_{growth} and Θ. At 720 K all Eu is intercalated, indicated by the red background colour. All borders are approximate. The structures are denoted as follows: (**2D clusters**): clusters of different sizes on graphene with a typical height of one or two layers. ($\sqrt{3}$ **ML**): monolayer high Eu islands on graphene in $(\sqrt{3}\times\sqrt{3})$R30° structure. ($\sqrt{3}$ **2.ML**): additional Eu islands on top of $\sqrt{3}$ islands, also in $(\sqrt{3}\times\sqrt{3})$R30° structure. (**3D clusters**): clusters with a typical height of ≥ 3 layers. (**stripes**): stripe patterns of intercalated Eu. (**p(2×2) islands**): islands of intercalated Eu with atoms arranged in a p(2×2) structure with respect to graphene. ($\sqrt{3}$ **Ir**): intercalated Eu with $(\sqrt{3}\times\sqrt{3})$R30° structure with respect to Ir(111). ($\sqrt{3}$ **gr**): intercalated Eu in the $(\sqrt{3}\times\sqrt{3})$R30° structure with respect to graphene.

Above 400 K the Eu begins to intercalate between the graphene and the Ir, a process which gains 2 eV per Eu atom. For deposition at T_{growth} =720 K a variety of equilibrium intercalate structures occur dependent on Θ, all of which have a height of one monolayer. This height is never exceeded and limits the maximum amount of intercalated Eu atoms. For low Θ the intercalate builds *stripes* of equal breadth, the dimensions and orientations of which are determined by the graphene moiré on Ir(111). With increasing Θ hexagonal intercalate islands emerge with the Eu atoms arranged in a *p(2×2)* structure with respect to graphene [denoted as *p(2×2)* islands in Fig. 8.25]. The dimensions and orientations of the *p(2×2)* islands are also determined by the graphene moiré. This originates in the binding energy differences within the moiré unit cell, which lead to a preferential presence of Eu at regions where the binding energy between graphene and Ir is ~ 0.

After the intercalate layer in the preferred *p(2×2)* structure is saturated at $\Theta \approx 25\%$ ML, the systems gains energy by building denser intercalate structures which are a $(\sqrt{3}\times\sqrt{3})$R30° structure with respect to Ir(111) [$\sqrt{3}$ *Ir* in Fig. 8.25] and finally a $(\sqrt{3}\times\sqrt{3})$R30° structure with respect to graphene [$\sqrt{3}$ *gr* in Fig. 8.25]. At 720 K additionally deposited Eu is re-evaporated into the vacuum. A shift of the Dirac cone of ~ -1.5 eV compared to pure graphene was found for both, the *p(2×2)* and the $\sqrt{3}$ *gr* structure. Thus, the degree of n-doping of graphene does not further increase upon transformation to the densest structure. For coexistence of phases with different doping affinities also coexistence of differently shifted Dirac cones were found. This indicates that the distribution of the electrons supplied to the graphene is limited within a few nanometres around the adsorbate or intercalate. The work function of Ir(111) is reduced by ~ 1.2 eV due to the presence of the graphene film on top and further reduced by up to 1.4 eV by adsorbed or intercalated Eu.

9 Summary and outlook

9.1 Summary

The ferromagnetic semiconductor EuO was grown on the metal single crystals Ni(100), Ir(100), Ir(111), and on graphene. The motivation for this study was to achieve epitaxial EuO films which are well suited for temperature and thickness dependent studies of EuO by scanning tunnelling spectroscopy (STS). These could give further insight into the nature of the metal-to-insulator transition which occurs for slightly O deficient EuO_{1-x}.

Characterisation was primarily done by means of in-situ scanning tunnelling microscopy (STM) and low energy electron diffraction (LEED). For the Ni(100) substrate, additional magneto optical Kerr effect (MOKE) and soft x-ray adsorption spectroscopy (XAS) measurements were performed ex-situ.

For the metal crystals the epitaxial growth is strongly influenced by interface effects. Therefore, the initial growth is described in detail for these substrates.

Eu oxide growth on Ni(100) shows a variety of different surface phases in the sub-monolayer regime, depending on the growth temperature (T_{growth}) and the flux ratio of Eu to O ($f_{\mathrm{Eu}}/f_{\mathrm{O}}$). At $T_{\mathrm{growth}} = 623$ K these phases include polar EuO(111), clusters which occur in three "magic" sizes, islands with a centred rectangular lattice which are decorated by stripes, and a EuO(100) like surface oxide with increased lattice constant and O vacancies arranged in a p(5×5) superstructure with respect to the Ni substrate. The latter structure is the optimum base for growing single phase EuO(100) films. Epitaxial EuO(100) with its [001] direction parallel to Ni[011] forms at $T_{\mathrm{growth}} = 723$ K and $f_{\mathrm{Eu}}/f_{\mathrm{O}} = 1.4$, and is compressively strained by 3% for thicknesses between 2 ML and 3 ML. For thicknesses above 3 ML the lattice increases to that of bulk EuO within the first 30 ML deposited.

After creation of a fully coalesced film of 2.5 ML thickness the growth parameters may be changed, as long as they comply with the used molecular beam epitaxy distillation technique. This is fulfilled as long as a sufficient Eu surplus is used and T_{growth} is high enough for re-evaporation of the excess Eu atoms. Even at $T_{\mathrm{growth}} = 593$ K and $f_{\mathrm{Eu}}/f_{\mathrm{O}} = 1.6$, i.e. at a drastically increased probability to introduce O vacancies into the EuO lattice, the films are stoichiometric within the detection limits of XAS and show no metallic behaviour in STM at 35 K. The Curie temperature, as determined by MOKE, is about 70 K for a 100 nm thick film, comparable to bulk EuO. Annealing at 673 K in Eu vapour (using the same Eu flux as during growth) generates sufficient conductivity to enable STM imaging even for a 100 nm thick film. This annealing introduces O vacancies into the film with a concentration of less than 1% at the surface as imaged by STM. Flat and large terraces, together with sharp LEED patterns with low diffuse intensity indicate the high crystalline quality of the EuO films on Ni(100).

On Ir(111) EuO grows without formation of surface oxides which have no structural counterpart in bulk EuO, contrary to the case of the Ni(100) substrate. Initially, a bilayer (BL) of Eu(111) forms in the flux ratio range $0.85 \leq f_{\mathrm{Eu}}/f_{\mathrm{O}} \leq 1.7$, and for $623\,\mathrm{K} \leq T_{\mathrm{growth}} \leq 723\,\mathrm{K}$. This BL EuO(111) has characteristic superstructures which range from a p(3×3) to a $(\sqrt{7}\times\sqrt{7})$R19.1° whereby the p(3×3) is preferred for lower T_{growth}. The work function of the BL EuO(111) is considerably increased by about 6 eV compared to the (100) surface of a EuO single crystal, whereby the additional surface dipole is created by the polarity of the rock-salt (111) surface. This proves that this BL is terminated by a negatively charged layer, i.e. by O-ions.

With increasing coverage additional phases emerge. For a nominal film thickness of one monolayer (ML) EuO(100), the Ir(111) is additionally covered by three rotational domains of a rock-salt structured ML of EuO(100), which has a lattice contracted by 7% compared to bulk EuO. A similar contraction was found for a BL EuO(100) on Ni(100), hence these smaller lattices origin probably in finite size effects. In contrast, the BL EuO(111) has a bulk-like or even slightly expanded lattice which enables a reduction of the surface electron density and thus a reduction of the polarity. The characteristic superstructures of the BL EuO(111) are no longer present for this deposited amount, indicating that the third layer of EuO(111) already reconstructs to lower the electrostatic potential. At least for $f_{\mathrm{Eu}}/f_{\mathrm{O}} = 1.7$ additionally a third phase is present at this nominal film thickness of 1 ML, which consists most probably of metallic Eu islands. For thicknesses of a few ML the films consist of EuO(100) and EuO(111) grains, whereby the ratio of EuO(100) to EuO(111) can be increased by initial usage of lower $f_{\mathrm{Eu}}/f_{\mathrm{O}}$.

Growth on the Ir(100) substrate was only briefly analysed by LEED. Also on this substrate the films consist of EuO(100) and EuO(111) grains for thicknesses of a few ML and the ratio of EuO(100)/EuO(111) can be increased by initial usage of lower $f_{\mathrm{Eu}}/f_{\mathrm{O}}$. Contrary to the case of Ir(111) the misalignment between EuO(100) and Ir(100) is high.

On graphene EuO can be grown as thin films of distinct, {100}-faceted grains. Depending on T_{growth}, the grains orient with EuO$\langle010\rangle \parallel \mathrm{C}\langle11\bar{2}0\rangle$ (for both $T_{\mathrm{growth}} = 723\,\mathrm{K}$ and $T_{\mathrm{growth}} = 553\,\mathrm{K}$) and EuO$\langle011\rangle \parallel \mathrm{C}\langle11\bar{2}0\rangle$ (for $T_{\mathrm{growth}} = 553\,\mathrm{K}$ only). For $T_{\mathrm{growth}} = 300\,\mathrm{K}$ no in-plane orientation of the grains was found, even after annealing to 873 K.

The morphology of the grains for a given film thickness is mainly determined by T_{growth} and by the annealing procedure. For films with a nominal thickness of about 3 ML the grains have a surface area in the order of several thousand square nanometres. Their typical height varies from 1.5 nm for a non annealed film grown at $T_{\mathrm{growth}} = 723\,\mathrm{K}$ to 3 nm for a film grown at $T_{\mathrm{growth}} = 300\,\mathrm{K}$ and annealed up to 873 K. As expectable, the grains' surface area decreases with increasing grain height for the same nominal film thickness. The grains' height influences their surface lattice constant which is $a_{\mathrm{EuO(100)}} = 3.5\,\text{Å}$ for 1.5 nm grain height and increases to 3.6 Å (i.e., almost to the bulk value) for 3 nm high grains. These values are similar to those found for the relaxation of EuO(100) on Ni(100) with increasing film thickness.

Except Ir(100), all tested substrates are suitable to grow high quality EuO films which are applicable for high resolution STM and STS measurements, but also have all their own restrictions. EuO on Ir(111) is the ideal system to analyse ML EuO(100) and BL EuO(111). It will also be

suitable to analyse the reconstruction of the third layer of the polar EuO(111). For analysis of thicker films it is less suitable as no method to grow single-phase EuO(100) or EuO(111) films was found. The inclusion of (111)-oriented grains makes STM very difficult for thicker films.

The single crystal quality of the EuO(100) films on Ni(100) together with their smooth surface makes Ni(100) a well suited substrate for temperature and thickness dependent studies of EuO by STS. The disadvantages of this substrate are (I) the difficulties to control the initial growth towards formation of single phase EuO(100) and (II) the ferromagnetism which complicates or even impedes magnetic measurements of the EuO films.

The EuO grains on graphene allow one to analyse distinct {100}-faceted grains of precisely measurable dimensions. The growth of these grains does not require a calibration of the Eu and O fluxes as precise as in the case of the films on Ni(100) because the initial growth phase on graphene is not crucial. The 90° angles between the grains' sides and the graphene require very slow scanning speeds for STM, especially for high grains, as otherwise tip crashes occur. But, after the tip is positioned on top of a grain STS measurements can be easily performed. The first recorded tunnelling spectra of EuO(100) with 1% O vacancies in the topmost layer exhibit states about 500 meV above the Fermi level which are most probably related to O vacancies.

The O vacancy concentration of the EuO(100) can be controlled by annealing in Eu vapour and by choosing an appropriate Eu surplus and temperature for the growth. This method can be used for EuO(100) on graphene without restrictions and for Ni(100) after a fully coalesced film has formed.

For a decreased lattice constant the ferromagnetic transition temperature (T_C) of EuO increases which lead to the idea of increasing T_C by epitaxial strain. A common behaviour of the EuO(100) films on Ni(100), Ir(111), and graphene was that the lattice constant of the first layers(s) was smaller than that of bulk EuO but increased to the bulk value with increasing film thickness within the first ~ 20 layers. Hence, this is probably a general behaviour and the exciting idea of increasing T_C of EuO through epitaxial strain probably must be buried.

During the investigation of the EuO on graphene, intercalation of Eu between the graphene and its Ir(111) substrate was observed. The intercalation is driven by an energy gain of 2 eV compared to Eu on top of graphene, but is, for closed graphene films, hindered by a penetration barrier for $T_{\mathrm{growth}} \leq 400\,\mathrm{K}$. The analysis of the systems Eu on and under graphene/Ir(111) was supported by density functional theory (DFT) calculations and angular resolved photoemission spectroscopy (ARPES).

In the lower temperature regime ($T_{\mathrm{growth}} \leq 400\,\mathrm{K}$) and for closed graphene films the Eu stays on top of the graphene and preferentially builds clusters, the sizes of which increase with both T_{growth} and Θ. The formation of the clusters is driven by the interplay of three effects: First, the metallic Eu-Eu binding leads to the local stability of $(\sqrt{3}\times\sqrt{3})$R30° structures. Second, electrons lower their kinetic energy by leaving the Eu clusters, thereby doping the graphene. Third, the Coulomb energy penalty associated with the charge transfer from Eu to graphene is strongly reduced for smaller clusters. These combined effects together with kinetic limitations lead initially to the preferential growth of dimers at 35 K in a local hexagonal arrangement. Upon further deposition at 35 K 2D

clusters form, which have a $(\sqrt{3} \times \sqrt{3})$R30° structure with respect to the graphene, demonstrating the epitaxial growth of the clusters.

With increasing T_{growth} the 2D clusters grow in size and keep a larger distance between them while their local hexagonal order is maintained even for separations $\sim 5\,\mathrm{nm}$. Especially remarkable is the phase coexistence - in an intermediate coverage range at 300 K - of 2D clusters in two dimensional equilibrium with large, monolayer high Eu-islands in the $(\sqrt{3} \times \sqrt{3})$R30° structure. Shortly before the saturation coverage of the first layer is reached, island formation in the second Eu layer sets in. The structure of the second layer remains the same as of the first layer instead of building the bulk *bcc* structure of Eu. At 400 K the kinetic limitations for Eu growth are almost lifted and 3D clusters form instead of the above mentioned phase equilibrium.

For deposition at T_{growth} =720 K a variety of equilibrium intercalate structures occur dependent on the deposited amount (Θ), all of which have a height of one monolayer. For low Θ the intercalate builds stripes of equal breadth, the dimensions and orientations of which are determined by the graphene moiré on Ir(111). With increasing Θ hexagonal intercalate islands emerge with the Eu atoms arranged in a p(2×2) structure with respect to graphene. The dimensions and orientations of the p(2×2) islands are also determined by the graphene moiré. This originates in the binding energy differences within the moiré unit cell, which lead to a preferential presence of Eu at regions where (almost) no binding between graphene and Ir occurs. After the intercalate layer in the preferred p(2×2) structure is saturated, the system gains energy by building denser intercalate structures up to a $(\sqrt{3} \times \sqrt{3})$R30° structure with respect to graphene.

The n-doping of the graphene shifts its Dirac cone by $\sim -1.5\,\mathrm{eV}$ for the intercalated p(2×2) structure and does not further increase for the $(\sqrt{3} \times \sqrt{3})$R30° phases. For coexistence of differently structured phases also differently shifted Dirac cones were found. This indicates that the distribution of the electrons supplied to the graphene is limited within a few nanometres around the adsorbate or intercalate. The work function of the Ir(111) is reduced by $\sim 1.2\,\mathrm{eV}$ due to the presence of the graphene film on top and further reduced by up to 1.4 eV by adsorbed or intercalated Eu.

9.2 Outlook

In this work, high quality EuO films were achieved which are well suited for scanning tunnelling spectroscopy. The next step ahead is thus to record point spectra and spectroscopy maps on the EuO surfaces. Doing this for different O vacancy concentrations and at different temperatures around T_{C} should give further insight into the mechanism of the metal-to-insulator transition of $EuO_{1\text{-}x}$.

Annealing of the films in Eu vapour is successful in creating O vacancies. An alternative procedure could be electron-stimulated desorption of oxygen [272] (i.e., electron bombardment), which could also be tested. Both of these methods have the disadvantage of creating the O vacancies at the surface which then have to diffuse through the bulk. Thus, it is possible that a vacancy concentration gradient is created in such samples, whereby the defect density is expected to decrease from the film surface to the substrate interface. Therefore, it is desirable to be able to control the

concentration of the Eu vacancies already during growth by adjusting T_{growth} and $f_{\mathrm{Eu}}/f_{\mathrm{O}}$. Due to the distillation mechanism [27], the O vacancy concentration increases with increasing $f_{\mathrm{Eu}}/f_{\mathrm{O}}$ and/or decreasing T_{growth}. To determine suitable parameter sets, series of films with different Eu excess and different T_{growth} should be grown. If such experiments are carried out on the Ni(100) substrate, the growth of the first three layers must be done with $T_{\mathrm{growth}} = 723$ K and $f_{\mathrm{Eu}}/f_{\mathrm{O}} = 1.4$ to avoid interface effects.

Due to the predicted finite size effects on T_{C} [69; 85] also experiments with different EuO film thicknesses are of interest, whereby MOKE measurements are the best choice if the thickness is homogeneous on the whole sample. For thickness dependent STS experiments, graphene is the most suitable substrate as it allows one to measure on EuO grains of different thickness on the same sample, while simultaneously a precise thickness determination of each grain by STM is possible.

Beside the achievement of EuO growth recipes on different conductive substrates for spectroscopic measurements, novel surface and interface structures were analysed. While some of these structures could be resolved unambiguously, several open questions remain.

The Eu surface oxides on Ni(100) were explored only for a small variation of the flux ratio range between $0.8 \leq f_{\mathrm{Eu}}/f_{\mathrm{O}} \leq 1.7$ at 623 K. To get a more complete overview of the surface phases a larger variation of $f_{\mathrm{Eu}}/f_{\mathrm{O}}$ is necessary and also a variation of T_{growth} is desirable. Pure Eu adsorption ($f_{\mathrm{Eu}}/f_{\mathrm{O}} = \infty$) was already tested. Thereby, the substrate was full of adsorbates and Eu islands had nucleated at ascending step edges. For $f_{\mathrm{Eu}}/f_{\mathrm{O}} \leq 0.8$ higher oxidation states of Eu than 2+ are expected and at least for considerably lower $f_{\mathrm{Eu}}/f_{\mathrm{O}}$ already completely different structures were observed [246]. The exploration of these further Eu surface phases could lead to a more complete understanding of the initial EuO film growth, especially of the period during which the Eu and O fluxes are established and larger variations of $f_{\mathrm{Eu}}/f_{\mathrm{O}}$ occur.

Highly valuable for the confirmation and/or improvement of the proposed models for the 'magic' clusters, the stripe islands and the p(5×5) superstructure oxide would be DFT calculations. Furthermore, the formation of EuO(100) on top of the p(5×5) phase could be analysed in more detail.

For the EuO growth on Ir(111) one of the three observed surface structures at $T_{\mathrm{growth}} = 723$ K remained undetermined as only its hexagonal superstructure could be resolved. From the deposited amounts of Eu and O and the areas of the other surface structures it was proposed that this phase consists of metallic Eu. This could be confirmed by adsorption of a full layer of pure Eu at 723 K. Such a pure layer should also allow one to determine the structure by LEED, if it is not possible to achieve atomic resolution with the STM.

On Ir(111), for sub-monolayer coverages initially only bilayers of EuO(111) grow while additionally monolayer high EuO(100) is found for a fully covered Ir surface. For thicker films it was found that the ratio of EuO(100) to Eu(111) surface increases with decreasing $f_{\mathrm{Eu}}/f_{\mathrm{O}}$. Thus, it is of interest to analyse by sub-monolayer growth in dependence of $f_{\mathrm{Eu}}/f_{\mathrm{O}}$ when the growth of EuO(100) sets in. This could possible reveal the reason for the nucleation of EuO(100) and also lead to a recipe to grow (almost) pure phases of either EuO(111) or EuO(100). Single phase EuO(111) would be especially valuable to analyse the reconstruction of this polar EuO with increasing thickness.

With spintronic applications in mind, it was proposed to use EuO to achieve proximity-induced

ferromagnetism in graphene [64]. For EuO on graphene/Ir(111) the magnetism could even be amplified by the presence of the intercalated Eu beneath the graphene. Thus, the investigation of the magnetic properties of this system is of great interest.

The Eu adsorption on graphene/Ir(111) demonstrates that the interplay of graphene's peculiar band structure, Coulomb energies and the chemistry of adsorbates determines their phase diagram and can lead to new phases like the phase of diluted Eu clusters coexisting with Eu islands.

Taking into account that adsorbates may play an important role for the functionalisation of graphene, more studies of such systems are desirable. An intriguing possibility is that one might be able to control the physics of adsorbates and their phases by gate voltages. Due to the delicate balance of two coexisting phases, which react sensitively to Pauli blocking and small changes of kinetic energy, Eu on graphene might be an ideal model system to study this physics. Furthermore, it will be interesting to investigate the magnetic properties of Eu islands and Eu clusters on graphene.

The investigation of magnetic properties will also be interesting for the intercalated Eu, especially as this system is stable in air which eases possible applications. Regarding the complex intercalate patterns, model calculations are desirable which make use of the proposed energy contributions and determine their relevance.

References

[1] H. A. Eick, N. C. Baenziger, and L. Eyring. J. Am. Chem. Soc. **78**, 5147 (1956). *Lower Oxides of Samarium and Europium. The Preparation and Crystal Structure of $SmO_{0.4-0.6}$, SmO and EuO.* 1

[2] B. T. Matthias, R. M. Bozorth, and J. H. Van Vleck. Phys. Rev. Lett. **7**, 160 (1961). *Ferromagnetic Interaction in EuO.* doi:10.1103/PhysRevLett.7.160. 1

[3] P. Wachter. Crit. Rev. Solid State Mater. Sci. **3**, 189 (1972). *The optical electrical and magnetic properties of the europium chalcogenides and the rare earth pnictides.* 1

[4] P. G. Steeneken, L. H. Tjeng, I. Elfimov, G. A. Sawatzky, G. Ghiringhelli, N. B. Brookes, and D.-J. Huang. Phys. Rev. Lett. **88**, 047201 (2002). *Exchange Splitting and Charge Carrier Spin Polarization in EuO.* doi:10.1103/PhysRevLett.88.047201. 1, 3, 4, 6, 7, 68

[5] T. S. Santos, J. S. Moodera, K. V. Raman, E. Negusse, J. Holroyd, J. Dvorak, M. Liberati, Y. U. Idzerda, and E. Arenholz. Phys. Rev. Lett. **101**, 147201 (2008). *Determining Exchange Splitting in a Magnetic Semiconductor by Spin-Filter Tunneling.* doi:10.1103/PhysRevLett.101.147201. 1

[6] J. Lettieri, V. Vaithyanathan, S. K. Eah, J. Stephens, V. Sih, D. D. Awschalom, J. Levy, and D. G. Schlom. Appl. Phys. Lett. **83**, 975 (2003). *Epitaxial growth and magnetic properties of EuO on (001) Si by molecular-beam epitaxy.* doi:10.1063/1.1593832, [link]. 7

[7] J. Holroyd, Y. U. Idzerda, and S. Stadler. J. Appl. Phys. **95**, 6571 (2004). *Properties of thin film europium oxide by x-ray magnetic circular dichroism.* doi:10.1063/1.1688653, [link].

[8] T. Matsumoto, K. Yamaguchi, M. Yuri, K. Kawaguchi, N. Koshizaki, and K. Yamada. J. Phys.: Condens. Matter **16**, 6017 (2004). *Preparation of Gd-doped EuO_{1-x} thin films and the magnetic and magneto-transport properties.* doi:10.1088/0953-8984/16/34/003, [link]. 1, 5, 66

[9] T. S. Santos and J. S. Moodera. Phys. Rev. B **69**, 241203 (2004). *Observation of spin filtering with a ferromagnetic EuO tunnel barrier.* doi:10.1103/PhysRevB.69.241203. 3, 7, 66

[10] A. Comment, J.-P. Ansermet, C. P. Slichter, H. Rho, C. S. Snow, and S. L. Cooper. Phys. Rev. B **72**, 014428 (2005). *Magnetic properties of pure and Gd-doped EuO probed by NMR.* doi:10.1103/PhysRevB.72.014428. 2

[11] J. Kuneš, W. Ku, and W. E. Pickett. J. Phys. Soc. Jpn. **74**, 1408 (2005). *Exchange coupling in Eu monochalcogenides from first principles.* doi:10.1143/JPSJ.74.1408. 4

[12] A. S. Borukhovich, N. I. Ignat'eva, A. I. Galyas, S. S. Dorofeĭchik, and K. I. Yanushkevich. JETP Lett. **84**, 502 (2006). *Thin-film ferromagnetic composite material for spintronics*. doi:10.1134/S0021364006210077.

[13] E. Negusse, J. Holroyd, M. Liberati, J. Dvorak, Y. U. Idzerda, T. S. Santos, J. S. Moodera, and E. Arenholz. J. Appl. Phys. **99**, 08E507 (2006). *Effect of electrode and EuO thickness on EuO-electrode interface in tunneling spin filter*. doi:10.1063/1.2176590, [link]. 7, 66

[14] H. Ott, S. J. Heise, R. Sutarto, Z. Hu, C. F. Chang, H. H. Hsieh, H.-J. Lin, C. T. Chen, and L. H. Tjeng. Phys. Rev. B **73**, 094407 (2006). *Soft x-ray magnetic circular dichroism study on Gd-doped EuO thin films*. doi:10.1103/PhysRevB.73.094407. 1, 5, 7

[15] M. J. Bierman, K. M. Van Heuvelen, D. Schmeißer, T. C. Brunold, and S. Jin. Adv. Mater. **19**, 2677 (2007). *Ferromagnetic Semiconducting EuO Nanorods*. doi:10.1002/adma.200602612, [link].

[16] A. Schmehl, V. Vaithyanathan, A. Herrnberger, S. Thiel, C. Richter, M. Liberati, T. Heeg, M. Röckerath, L. F. Kourkoutis, S. Mühlbauer, P. Böni, D. A. Muller, Y. Barash, J. Schubert, Y. Idzerda, J. Mannhart, and D. G. Schlom. Nat. Mater. **6**, 882 (2007). *Epitaxial integration of the highly spin-polarized ferromagnetic semiconductor EuO with silicon and GaN*. doi:10.1038/nmat2012. 1, 7, 8

[17] N. J. C. Ingle and I. S. Elfimov. Phys. Rev. B **77**, 121202 (2008). *Influence of epitaxial strain on the ferromagnetic semiconductor EuO: First-principles calculations*. doi:10.1103/PhysRevB.77.121202. 1, 4, 5, 8, 69

[18] G. van der Laan, E. Arenholz, A. Schmehl, and D. G. Schlom. Phys. Rev. Lett. **100**, 067403 (2008). *Weak Anisotropic X-Ray Magnetic Linear Dichroism at the Eu $M_{4,5}$ Edges of Ferromagnetic EuO(001): Evidence for $4f$-State Contributions*. doi:10.1103/PhysRevLett.100.067403.

[19] S. Mühlbauer, P. Böni, R. Georgii, A. Schmehl, D. G. Schlom, and J. Mannhart. J. Phys.: Condens. Matter **20**, 104230 (2008). *Field and temperature dependence of the magnetization in ferromagnetic EuO thin films*. doi:10.1088/0953-8984/20/10/104230, [link].

[20] R. P. Panguluri, T. S. Santos, E. Negusse, J. Dvorak, Y. Idzerda, J. S. Moodera, and B. Nadgorny. Phys. Rev. B **78**, 125307 (2008). *Half-metallicity in europium oxide conductively matched with silicon*. doi:10.1103/PhysRevB.78.125307. 66

[21] R. W. Ulbricht, A. Schmehl, T. Heeg, J. Schubert, and D. G. Schlom. Appl. Phys. Lett. **93**, 102105 (2008). *Adsorption-controlled growth of EuO by molecular-beam epitaxy*. doi:10.1063/1.2973180, [link]. 7

[22] E. Arenholz, A. Schmehl, D. G. Schlom, and G. van der Laan. J. of Appl. Phys. **105**, 07E101 (2009). *Contribution of Eu 4f states to the magnetic anisotropy of EuO*. doi:10.1063/1.3054364, [link].

[23] A. Borukhovich, N. Ignat'eva, K. Yanushkevich, A. Stognii, and Y. A. Fedotova. JETP Lett. **89**, 191 (2009). *Mössbauer spectroscopy study of the EuO:Fe spintronic material*. doi:10.1134/S0021364009040067, [link].

[24] M. Kok, J. N. Beukers, and A. Brinkman. J. Appl. Phys. **105**, 07C919 (2009). *Spin-polarized tunneling through a ferromagnetic insulator*. doi:10.1063/1.3068643, [link].

[25] M. Müller, G.-X. Miao, and J. S. Moodera. Europhys. Lett. **88**, 47006 (2009). *Exchange splitting and bias-dependent transport in EuO spin filter tunnel barriers*. doi:10.1209/0295-5075/88/47006, [link]. 66

[26] N. M. Souza-Neto, D. Haskel, Y.-C. Tseng, and G. Lapertot. Phys. Rev. Lett. **102**, 057206 (2009). *Pressure-Induced Electronic Mixing and Enhancement of Ferromagnetic Ordering in EuX (X = Te, Se, S, O) Magnetic Semiconductors*. doi:10.1103/PhysRevLett.102.057206.

[27] R. Sutarto, S. G. Altendorf, B. Coloru, M. Moretti Sala, T. Haupricht, C. F. Chang, Z. Hu, C. Schüßler-Langeheine, N. Hollmann, H. Kierspel, H. H. Hsieh, H.-J. Lin, C. T. Chen, and L. H. Tjeng. Phys. Rev. B **79**, 205318 (2009). *Epitaxial and layer-by-layer growth of EuO thin films on yttria-stabilized cubic zirconia (001) using MBE distillation*. doi:10.1103/PhysRevB.79.205318. 7, 8, 33, 71, 143

[28] R. Sutarto, S. G. Altendorf, B. Coloru, M. Moretti Sala, T. Haupricht, C. F. Chang, Z. Hu, C. Schüßler-Langeheine, N. Hollmann, H. Kierspel, J. A. Mydosh, H. H. Hsieh, H.-J. Lin, C. T. Chen, and L. H. Tjeng. Phys. Rev. B **80**, 085308 (2009). *Epitaxy, stoichiometry, and magnetic properties of Gd-doped EuO films on YSZ (001)*. doi:10.1103/PhysRevB.80.085308. 5, 95

[29] Y. Wang, M. K. Niranjan, J. D. Burton, J. M. An, K. D. Belashchenko, and E. Y. Tsymbal. Phys. Rev. B **79**, 212408 (2009). *Prediction of a spin-polarized two-dimensional electron gas at the $LaAlO_3/EuO(001)$ interface*. doi:10.1103/PhysRevB.79.212408.

[30] J. Beukers, J. Kleibeuker, G. Koster, D. Blank, G. Rijnders, H. Hilgenkamp, and A. Brinkman. Thin Solid Films **518**, 5173 (2010). *Epitaxial EuO thin films by pulsed laser deposition monitored by in situ x-ray photoelectron spectroscopy*. doi:10.1016/j.tsf.2010.04.071, [link]. 4

[31] S. J. Blundell, T. Lancaster, F. L. Pratt, P. J. Baker, W. Hayes, J.-P. Ansermet, and A. Comment. Phys. Rev. B **81**, 092407 (2010). *Phase transition in the localized ferromagnet EuO probed by μSR*. doi:10.1103/PhysRevB.81.092407.

[32] M. Matsubara, A. Schmehl, J. Mannhart, D. G. Schlom, and M. Fiebig. Phys. Rev. B **81**, 214447 (2010). *Large nonlinear magneto-optical effect in the centrosymmetric ferromagnetic semiconductor EuO*. doi:10.1103/PhysRevB.81.214447.

[33] H. Miyazaki, H. J. Im, K. Terashima, S. Yagi, M. Kato, K. Soda, T. Ito, and S. Kimura. Appl. Phys. Lett. **96**, 232503 (2010). *La-doped EuO: A rare earth ferromagnetic semiconductor with the highest Curie temperature*. doi:10.1063/1.3416911, [link].

[34] V. G. Storchak, D. G. Eshchenko, E. Morenzoni, N. Ingle, W. Heiss, T. Schwarzl, G. Springholz, R. L. Kallaher, and S. von Molnár. Phys. Rev. B **81**, 153201 (2010). *Magnetic polarons in Eu-based films of magnetic semiconductors*. doi:10.1103/PhysRevB.81.153201.

[35] A. G. Swartz, J. Ciraldo, J. J. I. Wong, Y. Li, W. Han, T. Lin, S. Mack, J. Shi, D. D. Awschalom, and R. K. Kawakami. Appl. Phys. Lett. **97**, 112509 (2010). *Epitaxial EuO thin films on GaAs*. doi:10.1063/1.3490649, [link]. 1

[36] I. Žutić, J. Fabian, and S. Das Sarma. Rev. Mod. Phys. **76**, 323 (2004). *Spintronics: Fundamentals and applications*. doi:10.1103/RevModPhys.76.323. 1

[37] S. A. Wolf, D. D. Awschalom, R. A. Buhrman, J. M. Daughton, S. Von Molnar, M. L. Roukes, A. Y. Chtchelkanova, and D. M. Treger. Science **294**, 1488 (2001). *Spintronics: A spin-based electronics vision for the future*. doi:10.1126/science.1065389. 1

[38] G. Schmidt, D. Ferrand, L. W. Molenkamp, A. T. Filip, and B. J. van Wees. Phys. Rev. B **62**, R4790 (2000). *Fundamental obstacle for electrical spin injection from a ferromagnetic metal into a diffusive semiconductor*. doi:10.1103/PhysRevB.62.R4790. 1

[39] A. Mauger and C. Godart. Phys. Rep. **141**, 51 (1986). *The magnetic, optical, and transport properties of representatives of a class of magnetic semiconductors: The europium chalcogenides*. doi:10.1016/0370-1573(86)90139-0, [link]. 1, 4, 5, 65

[40] D. DiMarzio, M. Croft, N. Sakai, and M. W. Shafer. Phys. Rev. B **35**, 8891 (1987). *Effect of pressure on the electrical resistance of EuO*. doi:10.1103/PhysRevB.35.8891. 1, 8

[41] M. M. Abd-Elmeguid and R. D. Taylor. Phys. Rev. B **42**, 1048 (1990). *Onset of valence and magnetic instabilities in the ferromagnetic semiconductor EuO at high pressures*. doi:10.1103/PhysRevB.42.1048. 1

[42] M. R. Oliver, J. O. Dimmock, A. L. McWhorter, and T. B. Reed. Phys. Rev. B **5**, 1078 (1972). *Conductivity Studies in Europium Oxide*. doi:10.1103/PhysRevB.5.1078. 1

[43] Y. Shapira, S. Foner, and T. B. Reed. Phys. Rev. B **8**, 2299 (1973). *EuO. I. Resistivity and Hall Effect in Fields up to 150 kOe*. doi:10.1103/PhysRevB.8.2299. 4

[44] T. Penney, M. W. Shafer, and J. B. Torrance. Phys. Rev. B **5**, 3669 (1972). *Insulator-Metal Transition and Long-Range Magnetic Order in EuO*. doi:10.1103/PhysRevB.5.3669. 1

[45] M. R. Oliver, J. A. Kafalas, J. O. Dimmock, and T. B. Reed. Phys. Rev. Lett. **24**, 1064 (1970). *Pressure Dependence of the Electrical Resistivity of EuO*. doi:10.1103/PhysRevLett.24.1064. 1, 2

[46] S. von Molnar and M. W. Shafer. J. Appl. Phys. **41**, 1093 (1970). *Transport in Gd-Doped EuO*. doi:10.1063/1.1658826, [link]. 1, 5

[47] J. B. Torrance, M. W. Shafer, and T. R. McGuire. Phys. Rev. Lett. **29**, 1168 (1972). *Bound Magnetic Polarons and the Insulator-Metal Transition in EuO*. doi:10.1103/PhysRevLett.29.1168. 2, 65

[48] R. Schiller and W. Nolting. Phys. Rev. Lett. **86**, 3847 (2001). *Prediction of a Surface State and a Related Surface Insulator-Metal Transition for the (100) Surface of Stochiometric EuO*. doi:10.1103/PhysRevLett.86.3847. 6, 7, 98

[49] R. Schiller, W. Müller, and W. Nolting. Phys. Rev. B **64**, 134409 (2001). *Kondo lattice model: Application to the temperature-dependent electronic structure of EuO(100) films*. doi:10.1103/PhysRevB.64.134409. 2, 4, 6, 8

[50] H. Rho, C. S. Snow, S. L. Cooper, Z. Fisk, A. Comment, and J.-P. Ansermet. Phys. Rev. Lett. **88**, 127401 (2002). *Evolution of Magnetic Polarons and Spin-Carrier Interactions through the Metal-Insulator Transition in* $Eu1 - xGdxO$. doi:10.1103/PhysRevLett.88.127401. 2

[51] P. Sinjukow and W. Nolting. Phys. Rev. B **68**, 125107 (2003). *Metal-insulator transition in EuO*. doi:10.1103/PhysRevB.68.125107. 2, 6

[52] P. Sinjukow and W. Nolting. Phys. Rev. B **69**, 214432 (2004). *Fully self-consistent determination of transport properties in Eu -rich EuO*. doi:10.1103/PhysRevB.69.214432. 2, 4

[53] U. Yu and B. I. Min. Phys. Rev. B **74**, 094413 (2006). *Magnetic-phase transition in the magnetic-polaron system studied with the Monte Carlo method: Anomalous specific heat of* $EuB6$. doi:10.1103/PhysRevB.74.094413. 2

[54] M. Arnold and J. Kroha. Physica C **460-462**, 1137 (2007). *Simultaneous ferromagnetic and semiconductor-metal transition in EuO*. doi:10.1016/j.physc.2007.03.240, [link].

[55] M. Arnold and J. Kroha. Phys. Rev. Lett. **100**, 046404 (2008). *Simultaneous Ferromagnetic Metal-Semiconductor Transition in Electron-Doped EuO*. doi:10.1103/PhysRevLett.100.046404. 1

[56] M. Müller, G.-X. Miao, and J. S. Moodera. J. Appl. Phys. **105**, 07C917 (2009). *Thickness dependence of ferromagnetic- and metal-insulator transition in thin EuO films*. doi:10.1063/1.3063673, [link]. 1, 8, 66

[57] J. Schoenes and P. Wachter. Phys. Rev. B **9**, 3097 (1974). *Exchange optics in Gd-doped EuO*. doi:10.1103/PhysRevB.9.3097. 1, 4, 5

[58] S.-i. Kimura, T. Ito, H. Miyazaki, T. Mizuno, T. Iizuka, and T. Takahashi. Phys. Rev. B **78**, 052409 (2008). *Electronic inhomogeneity EuO: Possibility of magnetic polaron states*. doi:10.1103/PhysRevB.78.052409. 2

[59] M. Fäth, S. Freisem, A. A. Menovsky, Y. Tomioka, J. Aarts, and J. A. Mydosh. Science **285**, 1540 (1999). *Spatially Inhomogeneous Metal-Insulator Transition in Doped Manganites.* doi:10.1126/science.285.5433.1540, [link]. 2

[60] C. Renner, G. Aeppli, and H. Ronnow. Mater. Sci. Eng. C **25**, 775 (2005). *Charge ordering, stripes and phase separation in manganese perovskite oxides: An STM/STS study.* doi:10.1016/j.msec.2005.06.042, [link].

[61] Y. J. Chang, J. S. Yang, Y. S. Kim, D. H. Kim, T. W. Noh, D.-W. Kim, E. Oh, B. Kahng, and J.-S. Chung. Phys. Rev. B **76**, 075118 (2007). *Surface versus bulk characterizations of electronic inhomogeneity in a $VO2$ thin film.* doi:10.1103/PhysRevB.76.075118. 2

[62] F. Meier, L. Zhou, J. Wiebe, and R. Wiesendanger. Science **320**, 82 (2008). *Revealing magnetic interactions from single-atom magnetization curves.* 2

[63] J. Fransson, O. Eriksson, and A. V. Balatsky. Phys. Rev. B **81**, 115454 (2010). *Theory of spin-polarized scanning tunneling microscopy applied to local spins.* doi:10.1103/PhysRevB.81.115454. 2

[64] H. Haugen, D. Huertas-Hernando, and A. Brataas. Phys. Rev. B **77**, 115406 (2008). *Spin transport in proximity-induced ferromagnetic graphene.* doi:10.1103/PhysRevB.77.115406. 2, 13, 144

[65] R. Bachmann and P. Wachter. Solid State Commun. **6**, 711 (1968). *Magnetic effects on the low temperature photoconductivity of EuO and EuS.* doi:10.1016/0038-1098(68)90570-X, [link]. 4

[66] J. H. Greiner and G. J. Fan. Appl. Phys. Lett. **9**, 27 (1966). *LONGITUDINAL MAGNETO-OPTICAL KERR EFFECT IN EuO AND EuS.* doi:10.1063/1.1754584, [link]. 4

[67] J. C. Suits and K. Lee. J. Appl. Phys. **42**, 3258 (1971). *Giant Magneto-Optical Kerr Effect in EuO.* doi:10.1063/1.1660721, [link]. 4, 7

[68] S. Q. Shi, C. Y. Ouyang, Q. Fang, J. Q. Shen, W. H. Tang, and C. R. Li. Europhys. Lett. **83**, 69001 (2008). *Electronic structure and magnetism of EuX (X = O, S, Se and Te): A first-principles investigation.* doi:10.1209/0295-5075/83/69001, [link]. 4

[69] R. Rausch and W. Nolting. J. Phys.: Condens. Matter **21**, 376002 (6pp) (2009). *The Curie temperature of thin ferromagnetic films.* doi:10.1088/0953-8984/21/37/376002, [link]. 8, 70, 143

[70] W. Söllinger, W. Heiss, R. T. Lechner, K. Rumpf, P. Granitzer, H. Krenn, and G. Springholz. Phys. Rev. B **81**, 155213 (2010). *Exchange interactions in europium monochalcogenide magnetic semiconductors and their dependence on hydrostatic strain.* doi:10.1103/PhysRevB.81.155213. 4

[71] X. Wan, J. Dong, and S. Y. Savrasov. Phys. Rev. B **83**, 205201 (2011). *Mechanism of magnetic exchange interactions in europium monochalcogenides*. doi:10.1103/PhysRevB.83.205201. 4

[72] H. A. Mook. Phys. Rev. Lett. **46**, 508 (1981). *Temperature Dependence of the Spin Dynamics of EuO*. doi:10.1103/PhysRevLett.46.508. 4

[73] H. Lee, J.-Y. Kim, K.-J. Rho, B.-G. Park, and J.-H. Park. J. Appl. Phys. **102**, 053903 (2007). *Temperature dependent phase transition of EuO on MgO(100)*. doi:10.1063/1.2775297, [link]. 4, 7

[74] W. Nolting, G. Borstel, and W. Borgiel. Phys. Rev. B **35**, 7015 (1987). *Dynamical corrections to density-functional theory for quasiparticles in ferromagnetic 4f systems. I. T=0 results for EuO*. doi:10.1103/PhysRevB.35.7015. 4

[75] M. W. Shafer, J. B. Torrance, and T. Penney. J. Phys. Chem. Solids **33**, 2251 (1972). *Relationship of crystal growth parameters to the stoichiometry of EuO as determined by I.R. and conductivity measurements*. doi:10.1016/S0022-3697(72)80299-3, [link]. 5, 7, 33, 65

[76] M. Schöck, C. Sürgers, and H. v. Löhneysen. Thin Solid Films **428**, 11 (2003). *Structure and electronic properties of ultrathin gold films on vicinal silicon(111)*. doi:10.1016/S0040-6090(02)01248-8, [link]. 6

[77] K. Ahn and J. Suits. IEEE Trans. Magn. **3**, 453 (1967). *Preparation and properties of EuO films*. doi:10.1109/TMAG.1967.1066089. 7

[78] K. Y. Ahn and T. R. McGuire. J. Appl. Phys. **39**, 5061 (1968). *Magnetic and Magneto-optic Properties of EuO Films Doped with Trivalent Rare-Earth Oxide*. doi:10.1063/1.1655924, [link]. 7

[79] K. Y. Ahn, K. N. Tu, and W. Reuter. J. Appl. Phys. **42**, 1769 (1971). *Preparation and Structure of Fe-Doped EuO Films*. doi:10.1063/1.1660425, [link].

[80] T. R. McGuire, G. F. Petrich, B. L. Olson, V. L. Moruzzi, and K. Y. Ahn. J. Appl. Phys. **42**, 1775 (1971). *Magnetic and Magneto-Optical Properties of Fe-Doped EuO Films*. doi:10.1063/1.1660428, [link]. 7

[81] O. Massenet, Y. Capiomont, and N. V. Dang. J. Appl. Phys. **45**, 3593 (1974). *Effects of high nonstoichiometry on EuO properties*. doi:10.1063/1.1663822, [link]. 7

[82] N. Iwata, G. Pindoria, T. Morishita, and K. Kohn. J. Phys. Soc. Jpn. **69**, 230 (2000). *Preparation and Magnetic Properties of EuO Thin Films Epitaxially Grown on MgO and SrTiO3 Substrates*. doi:10.1143/JPSJ.69.230. 7, 66

[83] D. B. McWhan, P. C. Souers, and G. Jura. Phys. Rev. **143**, 385 (1966). *Magnetic and Structural Properties of Europium Metal and Europium Monoxide at High Pressure*. doi:10.1103/PhysRev.143.385. 8

[84] H. G. Zimmer, K. Takemura, K. Syassen, and K. Fischer. Phys. Rev. B **29**, 2350 (1984). *Insulator-metal transition and valence instability in EuO near 130 kbar.* doi:10.1103/PhysRevB.29.2350. 8

[85] R. Schiller and W. Nolting. Solid State Commun. **110**, 121 (1999). *Thickness dependent Curie temperatures of ferromagnetic Heisenberg films.* doi:10.1016/S0038-1098(98)00593-6, [link]. 8, 95, 143

[86] S. Altieri, L. H. Tjeng, and G. A. Sawatzky. Thin Solid Films **400**, 9 (2001). *Ultrathin oxide films on metals: new physics and new chemistry?* doi:10.1016/S0040-6090(01)01484-5. 8, 70

[87] S. Altieri, M. Finazzi, H. H. Hsieh, M. W. Haverkort, H.-J. Lin, C. T. Chen, S. Frabboni, G. C. Gazzadi, A. Rota, S. Valeri, and L. H. Tjeng. Phys. Rev. B **79**, 174431 (2009). *Image charge screening: A new approach to enhance magnetic ordering temperatures in ultrathin correlated oxide films.* doi:10.1103/PhysRevB.79.174431. 8, 70

[88] C. Franchini, R. Podloucky, F. Allegretti, F. Li, G. Parteder, S. Surnev, and F. P. Netzer. Phys. Rev. B **79**, 035420 (2009). *Structural and vibrational properties of two-dimensional Mn_xO_y layers on Pd(100): Experiments and density functional theory calculations.* doi:10.1103/PhysRevB.79.035420. 8, 9, 50

[89] E. Lundgren, A. Mikkelsen, J. N. Andersen, G. Kresse, M. Schmid, and P. Varga. J. Phys. Condens. Matter **18**, R481 (2006). *Surface oxides on close-packed surfaces of late transition metals.* doi:10.1088/0953-8984/18/30/R01, [link]. 9, 58

[90] G. Zheng and E. I. Altman. Surf. Sci. **462**, 151 (2000). *The oxidation of Pd(111).* doi:10.1016/S0039-6028(00)00599-9, [link]. 9

[91] G. Zheng and E. I. Altman. Surf. Sci. **504**, 253 (2002). *The oxidation mechanism of Pd(100).* doi:10.1016/S0039-6028(02)01104-4, [link].

[92] E. Lundgren, G. Kresse, C. Klein, M. Borg, J. N. Andersen, M. De Santis, Y. Gauthier, C. Konvicka, M. Schmid, and P. Varga. Phys. Rev. Lett. **88**, 246103 (2002). *Two-Dimensional Oxide on Pd(111).* doi:10.1103/PhysRevLett.88.246103.

[93] M. Todorova, E. Lundgren, V. Blum, A. Mikkelsen, S. Gray, J. Gustafson, M. Borg, J. Rogal, K. Reuter, J. N. Andersen, and M. Scheffler. Surf. Sci. **541**, 101 (2003). *The Pd(100)–$(\sqrt{5} \times \sqrt{5})R27°$-O surface oxide revisited.* doi:10.1016/S0039-6028(03)00873-2, [link].

[94] J. Klikovits, E. Napetschnig, M. Schmid, N. Seriani, O. Dubay, G. Kresse, and P. Varga. Phys. Rev. B **76**, 045405 (2007). *Surface oxides on Pd(111): STM and density functional calculations.* doi:10.1103/PhysRevB.76.045405. 50, 58

[95] P. Kostelník, N. Seriani, G. Kresse, A. Mikkelsen, E. Lundgren, V. Blum, T. Šikola, P. Varga, and M. Schmid. Surf. Sci. **601**, 1574 (2007). *The Pd(100)-$(\sqrt{5} \times \sqrt{5})R27°$ surface oxide: A LEED, DFT and STM study.* doi:10.1016/j.susc.2007.01.026, [link]. 50

[96] H. H. Kan and J. F. Weaver. Surf. Sci. **603**, 2671 (2009). *Mechanism of PdO thin film formation during the oxidation of Pd(111).* doi:10.1016/j.susc.2009.06.023, [link]. 9

[97] J. Gustafson, A. Mikkelsen, M. Borg, E. Lundgren, L. Köhler, G. Kresse, M. Schmid, P. Varga, J. Yuhara, X. Torrelles, C. Quirós, and J. N. Andersen. Phys. Rev. Lett. **92**, 126102 (2004). *Self-Limited Growth of a Thin Oxide Layer on Rh(111).* doi:10.1103/PhysRevLett.92.126102. 9

[98] M. Ritter, W. Ranke, and W. Weiss. Phys. Rev. B **57**, 7240 (1998). *Growth and structure of ultrathin FeO films on Pt(111) studied by STM and LEED.* doi:10.1103/PhysRevB.57.7240. 9

[99] L. Giordano, G. Pacchioni, J. Goniakowski, N. Nilius, E. D. L. Rienks, and H.-J. Freund. Phys. Rev. B **76**, 075416 (2007). *Interplay between structural, magnetic, and electronic properties in a FeO/Pt(111) ultrathin film.* doi:10.1103/PhysRevB.76.075416. 9, 75

[100] G. Ketteler and W. Ranke. J. Phys. Chem. B **107**, 4320 (2003). *Heteroepitaxial Growth and Nucleation of Iron Oxide Films on Ru(0001).* doi:10.1021/jp027265f, [link]. 9

[101] S. Surnev, G. Kresse, M. G. Ramsey, and F. P. Netzer. Phys. Rev. Lett. **87**, 086102 (2001). *Novel Interface-Mediated Metastable Oxide Phases: Vanadium Oxides on Pd(111).* doi:10.1103/PhysRevLett.87.086102. 9

[102] J. Schoiswohl, S. Surnev, F. P. Netzer, and G. Kresse. J. Phys. Condens. Matter **18**, R1 (2006). *Vanadium oxide nanostructures: from zero- to three-dimensional.* doi:10.1088/0953-8984/18/4/R01, [link]. 9

[103] S. Agnoli, M. Sambi, G. Granozzi, J. Schoiswohl, S. Surnev, F. P. Netzer, M. Ferrero, A. M. Ferrari, and C. Pisani. J. Phys. Chem. B **109**, 17197 (2005). *Experimental and Theoretical Study of a Surface Stabilized Monolayer Phase of Nickel Oxide on Pd(100).* doi:10.1021/jp052394s, [link]. 9

[104] M. Caffio, B. Cortigiani, G. Rovida, A. Atrei, and C. Giovanardi. J. Phys. Chem. B **108**, 9919 (2004). *Early Stages of NiO Growth on Ag(001): A Study by LEIS, XPS, and LEED.* doi:10.1021/jp037805o, [link]. 9

[105] M. Caffio, A. Atrei, B. Cortigiani, and G. Rovida. J. Phys. Condens. Matter **18**, 2379 (2006). *STM study of the nanostructures prepared by deposition of NiO on Ag(001).* doi:10.1088/0953-8984/18/8/003, [link]. 9

[106] W. Meyer, D. Hock, K. Biedermann, M. Gubo, S. Müller, L. Hammer, and K. Heinz. Phys. Rev. Lett. **101**, 016103 (2008). *Coexistence of Rocksalt and Wurtzite Structure in Nanosized CoO Films.* doi:10.1103/PhysRevLett.101.016103. 9

[107] C. Hagendorf, S. Sachert, B. Bochmann, K. Kostov, and W. Widdra. Phys. Rev. B **77**, 075406 (2008). *Growth, atomic structure, and vibrational properties of MnO ultrathin films on Pt(111).* doi:10.1103/PhysRevB.77.075406. 9

[108] F. Li, G. Parteder, F. Allegretti, C. Franchini, R. Podloucky, S. Surnev, and F. P. Netzer. J. Phys. Condens. Matter **21**, 134008 (2009). *Two-dimensional manganese oxide nanolayers on Pd (100): the surface phase diagram.* 9, 43

[109] P. W. Tasker. J. Phys. C: Solid State Phys. **12**, 4977 (1979). *The stability of ionic crystal surfaces.* doi:10.1088/0022-3719/12/22/036, [link]. 9

[110] D. Wolf. Phys. Rev. Lett. **68**, 3315 (1992). *Reconstruction of NaCl surfaces from a dipolar solution to the Madelung problem.* doi:10.1103/PhysRevLett.68.3315. 9, 11

[111] M. Bowker, P. Stone, R. Smith, E. Fourre, M. Ishii, and N. H. de Leeuw. Surf. Sci. **600**, 1973 (2006). *The surface structure of BaO on Pt(111): (2×2)-reconstructed BaO(111).* doi:10.1016/j.susc.2006.02.041, [link]. 9, 11

[112] J. Goniakowski, F. Finocchi, and C. Noguera. Rep. Prog. Phys. **71**, 016501 (2008). *Polarity of oxide surfaces and nanostructures.* doi:10.1088/0034-4885/71/1/016501, [link]. 10, 11

[113] M. Kiguchi, S. Entani, K. Saiki, T. Goto, and A. Koma. Phys. Rev. B **68**, 115402 (2003). *Atomic and electronic structure of an unreconstructed polar MgO(111) thin film on Ag(111).* doi:10.1103/PhysRevB.68.115402. 11, 87

[114] W. Hebenstreit, M. Schmid, J. Redinger, R. Podloucky, and P. Varga. Phys. Rev. Lett. **85**, 5376 (2000). *Bulk Terminated NaCl(111) on Aluminum: A Polar Surface of an Ionic Crystal?* doi:10.1103/PhysRevLett.85.5376. 11

[115] S. Sindhu, M. Heiler, K.-M. Schindler, and H. Neddermeyer. Surf. Sci. **541**, 197 (2003). *A photoemission study of CoO-films on Au(111).* doi:10.1016/S0039-6028(03)00917-8, [link]. 11

[116] F. Rohr, K. Wirth, J. Libuda, D. Cappus, M. Bäumer, and H.-J. Freund. Surf. Sci. **315**, L977 (1994). *Hydroxyl driven reconstruction of the polar NiO(111) surface.* doi:10.1016/0039-6028(94)90529-0, [link]. 11

[117] A. Barbier, G. Renaud, and A. Stierle. Surf. Sci. **402-404**, 757 (1998). *The NiO(111)-(1×1) surface.* doi:10.1016/S0039-6028(97)01020-0, [link]. 11

[118] G. Binnig, H. Rohrer, C. Gerber, and E. Weibel. Phys. Rev. Lett. **50**, 120 (1983). *7 × 7 Reconstruction on Si(111) Resolved in Real Space.* doi:10.1103/PhysRevLett.50.120. 11

[119] D. D. Chambliss, R. J. Wilson, and S. Chiang. Phys. Rev. Lett. **66**, 1721 (1991). *Nucleation of ordered Ni island arrays on Au(111) by surface-lattice dislocations.* doi:10.1103/PhysRevLett.66.1721. 11

[120] A. Schmidt, W. Meier, L. Hammer, and K. Heinz. J. Phys. Condens. Matter **14**, 12353 (2002). *Deep-going reconstruction of Ir(100)-5x1.* doi:10.1088/0953-8984/14/47/310. 11, 29

[121] H. P. Bonzel, C. R. Helms, and S. Kelemen. Phys. Rev. Lett. **35**, 1237 (1975). *Observation of a Change in the Surface Electronic Structure of Pt(100) Induced by Reconstruction.* doi:10.1103/PhysRevLett.35.1237. 11

[122] F. Finocchi, A. Barbier, J. Jupille, and C. Noguera. Phys. Rev. Lett. **92**, 136101 (2004). *Stability of Rocksalt (111) Polar Surfaces: Beyond the Octopole.* doi:10.1103/PhysRevLett.92.136101. 11

[123] A. Barbier, C. Mocuta, H. Kuhlenbeck, K. F. Peters, B. Richter, and G. Renaud. Phys. Rev. Lett. **84**, 2897 (2000). *Atomic Structure of the Polar NiO(111)- p(2×2) Surface.* doi:10.1103/PhysRevLett.84.2897. 11

[124] O. Dulub, U. Diebold, and G. Kresse. Phys. Rev. Lett. **90**, 016102 (2003). *Novel Stabilization Mechanism on Polar Surfaces: ZnO(0001)-Zn.* doi:10.1103/PhysRevLett.90.016102. 11

[125] C. A. Ventrice, T. Bertrams, H. Hannemann, A. Brodde, and H. Neddermeyer. Phys. Rev. B **49**, 5773 (1994). *Stable reconstruction of the polar (111) surface of NiO on Au(111).* doi:10.1103/PhysRevB.49.5773. 11

[126] F. Allegretti, C. Franchini, V. Bayer, M. Leitner, G. Parteder, B. Xu, A. Fleming, M. G. Ramsey, R. Podloucky, S. Surnev, and F. P. Netzer. Phys. Rev. B **75**, 224120 (2007). *Epitaxial stabilization of MnO(111) overlayers on a Pd(100) surface.* doi:10.1103/PhysRevB.75.224120. 11, 61

[127] C. Noguera. J. Phys. Condens. Matter **12**, R367 (2000). *Polar oxide surfaces.* doi:10.1088/0953-8984/12/31/201, [link]. 11

[128] A. Ohtomo and H. Y. Hwang. Nature **427**, 423 (2004). *A high-mobility electron gas at the $LaAlO_3/SrTiO_3$ heterointerface.* doi:10.1038/nature0230. 11

[129] S. A. Pauli, S. J. Leake, B. Delley, M. Björck, C. W. Schneider, C. M. Schlepütz, D. Martoccia, S. Paetel, J. Mannhart, and P. R. Willmott. Phys. Rev. Lett. **106**, 036101 (2011). *Evolution of the Interfacial Structure of $LaAlO_3$ on $SrTiO_3$.* doi:10.1103/PhysRevLett.106.036101. 11

[130] P. Trucano and R. Chen. Nature **258**, 136 (1975). *Structure of graphite by neutron diffraction.* doi:10.1038/258136a0. 12, 18

[131] H.-P. Boehm, R. Setton, and E. Stumpp. Pure Appl. Chem. **66**, 1893 (1994). *Nomenclature and terminology of graphite intercalation compounds (IUPAC Recommendations 1994).* doi:10.1351/pac199466091893. 12, 17

[132] K. S. Novoselov, A. K. Geim, S. V. Morozov, D. Jiang, Y. Zhang, S. V. Dubonos, I. V. Grigorieva, and A. A. Firsov. Science **306**, 666 (2004). *Electric Field Effect in Atomically Thin Carbon Films.* doi:10.1126/science.1102896. 12

[133] S. Wang, Y. Zhang, N. Abidi, and L. Cabrales. Langmuir **25**, 11078 (2009). *Wettability and Surface Free Energy of Graphene Films*. doi:10.1021/la901402f, [link]. 12

[134] K. V. Emtsev, F. Speck, T. Seyller, L. Ley, and J. D. Riley. Phys. Rev. B **77**, 155303 (2008). *Interaction, growth, and ordering of epitaxial graphene on SiC{0001} surfaces: A comparative photoelectron spectroscopy study*. doi:10.1103/PhysRevB.77.155303. 12

[135] T. Ohta, F. E. Gabaly, A. Bostwick, J. L. McChesney, K. V. Emtsev, A. K. Schmid, T. Seyller, K. Horn, and E. Rotenberg. New J. Phys. **10**, 023034 (2008). *Morphology of graphene thin film growth on SiC(0001)*. doi:10.1088/1367-2630/10/2/023034, [link]. 12

[136] J. Wintterlin and M.-L. Bocquet. Surf. Sci. **603**, 1841 (2009). *Graphene on metal surfaces*. doi:10.1016/j.susc.2008.08.037, [link]. 12

[137] Y. Gamo, A. Nagashima, M. Wakabayashi, M. Terai, and C. Oshima. Surf. Sci. **374**, 61 (1997). *Atomic structure of monolayer graphite formed on Ni(111)*. doi:10.1016/S0039-6028(96)00785-6, [link].

[138] H. Ueta, M. Saida, C. Nakai, Y. Yamada, M. Sasaki, and S. Yamamoto. Surf. Sci. **560**, 183 (2004). *Highly oriented monolayer graphite formation on Pt(111) by a supersonic methane beam*. doi:10.1016/j.susc.2004.04.039, [link].

[139] J. Coraux, A. T. N'Diaye, M. Engler, C. Busse, D. Wall, N. Buckanie, F.-J. Meyer zu Heringdorf, R. van Gastel, B. Poelsema, and T. Michely. New J. Phys. **11**, 023006 (2009). *Growth of graphene on Ir(111)*. doi:10.1088/1367-2630/11/2/023006, [link].

[140] P. W. Sutter, J.-I. Flege, and E. A. Sutter. Nat. Mat. **7**, 406 (2008). *Epitaxial graphene on ruthenium*. doi:doi:10.1038/nmat2166. 12

[141] P. R. Wallace. Phys. Rev. **71**, 622 (1947). *The Band Theory of Graphite*. doi:10.1103/PhysRev.71.622. 12

[142] A. H. Castro Neto, F. Guinea, N. M. R. Peres, K. S. Novoselov, and A. K. Geim. Rev. Mod. Phys. **81**, 109 (2009). *The electronic properties of graphene*. doi:10.1103/RevModPhys.81.109. 12

[143] L. Brey and H. A. Fertig. Phys. Rev. B **76**, 205435 (2007). *Magnetoresistance of graphene-based spin valves*. doi:10.1103/PhysRevB.76.205435. 12

[144] M. Dragoman, D. Dragoman, G. Deligiorgis, G. Konstantinidis, D. Neculoiu, A. Cismaru, and R. Plana. J. Appl. Phys. **106**, 044312 (2009). *Current oscillations in a wide graphene sheet*. doi:10.1063/1.3208061, [link]. 12

[145] H. Min, J. E. Hill, N. A. Sinitsyn, B. R. Sahu, L. Kleinman, and A. H. MacDonald. Phys. Rev. B **74**, 165310 (2006). *Intrinsic and Rashba spin-orbit interactions in graphene sheets*. doi:10.1103/PhysRevB.74.165310. 12

[146] B. Trauzettel, D. V. Bulaev, D. Loss, and G. Burkard. Nat. Phys. **3**, 192 (2007). *Spin qubits in graphene quantum dots*. doi:10.1038/nphys544. 12

[147] V. M. Karpan, G. Giovannetti, P. A. Khomyakov, M. Talanana, A. A. Starikov, M. Zwierzycki, J. van den Brink, G. Brocks, and P. J. Kelly. Phys. Rev. Lett. **99**, 176602 (2007). *Graphite and Graphene as Perfect Spin Filters*. doi:10.1103/PhysRevLett.99.176602. 12

[148] K. T. Chan, J. B. Neaton, and M. L. Cohen. Phys. Rev. B **77**, 235430 (2008). *First-principles study of metal adatom adsorption on graphene*. doi:10.1103/PhysRevB.77.235430. 13

[149] G. Giovannetti, P. A. Khomyakov, G. Brocks, V. M. Karpan, J. van den Brink, and P. J. Kelly. Phys. Rev. Lett. **101**, 026803 (2008). *Doping Graphene with Metal Contacts*. doi:10.1103/PhysRevLett.101.026803. 13

[150] K. Pi, K. M. McCreary, W. Bao, W. Han, Y. F. Chiang, Y. Li, S.-W. Tsai, C. N. Lau, and R. K. Kawakami. Phys. Rev. B **80**, 075406 (2009). *Electronic doping and scattering by transition metals on graphene*. doi:10.1103/PhysRevB.80.075406.

[151] T. O. Wehling, M. I. Katsnelson, and A. I. Lichtenstein. Chem. Phys. Lett. **476**, 125 (2009). *Adsorbates on graphene: Impurity states and electron scattering*. doi:10.1016/j.cplett.2009.06.005, [link]. 15, 16

[152] T. O. Wehling, M. I. Katsnelson, and A. I. Lichtenstein. Phys. Rev. B **80**, 085428 (2009). *Impurities on graphene: Midgap states and migration barriers*. doi:10.1103/PhysRevB.80.085428. 16, 125

[153] R. Balog, B. Jørgensen, L. Nilsson, M. Andersen, E. Rienks, M. Bianchi, M. Fanetti, E. Lægsgaard, A. Baraldi, S. Lizzit, Z. Sljivancanin, F. Besenbacher, T. G. Hammer, B. Pedersen, P. Hofmann, and L. Hornekær. Nat. Mater. **9**, 315 (2010). *Bandgap opening in graphene induced by patterned hydrogen adsorption*. doi:10.1038/nmat2710. 13

[154] A. Varykhalov, M. R. Scholz, T. K. Kim, and O. Rader. Phys. Rev. B **82**, 121101 (2010). *Effect of noble-metal contacts on doping and band gap of graphene*. doi:10.1103/PhysRevB.82.121101. 13, 114

[155] Y. S. Dedkov and M. Fonin. New J. Phys. **12**, 125004 (2010). *Electronic and magnetic properties of the graphene-ferromagnet interface*. doi:10.1088/1367-2630/12/12/125004, [link].

[156] J. L. McChesney, A. Bostwick, T. Ohta, T. Seyller, K. Horn, J. González, and E. Rotenberg. Phys. Rev. Lett. **104**, 136803 (2010). *Extended van Hove Singularity and Superconducting Instability in Doped Graphene*. doi:10.1103/PhysRevLett.104.136803. 13

[157] J.-H. Chen, C. Jang, S. Adam, M. S. Fuhrer, E. D. Williams, and M. Ishigami. Nat. Phys. **4**, 377 (2008). *Charged-impurity scattering in graphene*. doi:10.1038/nphys935. 13

[158] W. Pan, S. W. Howell, A. J. Ross III, T. Ohta, and T. A. Friedmann. Appl. Phys. Lett. **97**, 252101 (2010). *Observation of the integer quantum Hall effect in high quality, uniform wafer-scale epitaxial graphene films*. doi:10.1063/1.3525588, [link]. 13

[159] J.-H. Chen, C. Jang, S. Xiao, M. Ishigami, and M. S. Fuhrer. Nat. Nanotechnol. **3**, 206 (2008). *Intrinsic and extrinsic performance limits of graphene devices on SiO_2*. doi:10.1038/nnano.2008.58. 13

[160] X. Du, I. Skachko, A. Barker, and E. Y. Andrei. Nat. Nanotechnol. **3**, 491 (2008). *Approaching ballistic transport in suspended graphene*. doi:10.1038/nnano.2008.199. 13

[161] J. Coraux, A. T. N'Diaye, C. Busse, and T. Michely. Nano Lett. **8**, 565 (2008). *Structural Coherency of Graphene on Ir(111)*. doi:10.1021/nl0728874, [link]. 13, 105, 111

[162] A. T. N'Diaye, J. Coraux, T. N. Plasa, C. Busse, and T. Michely. New J. Phys. **10**, 043033 (2008). *Structure of epitaxial graphene on Ir(111)*. doi:10.1088/1367-2630/10/4/043033, [link]. 13, 14, 15, 16, 30, 31

[163] A. T. N'Diaye, R. van Gastel, A. J. Martínez-Galera, J. Coraux, H. Hattab, D. Wall, F.-J. Meyer zu Heringdorf, M. Horn von Hoegen, J. M. Gómez-Rodríguez, B. Poelsema, C. Busse, and T. Michely. New J. Phys. **11**, 113056 (2009). *In situ observation of stress relaxation in epitaxial graphene*. doi:10.1088/1367-2630/11/11/113056, [link]. 13, 111

[164] A. T. N'Diaye, S. Bleikamp, P. J. Feibelman, and T. Michely. Phys. Rev. Lett. **97**, 215501 (2006). *Two-Dimensional Ir Cluster Lattice on a Graphene Moiré on Ir(111)*. doi:10.1103/PhysRevLett.97.215501. 14, 16

[165] C. Busse, P. Lazić, R. Djemour, J. Coraux, T. Gerber, N. Atodiresei, V. Caciuc, R. Brako, A. T. N'Diaye, S. Blügel, J. Zegenhagen, and T. Michely. Phys. Rev. Lett. **107**, 036101 (2011). *Graphene on Ir(111): Physisorption with Chemical Modulation*. doi:10.1103/PhysRevLett.107.036101. 14, 15, 117, 121

[166] J. Knudsen, P. J. Feibelman, T. Gerber, E. Grånäs, K. Schulte, P. Stratmann, J. N. Andersen, and T. Michely. Submitted to Phys. Rev. B (2011). *How clusters bind to the graphene moiré on Ir(111) - XPS compared to DFT*. 15

[167] I. Pletikosić, M. Kralj, P. Pervan, R. Brako, J. Coraux, A. T. N'Diaye, C. Busse, and T. Michely. Phys. Rev. Lett. **102**, 056808 (2009). *Dirac Cones and Minigaps for Graphene on Ir(111)*. doi:10.1103/PhysRevLett.102.056808. 15, 102

[168] E. Starodub, A. Bostwick, L. Moreschini, S. Nie, F. E. Gabaly, K. F. McCarty, and E. Rotenberg. Phys. Rev. B **83**, 125428 (2011). *In-plane orientation effects on the electronic structure, stability, and Raman scattering of monolayer graphene on Ir(111)*. doi:10.1103/PhysRevB.83.125428. 15, 135

[169] T. Langer, D. F. Förster, C. Busse, T. Michely, H. Pfnür, and C. Tegenkamp. New J. Phys. **13**, 053006 (2011). *Sheet plasmons in modulated graphene on Ir(111).* doi:10.1088/1367-2630/13/5/053006, [link]. 15, 31

[170] X. Liu, C. Z. Wang, M. Hupalo, Y. X. Yao, M. C. Tringides, W. C. Lu, and K. M. Ho. Phys. Rev. B **82**, 245408 (2010). *Adsorption and growth morphology of rare-earth metals on graphene studied by ab initio calculations and scanning tunneling microscopy.* doi:10.1103/PhysRevB.82.245408. 16

[171] A. T. N'Diaye, T. Gerber, C. Busse, J. Mysliveček, J. Coraux, and T. Michely. New J. Phys. **11**, 103045 (2009). *A versatile fabrication method for cluster superlattices.* doi:10.1088/1367-2630/11/10/103045, [link]. 16

[172] P. J. Feibelman. Phys. Rev. B **77**, 165419 (2008). *Pinning of graphene to Ir(111) by flat Ir dots.* doi:10.1103/PhysRevB.77.165419. 16, 110

[173] W. Rüdorff and E. Schulze. Z. Anorg. Allg. Chem. **277**, 156 (1954). *Über Alkaligraphitverbindungen.* doi:10.1002/zaac.19542770307, [link]. 16

[174] M. S. Dresselhaus and G. Dresselhaus. Adv. Phys. **30**, 139 (1981). *Intercalation compounds of graphite.* doi:10.1080/00018738100101367, [link]. 16, 17, 18

[175] G. P. Carver. Phys. Rev. B **2**, 2284 (1970). *Nuclear Magnetic Resonance in the Cesium-Graphite Intercalation Compounds.* doi:10.1103/PhysRevB.2.2284. 17

[176] N. Emery, C. Hérold, J.-F. Marêché, P. Lagrange, C. Bellouard, G. Lamura, E. D. Gennaro, and A. Andreone. Solid State Sci. **10**, 466 (2008). *Superconducting graphite intercalation compounds with calcium.* doi:10.1016/j.solidstatesciences.2007.11.034, [link]. 18

[177] J. Algdal, T. Balasubramanian, M. Breitholtz, T. Kihlgren, and L. Walldén. Surf. Sci. **601**, 1167 (2007). *Thin graphite overlayers: Graphene and alkali metal intercalation.* doi:10.1016/j.susc.2006.12.039, [link]. 18

[178] J. Sánchez-Barriga, A. Varykhalov, M. Scholz, O. Rader, D. Marchenko, A. Rybkin, A. Shikin, and E. Vescovo. Diamond Relat. Mater. **19**, 734 (2010). *Chemical vapour deposition of graphene on Ni(111) and Co(0001) and intercalation with Au to study Dirac-cone formation and Rashba splitting.* doi:10.1016/j.diamond.2010.01.047, [link]. 18

[179] N. Gall, E. Rut'kov, A. Tontegode, and M. Usufov. Tech. Phys. **44**, 1066 (1999). *Intercalation of two-dimensional graphite films on metals by atoms and molecules.* doi:10.1134/1.1259472, [link]. 18, 107

[180] N. R. Gall, E. V. Rut'kov, and A. Y. Tontegode. Carbon **38**, 663 (2000). *Intercalation of nickel atoms under two-dimensional graphene film on (111)Ir.* doi:10.1016/S0008-6223(99)00135-9, [link]. 18

[181] M. E. Makrini, D. Guérard, P. Lagrange, and A. Hérold. Physica B+C **99**, 481 (1980). *Intercalation of rare earth metals in graphite.* doi:10.1016/0378-4363(80)90282-X, [link]. 18

[182] H. Suematsu, K. Ohmatsu, K. Sugiyama, T. Sakakibara, M. Motokawa, and M. Date. Solid State Commun. **40**, 241 (1981). *High field magnetization of europium-graphite intercalation compound C6Eu.* doi:10.1016/0038-1098(81)90749-3, [link]. 18

[183] S. L. Molodtsov, C. Laubschat, M. Richter, T. Gantz, and A. M. Shikin. Phys. Rev. B **53**, 16621 (1996). *Electronic structure of Eu and Yb graphite intercalation compounds.* doi:10.1103/PhysRevB.53.16621. 18

[184] *SPS-CreaTec GmbH, Magnusstr. 11, 12489 Berlin, Germany* www.sps-createc.com. 19, 25

[185] A. Redinger, PhD thesis, RWTH Aachen (2009), *Surface damage through grazing incidence ions investigated by scanning tunneling microscopy.* [link]. 20

[186] Coating made out of oxides of Ti, N, and Al. Coated by *Wolf Beschichtungstechnologie GmbH, Am Güterbahnhof 12-18, D-66892 Bruchmühlbach-Miesau.* www.wolf-gruppe.com. 20

[187] Ceramic glue with very low outgassing from *KAGER Industrieprodukte GmbH, Paul-Ehrlich-Straße 10a, D-63128 Dietzenbach.* www.kager.de. 21

[188] Temperature controller from the manufacturer *Eurotherm UK, Faraday Close, Durrington, Worthing, West Sussex BN13 3PL.* www.eurotherm.co.uk. 21

[189] Thermovoltage database ITS-90 available at the *National Institute of Standards and Technology* srdata.nist.gov. 22

[190] Welding was done at the department *Sonderfügetechnik in the Zentralabteilung Technologie (ZAT) of the Forschungszentrum Jülich GmbH, D-52425 Jülich.* www.fz-juelich.de/zat. 22

[191] *Dr. Eberl MBE-Komponenten GmbH, Gutenbergstrasse 8, D-71263 Weil der Stadt.* www.mbe-components.com. 23

[192] W. D. Wang, N. J. Wu, and P. A. Thiel. J. Chem. Phys. **92**, 2025 (1990). *Structural steps to oxidation of Ni (100).* doi:10.1063/1.458036. 25, 32

[193] T. Michely, M. Kaiser, and M. J. Rost. Rev. Sci. Instr. **71**, 4461 (2000). *Plug "n" play scanning probe microscopy.* doi:10.1063/1.1322587. 25

[194] *RHK Technology Inc., 1050 East Maple Road, Troy MI 48083 USA.* www.rhk-tech.com. 26

[195] M. W. Hooker, NASA/CR-1998-208708 (1998), *Properties of PZT-Based Piezoelectric Ceramics Between −150 °C and 200 °C*. [link]. 27

[196] *EBL Products Inc., 22 Prestige Park Circle, East Hartford CT 06108 USA.* www.eblproducts.com. 26

[197] C. J. Chen. Appl.Phys. Lett. **60**, 132 (1992). *Electromechanical deflections of piezoelectric tubes with quartered electrodes*. doi:10.1063/1.107348, [link]. 27

[198] L. Isett and J. Blakely. Surf. Sci. **47**, 645 (1975). *Binding energies of carbon to Ni(100) from equilibrium segregation studies*. doi:10.1016/0039-6028(75)90208-3, [link]. 29

[199] K. Heinz, G. Schmidt, L. Hammer, and K. Müller. Phys. Rev. B **32**, 6214 (1985). *Dynamics of the reconstruction process Ir(100)* $1 \times 1 \rightarrow 1 \times 5$. doi:10.1103/PhysRevB.32.6214, [link]. 29

[200] S. Schmumacher, Diplom, Universität zu Köln (2010), *Wachstum von Europium und Europiumoxid auf Iridiumoberflächen und Graphen*. 29

[201] R. van Gastel, A. T. N'Diaye, D. Wall, J. Coraux, C. Busse, N. M. Buckanie, F.-J. Meyer zu Heringdorf, M. Horn von Hoegen, T. Michely, and B. Poelsema. Appl.Phys. Lett. **95**, 121901 (2009). *Selecting a single orientation for millimeter sized graphene sheets*. doi:10.1063/1.3225554, [link]. 30

[202] E. Loginova, S. Nie, K. Thürmer, N. C. Bartelt, and K. F. McCarty. Phys. Rev. B **80**, 085430 (2009). *Defects of graphene on Ir(111): Rotational domains and ridges*. doi:10.1103/PhysRevB.80.085430. 31

[203] Ames Laboratory (Materials Preparation Center) of the US DOE, Iowa State University, Ames, Iowa 50011-3020, USA. 32

[204] I. Horcas, R. Fernández, J. M. Gómez-Rodríguez, J. Colchero, J. Gómez-Herrero, and A. M. Baro. Rev. Sci. Instrum. **78**, 013705 (2007). *WSXM: A software for scanning probe microscopy and a tool for nanotechnology*. doi:10.1063/1.2432410. 33

[205] V. A. Ukraintsev. Phys. Rev. B **53**, 11176 (1996). *Data evaluation technique for electron-tunneling spectroscopy*. doi:10.1103/PhysRevB.53.11176. 34, 36, 37

[206] C. J. Chen, *Introduction to scanning tunneling microscopy*, Oxford University Press, USA, 1993, ISBN 0195071506. 34, 35, 36

[207] J. A. Stroscio, R. M. Feenstra, and A. P. Fein. Phys. Rev. Lett. **57**, 2579 (1986). *Electronic Structure of the Si(111)2* $\times$ *1 Surface by Scanning-Tunneling Microscopy*. doi:10.1103/PhysRevLett.57.2579. 37

[208] M. Passoni, F. Donati, A. Li Bassi, C. S. Casari, and C. E. Bottani. Phys. Rev. B **79**, 045404 (2009). *Recovery of local density of states using scanning tunneling spectroscopy*. doi:10.1103/PhysRevB.79.045404. 37

[209] P. Mårtensson and R. M. Feenstra. Phys. Rev. B **39**, 7744 (1989). *Geometric and electronic structure of antimony on the GaAs(110) surface studied by scanning tunneling microscopy.* doi:10.1103/PhysRevB.39.7744. 37

[210] L. Scandella and H.-J. Güntherodt. Ultramicroscopy **42-44**, 546 (1992). *Field emission resonances studied with dI/ds(V) and dI/dV(V) curves.* doi:10.1016/0304-3991(92)90321-A, [link]. 38

[211] K. Gundlach. Solid-State Electron. **9**, 949 (1966). *Zur Berechnung des Tunnelstroms durch eine trapezförmige Potentialstufe.* doi:10.1016/0038-1101(66)90071-2, [link]. 38

[212] E. D. L. Rienks, N. Nilius, H.-P. Rust, and H.-J. Freund. Phys. Rev. B **71**, 241404 (2005). *Surface potential of a polar oxide film: FeO on Pt(111).* doi:10.1103/PhysRevB.71.241404. 38

[213] L. Olesen, M. Brandbyge, M. R. Sørensen, K. W. Jacobsen, E. Lægsgaard, I. Stensgaard, and F. Besenbacher. Phys. Rev. Lett. **76**, 1485 (1996). *Apparent Barrier Height in Scanning Tunneling Microscopy Revisited.* doi:10.1103/PhysRevLett.76.1485. 39, 136

[214] J. Klinkhammer, Diplom, Universität zu Köln (2009), *EuO auf Ni(100) - Grenzflächenoxide und dünne Filme.* 40

[215] T. B. Massalski, H. Okamoto, P. R. Subramanian, and L. Kacprzak, *Binary Alloy Phase Diagrams. Vol. 3*, ASM International, Ohio, 1990, ISBN 087170403X. 41

[216] M. B˙ Surf. Sci. **253**, 116 (1991). *The structure of thin NiO(100) films grown on Ni(100) as determined by low-energy-electron diffraction and scanning tunneling microscopy.* doi:10.1016/0039-6028(91)90585-G, [link]. 41

[217] B. J. Boyle, E. G. King, and K. C. Conway. J. Am. Chem. Soc. **76**, 3835 (1954). *Heats of Formation of Nickel and Cobalt Oxides (NiO and CoO) of Combustion Calorimetry.* doi:10.1021/ja01643a072, [link]. 41

[218] C. Castellarin-Cudia, S. Surnev, G. Schneider, R. Podlucky, M. G. Ramsey, and F. P. Netzer. Surf. Sci. **554**, L120 (2004). *Strain-induced formation of arrays of catalytically active sites at the metal-oxide interface.* doi:10.1016/j.susc.2004.01.059, [link]. 50, 53

[219] L. R. Merte, J. Knudsen, L. C. Grabow, R. T. Vang, E. Lægsgaard, M. Mavrikakis, and F. Besenbacher. Surf. Sci. **603**, L15 (2009). *Correlating STM contrast and atomic-scale structure by chemical modification: Vacancy dislocation loops on FeO/Pt(111).* doi:10.1016/j.susc.2008.11.014, [link]. 50

[220] Calculated with LEED simulation software LEEDpat
URL http://www.fhi-berlin.mpg.de/KHsoftware/LEEDpat/. 50

[221] D. F. Förster, J. Klinkhammer, C. Busse, S. G. Altendorf, T. Michely, Z. Hu, Y.-Y. Chin, L. H. Tjeng, J. Coraux, and D. Bourgault. Phys. Rev. B **83**, 045424 (2011). *Epitaxial*

europium oxide on Ni(100) with single-crystal quality. doi:10.1103/PhysRevB.83.045424. 55

[222] A. Villaume, A. Antonevici, D. Bourgault, J. P. Leggeri, L. Porcar, and C. Villard. Rev. Sci. Instr. **79**, 023904 (2008). *Magneto-optical setup for in situ strain and transport measurements on superconductors*. doi:10.1063/1.2841806. 58

[223] K. Heinz, D. K. Saldin, and J. B. Pendry. Phys. Rev. Lett. **55**, 2312 (1985). *Diffuse LEED and Surface Crystallography*. doi:10.1103/PhysRevLett.55.2312. 61

[224] G. Barcaro, I. O. Thomas, and A. Fortunelli. J. Chem. Phys. **132**, 124703 (2010). *Validation of density-functional versus density-functional + U approaches for oxide ultrathin films*. doi:10.1063/1.3366689, [link]. 62, 76

[225] M. Pivetta, F. Patthey, M. Stengel, A. Baldereschi, and W.-D. Schneider. Phys. Rev. B **72**, 115404 (2005). *Local work function Moiré pattern on ultrathin ionic films: NaCl on Ag(100)*. doi:10.1103/PhysRevB.72.115404. 62, 76

[226] A. Atkinson and R. I. Taylor. Philos. Mag. A **43**, 979 (1981). *The diffusion of ^{63}Ni along grain boundaries in nickel oxide*. doi:10.1080/01418618108239506. 65

[227] S. Chevalier, F. Desserrey, and J. P. Larpin. Oxid. Met. **64**, 219 (2005). *Oxygen transport during the high temperature oxidation of pure nickel*. doi:10.1007/s11085-005-6560-x. 65

[228] A. Atkinson and R. I. Taylor. Philos. Mag. A **39**, 581 (1979). *The diffusion of Ni in the bulk and along dislocations in NiO single crystals*. doi:10.1080/01418617908239293. 65

[229] E. Negusse, J. Dvorak, J. S. Holroyd, M. Liberati, T. S. Santos, J. S. Moodera, E. Arenholz, and Y. U. Idzerda. J. Appl. Phys. **105**, 07C930 (2009). *Magnetic characterization of ultrathin EuO films with XMCD*. doi:10.1063/1.3076044, [link]. 66

[230] K. Fischer and U. K˙ J. Cryst. Growth **128**, 846 (1993). *Growth of EuO crystals by a solution sintering process*. doi:10.1016/S0022-0248(07)80056-X, [link]. 67

[231] B. T. Thole, G. van der Laan, J. C. Fuggle, G. A. Sawatzky, R. C. Karnatak, and J.-M. Esteva. Phys. Rev. B **32**, 5107 (1985). *3d x-ray-absorption lines and the $3d^9 4f^{n+1}$ multiplets of the lanthanides*. doi:10.1103/PhysRevB.32.5107. 67

[232] M. W. Pieper, D. Bätjer, and K. Fischer. Z. Phys. B: Condens. Matter **98**, 1 (1995). *Magnetic anisotropies in the nuclear magnetic resonance of the Heisenberg-ferromagnet EuO*. doi:10.1007/BF01318271. 69

[233] J. Schoiswohl, W. Zheng, S. Surnev, M. G. Ramsey, G. Granozzi, S. Agnoli, and F. P. Netzer. Surf. Sci. **600**, 1099 (2006). *Strain relaxation and surface morphology of nickel oxide nanolayers*. doi:10.1016/j.susc.2005.12.038, [link]. 70, 71

[234] A. Chassé, C. Langheinrich, F. Müller, and S. Hüfner. Surf. Sci. **602**, 597 (2008). *Growth and structure of thin MnO films on Ag(001) in dependence on film thickness*. doi:10.1016/j.susc.2007.11.014, [link]. 70

[235] S. Valeri, S. Altieri, A. Di Bona, P. Luches, C. Giovanardi, and T. S. Moia. Surf. Sci. **507**, 311 (2002). *Thickness-dependent strain in epitaxial MgO layers on Ag(001)*. doi:10.1016/S0039-6028(02)01263-3. 70, 71

[236] D. R. Lide, *CRC Handbook of chemistry and physics*, 81st edition, CRC Press, 2000. 73

[237] C. Busse, PhD thesis, RWTH Aachen (2003), *Nucleation and stacking-faults on the Iridium (111) surface*. [link]. 73

[238] P. H. T. Philipsen and E. J. Baerends. Phys. Rev. B **54**, 5326 (1996). *Cohesive energy of 3d transition metals: Density functional theory atomic and bulk calculations*. doi:10.1103/PhysRevB.54.5326. 73

[239] R. Smoluchowski. Phys. Rev. **60**, 661 (1941). *Anisotropy of the Electronic Work Function of Metals*. doi:10.1103/PhysRev.60.661. 75

[240] T. König, G. H. Simon, H.-P. Rust, and M. Heyde. J. Phys. Chem. C **113**, 11301 (2009). *Work Function Measurements of Thin Oxide Films on Metals - MgO on Ag(001)*. doi:10.1021/jp901226q, [link]. 82, 83

[241] R. W. Strayer, W. Mackie, and L. W. Swanson. Surf. Sci. **34**, 225 (1973). *Work function measurements by the field emission retarding potential method*. doi:10.1016/0039-6028(73)90117-9, [link]. 83, 135

[242] D. E. Eastman, F. Holtzberg, and S. Methfessel. Phys. Rev. Lett. **23**, 226 (1969). *Photoemission Studies of the Electronic Structure of EuO, EuS, EuSe, And GdS*. doi:10.1103/PhysRevLett.23.226. 83

[243] H. C. Galloway, J. J. Benítez, and M. Salmeron. Surf. Sci. **298**, 127 (1993). *The structure of monolayer films of FeO on Pt(111)*. doi:10.1016/0039-6028(93)90089-3, [link]. 87

[244] D. Sander and H. Ibach: *4.4.7 Clean surfaces - 4.4.8 Adsorbate-induced surface stress on Pt(111)*. A. P. Bonzel (ed.). SpringerMaterials - The Landolt-Börnstein Database (http://www.springermaterials.com). doi:10.1007/10783464_13. 91

[245] L. Vitos, A. V. Ruban, H. L. Skriver, and J. Kollár. Surf. Sci. **411**, 186 (1998). *The surface energy of metals*. doi:10.1016/S0039-6028(98)00363-X, [link]. 91

[246] Jürgen Klinkhammer, *private communication* (2011). 98, 143

[247] J. P. Perdew, K. Burke, and M. Ernzerhof. Phys. Rev. Lett. **77**, 3865 (1996). *Generalized Gradient Approximation Made Simple*. doi:10.1103/PhysRevLett.77.3865. 102

[248] V. I. Anisimov, F. Aryasetiawan, and A. I. Lichtenstein. J. Phys. Condens. Matter **9**, 767 (1997). *First-principles calculations of the electronic structure and spectra of strongly correlated systems: the LDA + U method*. doi:10.1088/0953-8984/9/4/002, [link]. 102

[249] P. Larson, W. R. L. Lambrecht, A. Chantis, and M. van Schilfgaarde. Phys. Rev. B **75**, 045114 (2007). *Electronic structure of rare-earth nitrides using the LSDA+U approach: Importance of allowing 4f orbitals to break the cubic crystal symmetry*. doi:10.1103/PhysRevB.75.045114. 102

[250] G. Kresse and J. Hafner. J. Phys. Condes. Matter **6**, 8245 (1994). *Norm-conserving and ultrasoft pseudopotentials for first-row and transition elements*. doi:10.1088/0953-8984/6/40/015. 102

[251] P. E. Blöchl. Phys. Rev. B **50**, 17953 (1994). *Projector augmented-wave method*. doi:10.1103/PhysRevB.50.17953. 102

[252] G. Kresse and D. Joubert. Phys. Rev. B **59**, 1758 (1999). *From ultrasoft pseudopotentials to the projector augmented-wave method*. doi:10.1103/PhysRevB.59.1758, [link]. 102

[253] S. Reich, J. Maultzsch, C. Thomsen, and P. Ordejón. Phys. Rev. B **66**, 035412 (2002). *Tight-binding description of graphene*. doi:10.1103/PhysRevB.66.035412. 102

[254] *SAES getters, Viale Italia 77, 20020 Lainate (MI), Italy*. www.saesgetters.com. 102

[255] Stefan Schumacher, *private communication* (2011). 104

[256] R. Brako, D. Šokčević, P. Lazić, and N. Atodiresei. New J. Phys. **12**, 113016 (2010). *Graphene on the Ir(111) surface: from van der Waals to strong bonding*. doi:10.1088/1367-2630/12/11/113016, [link]. 110

[257] M. Mucha-Kruczyński, O. Tsyplyatyev, A. Grishin, E. McCann, V. I. Fal'ko, A. Bostwick, and E. Rotenberg. Phys. Rev. B **77**, 195403 (2008). *Characterization of graphene through anisotropy of constant-energy maps in angle-resolved photoemission*. doi:10.1103/PhysRevB.77.195403. 113

[258] Sven Runte, *private communication* (2011). 115

[259] Z. P. Hu, N. J. Wu, and A. Ignatiev. Phys. Rev. B **33**, 7683 (1986). *Cesium adsorption on graphite (0001) surface: The phase diagram*. doi:10.1103/PhysRevB.33.7683. 115

[260] H. Ishida and R. E. Palmer. Phys. Rev. B **46**, 15484 (1992). *Electronic structure and phase transitions of submonolayer potassium on graphite*. doi:10.1103/PhysRevB.46.15484. 127, 131, 132, 133

[261] C. Kittel, *Introduction to Solid State Physics*, Wiley & Sons, New York, 1995, ISBN 0471111813. 128

[262] T. Michely and J. Krug, *Islands, mounds and atoms: Patterns and processes in crystal growth far from equilibrium, Springer Series in Surface Sciences Vol. 42*, Springer, Berlin, 2004. 129

[263] Z. Y. Li, K. M. Hock, and R. E. Palmer. Phys. Rev. Lett. **67**, 1562 (1991). *Phase transitions and excitation spectrum of submonolayer potassium on graphite*. doi:10.1103/PhysRevLett.67.1562. 133

[264] K. M. Hock and R. E. Palmer. Surf. Sci. **284**, 349 (1993). *Temperature dependent behaviour in the adsorption of submonolayer potassium on graphite*. doi:10.1016/0039-6028(93)90505-E, [link].

[265] K. Rytkönen, J. Akola, and M. Manninen. Phys. Rev. B **75**, 075401 (2007). *Density functional study of alkali-metal atoms and monolayers on graphite (0001)*. doi:10.1103/PhysRevB.75.075401. 134

[266] F. Yin, J. Akola, P. Koskinen, M. Manninen, and R. Palmer. Phys. Rev. Lett. **102**, 106102 (2009). *Bright beaches of nanoscale potassium islands on graphite in STM imaging*. doi:10.1103/PhysRevLett.102.106102.

[267] M. Caragiu and S. Finberg. J. Phys. Condens. Matter **17**, R995 (2005). *Alkali metal adsorption on graphite: a review*. doi:10.1088/0953-8984/17/35/R02, [link]. 133

[268] R. D. Diehl and R. McGrath. Surface Science Reports **23**, 43 (1996). *Structural studies of alkali metal adsorption and coadsorption on metal surfaces*. doi:10.1016/0167-5729(95)00010-0, [link]. 133, 169

[269] H. P. Bonzel, A. M. Bradshaw, and G. Ertl, *Physics and chemistry of alkali metal adsorption*, Elsevier Science Publishers B.V., 1989, ISBN 0-444-88338-X. 133, 169

[270] G. Makov and M. C. Payne. Phys. Rev. B **51**, 4014 (1995). *Periodic boundary conditions in ab initio calculations*. doi:10.1103/PhysRevB.51.4014. 134

[271] M. Kaack and D. Fick. Surf. Sci. **342**, 111 (1995). *Determination of the work functions of Pt(lll) and Ir(lll) beyond 1100 K surface temperature*. doi:10.1016/0039-6028(95)00758-X. 135

[272] M. L. Knotek and P. J. Feibelman. Phys. Rev. Lett. **40**, 964 (1978). *Ion Desorption by Core-Hole Auger Decay*. doi:10.1103/PhysRevLett.40.964. 142

[273] T. von Hofe, J. Kröger, and R. Berndt. Phys. Rev. B **73**, 245434 (2006). *Adsorption geometry of Cu(111)-Cs studied by scanning tunneling microscopy*. doi:10.1103/PhysRevB.73.245434. 169

[274] K. H. Lau and W. Kohn. Surf. Sci. **75**, 69 (1978). *Indirect long-range oscillatory interaction between adsorbed atoms*. doi:10.1016/0039-6028(78)90053-5, [link]. 169

[275] M. F. Crommie, C. P. Lutz, and D. M. Eigler. Nature **363**, 69 (1993). *Imaging standing waves in a two-dimensional electron gas*. doi:10.1038/363524a0. 169

[276] I. Pletikosić, M. Kralj, D. Šokčević, R. Brako, P. Lazić, and P. Pervan. J. Phys. Condens. Matter **22**, 135006 (2010). *Photoemission and density functional theory study of Ir(111); energy band gap mapping.* doi:10.1088/0953-8984/22/13/135006, [link]. 169

A Eu adsorption on Ir(111)

In this appendix a brief introduction to Eu adsorption on Ir(111) is given. There will be no detailed scientific discussion as the main motivation of this chapter is to describe the possibility of a precise Eu flux measurement. This is given by the fact that up to a certain deposited amount Θ Eu forms no islands on Ir, but a variety of sparse phases with prevailing mutual distances and increasing order with increasing coverage. The situation is comparable to alkali metal adsorption on metal surfaces [268; 269], e.g., to the case of Cs on Cu(111) [273].

For low coverages the bonding of alkali adsorbates is more of ionic nature due to charge transfer from the adsorbed alkali atoms to the substrate. Thus the alkali adatoms become partially charged and the induced dipole moment then causes the alkali atoms to mutually repel, leading to a homogeneous adatom arrangement with a prevailing mutual distance. In contrast, higher coverages lead to periodic superstructures with long-range order. Furthermore the nature of the bonding of the alkali atoms becomes more metallic for higher coverages [269].

Stabilization of the superstructures may arise from long-range adsorbate-adsorbate interactions mediated by substrate electrons. Adsorbates may interact via Friedel oscillations through the fact that the binding energy of one adsorbate depends on the substrate electron density, which oscillates around the other adsorbate [273]. For a two-dimensional electron gas the distance dependence of these interactions is related to the Fermi vector [274]. The Cu(111) surface hosts an electronic surface state which is a model system for a two-dimensional free electron gas [275] and thus leads to the adsorbate-adsorbate interactions. Hence the Ir(111) surface states [276] may contribute to a similar behaviour of adsorbates.

A.1 Eu adsorbate structures on Ir(111)

For imaging, the sample was cooled to 35 K because at 300 K only a noisy Ir surface was seen beside the Eu islands. Figure A.1 shows a series of Eu adsorption experiments with different coverages. The Eu exposure Θ is given in $\mathrm{MLE_{Ir}}$, whereby $1\,\mathrm{MLE_{Ir}} = 1.57 \times 10^{19}\,\mathrm{atoms\,m^{-2}}$ is defined with respect to the substrate atomic density of Ir(111). The small dots are all single atoms, hence one can easily determine the deposited amount of Eu. Assuming a Eu sticking coefficient of 1 at 35 K this allows one a comparison between the nominal exposure as calculated out of the microbalance rate and the real exposure. The values are given in table A.1.

Fig.	$\Theta_{\mathrm{balance}}$ (% $\mathrm{MLE_{Ir}}$)	$\Theta_{\mathrm{adsorbed}}$ (% $\mathrm{MLE_{Ir}}$)
A.1(a)	0.8	0.9
A.1(b,c)	2.4	3.1
A.1(d,e)	5.0	6.5

Table A.1: Eu exposure verification: $\Theta_{\mathrm{balance}}$ is the value calculated out of the microbalance measurement and $\Theta_{\mathrm{adsorbed}}$ out of the adatom concentration.

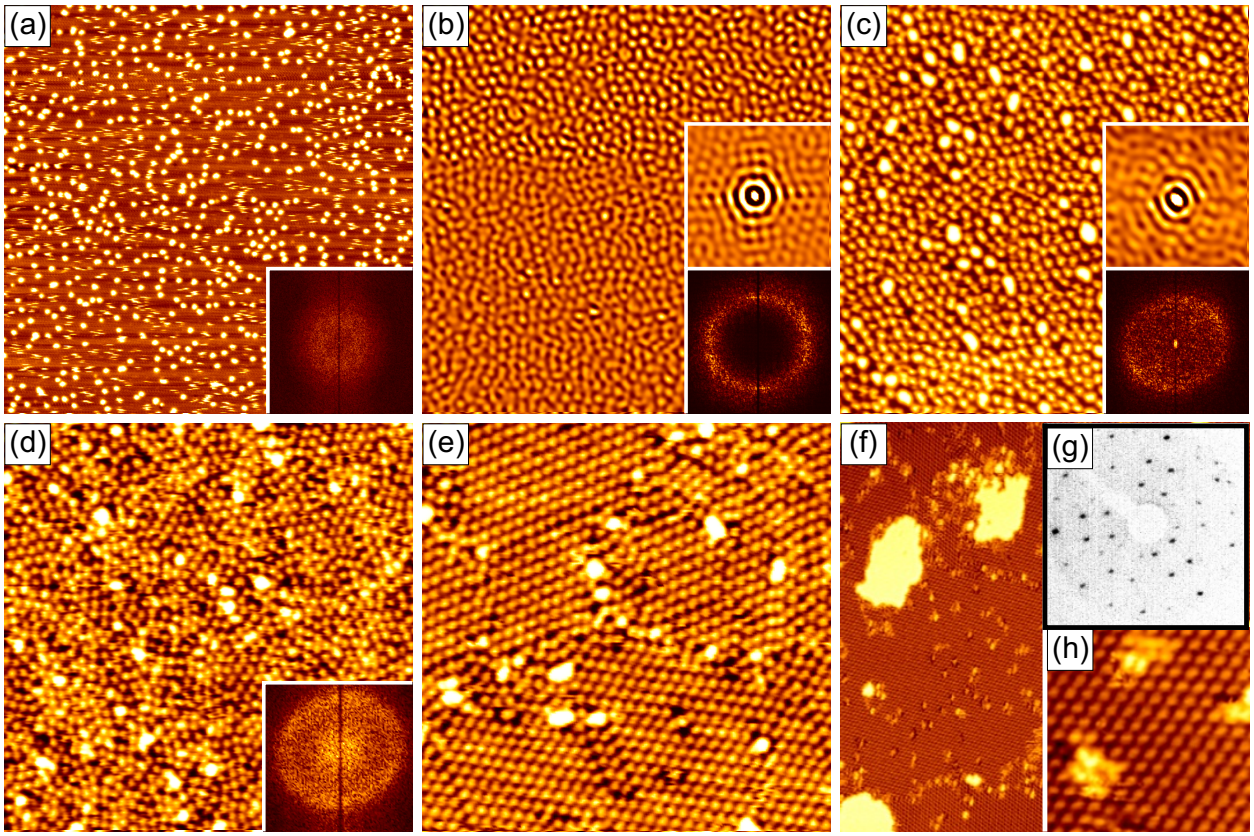

Figure A.1: Adsorbate structures of Eu on Ir(111) for different Θ. Adsorption temperature was 35 K for (a-e) and 300 K for (f). **(a)** $\Theta = 8 \times 10^{-3}\,\mathrm{MLE_{Ir}}$, image size 80 × 80 nm. Inset: Fourier transform of the topograph. **(b)** $\Theta = 2.4 \times 10^{-2}\,\mathrm{MLE_{Ir}}$, image size 45 × 45 nm. Top inset: Self-correlation of the topograph, bottom inset: Fourier transform. **(c)** same as (b) after annealing to 190 K. Top inset: Self-correlation of the topograph, Bottom inset: Fourier transform. **(d)** $\Theta = 5.0 \times 10^{-2}\,\mathrm{MLE_{Ir}}$, image size 40 × 40 nm. Inset: Fourier transform. **(e)** same as (d) after annealing to 275 K, image size 32 × 32 nm. **(f)** $\Theta = 0.15\,\mathrm{MLE_{Ir}}$, image size 40 × 80 nm. **(g)** LEED pattern of the experiment shown in (f), 58 eV. **(h)** zoom into (f), 10 × 10 nm.

$\Theta_{\mathrm{adsorbed}}$ is thereby calculated by dividing the number of atoms through the image area. While the atom amount can determined very precisely, the image area relies on the calibration of the STM and on the assumption that the piezo elongation changes linearly with increasing voltage.

The Figs. A.1(a), (b), and (d) show the low temperature adsorption series. The adatom arrangements have prevailing mutual distances, similar to the case of Cs on Cu(111). This is better seen in the inset Fourier transforms and self correlations. Annealing to 195 K did not significantly improve the order of the adatoms as can be seen in Fig. A.1(c), but annealing to 275 K lead to a perfect hexagonal arrangement within distinct domains as can be seen in Fig. A.1(e).

Figure A.1(f) shows the situation where the repulsive adatom phase has reached its densest structure and already Eu metal islands have formed. The structure of the latter could not be resolved by the obtained LEED and STM data. The adsorption has taken place at 300 K, thus the adatoms are highly ordered. In the densest structure, the adatoms arrange in a $(\sqrt{7} \times \sqrt{7})\mathrm{R}19.1°$

superstructure as verified by LEED [Fig. A.1(g)], hence their distance is 7.17 Å. Thus the Eu adatom saturation coverage is $\Theta = 1/7\,\mathrm{MLE_{Ir}}$ or 14% of the Ir(111) surface atom density. The knowledge of the exact Eu atom density gives the possibility to estimate the error of the above mentioned method to determine $\Theta_{\mathrm{adsorbed}}$. Therefore, several measurements of $\Theta_{\mathrm{adsorbed}}$ were performed for the experiment of Figs. A.1 (f-h). The deviation from $1/7\,\mathrm{MLE_{Ir}}$ never exceeded 5%, hence this should be an upper limit for the error of $\Theta_{\mathrm{adsorbed}}$ in Tab. A.1.

B Construction plans

In this appendix the most relevant construction plans which were drawn during this thesis are shown. The criterions for their relevance are either the complexity or the importance of the corresponding part.

- Figures B.1 through B.6 show the plans for the sample holder, including the ramps.
- Figures B.7 and B.8 show the plans of the fork for transferring the sample holder.
- Figure B.9 shows the plan of the base plate which hosts the sample holder.
- Figure B.10 shows the plan of the heavy tube for the damping of the cryostat and Figs. B.11 through B.13 that of the glide bearing which disburdens the cryostat from the tube weight.
- Figure B.14 and B.15 show the plans for the MBE flange.
- Figure B.16 and B.17 show the plans for the final version of the hedgehog STM and Fig. B.18 the segmentation plans for the corresponding piezos.

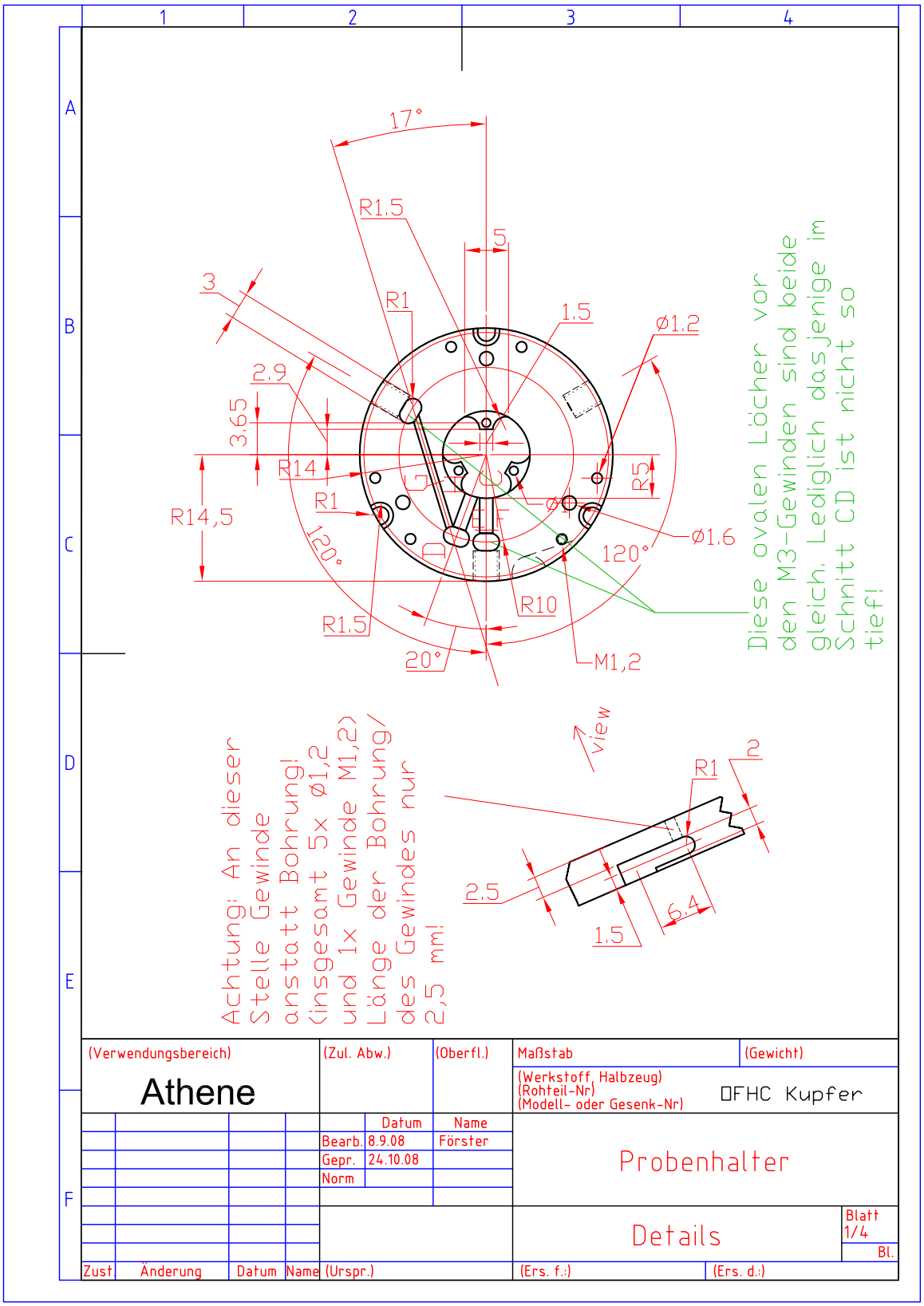

Figure B.1: Plan of the sample holder, top view.

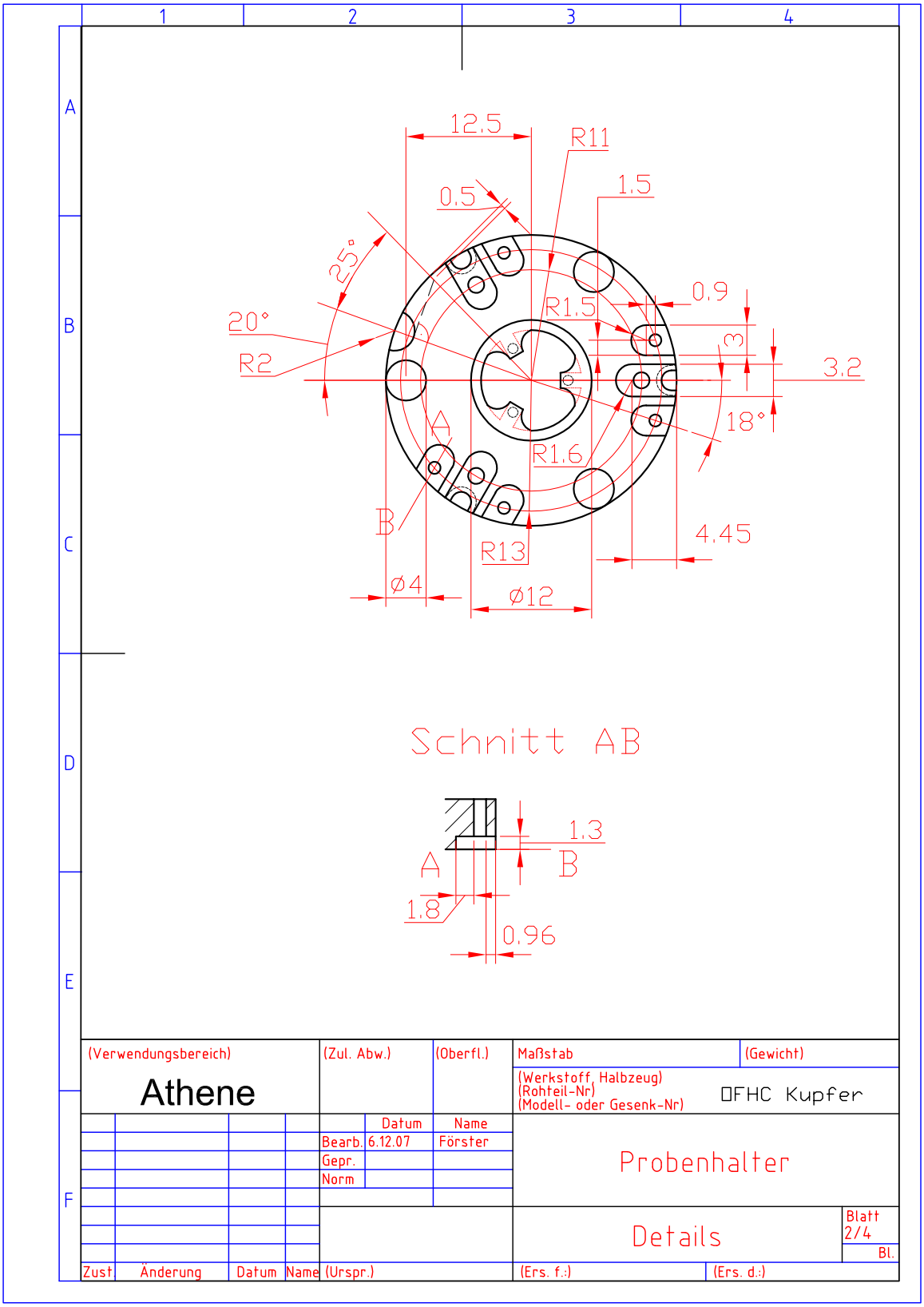

Figure B.2: Plan of the sample holder, bottom view.

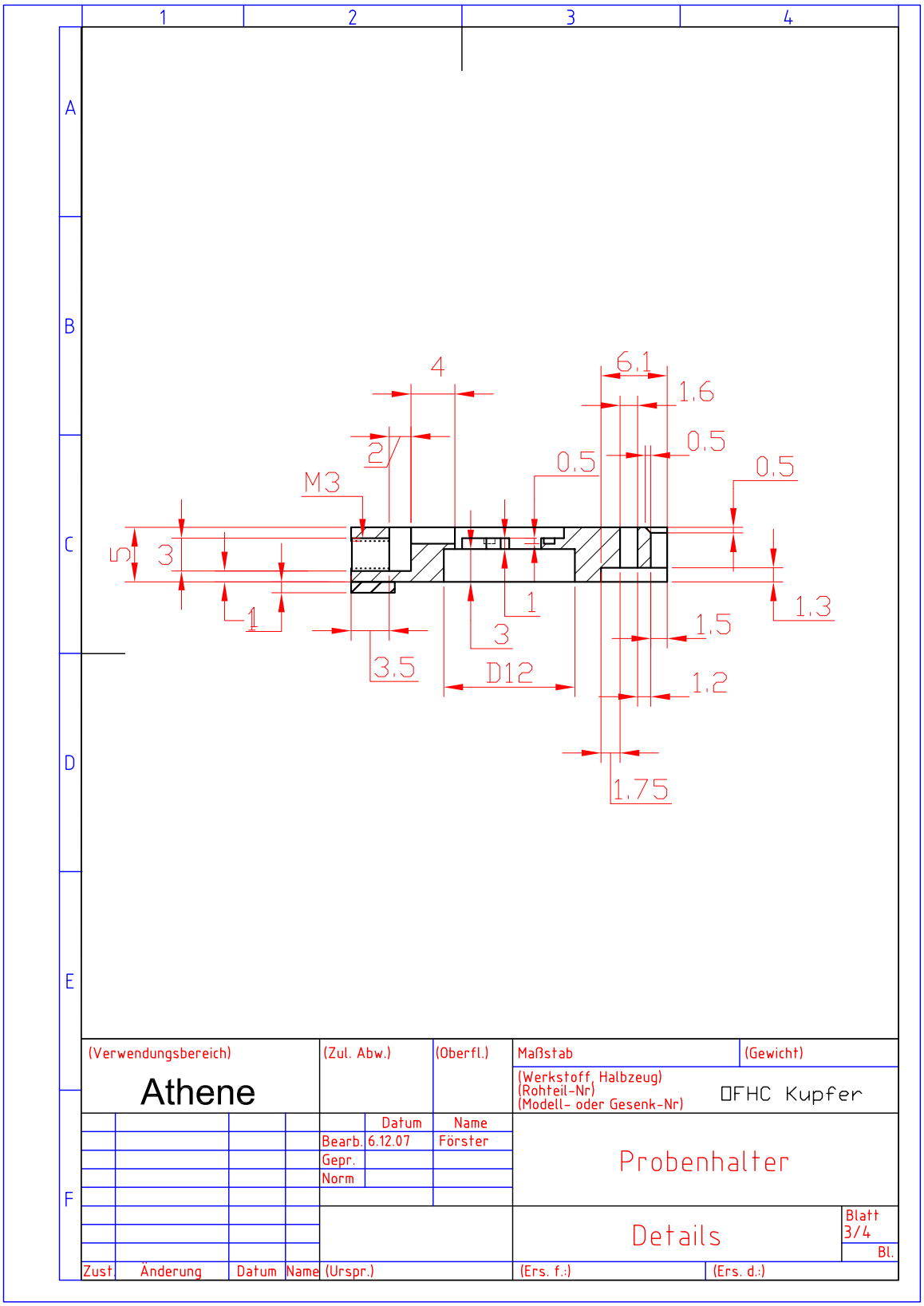

Figure B.3: Plan of the sample holder, cross-section.

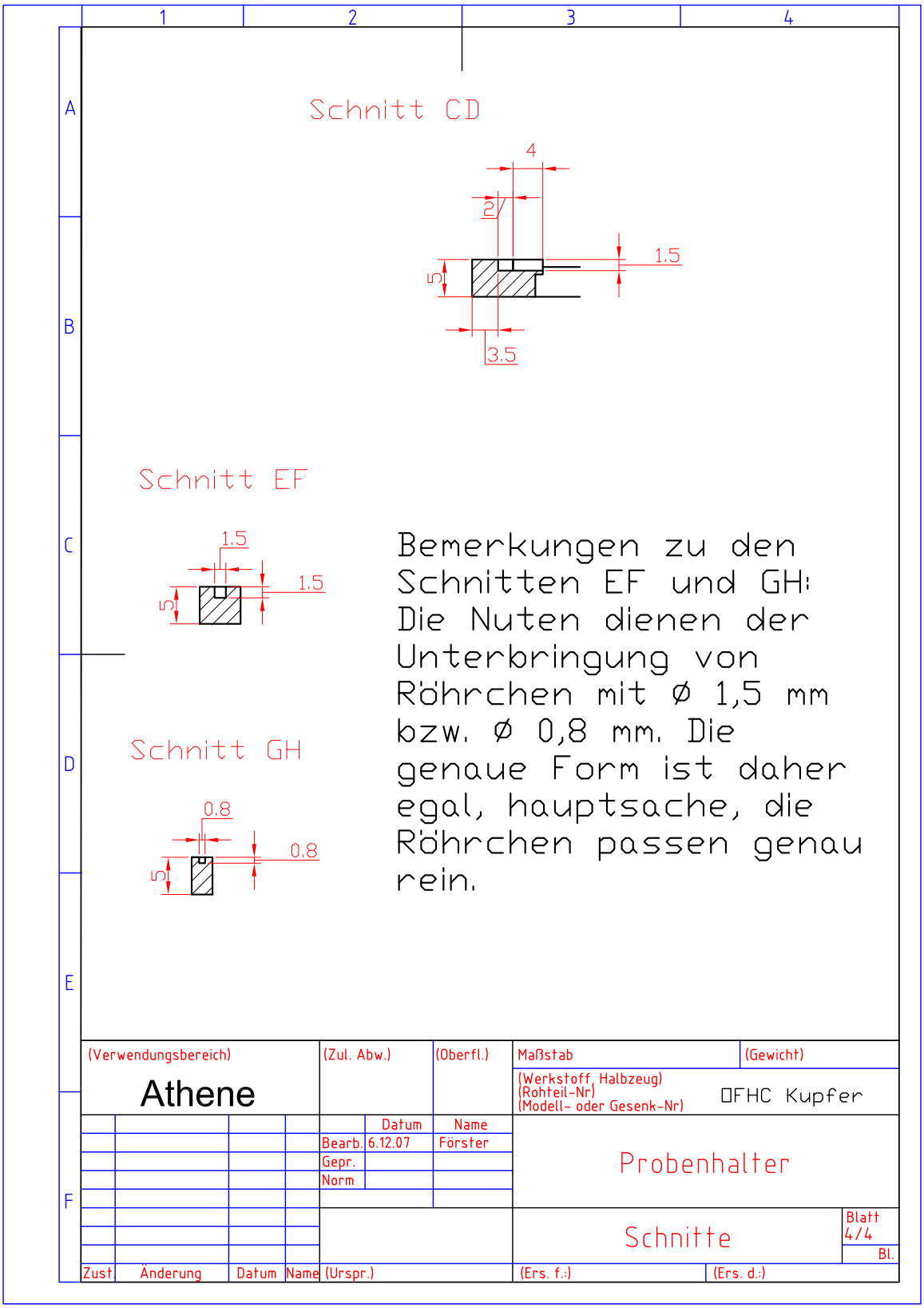

Figure B.4: Plan of the sample holder, smaller cross-sections as indicated in Fig. B.1.

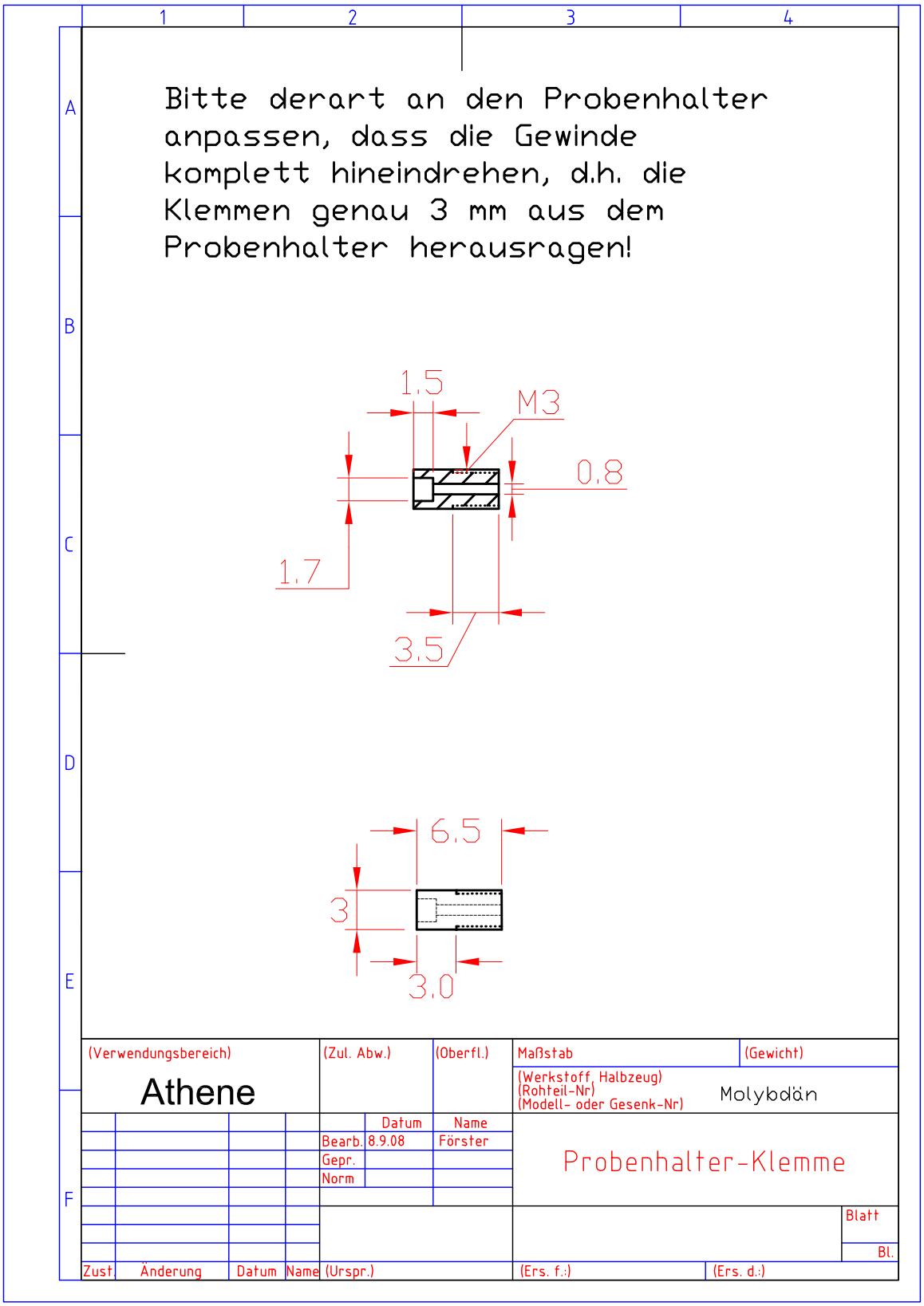

Figure B.5: Plan for the three clamping pins of the sample holder.

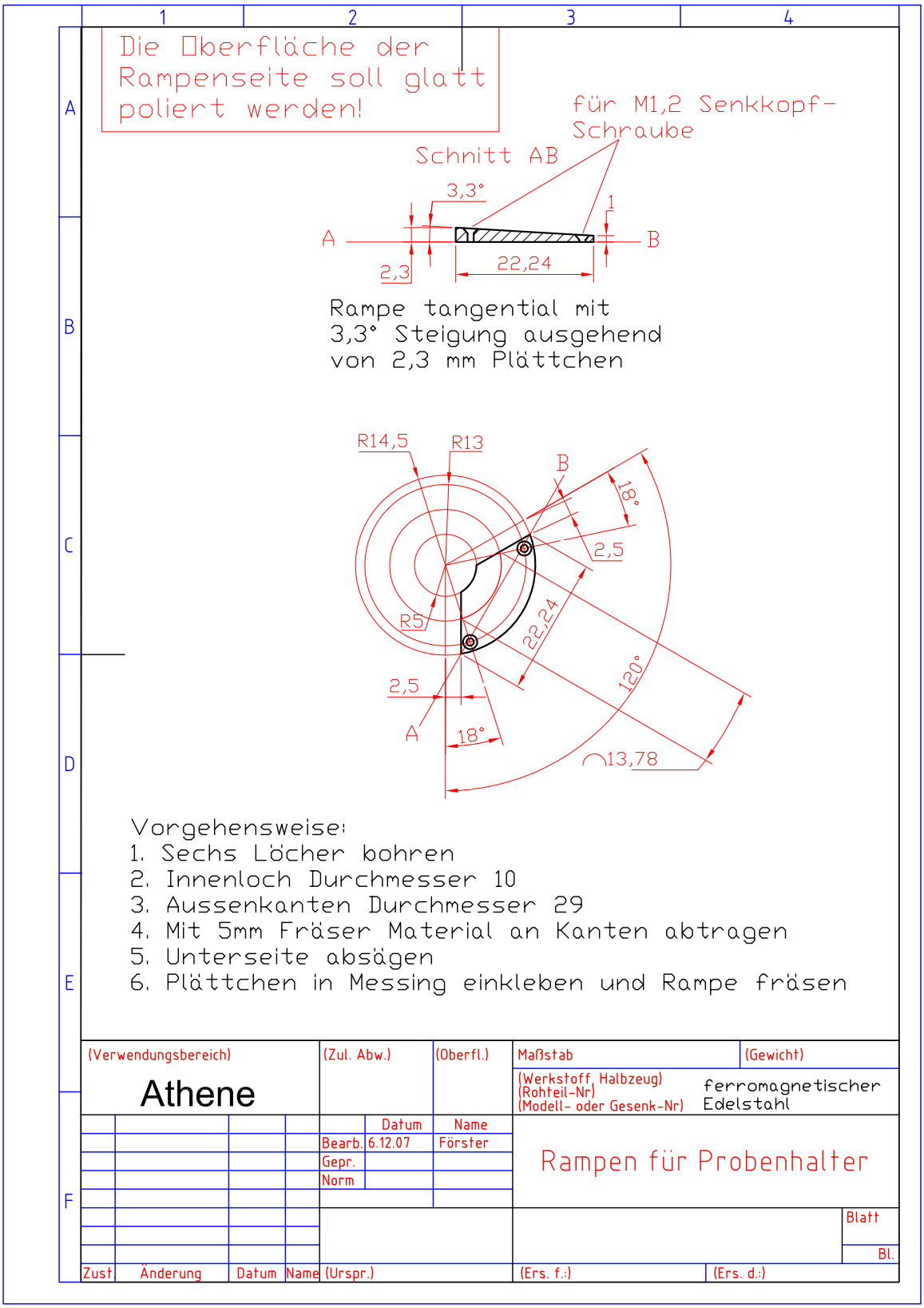

Figure B.6: Plan of the three ferritic steel ramps.

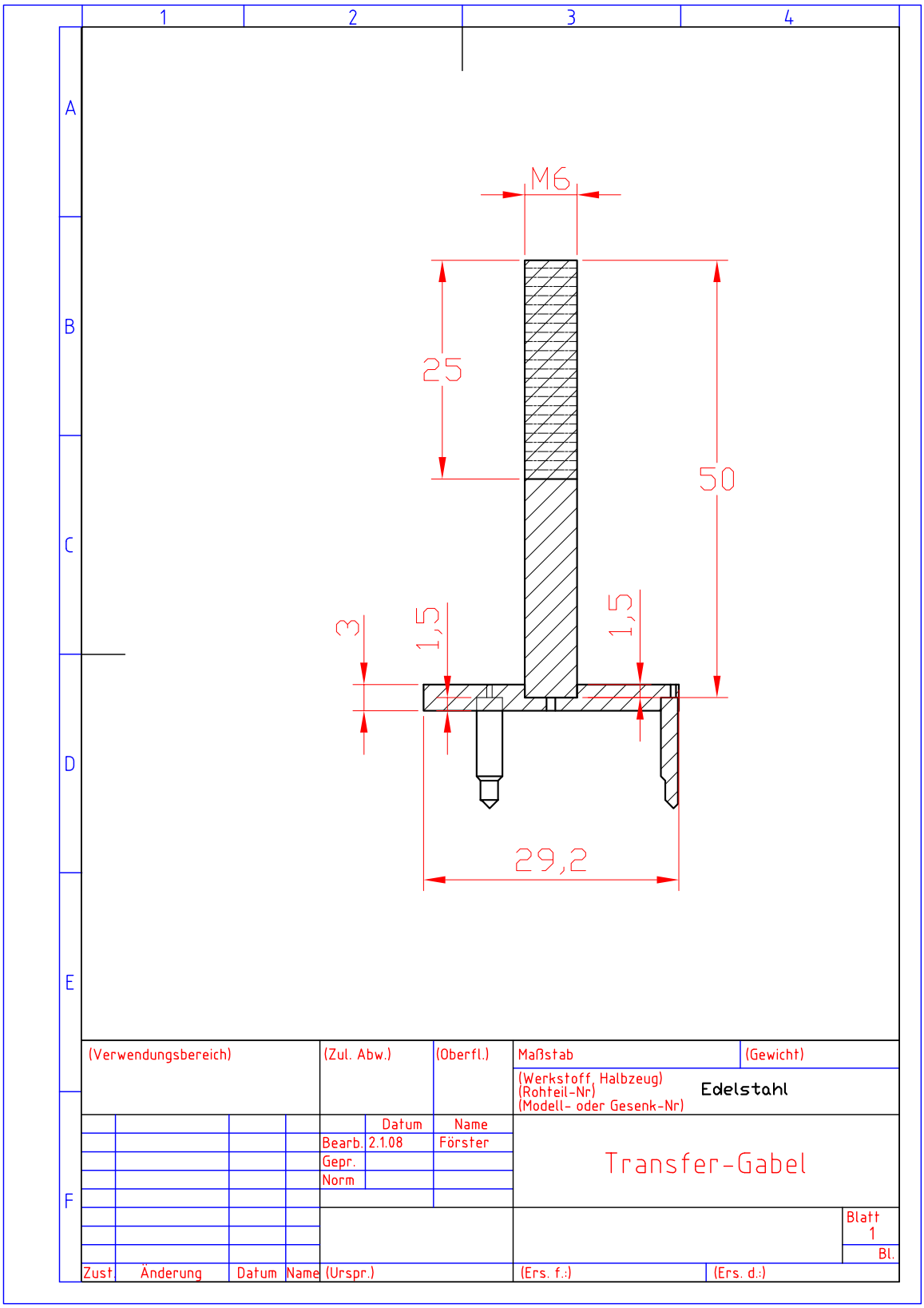

Figure B.7: Plan of the fork for transferring the sample holder.

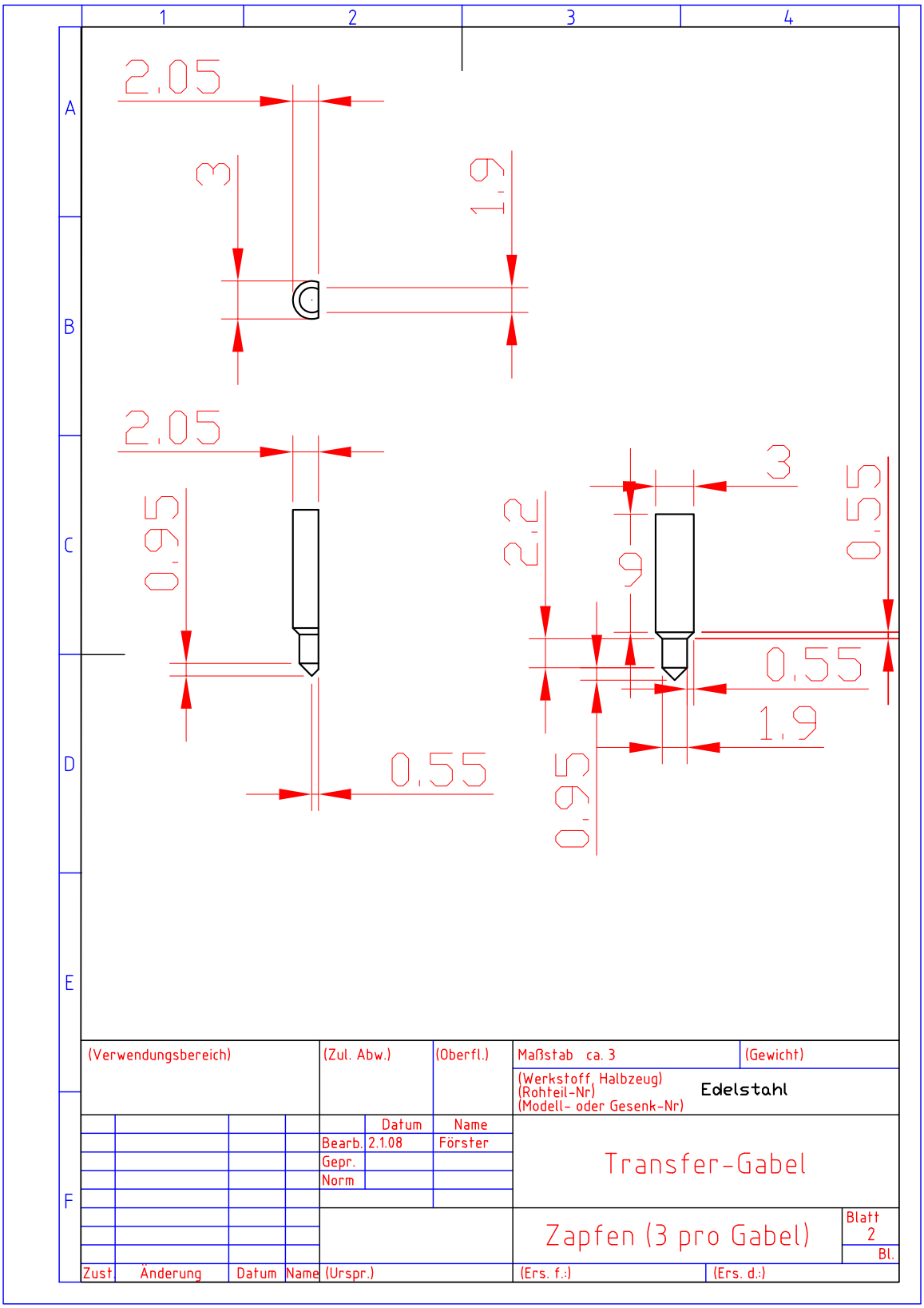

Figure B.8: Detail plan of the transfer fork pins.

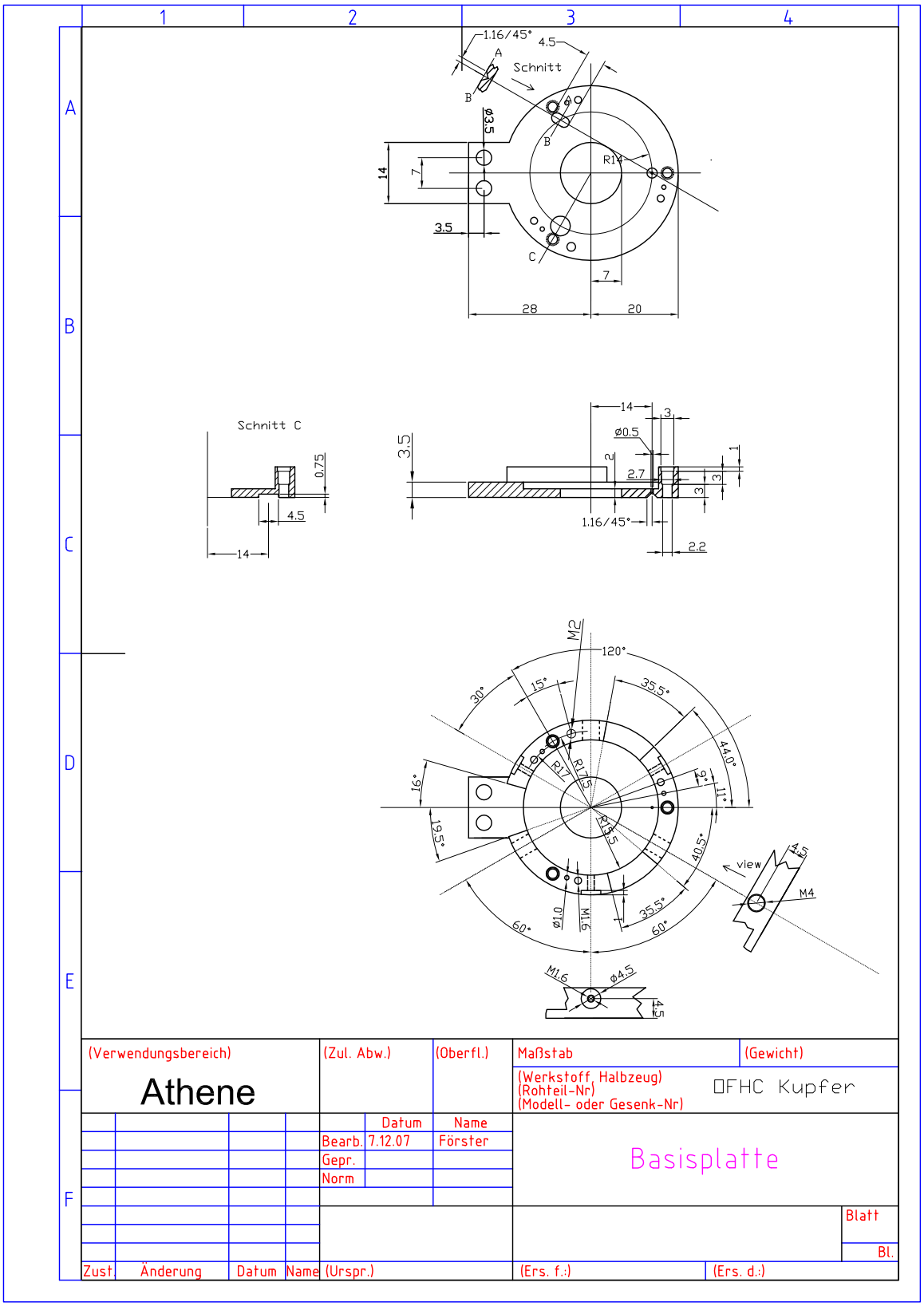

Figure B.9: Plan of the base plate.

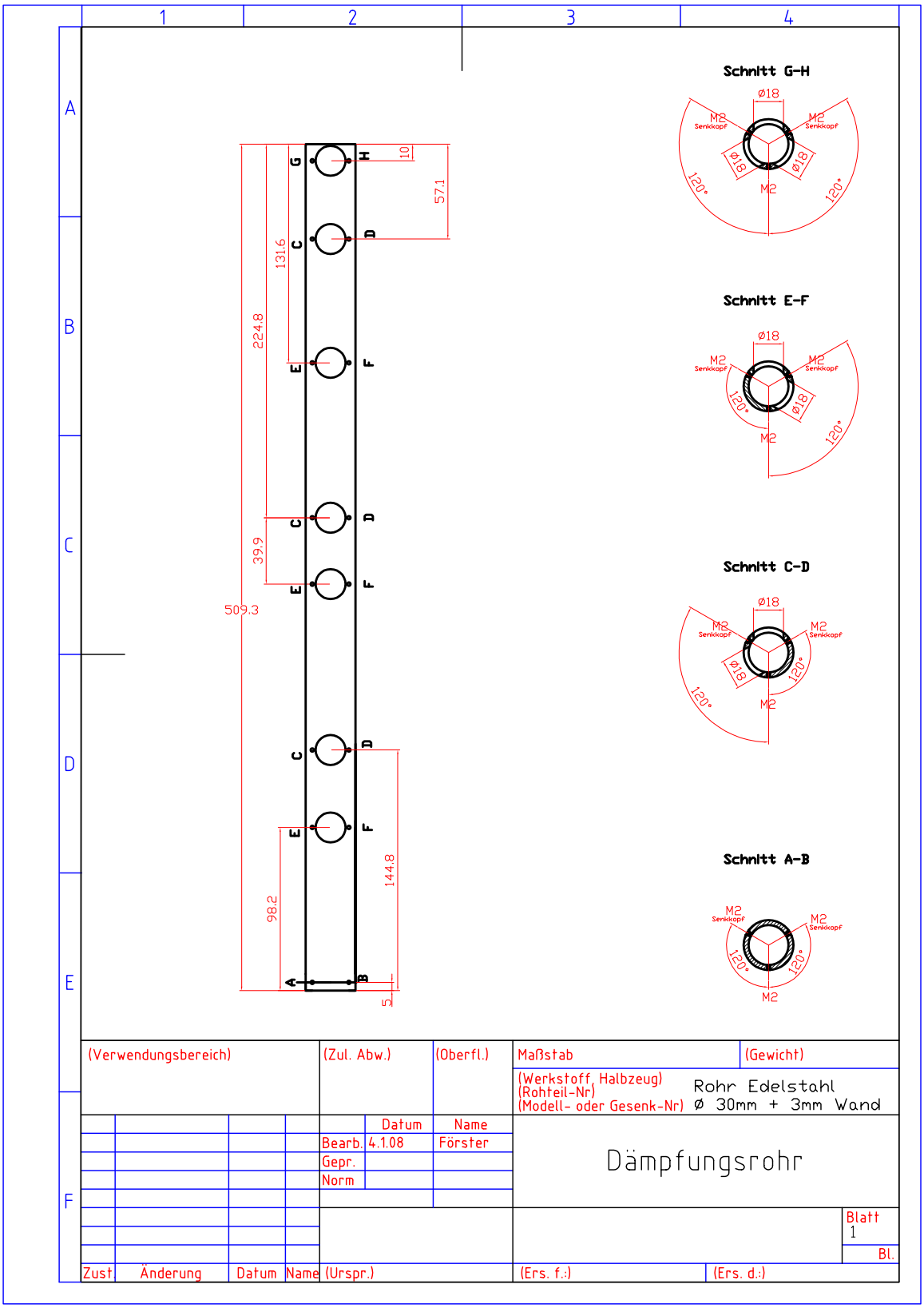

Figure B.10: Plan of the cryostat damping tube.

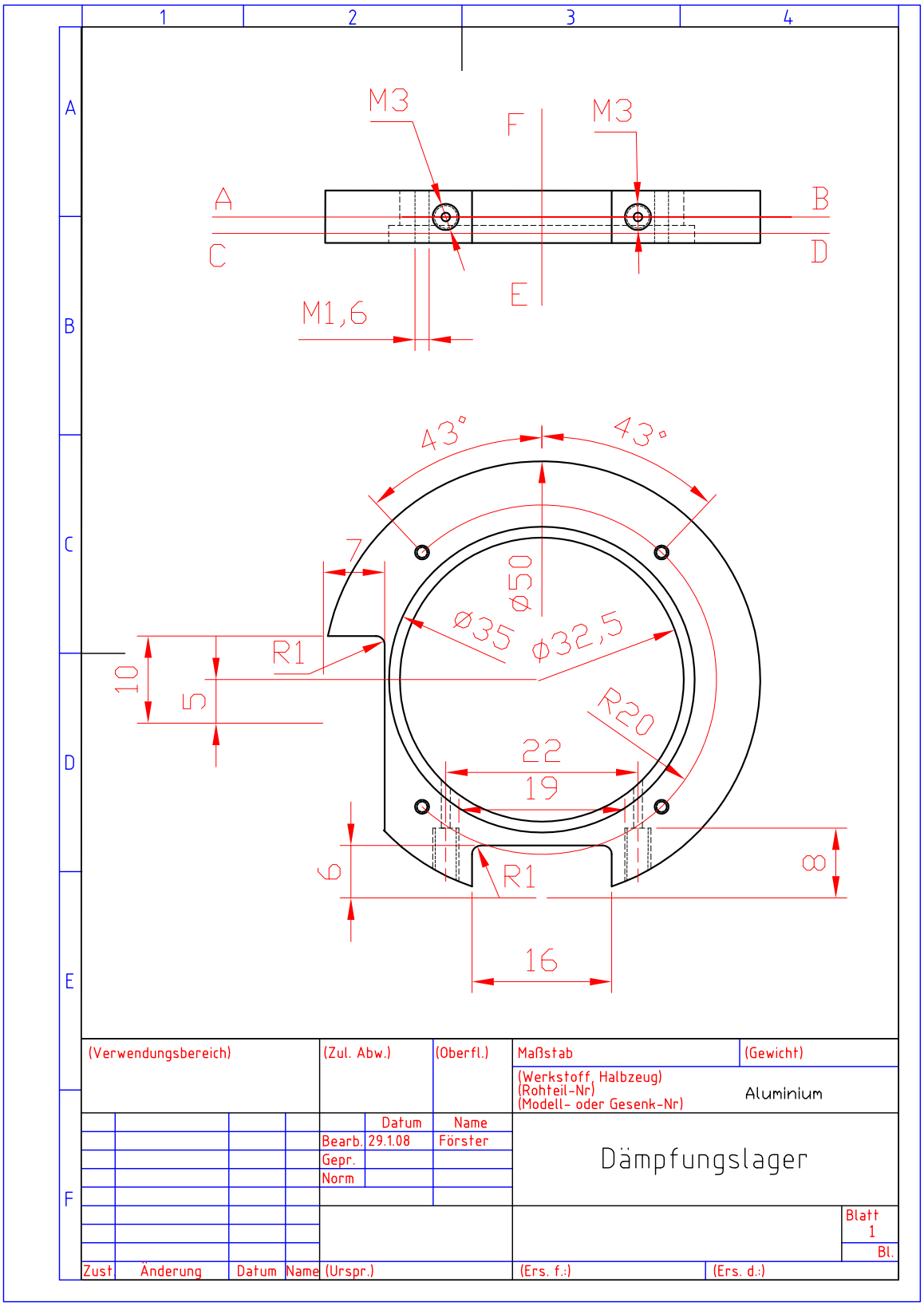

Figure B.11: Plan of the casing for the Teflon slide bearing of the cryostat.

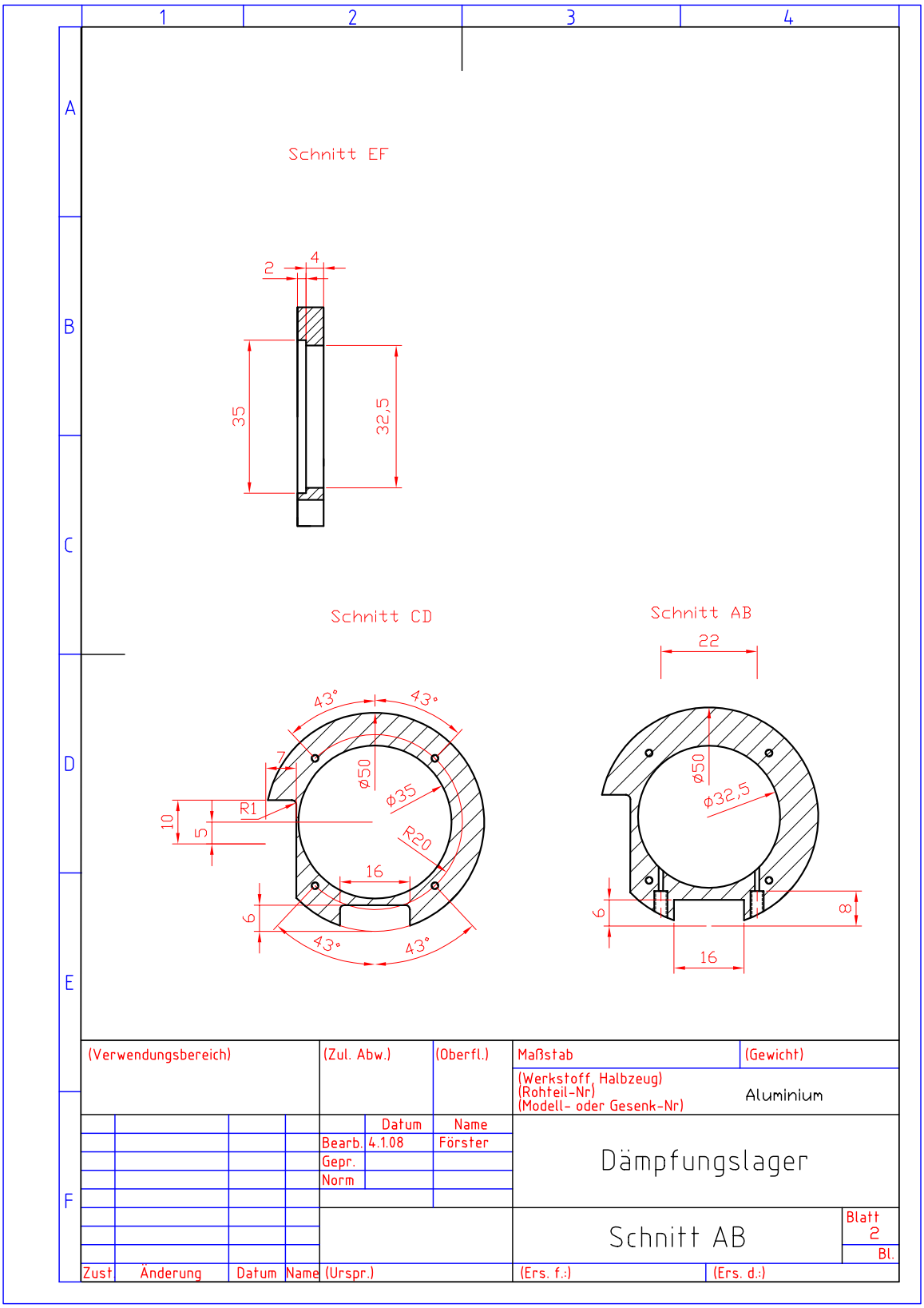

Figure B.12: Cross sections as shown in Fig. B.11.

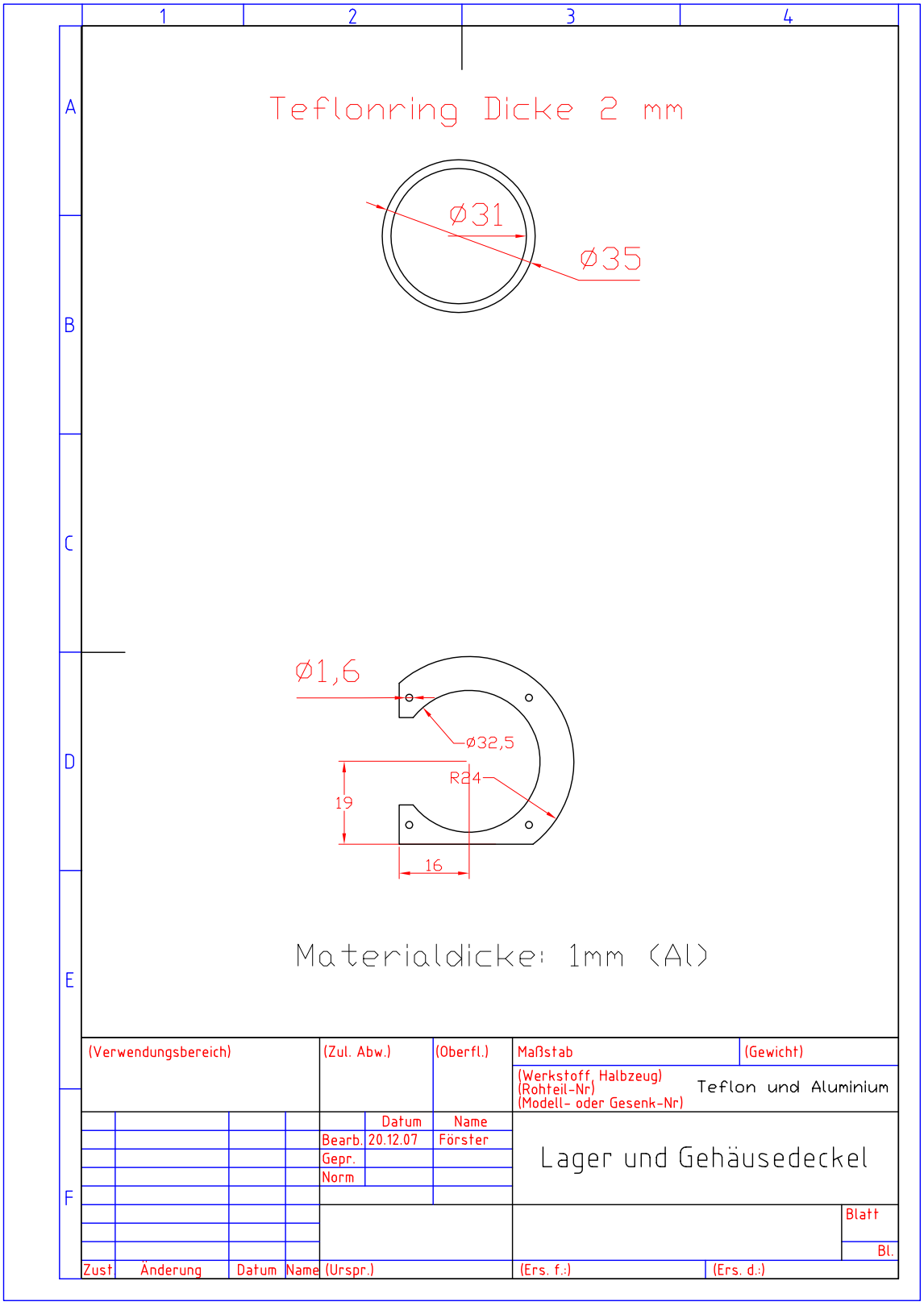

Figure B.13: Plan of the Teflon slide bearing (top) and of the casing back cover.

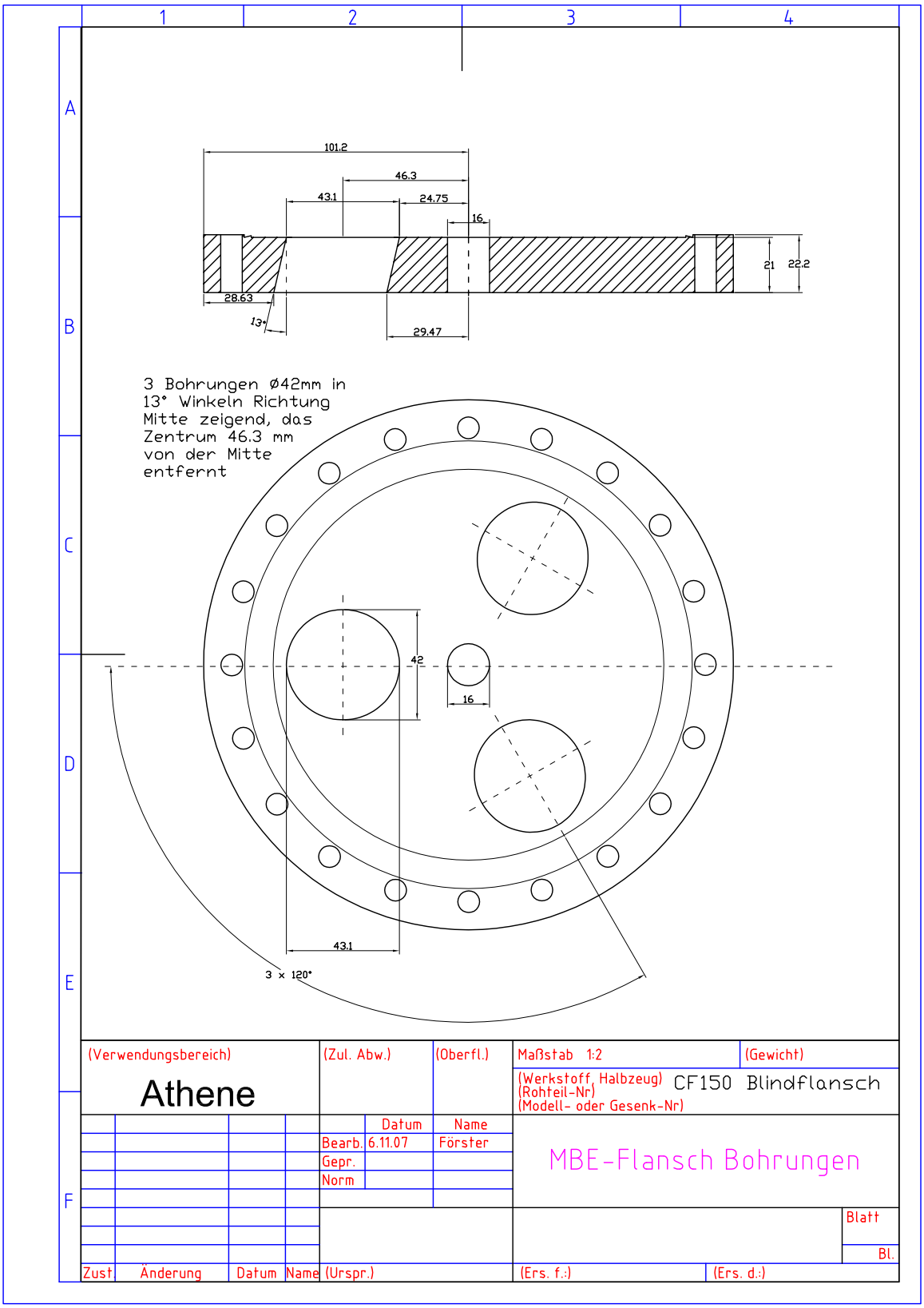

Figure B.14: Plan of the flange for the MBE station.

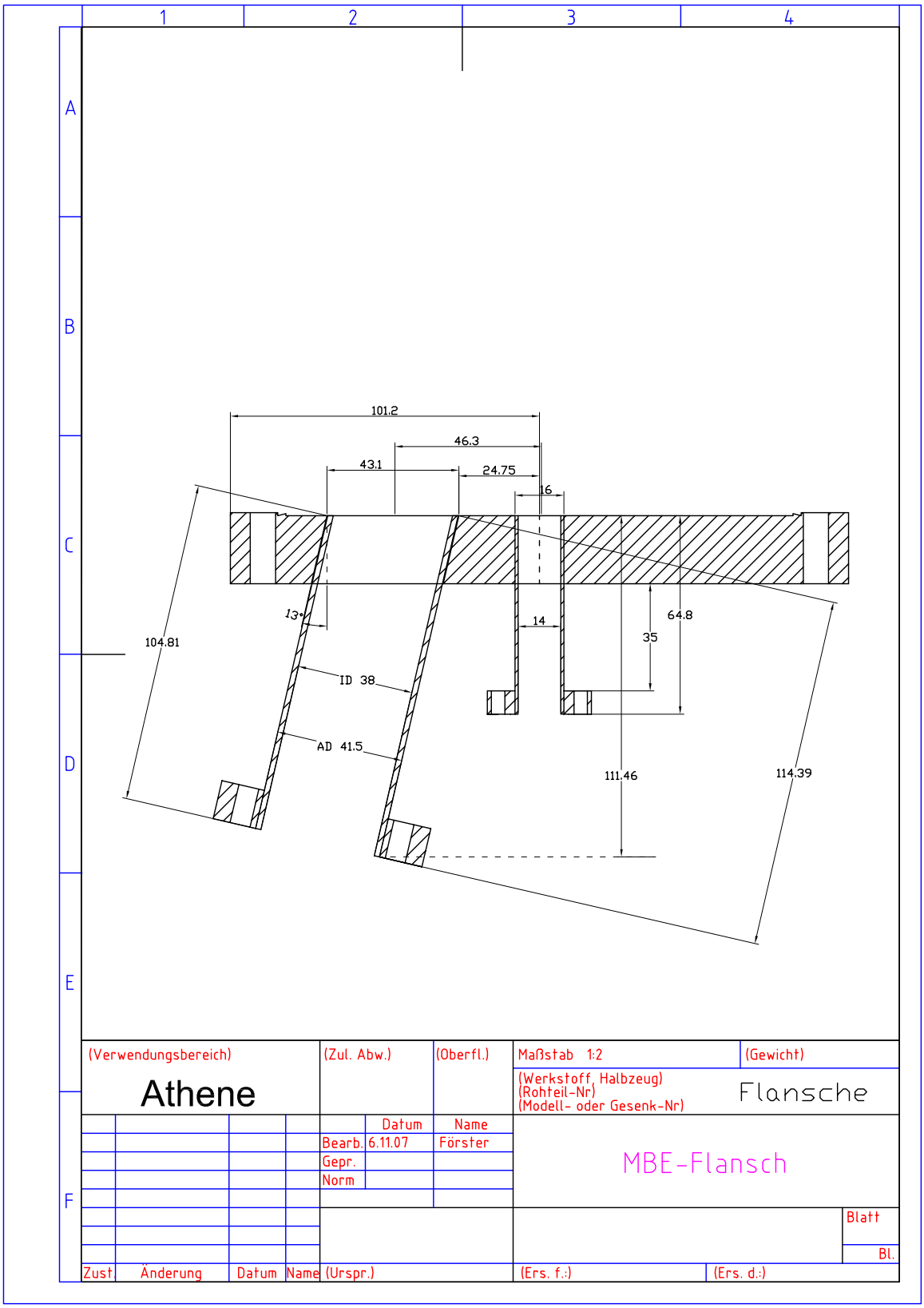

Figure B.15: Cross section plan of the flange for the MBE station with tubes.

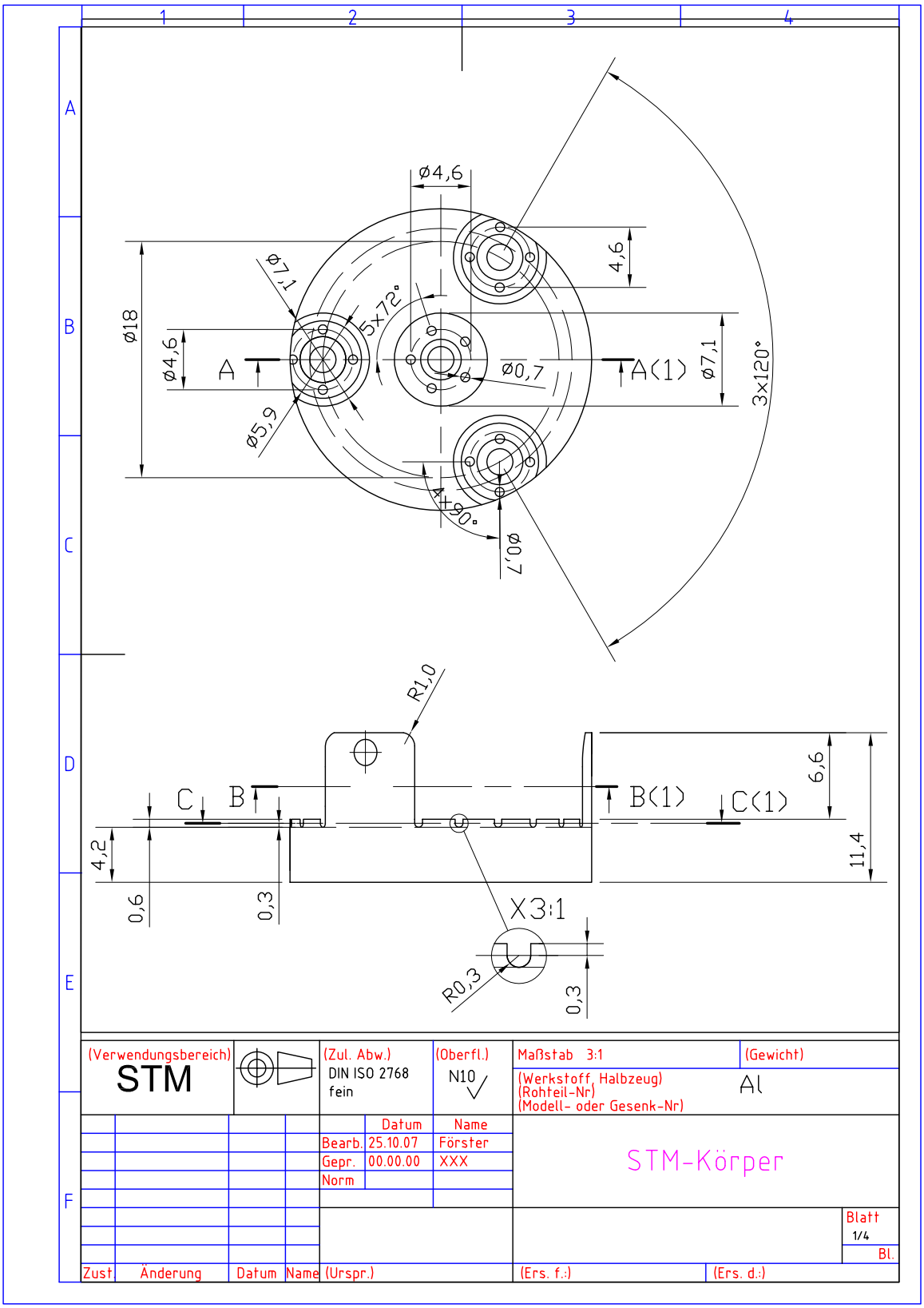

Figure B.16: Plan of the second version of the hedgehog STM's main body.

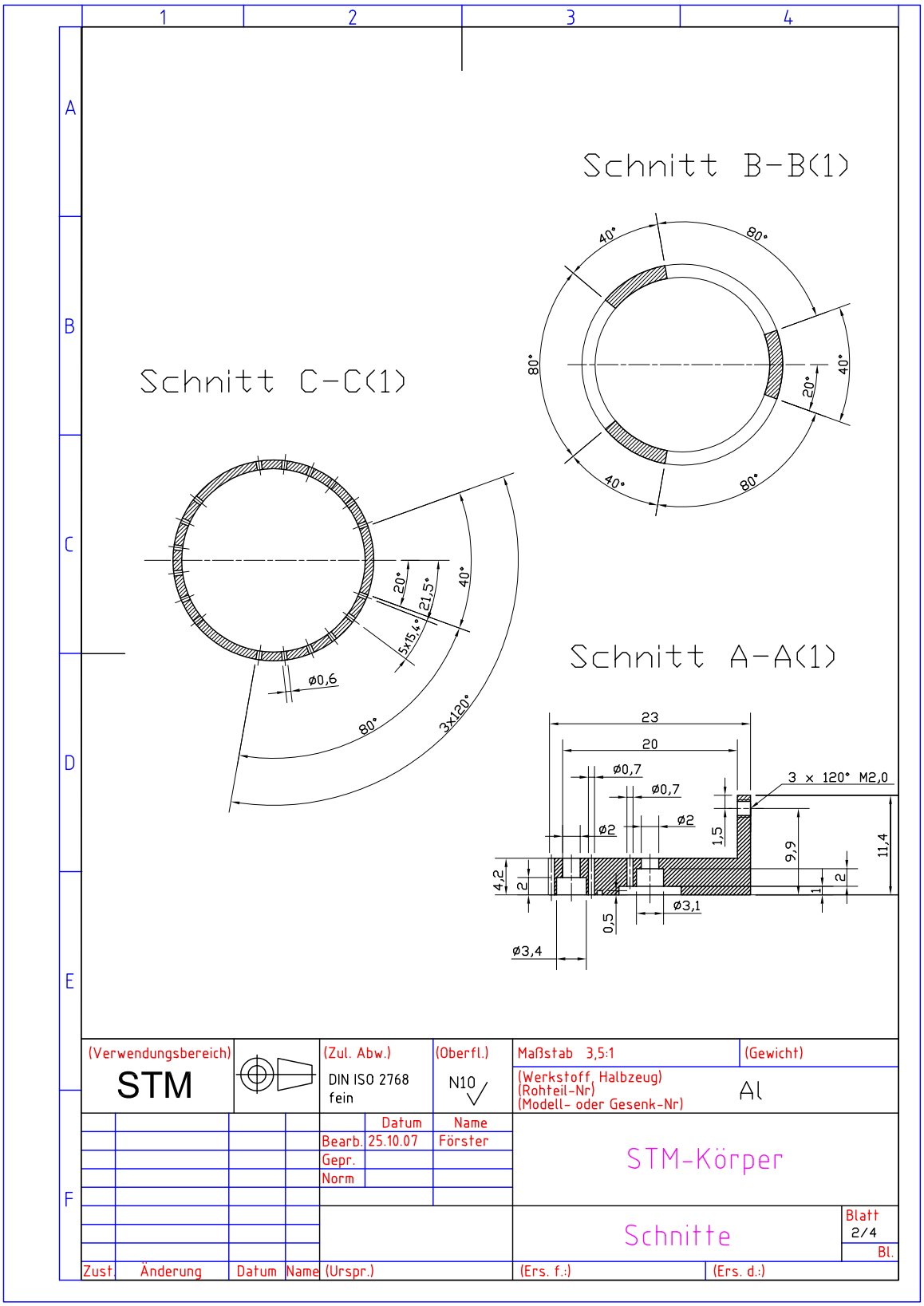

Figure B.17: Cross section plans of the hedgehog STM's main body as indicated in Fig. B.16.

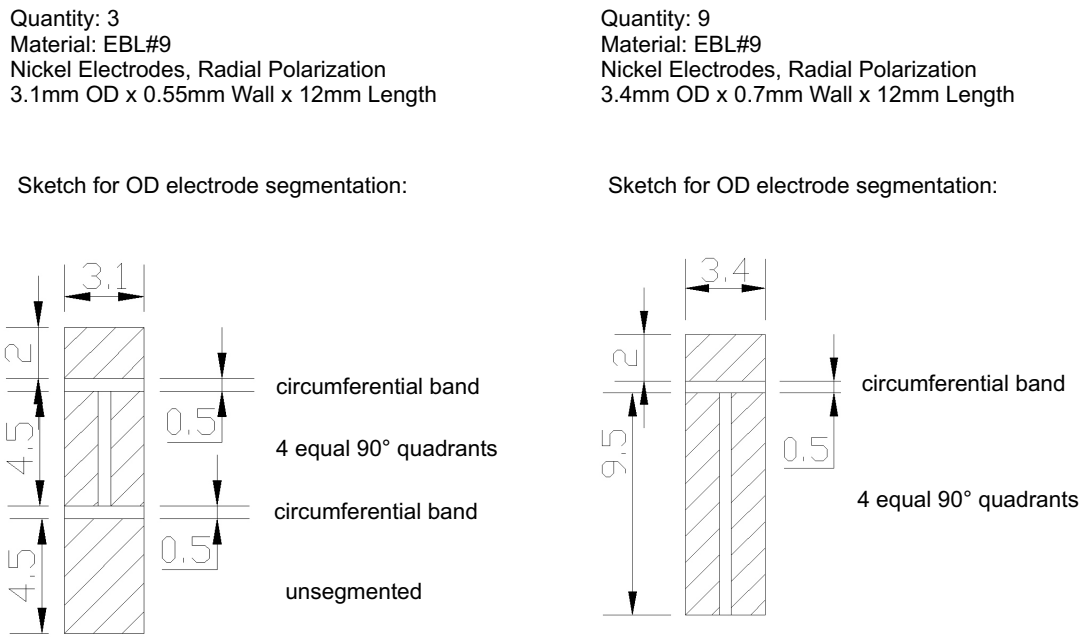

(a) Central piezo

(b) Outer piezos

Figure B.18: Segmentation plans for the two different piezo types of the hedgehog STM.

C Publications

Parts of the results presented in this thesis can be found in the following publications:

- D. F. Förster, J. Klinkhammer, C. Busse, S. G. Altendorf, T. Michely, Z. Hu, Y.-Y. Chin, L. H. Tjeng, J. Coraux, and D. Bourgault. Phys. Rev. B **83**, 045424 (2011). *Epitaxial europium oxide on Ni(100) with single-crystal quality.* doi:10.1103/PhysRevB.83.045424.
- T. Langer, D. F. Förster, C. Busse, T. Michely, H Pfnür, and C. Tegenkamp. New J. Phys. **13**, 053006 (2011). *Sheet plasmons in modulated graphene on Ir(111).* doi:10.1088/1367-2630/13/5/053006.
- D. F. Förster, T. O. Wehling, S. Schumacher, A. Rosch, and T. Michely. *Phase coexistence of clusters and islands: Europium on graphene.* New J. Phys., accepted.
- D. F. Förster, J. Klinkhammer, and T. Michely. *Eu oxides on Ni(100): polar surfaces, magic clusters and structures with large lattice dilation.* Submitted to Surf. Sci..

Apart from the topics EuO and graphene I also contributed to the following articles:

- D. F. Förster, S. Bleikamp, and T. Michely. Thin Solid Films **519**, 598 (2010). *Biaxially textured Ag films by grazing ion beam assisted deposition.* doi:10.1016/j.tsf.2010.06.007.
- S. Macko, F. Frost, B. Ziberi, D. F. Förster, and T. Michely. Nanotechnology **21**, 085301 (2010). *Is keV ion-induced pattern formation on Si(001) caused by metal impurities?.* doi:10.1088/0957-4484/21/8/085301.

D Kurzzusammenfassung

Das Wachstum des ferromagnetischen Halbleiters EuO wurde auf den Metallkristallen Ni(100) und Ir(111), sowie auf Graphen untersucht. Zur Charakterisierung wurden hauptsächlich in-situ Rastertunnelmikroskopie (RTM) und niederenergetische Elektronenbeugung benutzt. Die Epitaxie auf den Metallkristallen ist stark durch Grenzflächeneffekte bestimmt, welche zu einem komplizierten Wachstumsverhalten im Submonolagenbereich führen, vor allen auf Ni(100). Daher wurde für diese Substrate auch das Wachstum im Submonolagenbereich detailliert analysiert.

Europiumoxid zeigt auf Ni(100) eine Vielfalt verschiedener Oberflächenphasen im Submonolagenbereich, welche von der Wachstumstemperatur und vom Flussverhältnis von Eu zu O abhängen. Daher ist eine sorgfältige Einstellung der anfänglichen Wachstumsparameter entscheidend für die Erlangung eines Oberflächenoxids, das sich für die nachfolgende Epitaxie einer reinen EuO(100) Phase eignet. Nachdem ein drei Lagen dicker koaleszierter Oxidfilm erstellt wurde, kann für das weitere Wachstum eine Destillationsmethode benutzt werden. Ex-situ Röntgenadsorptionsspektroskopie und magneto-optische Kerr-Effekt Mikroskopie von dickeren Filmen auf Ni(100) liefern die gleichen Resultate wie für stöchiometrische, reine EuO Einkristalle.

Auf Ir(111) wachsen anfänglich lediglich polare EuO(111) Inseln, aber bereits vor Abschluss der ersten Oxidlage bildet sich auch EuO(100). Das Verhältnis von EuO(100) zu EuO(111) wird dabei vom Verhältnis der Flüsse von Eu zu O beeinflusst. Auf Ir(111) bestehen die EuO Filme also aus einer Mischung von EuO(111) und drei Rotationsdomänen EuO(100). Die dünnste mögliche Struktur des EuO(111) ist eine Bilage, für welche mittels Feldemissionsresonanzen eine Erhöhung der Austrittsarbeit um 6 eV gegenüber EuO(100) gefunden wurde. Trotz ihrer Polarität zeigt diese Bilage kein Zeichen einer Rekonstruktion welche das hohe elektrische Feld reduzieren könnte. Hingegen wurden in der dritten EuO(111) Lage dreieckige Rekonstruktionsmotive beobachtet.

Auf Graphen können EuO Filme gewachsen werden, welche aus einzelnen {100}-facettierten Körnern bestehen. Diese sind bei ausreichend hoher Wachstumstemperatur am Substrat orientiert. Da EuO auf dem Graphen nicht durch Grenzflächeneffekte beeinflusst wird, ist die anfängliche Wachstumsphase nicht entscheidend. Daher reagiert das Wachstum dieser Körner viel unsensibler auf das Verhältnis der Flüsse von Eu zu O als das EuO-Wachstum auf Ni(100).

Geeignete Ausheilprozeduren können die Leitfähigkeit von EuO hinreichend erhöhen um RTM und elektronenspektroskopische Untersuchungen durchzuführen, selbst für Filme von 100 nm Dicke. Mittels RTM wurden direkt Sauerstoffleerstellen abgebildet. Diese sind entscheidend für den Metall-Isolator-Übergang von EuO, welcher bei der Temperatur des paramagnetisch-ferromagnetischen Phasenübergangs auftritt. Zum ersten Mal wurden Tunnelspektren von EuO aufgenommen. Für EuO(100) mit 1% Sauerstoffleerstellen in der obersten Lage zeigen diese ungefähr 500 meV oberhalb des Ferminiveaus Zustände, welche sehr wahrscheinlich auf die Sauerstoffleerstellen zurückzuführen sind.

Auf allen Substraten ist das Gitter von einlagigen EuO(100) Filmen kontrahiert und vergrößert

sich wieder mit zunehmender Filmdicke. Selbst wenn das Substrat biaxialen Kompressionsdruck ausübt wird die Gitterkonstante von EuO Einkristallen bereits für 5 nm dicke Schichten annähernd erreicht. Daher besteht wenig Hoffnung die Curie-Temperatur von EuO durch epitaktische Kompression zu erhöhen.

Während der Untersuchung von EuO auf Graphen wurde Interkalation von Eu zwischen das Graphen und seinem Ir(111) Substrat beobachtet und weitergehend analysiert. Eu Deposition bei 720 K ergibt eine Vielzahl von Gleichgewichts-Interkalationsstrukturen in Abhängigkeit von der deponierten Eu Menge. Das Interkalat ist dabei niemals dicker als eine Monolage. Die Abmessungen und Orientierungen dieser Strukturen werden von Bindungsenergieunterschieden innerhalb der Einheitszelle des Moiré von Graphen auf Ir(111) bestimmt. Das energetisch bevorzugte Gitter des interkalierten Eu ist eine p(2×2) Struktur, aber die Interkalation endet erst nach der Sättigung der dichteren $(\sqrt{3} \times \sqrt{3})$R30° Struktur. Für beide Strukturen wurde mittels winkelaufgelöster Photoemissionsspektroskopie eine Verschiebung des Dirac-Kegels des Graphens um -1.5 eV gemessen.

Unterhalb von 400 K bleibt das Eu für geschlossene Graphenfilme aufgrund der Interkalationsbarriere obenauf. Die Adsorption und die Gleichgewichtsoberflächenphasen von Eu auf Graphen wurden im Temperaturbereich zwischen 35 K und 400 K untersucht, wobei die Bedeckungen zwischen einem kleinen Bruchteil einer Lage und etwas mehr als einer Lage variiert wurden. Mittels Dichtefunktional-Theorie, welche die Coulomb-Wechselwirkung der 4f-Elektronen berücksichtigt und elektronische Wechselwirkungen modelliert, wurde eine hervorragende Übereinstimmung mit den experimentellen Daten für die Gleichgewichtsadsorptionsphase, die Oberflächendiffusion und die Austrittsarbeit erlangt. Besonders erwähnenswert ist die Koexistenz einer Phase gleichmäßig verteilter Eu Cluster und großer Eu Inseln mit $(\sqrt{3}\times\sqrt{3})$R30° Struktur in einem zweidimensionalen Gleichgewicht, welche für eine mittelgroße Bedeckung bei 300 K auftritt. Die Bildung der Clusterphase entsteht durch das Zusammenspiel dreier Effekte: Erstens führt die metallische Eu-Eu Bindung zu einer lokalen Stabilität von $(\sqrt{3} \times \sqrt{3})$R30° Strukturen. Zweitens sinkt die kinetische Energie der Elektronen, wenn diese das Eu verlassen und das Graphen dotieren. Drittens wird für kleine Cluster weniger Coulomb-Energie durch den Ladungstransfer von Eu nach Graphen aufgebaut.

Acknowledgements

This work has greatly benefited from several people to whom I want to express my gratitude.

- First and foremost I would like to thank Thomas Michely. His scientific spirit, remarkable breadth of knowledge, and way of leading the workgroup is very inspiring and made me enjoying to work on this thesis.
- I would like to thank Hao Tjeng for being referee of this thesis. His strong interest in EuO was the nucleus of this work.
- I am grateful to Achim Rosch and Tim Wehling for the fruitful discussions and their theoretical input on the topic Eu on and under graphene. Without their help, the understanding this system would have been impossible.
- I want to thank Marko Kralj, Marin Petrović, Iva Šrut, Ivo Pletikosić, Petar Pervan, and Milorad Milun for the ARPES measurements of the intercalated Eu and for their hospitality during my stay in Zagreb.
- I would like to thank Zhiwei Hu, Simone Altendorf, and Yi-Ying Chin for the XAS measurements of the EuO film on the Ni substrate.
- I am thankful to Johann Coraux and Daniel Bourgault for performing the MOKE microscopy measurements of the EuO film on the Ni substrate.
- I thank Christoph Tegenkamp, Thomas Langer and Herbert Pfnür for the opportunity to attend the SPA-LEED and EELS measurements of graphene on Ir(111) and for their hospitality during my stay in Hannover.
- I would like to thank Carsten Busse for contributing to fruitful discussions about the EuO films and also for a lot of funny jokes during lunch time.
- A special thanks goes to Stefan Schumacher and Jürgen Klinkhammer. They contributed to this thesis with several measurements and analyses which they performed during their diploma thesis. They also did a lot of proofreading.
- I also want to thank the further proofreaders Sven Macko, Fabian Craes, Timm Gerber, Sebastian Standop, and Sven Runte.
- I am very thankful to Nobert Henn for numerous technical improvements of the system as well as for many interesting discussions.
- I owe a lot of thanks to the staff of the mechanical workshop of the II. Physikalisches Institut. This thesis would have been impossible without their work as they

manufactured many parts for the UHV system. I also want to thank the staff of the electrical workshop for their support on several occasions. Additionally, I am grateful to all the people who contributed to run the infrastructure of the II. Physikalisches Institut.

- I thank all actual members of our workgroup and also the former ones (especially Alpha N'Diaye and Alex Redinger) for the nice and friendly atmosphere and for the fun, especially during the table football sessions.
- Finally, I want to thank my mother who supported me during the whole period.

I also want to acknowledge the extensive funding of this project by the Deutsche Forschungsgemeinschaft through the Sonderforschungsbereich 608. My stay in Zagreb was financially supported by the Deutscher Akademischer Austausch Dienst.

Offizielle Erklärung

Ich versichere, dass ich die von mir vorgelegte Dissertation selbständig angefertigt, die benutzten Quellen und Hilfsmittel vollständig angegeben und die Stellen der Arbeit - einschließlich Tabellen, Karten und Abbildungen -, die anderen Werken im Wortlaut oder dem Sinn nach entnommen sind, in jedem Einzelfall als Entlehnung kenntlich gemacht habe; dass diese Dissertation noch keiner anderen Fakultät oder Universität zur Prüfung vorgelegen hat; dass sie - abgesehen von den angegebenen Teilpublikationen - noch nicht veröffentlicht worden ist sowie, dass ich eine solche Veröffentlichung vor Abschluss des Promotionsverfahrens nicht vornehmen werde. Die Bestimmungen der Promotionsordnung sind mir bekannt. Die von mir vorgelegte Dissertation ist von Prof. Dr. Thomas Michely betreut worden.

Köln, den 22. August 2011

Daniel Förster